NACA RM L55J03

NACA

RESEARCH MEMORANDUM

PRESSURE DISTRIBUTIONS AND AERODYNAMIC LOADINGS FOR SEVERAL FLAP-TYPE TRAILING-EDGE CONTROLS ON A TRAPEZOIDAL WING AT MACH NUMBERS OF 1.61 AND 2.01

By Douglas R. Lord and K. R. Czarnecki

Langley Aeronautical Laboratory
Langley Field, Va.

NATIONAL ADVISORY COMMITTEE
FOR AERONAUTICS

WASHINGTON

March 12, 1956

Declassified March 18, 1960

CONTENTS

	Page	Figure
SUMMARY	1	
INTRODUCTION	2	
SYMBOLS	2	
APPARATUS	4	
Wind Tunnel	4	
Model and Model Mounting	5	1 to 4
TESTS	5	
Techniques	5	3
Range of Conditions	6	
PRECISION OF DATA	6	
RESULTS	7	
DISCUSSION	7	
Pressure Distributions	7	
Effects of thickness distribution	7	5
Effects of δ	8	6 and 7
Effects of α	9	8 and 9
Boundary-layer separation	10	10 and 11
Variations across the wing span	12	12 and 13
Effects of parting lines	12	14 to 19
Effects of the wing tip	14	20 to 23
Effects of trailing-edge thickness	15	24 and 25
Effects of hinge-line gap	16	26
Effects of Reynolds number	17	27
Effects of Mach number	17	28
Chordwise Loadings	17	
Effects of δ	18	29
Effects of α	18	30 and 31
Effects of parting lines	19	32 to 38
Spanwise Loadings	21	
Normal-force loadings due to δ	21	39 to 48
Normal-force loadings due to α	22	39 to 48
Pitching-moment loadings due to δ	23	49 to 58
Pitching-moment loadings due to α	23	49 to 58

	Page	Figure
Centers of Pressure	24	59
CONCLUSIONS	25	
Pressure Distributions	25	
Chordwise Loadings	25	
Spanwise Loadings	26	
Centers of Pressure	26	
REFERENCES	28	
TABLE	30	
FIGURES	31	

NATIONAL ADVISORY COMMITTEE FOR AERONAUTICS

RESEARCH MEMORANDUM

PRESSURE DISTRIBUTIONS AND AERODYNAMIC LOADINGS FOR SEVERAL FLAP-TYPE TRAILING-EDGE CONTROLS ON A TRAPEZOIDAL WING AT MACH NUMBERS OF 1.61 AND 2.01

By Douglas R. Lord and K. R. Czarnecki

SUMMARY

An investigation has been made at Mach numbers of 1.61 and 2.01 for a range of Reynolds number from 1.7×10^6 to 5.6×10^6 to determine the pressure distributions, chordwise loadings, and spanwise loadings for a series of 25.4-percent-chord trailing-edge controls on a trapezoidal wing having a 23° sweptback leading edge, aspect ratio of 3.1, and taper ratio of 0.4. Measurements were made at angles of attack from 0° to ±15° for control deflections from -30° to 30°.

The pressure changes due to increasing the Mach number M were in fair agreement with the changes predicted by the $1/\sqrt{M^2 - 1}$ relationship. Variations in Reynolds number had a negligible effect. Flow through an enlarged hinge-line gap was in the direction from the high- to the low-pressure surface of the control. Shock-expansion theory and the semi-infinite line source and sink linear-theory method predicted the pressures due to wing thickness, whereas shock-expansion theory predicted the pressures due to control deflection; however, linear theory was generally unsuccessful in estimating the pressures in the regions affected by the wing-tip or wing-control parting lines. The chordwise loadings on the control tended to be rectangular due to control deflection or angle of attack, and on the complete wing tended to be triangular due to angle of attack. Separation and/or shock detachment ahead of the hinge line had little effect on the control spanwise normal-force loadings, but caused increased wing spanwise normal-force loadings. Increasing the trailing-edge thickness increased both the wing and control spanwise loadings. The experimental variations in loading across the span were linear and about 70 percent of the two-dimensional value predicted by linear theory, except for the wing normal-force loadings due to angle of attack which agreed with linear theory. Both the experimental carryovers of load from control to wing and losses in load from two dimensional to control tip region were less than predicted. The movements of the centers of pressure of the wing load with angle of attack and control deflection were, in general, smooth. The centers of pressure of the control loadings were located approximately at the control centroids.

INTRODUCTION

As part of a general program of research on controls, an investigation is under way in the Langley 4- by 4-foot supersonic pressure tunnel to determine the important parameters in the design of controls for use on a trapezoidal wing at supersonic speeds. The first results of the tests were reported in reference 1 and showed the control effectiveness and hinge-moment characteristics for a series of flap-type trailing-edge controls on a wing having 23° of sweep of the leading edge, an aspect ratio of 3.1, and a taper ratio of 0.4.

The present report is intended to be complementary to reference 1 in presenting the pressure distributions and discussing the basic flow phenomena involved in the flow over the wing-control configurations which produced the variations in integrated coefficients shown therein. In addition, the present report will present the chordwise and spanwise loadings associated with these wing-control configurations for the information of the structural designer. The use of available theoretical methods for predicting the pressure distributions and loadings will also be considered.

The wing angle-of-attack range for these tests was from 0° to ±12° or ±15° and the control deflection range, relative to the wing, was from -30° to 30°. The tests were conducted at Mach numbers of 1.61 and 2.01 for a Reynolds number range from 1.7×10^6 to 5.6×10^6, based on wing mean aerodynamic chord of 11.72 inches. The complete pressure-distribution results for these tests are presented in tabular form in reference 2.

SYMBOLS

c_m	section pitching-moment coefficient (taken about midchord of wing mean aerodynamic chord)
c_{m_f}	section pitching-moment coefficient due to control load
c_n	section normal-force coefficient
c_{n_f}	section normal-force coefficient due to control load
$b/2$	wing semispan
c	wing local chord
$\bar{c}$	wing average chord

c_R	wing root chord
M	stream Mach number
M_l	local Mach number on surface ahead of hinge-line shock
p	stream static pressure
p_l	local surface pressure
p_1	local static pressure on surface ahead of hinge-line shock
p_2	local static pressure on surface behind hinge-line shock
$\left(\frac{p_2}{p_1}\right)_{cr}$	critical pressure ratio for causing flow separation
$\left(\frac{p_2 - p_1}{q_1}\right)_{cr}$	critical pressure-rise coefficient for causing flow separation
P	pressure coefficient, $\frac{p_l - p}{q} = \frac{2}{\gamma M^2}\left(\frac{p_l - p}{p}\right)$
P_R	resultant pressure coefficient (lower surface P minus upper surface P)
P_S	pressure coefficient corresponding to sonic local velocity
q	stream dynamic pressure
q_1	local dynamic pressure ahead of hinge-line shock
R	Reynolds number (based on wing mean aerodynamic chord)
t	ratio of control trailing-edge thickness to hinge-line thickness
x	distance in chordwise direction: (a) from wing apex in x/c_R plots (b) from local leading edge in x/c plots

$\bar{x}$ chordwise distance from wing apex to center of pressure of wing plus control loading

$\bar{x}'$ chordwise distance from hinge line to center of pressure of control loading

y distance in spanwise direction from wing root chord

$\bar{y}$ spanwise distance from wing root chord to center of pressure of wing plus control loading

$\bar{y}'$ spanwise distance from wing root chord to center of pressure of control loading

α wing angle of attack streamwise, deg

$\beta = \sqrt{M^2 - 1}$

γ ratio of specific heat at constant pressure to specific heat at constant volume

δ control deflection relative to wing (positive when control trailing edge is down), deg

δ_s effective flow separation angle

δ_{max} maximum turning angle possible

Δ prefix indicating change due to α or δ

APPARATUS

Wind Tunnel

This investigation was conducted in the Langley 4- by 4-foot supersonic pressure tunnel, which is a rectangular, closed-throat, single-return type of wind tunnel with provisions for the control of the pressure, temperature, and humidity of the enclosed air. Flexible nozzle walls were adjusted to give the desired test-section Mach numbers of 1.61 and 2.01. During the tests, the dewpoint was kept below -20° F at atmospheric pressure so that the effects of water condensation in the supersonic nozzle were negligible.

Model and Model Mounting

The model used in this investigation consisted of a trapezoidal wing having six interchangeable trailing-edge controls and various associated control adapters (or replacement sections) required to fit the controls to the basic wing. A sketch of the six model configurations is shown in figure 1 with the shaded areas denoting the movable controls.

The basic wing had a 23° sweptback leading edge, a root chord of 15.88 inches, a tip chord of 6.17 inches, and a semispan of 17.02 inches. The wing section was a modified hexagon having a constant ratio of local thickness to local chord of 4.5 percent. The flat midsection extended from 30-percent chord to 70-percent chord and the corners joining the flat midsection to the leading- and trailing-edge wedges were rounded to a 22.5-inch radius. The unswept hinge lines were located at the 74.6-percent-chord line for all control configurations. As shown in figure 1 control configurations 4, 5, and 6 had identical plan forms, but varying amounts of trailing-edge thickness; t = 0, 0.5, and 1.0, respectively. The hinge-line gap was maintained at 0.01 inch (0.08 percent $\bar{c}$) for all configurations except for one series of tests with configuration 4 in which the gap was increased to 0.20 inch (1.71 percent $\bar{c}$) by moving the control and hinge line rearward.

The model was constructed of steel, with the pressure-tube installations made in grooves in the surface which were faired over with a transparent plastic material. The 144 to 169 pressure orifices were located at five spanwise stations on the main wing ahead of the control hinge line and at five to eight spanwise stations behind the hinge line, depending on the configuration being tested. The chordwise locations of the pressure orifices are listed in table I and the spanwise locations of the orifice stations are shown in figure 2. All screw holes, pits, and mating lines were filled with dental plaster and faired smooth.

The semispan wing was mounted horizontally in the tunnel from a turntable in a steel boundary-layer bypass plate which was located vertically in the test section about 10 inches from the side wall as shown in figure 3. A photograph of model configuration 2 mounted for testing is shown in figure 4. Although the clearness of the plastic material over the tubing installations makes it appear that the wing surface is rough, actually the finish was very smooth.

TESTS

Techniques

The model angle of attack was changed by rotating the turntable in the bypass plate on which the wing was mounted. (See fig. 3.) The angle

of attack was measured by a vernier on the outside of the tunnel, inasmuch as the angular deflection of the wing under load was negligible. Control deflection was changed by a gear mechanism mounted on the pressure box which rotated the strain-gage balance, the torque tube, and the control as a unit. The control angles were set with the aid of an electrical control-position indicator mounted inside the wing at the hinge line and were checked with a cathetometer mounted outside the tunnel. The pressure distributions were determined from photographs of the multiple-tube manometer boards to which the pressure leads from the model orifices were connected.

Most of the controls were equipped with orifices on one surface only, because structural limitations made it impossible to get the necessary pressure tubes through the torque tube to instrument both surfaces. For these models, the tests were run at positive and negative angles of attack over the control-deflection range and the necessary summations of the pressures on the individual surfaces for determining the loadings were made at reversed angular conditions.

Range of Conditions

The majority of the test configurations had a control deflection range from -30° to 30° for angles of attack of 0°, $\pm 6^\circ$, and $\pm 12^\circ$ and an angle-of-attack range from 0° to $\pm 15^\circ$ for 0° control deflection. Most of the tests were made at tunnel stagnation pressures of 13.0 and 15.1 pounds per square inch at Mach numbers of 1.61 and 2.01, respectively, corresponding to a Reynolds number of 3.6×10^6 based on the wing mean aerodynamic chord. Additional tests were made with configuration 4 in which the tunnel stagnation pressure was varied to give Reynolds numbers of 1.7×10^6 and 5.6×10^6 at $M = 1.61$ and Reynolds numbers of 1.7×10^6 and 4.5×10^6 at $M = 2.01$. In order to insure a turbulent boundary layer over the model during the tests, 3/16-inch-wide strips of no. 60 carborundum were attached to the wing upper and lower surfaces at a distance of 1/4 inch from the leading edge. These strips completely spanned the model except within 1/4 inch of the orifice stations.

PRECISION OF DATA

The mean Mach numbers in the region occupied by the model are estimated from calibrations to be 1.61 and 2.01 with local variations being smaller than ± 0.02. There is no evidence of any significant flow angularities. The estimated accuracies in setting the wing angle of attack and control deflection are $\pm 0.05^\circ$ and $\pm 0.1^\circ$, respectively. The basic measured quantity P is believed accurate to ± 0.01.

RESULTS

The results of this investigation are presented in four sections. In the first section entitled "Pressure Distributions," covering figures 5 through 28, are presented some typical pressure-distribution results. While the plots presented in this section represent only a small fraction of the available data, an attempt has been made to indicate in sufficient detail the general features of the flow and the effects of the many variables studied in this investigation on this flow. In the second section entitled "Chordwise Loadings," corresponding to figures 29 through 38, a study is made of the chordwise loadings. Since the essential features of the flow generating these loadings were discussed in the first section, the discussion in this section is generally limited to that needed to orient the figures. The spanwise normal-force- and pitching-moment-loading distributions are covered in the third section entitled "Spanwise Loadings" and figures 39 through 58. Because of the condensed form of the data and the general interest in this type of loading, the data for all six configurations have been presented in entirety. The chordwise and spanwise center-of-pressure results are presented in entirety in the fourth section entitled "Centers of Pressure" and figure 59.

DISCUSSION

In considering the results of this investigation, it should be remembered that the integrated force and moment characteristics have already been presented in reference 1. The variations shown herein, whether of pressures or of loadings, illustrate in detail the reasons for the variations in forces and moments discussed in reference 1. Wherever possible, these points will be emphasized.

Pressure Distributions

Effects of thickness distribution.- Some typical chordwise pressure distributions obtained across the span of the model at α and $\delta = 0^\circ$ are presented in figure 5 for the two test Mach numbers of 1.61 and 2.01. The symbol P is the usual pressure coefficient and x/c_R the chordwise station in terms of the root chord. Data are shown for two configurations, 2 and 4, to illustrate the good agreement obtained between models. The experimental results are compared with the section thickness pressures computed by the semi-infinite line source and sink technique devised by Jones (ref. 3) and illustrated in somewhat more detail in reference 4. In order to save some computational time, it was assumed that the intersections of the flat surfaces of the wing section were sharp instead of

rounded as they really are. The comparison indicates very good agreement between theory and experiment except in the neighborhood of the intersections of the flat wing sections near the wing tip. This disagreement, of course, is primarily the result of the simplification in the theoretical calculations. A comparison of the chordwise pressure distributions at the various spanwise stations also indicates that, despite the sweepback and taper of this wing, the thickness effects are essentially two dimensional across the span. As a result of this two dimensionality, it is possible to estimate the thickness effects by use of the shock-expansion technique. These calculations indicate that the pressure coefficients on the front, middle, and rear flats of the wing section for $M = 1.61$ are 0.130, -0.001, and -0.109, respectively. These values are in good agreement with experiment.

Effects of δ.- Some typical effects of control deflection on the chordwise pressure distributions are shown in figure 6. These results were obtained at stations 3 and 7 on configuration 4 at $M = 1.61$ and $R = 3.6 \times 10^6$. The similarity of the results for the two spanwise stations shows that even at combined angle of attack and control deflection the flow is essentially two dimensional across the span. At low values of δ (10° or less for these plots), the chordwise pressure distributions are uniform on both sides of the control and there is no effect of δ on the pressures on the main wing ahead of the hinge line. At higher values of δ the pressure rise at the control hinge line is sufficiently high to separate the boundary layer some distance ahead of the control surface or to cause detachment of the hinge-line shock, and there is a resultant carryover of the control pressures to the main wing.

On the upper surface at positive control deflections and on the lower surface at large negative δ's, the pressures on the control surface show relatively little change with control deflection. There are two reasons for this small change: First, the pressures are asymptotically approaching a vacuum ($P = -0.55$ at $M = 1.61$), so that a large expansion of the flow results in only a small change in pressure. Second, boundary-layer separation occurs at the higher δ's due to the strong trailing-edge shock, thus limiting the amount of flow expansion that can be attained.

Another interesting observation made from the results of figure 6 and the other available data is that at sufficiently high angles of attack and control deflection the flow over the control on the control high-pressure surface becomes subsonic ($P > 0.64$). Any further increase in δ causes the pressures over the middle of the control surface to become more positive or more subsonic but the pressure at the trailing edge remains sonic. This latter fact is illustrated in figure 6 by the tendency of the pressure at high positive α's plus δ's to approach the sonic pressure point indicated at $P = 0.64$. This result is to be expected since the flow can expand to supersonic velocity again only

around a corner which in this case is the trailing edge. For the stipulated conditions, a tendency also was found for the peak positive pressure to reach a maximum value which could not be exceeded by any further control deflection. (See, e.g., lower surface: $\alpha = 6^\circ$; $\delta = 20^\circ$ and 25°.) This maximum was a function of the angle of attack of the wing.

The results presented in figure 6 contain, of course, the combined effects of thickness, angle of attack, and control deflection. In order to isolate the effects due to δ, the data have been replotted in figure 7 as $\Delta P/\delta$, the average increment in pressure coefficient due to unit control deflection. The experimental results also are compared with three-dimensional linear theory (e.g., ref. 5) and with some calculations in which three-dimensional linear theory was used to determine the conditions at the control hinge line and two-dimensional shock-expansion theory was used to compute the pressures over the control from these values. Linear theory was used instead of shock expansion to determine conditions on the wing just ahead of the hinge line because the pressure calculations could be carried to angles of attack beyond the point where the bow wave detaches and spanwise variations in flow could be included. For very large δ's, the combination linear-shock-expansion theory indicated shock detachment ahead of the control and hence no pressures could be determined over the control high-pressure surface.

In addition to the trends discussed in the previous figure, the plots in figure 7 indicate that the experimental results generally are not in good agreement with linear theory. The composite theory, however, provides a good approximation of the experimental data except for the conditions when the local supersonic Mach number at the hinge line becomes small. This trend becomes noticeable on the control lower surface at $\alpha = 6^\circ$ and $\delta = 10^\circ$ (fig. 7(b)) and becomes quite obvious at $\alpha = 12^\circ$ and $\delta = 10^\circ$ where shock detachment has occurred or is iminent (fig. 7(c)). In some cases the experimental results tend to diverge from the composite theory calculations on the upper control surface at positive δ's (e.g., fig. 7(a)) because of flow separation at the trailing edge which is not accounted for in the theory.

Effects of α.- The effects of α on wing and control chordwise pressure distributions are illustrated in figure 8. These results were obtained on the full-span control, configuration 4. In general, the changes in pressure distributions with α were quite regular. As α was increased the pressures on the lower wing surface near the leading edge lost their rectangular shape and increased rapidly. On the upper surface the pressures indicate localized flow separation at the wing leading edge. Both effects are somewhat more pronounced at the outboard station. These effects are due to bow-wave detachment with increasing angle of attack. The pressures on the control and just ahead of it vary uniformly with α when $\delta = 0^\circ$ or -20°. When $\delta = 20^\circ$, the pressures on the control upper surface vary only slightly with α, primarily because

the pressures are already close to a vacuum and partly because flow separation has occurred. On the lower control surface the pressure distributions indicate flow separation and/or shock detachment ahead of the hinge line which increases in severity with α. For conditions where the flow over the control is subsonic, the results again indicate a tendency for the pressures at the control trailing edge to remain fixed at the sonic value regardless of change in α.

In figure 9 the effects of angle of attack have been isolated by subtracting the pressures at $\alpha = 0^\circ$ from those at $\alpha = 6^\circ$ and 12° and dividing by the corresponding angle of attack. The experimental results are also compared with linear theory (e.g., refs. 6 and 7). The comparison shows that large disagreements exist between theory and experiment. On the wing lower surface near the leading edge, the disagreement is due to bow-wave detachment. On the control upper surface the experimental incremental pressures fall below the theoretical values at $\delta = 0^\circ$, indicating that the flow has separated as a result of the excessive pressure rise at the trailing-edge shock.

When $\delta = 20^\circ$, the pressures on the control upper surface already are close to vacuum at $\alpha = 0^\circ$ (see fig. 8) and any further increase in α causes only a very small further increase in negative pressure. On the lower surface there is only a small amount of flow separation ahead of the hinge line at $\alpha = 0^\circ$. Hence, an increase in angle of attack results in a large increase in pressure increment both on the control and on the wing ahead of the hinge line as the magnitude of the separation effect increases with α. These differences between theory and experiment may actually be ascribed to mutual interaction between the angle-of-attack and control-deflection effects.

When $\delta = -20^\circ$, the effects of α and δ oppose one another. As the angle of attack is increased, the pressures on the control upper surface produce a larger increment in $\Delta P/\alpha$ than occurs ahead of the control or than is predicted by linear theory. This result is a consequence of the nonlinear changes in pressure across the hinge-line shock. On the control lower surface the experimental pressures register considerably less gain than theory for the same reason as the loss in effectiveness of the control upper surface at positive δ's.

Boundary-layer separation.- In the discussion of the results presented in figures 6 through 9, it was pointed out that if the pressure rise at the trailing-edge or hinge-line shocks was very large, boundary-layer separation occurred and the pressure distributions over the separated regions were altered. If the local supersonic Mach number was low (as at the hinge line at high α's), shock detachment could occur before a pressure rise sufficiently high for separation was encountered. The angular conditions at which these effects will first appear can be determined approximately from the results presented in figure 10. The ratio

$(p_2\ p_1)_{cr}$ is defined as the pressure-rise ratio across the trailing-edge or hinge-line shock (see sketch in upper part of figure) for which the orifice nearest the trailing edge or hinge line first shows evidence of the pressure rise associated with separation or shock detachment. The coefficient $\left(\frac{p_2 - p_1}{q_1}\right)_{cr}$ was established similarly. The local Mach number immediately in front of the shock is defined as M_1. Both criterions for establishing the critical pressure are illustrated because it is not known at present which one may eventually prove more useful. The experimental data, indicated by the symbols, were obtained at the hinge line at several inboard pressure stations on configurations 4, 5, and 6 at both test Mach numbers. Similar data at the control trailing edge could not be obtained inasmuch as the pressures aft of the trailing-edge shock are unknown and separation usually extended to the control hinge line where there was too large a change in M_1 to be determined by the available orifices. It is expected that the results obtained at the hinge line should apply to flow at the control trailing edge.

The experimental results indicate that as the local Mach number M_1 increases, the pressure ratio $(p_2/p_1)_{cr}$ increases and the pressure-rise coefficient $\left(\frac{p_2 - p_1}{q_1}\right)_{cr}$ decreases. At $M_1 = 1.4$ or less, the pressure increases ahead of the hinge line or trailing edge are apparently the result of shock detachment. Boundary-layer separation may or may not be present within this range. A comparison of the present results with the calculations made by Mager (ref. 8) and the data compiled by Bogdonoff (ref. 9) and Holder, Pearcey, and Gadd (ref. 10) indicates that the present data are only in approximate agreement with any one of the predictions. An analysis of other available data at higher local Mach numbers with turbulent boundary layer (e.g., refs. 11 and 12) shows a tendency for the trend to follow that indicated by reference 10.

If δ is increased beyond the point required to separate the boundary layer or cause shock detachment, or if M_1 is further decreased after shock detachment has occurred, then the separation or shock-detachment point moves forward. On the control low-pressure surface, the separation point moves rapidly to the hinge line where it then remains relatively stationary and hence poses no problem as the movement can be assumed to be instantaneous for all practical purposes. On the high-pressure side, however, it is often desirable to estimate the approximate location of the separation or shock-detachment point. In figure 11, a study has been made to determine whether this is feasible. For the same configurations analysed in figure 10, an effective separation angle δ_S has been computed which is defined as the angle between the surface from which the flow is assumed to separate and a straight line drawn from the separation

point to the control trailing edge. The experimental angles thus determined are plotted as a function of the theoretical local Mach number. Theoretical values of M_1 are used to simplify the estimation procedure as the actual values sometimes may not be known.

The results indicate that at low values of M_1 (1.5 or less), the effective separation angle is about equal to the theoretical maximum turning angle deduced from shock-expansion theory. At higher values of M_1, the effective separation angle tends to increase and then steady out. The angles computed from the Mach 2.01 test data appear to be somewhat higher than those determined for the $M = 1.61$ tests for reasons which are not known. The results also are compared with the angles computed from the separation criterions presented in references 8, 9, and 10. The present data are underestimated by the predictions of references 8 and 10 but appear to follow the same trends.

Variations across the wing span.- In the previous discussions of the effects of control deflection and angle of attack, only stations 3 and 7 on the full-span controls were used. In figure 12 the pressure distributions are shown for all five stations on the full-span control (configuration 4) at several combinations of control deflection and angle of attack. It is obvious from this figure that the loadings at the first four stations are almost identical, regardless of the angle settings. The station near the tip, however (station 8), shows considerable end effect, particularly on the control when the control deflection and angle of attack are in opposition (e.g., fig. 12(b)). This effect will be discussed in more detail later.

A more graphic picture of the pressure distributions across the span of this control is presented in figure 13 for an extreme control deflection at $\alpha = 6^\circ$. Here the similarities in the pressures measured across the span are readily apparent. The most obvious tip effect that can be noted for the condition shown is on the wing ahead of the hinge line.

Effects of parting lines.- Since the control configurations investigated were all trailing-edge flap type of constant percent chord, the major change in configuration plan form or location involved a movement of the wing-control parting line. It will be significant then, to examine the pressure distributions in the neighborhoods of the various parting lines. Figures 14, 15, and 16 show the pressure distributions on the wing and on the control near the parting lines of the three partial-span control configurations tested.

The effect of control deflection on the pressures measured over the wing at stations some distance from the parting line (e.g., fig. 14, station 4; fig. 16, station 1) does not appear until the control deflection becomes quite large. This effect appears as an increasing pressure near

the wing trailing edge and the region affected becomes larger as the control deflection or angle of attack is increased. This loading carryover is much more pronounced on the side of the wing toward which the control is deflected.

At the wing stations immediately adjacent to the parting line, the effects of control deflection become apparent as soon as the control is deflected. The changes observed are associated with the unporting of the control as it is deflected, causing the lower surface of the control to be above the upper surface of the adjacent wing at negative deflections and the upper surface of the control to be below the lower surface of the adjacent wing at positive deflections. For the positive control deflections the lower surface of the wing is primarily affected with an increased pressure in the vicinity of the hinge line followed by a sharp reduction to a decrease in pressure near the trailing edge. This is caused first by the high pressure from the control lower surface feeding over onto the adjacent wing surface and second by the high pressure from the wing lower surface near the trailing edge feeding over onto the adjacent control upper surface which is experiencing a low pressure. When the control is deflected negatively, at angles of attack, both surfaces of the wing are affected. In this case the upper surface of the wing has a pressure variation similar to that previously described for the lower surface at the positive deflections, with the chordwise variations being modified somewhat because the control is now operating adjacent to the wing low-pressure flow field. The pressure on the wing lower surface tends to decrease as the control is deflected negatively because of the relieving tip effect possible at the wing parting line as the control unports.

The pressure distributions on the control are similar in nature to those previously shown on the full-span control; however, the relieving effect of the parting line causes some loss in loading which is apparent in the decreased pressures on the lower surface at station 6 as compared to station 7 on configuration 1 (fig. 14) or at station 3 as compared to station 4 on configuration 3 (fig. 16). Note that the pressure distributions at stations 3 and 5 on configuration 2 (fig. 15), both of which are adjacent to parting lines, are very much alike despite the difference in spanwise location and orientation of the station with respect to the parting line.

In view of the similarities shown for the effects of the various parting lines, let us now consider how well the parting-line effects for a typical case are predicted by linear theory. In figure 17 a comparison of the experimental and theoretical incremental pressure distributions divided by the control deflection is shown for the wing and control stations adjacent to the outboard parting line of configuration 2. In general, the linear theory fails to predict either the magnitude or the variation along the chord of the pressures at the stations shown. Since it was previously shown that the linear-theory prediction of the effect of

control deflection was very poor in the two-dimensional region, it would have been expected that the magnitudes of the theoretical pressures would be in error for the parting-line stations also. The fact that the experimental variation in pressure along the chord does not agree with the theoretical prediction indicates that the linear-theory assumptions do not properly account for the flow conditions at the parting lines. The unporting of the control to allow violent crossflows and interaction between upper and lower surfaces is in direct contrast to the assumptions of linear theory which require no unporting and small perturbations. The experimental data do show a consistent trend with increasing control deflection, although the scatter indicates the degree of nonlinearity existing.

In order to compare, qualitatively, the spanwise variation of the pressure distributions for the partial-span configurations with that previously shown (fig. 13) for the full-span configuration, schematic pressure distributions are shown in figure 18 for the three partial-span control configurations at $\alpha = 6^\circ$, $\delta = 30^\circ$. As a further means of demonstrating the extent of influence of a partial-span control due to control deflection, contour plots showing lines of constant pressure coefficient are shown in figure 19 for configuration 2 at $\alpha = 6^\circ$ as the control deflection is increased from 0° to 30°. The change in spanwise and chordwise influence of the control with increase of the control deflection is readily apparent from this type of plot.

Effects of the wing tip.- During the discussion of figures 12 and 13, the changes in pressure distribution due to wing-tip effects were briefly mentioned. In order to discuss these effects in more detail, the pressure distributions for the two stations closest to the wing tip are compared in figure 20 for $\alpha = 0^\circ$ and 6°. Configuration 4 has been used; however, it may be considered typical of the controls which extend to the wing tip. On station 8 at $\alpha = 0^\circ$, the effect of control deflection alone shows an increase in pressure on the lower surface near the hinge line followed by an expansion due to the relieving effect of the wing tip. On the upper surface, the reverse effect is present, first the expansion at the hinge line and then a sharp compression; however, on this surface an unexpected effect appears in the ensuing expansion ahead of the trailing edge. These variations in pressure distributions due to δ at station 8 are considerably different from those at the essentially two-dimensional station 7, which were discussed in detail previously (figs. 6 and 7). It is believed that these variations are caused by a vortex formation about the tip of the control which tends to wind up in the neighborhood of the upper surface. At an angle of attack of 6°, an additional vortex pattern is probably formed about the wing tip ahead of the control so that when the control is deflected a very complicated flow field would result, in particular for the negative deflections. The pressure distributions shown for $\alpha = 6^\circ$ tend to verify this conclusion.

The question arises then as to whether it is possible to predict these changes in pressure near the tip. The linear-theory predictions of the incremental pressure distributions corresponding to the conditions shown in figure 20 are presented in figure 21 as compared to the experimental values. The linear theory is, of course, unable to predict the effect of the separation or shock detachment ahead of the hinge line, and does a fair job in predicting the pressures over the control in the two cases where the vortex flow seems to have the least effect, that is, on the lower surface at $\alpha = 0^\circ$ and on the lower surface for the control deflected negatively at $\alpha = 6^\circ$. For the remaining cases, there is little agreement between linear theory and experiment.

A further refinement to the theoretical technique of estimating the loadings in the tip region of a simplified wing has been presented in reference 13. The increase in lifting pressures as a result of the formation of a tip vortex is in qualitative agreement with the results shown herein.

Now let us consider the effect of angle of attack on the pressure distributions near the wing tip. In figure 22 are presented the pressure distributions for stations 7 and 8 at $\delta = 20^\circ$, 0°, -20° as configuration 4 is varied in angle of attack from 0° to 12°. At $\delta = 0^\circ$, as the angle of attack is increased, the pressure distributions on the lower surface of the tip station over the rear 50 percent of the chord show little change. This again demonstrates the relieving effect of the tip which potential theory tells us to anticipate. On the upper surface, however, instead of the little change to be expected, the pressures show larger changes due to α than at station 7. This indicates that our previous assumption of a tip vortex decreasing the pressure on the upper surface in a small region near the tip is apparently sound. At $\delta = \pm 20^\circ$, the interaction of the angle of attack and control deflection effects makes it impossible to make any further deductions from the pressure distributions.

In an attempt to predict the angle-of-attack effects in the vicinity of the tip, the linear-theory values of incremental pressure coefficient due to α have been computed for station 8 and are compared in figure 23 with the experimental values obtained from figure 22. For the undeflected control, the trend of the variation in pressure along the chord on the lower surface is in fair agreement with the linear-theory predictions. On the upper surface, however, the predicted increase in pressure along the chord does not materialize because of the formation of the vortex previously discussed. For the control-deflected cases, the scatter in the experimental values for the two angles of attack is increased and the variations along the chord show increasing dissimilarities with theory.

Effects of trailing-edge thickness.- In figure 24, a few typical pressure distributions are presented to show the effect of increasing

the trailing-edge thickness ratio t from 0 to 1.0. In general, increasing the trailing-edge thickness increases the pressures over both surfaces of the control. The change in pressure coefficient due to increasing the trailing-edge thickness is generally greater on the compression side of the control than on the expansion side as would be expected from the nonlinear variation of pressure coefficient with flow deflection predicted by shock-expansion theory. It appears for many of the cases in figure 24 that increasing the thickness from $t = 0$ to $t = 0.5$ causes a considerable pressure increase, but further increasing the trailing-edge thickness causes little change. Analysis of all the results available, including some at negative angles of attack, indicates that this lack of a regular change in pressure with increasing thickness was due to a basic error in setting the control-deflection angles for configuration 5, for which $t = 0.5$. Since it is not possible to apply an accurate correction to the data for this model, the data are presented uncorrected; however, it is believed that were the data corrected, the changes in pressure (fig. 24) and integrated characteristics (see ref. 1) with increasing trailing-edge thickness would be regular.

The effects of trailing-edge thickness on the hinge-line and trailing-edge separation phenomena are readily apparent from the pressure-distribution comparison at $\alpha = 6^\circ$, $\delta = 20^\circ$. As the trailing-edge thickness increases, the flow separation ahead of the hinge line on the lower surface increases and the flow separation on the upper surface near the trailing edge decreases. These changes are a direct result of the changes in angle through which the flow must turn at the hinge line and at the trailing edge.

A correlation of the average final pressure coefficients attained on the surfaces of the controls on configurations 4, 5, and 6 with the values computed by the method of shock-expansion theory is shown in figure 25. For the purposes of this correlation, it was found that a parameter which provided good agreement was the angle between the control surface and the free stream. Thus, no matter how the flow negotiated the wing and control surfaces, from the value of this angle, shock-expansion theory was able to accurately predict the average pressure coefficient, except for conditions in which shock detachment or separation occurred ahead of the hinge line. As was shown previously, for angular conditions below which separation or shock detachment occurred ahead of the hinge line, the pressure distributions over the control were essentially flat; therefore, this method can be used to estimate the two-dimensional control loading with considerable accuracy.

Effects of hinge-line gap.- The effects on the pressure distributions of increasing the hinge-line gap from 0.01 to 0.20 inch are shown in figure 26. Although the change in gap is a relatively small one and therefore the resulting pressure changes are also small and situated almost entirely on the control itself, some systematic variations are

evident. In almost every instance, the large gap configuration has a higher pressure than does the small gap configuration on the control high-pressure surface and a smaller pressure on the control low-pressure surface. This indicates that regardless of the wing angle of attack, the air flow through the gap is always from the flap high-pressure side to the low-pressure side, thus increasing the angle through which the flow must be compressed by the flap on the high-pressure side, and further accelerating the air over the flap low-pressure surface. The final result of these pressure changes appears as an increased effectiveness and hinge moment due to increasing the gap (see ref. 1).

Effects of Reynolds number.- The changes in some typical pressure distributions due to increasing the Reynolds number from 1.7×10^6 to 3.6×10^6 or 5.6×10^6 are demonstrated in figure 27. In general, the changes are small and inconsistent with changes in Reynolds number and indicate that the lack of Reynolds number effect on the integrated coefficients shown in reference 1 is due to a lack of Reynolds number effect on the pressures, and is not due to compensating changes in the pressures.

Effects of Mach number.- Although the Mach number range of these tests was rather limited, it is of interest to see how close the Mach number effects can be estimated. In general, it is anticipated from theory that the pressure-distribution change with Mach number will be in the ratio of the corresponding β values. The normalized pressure distributions for a few angle conditions are compared in figure 28 for the two Mach numbers. The β relationship tends to give a fairly good correlation except in instances where large viscous separation effects appear. It was pointed out in reference 1 that this type of agreement may be possible at considerably higher Mach numbers. Comparison of the pressure distributions at both Mach numbers for the stations near the wing tip and near the wing-control parting lines indicates that the effects previously described at $M = 1.61$ are repeated at $M = 2.01$ with only minor variations in magnitude and extent of disturbances which are in agreement with the predicted effect of Mach number. This is in accord with the predicted effect of Mach number on the integrated coefficients shown in reference.

Chordwise Loadings

To the aerodynamicist, the previous discussion on the pressure distributions is of basic and therefore paramount interest in the present investigation. From the loads standpoint, however, it is of interest to discuss the effect of the primary variables on the distribution of loading along the chord. Figures 29 through 38 have been prepared, therefore, to show some typical effects of control deflection, angle of attack, and station location on the chordwise loading distributions at selected spanwise stations.

Effects of δ.- The chordwise loading distributions along the control chord at three spanwise stations on the full-span control configuration 4 at an angle of attack of 6° are shown in figure 29. On the left of the figure the resultant pressure-coefficient distribution is shown, in the center the incremental resultant pressure coefficients due to control deflection are plotted, and on the right of the figure the incremental pressure coefficients have been divided by the appropriate control deflection. At stations 1 and 4, where the flow is essentially two dimensional in nature, the $\Delta P_R/\delta$ points obtained have little scatter within the control-deflection range shown, indicating a linear variation of loading with control deflection, and the loading is rectangular in nature. Comparison of the experimental values with those computed by linear theory for these stations shows that the experimental loadings are approximately 70 percent of the theoretical values. At station 8, near the tip of the wing and control, a sharp reduction in loading occurs over the last 80 percent of the control chord at the negative control deflections as a result of the complicated vortex-flow pattern in this region which was discussed previously. As the negative control deflection is increased, the loss in loading at this station decreases. At $\delta = -10°$, where there is little tendency for vortex formation at the control tip, the loading variation along the chord is similar to but appreciably lower than that predicted by linear theory. Departure from this condition by increasing or decreasing the control deflection causes the loading to approach the rectangular shape.

Effects of α.- Since it has been previously demonstrated that the effects of angle of attack are concentrated in a region near the wing tip, the chordwise loadings at two stations near the wing tip are shown in figure 30 for control deflections of 0° and $\pm 20°$. At station 7, as the angle of attack is increased from 0° to 12° or 15°, the change in loading for a given control deflection is generally a change in magnitude, as the shapes of the distributions remain essentially similar. This conclusion is modified to some extent at $\delta = 20°$ when the separation ahead of the hinge line causes increased loadings in this region. At the tip (station 8), in addition to the changes in loading ahead of the hinge line, the shapes of the control loadings for $\delta = \pm 20°$ change in an erratic manner as the angle of attack is increased.

These variations are emphasized when the incremental loadings due to angle of attack are divided by the angle of attack, as shown in figure 31. In addition to the effects previously mentioned, it appears from this figure that the loading ahead of the hinge line at station 8 is much less than would be expected at $\alpha = 3°$, $\delta = 0°$ in view of the loadings obtained at the higher angles of attack. Examination of the discussion in reference 13 concerning the nonlinear effect of the tip vortex separation on the lift indicates that, for our case, at $\alpha = 3°$ the tip vortex has not built up sufficient strength to appreciably affect the loading at this station and the experimental variation therefore agrees fairly

well with the linear theory. It is interesting to note that when viscous separation effects are not present at station 7 (and stations farther inboard), the incremental loading due to angle of attack tends to be triangular in nature. Over the rear portion of the chord, the variation in loading conforms to that theoretically predicted, but with a magnitude of approximately 70 percent of the theoretical. On the forward portion of the wing, the bow-wave shock detachment previously described (see fig. 9) considerably increases the loading above the linear-theory value.

Effects of parting lines.- The chordwise loadings for several stations in the vicinity of a typical wing-control parting line on configuration 1 are presented in figure 32. The loadings are shown over the control-deflection range for each of three angles of attack at stations 4 and 5 on the wing and at stations 6 and 7 on the control. At station 4, there is no carryover of loading from the control due to control deflection until δ approaches 20°. The carryover appears first at the trailing edge and spreads forward as the control deflection is further increased. The carryover loading at this station always seems to be of the same sign as the control deflection. At station 5, immediately adjacent to the parting line, the carryover loading builds up to a peak soon after the hinge line and then drops off rapidly to a small or reversed loading at the trailing edge. By comparing the loadings on the control at stations 6 and 7, it can be seen that the parting line causes a more general decrease in loading across the control chord at station 6 rather than the large decrease toward the trailing edge that linear theory would predict. This point was shown in more detail in the pressure-distribution discussion.

A comparison of the incremental carryover loadings adjacent to the four wing-control parting lines investigated is presented in figure 33. It should be mentioned that for configuration 1 the control-deflection settings at the even 10° increments were not available at $\alpha = 6°$ and 12° and therefore the available control deflections closest to the desired angles were used in these cases. From figure 33, it can be seen that the loading carryovers are essentially identical, despite the different parting-line locations investigated. By fairing curves through the averages of these symbols, it is possible to illustrate more clearly the effect of angle of attack and control deflection on the parting-line carryovers in figure 34. It appears from figure 34 that for a given control deflection, the carryover changes from a rectangular loading at $\alpha = -12°$ to one having large loading near the hinge line and dropping off to a reversed loading at the trailing edge as the angle of attack is increased to 12°.

In order to see if the loading carryover due to control deflection is linear, the incremental loadings divided by control deflection are shown in figure 35. The spread of the curves and the gradual decrease in value of $\Delta P_R/\delta$ with increasing δ indicates that the loadings do not increase linearly, probably as a result of the crossflows in this

region due to the unporting of the control. Comparison of the experimental and linear-theory values shows that the loading carryovers obtained are considerably less then predicted. The largest differences are evident near the trailing edge at positive control deflections and are a result of the crossflow from the wing high-pressure side to the control low-pressure side which provides the greatest spanwise pressure differential on adjacent surfaces for any of the angular conditions.

It is of interest to compare the loss in loading due to δ on the control near the tip with the loss near the parting line. Figure 36 presents the incremental loadings for the three spanwise stations on the control of configuration 1. In each plot, the circular symbols defining the distribution at station 7 may be considered essentially two dimensional, and the differences between the distribution at station 7 and those at the other two stations show the losses at the tip and at the parting line. At positive control deflections, the tip station tends to exhibit somewhat greater losses near the hinge line and smaller losses near the trailing edge than does the parting-line station; however, they are in general quite similar, considering the lack of wing upwash and the presence of the extended wing adjacent to the parting-line station. At negative control deflections, the losses across the control chord are much greater at the tip station than at the station adjacent to the parting line.

When the incremental loadings across the control span are normalized by dividing by δ, the variations in loading with δ are more easily compared as in figure 37. Here the normalized loadings are shown for the three spanwise stations on the control at angles of attack of 0°, 6°, and 12°. In general, as the control deflection is increased, either positively or negatively, the loading per degree control deflection decreases in the area near the hinge line, but there tends to be little change further aft. At stations 6 and 7, the negative deflections give larger loadings than do the positive deflections; whereas at station 8, the tip effect previously discussed causes the negative deflections to produce smaller loadings.

To give a more illustrative picture of the changes, both chordwise and spanwise, of the loadings over two typical control configurations, some isometric loading diagrams are shown in figure 38. The diagrams shown are for an angle of attack of 6°, at the extreme control deflections tested, and the vertical heights of the shaded areas indicate the relative magnitudes of the loadings, positive above the plane of the wing and negative below.

Spanwise Loadings

In order to facilitate the presentation of the spanwise normal-force and moment-loading results for the complete range of the tests (excepting the variations in Reynolds number which have been shown to cause negligible changes), the normal-force-loading parameters due to control deflection or angle of attack, normalized by the proper angle, are plotted across the wing span in figures 39 through 48. Similarly, the pitching-moment-loading parameters are presented in figures 49 through 58. In each figure, the results for a given configuration and Mach number are presented in four parts: (a) the load over the complete wing chord due to control deflection; (b) the load over the control chord due to control deflection; (c) the load over the complete wing chord due to angle of attack; and (d) the load over the control chord due to angle of attack. When the effects due to control deflection are being considered, the data are presented for all of the available control deflections at the three basic angles of attack, 0°, 6°, and 12°. When the effects due to angle of attack are being considered, the data are presented for all the available angles of attack at three selected control deflections, -20°, 0°, and 20°.

Throughout this section on the spanwise loadings, the linear-theory predictions are used as a basis for discussion. Although it is realized that this is a first-order approximation technique and is therefore at times subject to considerable inaccuracies, it is not considered necessary to present a more elaborate theoretical method in view of the excellent predictions obtained by the simplified procedures discussed in reference 14 for the cases wherein separation or shock detachment ahead of the hinge line had not occurred. Since the basic data used in developing the method of reference 14 were taken from the data of the present report, repetition of the predictions herein would be superfluous.

Normal-force loadings due to δ.- In general, the normal-force loadings due to control deflection (figs. 39 through 48, parts (a) and (b)) exhibit considerably more scatter than do the normal-force loadings due to angle of attack. The linear theory overestimates the normal-force loading on the wing due to control deflection by a considerable amount except for the thickened trailing-edge configurations (figs. 43 and 44) and for all the configurations when the separation or shock-detachment phenomena prevail at the hinge line. Since the possibility of shock detachment tends to decrease toward the ends of the partial-span controls, this effect is more evident on the full-span controls. The overestimation of the loadings on the sharp trailing-edge controls by the linear theory explains the similar overestimation of the lift and bending-moment coefficient slopes for these configurations shown in reference 1. The assumption in reference 1 that the increase in lift and bending-moment coefficient slopes at the highest angles was caused by the shock-detachment or separation effect is borne out by the results shown here,

particularly in that the effect is more noticeable on the full-span controls. The effect of the thickened trailing edges on configurations 5 and 6, as has been discussed previously, is twofold: One effect is to increase the loading on the control as predicted by shock-expansion theory (see fig. 25) due to the increased pressure on the compression side, and the other is to increase the loading on the wing due to separation or shock-detachment effect, extending further forward as a result of the attendant increase in pressure-rise ratio. The spanwise plots of control normal-force loading due to control deflection also show the anticipated effect of thickening the trailing edge because whereas the linear theory considerably overestimates the loadings of the sharp trailing-edge controls, the linear theory is in closer agreement with the experimental loadings for the thickened trailing-edge configurations.

The wing normal-force-loading plots show that the integrated carry-over from the control to the station adjacent to the parting lines of the partial-span controls is considerably less than predicted and in many cases is negligible. From the pressure-distribution and chordwise-loading analyses, we know that this is caused by the nature of the loadings at these stations which showed a reversal in loading from hinge line to the trailing edge in some cases, and relatively small loadings otherwise. From the spanwise-loading plots, it is evident that at times the loadings due to the control are greater at the second station from the parting line on the wing than at the first (e.g., fig. 40(a)). This, too, was evident in the discussion of the chordwise loadings.

Both the wing and the control normal-force loadings show that although the linear theory overestimates the loadings near the midspan of the controls, the loadings near the parting lines and near the wing tip are in good agreement with the theory. This indicates that the dropoffs in loadings from the two-dimensional area to the parting line or wing tip are not as large as are predicted by the linear theory. The crossflows in the region of the parting lines and the formation of the tip vortex system, previously discussed in detail and not accounted for in theory, apparently explain the conservation of loading in these regions.

Normal-force loadings due to α.- The wing normal-force loadings due to angle of attack (figs. 39 through 48, part (c)) are, at $\delta = 0^\circ$, nothing more than those for a plain wing and should therefore be identical for all of the configurations tested except for those having thickened trailing edges. The remarkable thing (concerning the various parting-line gaps and the model inconsistencies) is that not only is this true but also the loadings at $\delta = \pm 20^\circ$ are identical with those at $\delta = 0^\circ$. The linear-theory predictions are excellent except for configurations 5 and 6 (figs. 43 and 44), where the loading obtained is greater than predicted as might be expected from the increased trailing-edge thickness. The major disagreement between experiment and theory for the wing loadings

occurs at the tip station where the experimental loadings are greater than theoretically predicted. Here again the formation of the tip vortex is believed to be the sustaining influence. The good agreement in linear theory and experimental normal-force loadings across the span is responsible for the excellent prediction of the wing lift and bending moment due to α shown in reference 1 for this configuration.

The normal-force loadings on the control due to angle of attack (figs. 39 through 48, part (d)) are generally similar at the three control deflections shown, and exhibit little scatter with angle of attack. The linear theory again overestimates the control-section loadings over the control spans except in regions near the wing tip. In view of the excellent prediction of the loading over the total wing chord, it appears that compensating flow characteristics were responsible. As was shown in the pressure-distribution discussion, the loading due to angle of attack was greater than predicted by linear theory near the wing leading edge and less near the trailing edge. (See fig. 31.) The experimental loading variation obtained across the control span tends to be almost linear except for the station near the tip for $\delta = -20^{\circ}$, and bears little resemblance to the spanwise variation predicted by linear theory. These conclusions were emphasized in the analysis of reference 14.

Pitching-moment loadings due to δ.- The points to be noted from observation of the wing or control pitching-moment loadings due to control deflection (figs. 49 through 58, parts (a) and (b)) are practically identical with those previously emphasized under the normal-force-loading discussion and will not therefore be discussed in detail. These are: overestimation by the linear theory of the loading in the midspan of the control except for the thickened trailing-edge configurations, lack of appreciable carryover near the parting lines, larger carryover effect at a station further from the control, and failure of the loadings on the control to decrease as much as predicted near the parting lines and wing tip. The effects of hinge-line separation or shock detachment, previously discussed in conjunction with the normal-force loadings, appears as a decrease in moment loadings at the highest angles due to the forward movement of the center of pressure of the loading. This is reflected in the decreased hinge-moment and pitching-moment slopes at the high angles (ref. 1).

Pitching-moment loadings due to α.- The wing pitching-moment loadings due to angle of attack (figs. 49 through 58, part (c)) do not show the agreement with theory that the wing spanwise normal-force loadings exhibited; the moments experimentally are more positive except at the tip station. The trend of the variation in pitching-moment loading across the span is in agreement with the linear-theory variation except for the tip station. From the discussion of the compensating factors causing the normal-force agreement, it appears that the moment difference gives further verification to the conclusions reached therein. The

experimental variation across the span of the moment loading due to angle of attack is approximately linear. The pitching-moment loading caused by the load on the control due to angle of attack (figs. 49 through 58, part (d)) is similar in nature to the normal-force loading. The loading is generally less than predicted except at the wing tip, and the variation across the control span is linear except for $\delta = -20^{\circ}$ near the tip.

Centers of Pressure

It is of interest now to examine the effect of configuration changes, angle of attack, and control deflection, on the locations of the centers of pressure of the integrated wing and control loadings. The chordwise variations with angle of attack are presented in figure 59 as plots of distances in the chordwise direction from the wing apex to the total wing-load center of pressure and from the hinge line to the control-load center of pressure. The spanwise variations with angle of attack are also presented in figure 59 as plots of distances from the wing root chord to the total wing-load center of pressure and from the wing root chord to the control-load center of pressure.

Although the data of figure 59 show some scatter, in general, the movement of the centers of pressure with angle of attack and control deflection is regular and consistent. The chordwise movement of the center of pressure of the wing loading with angle of attack is similar for the various configurations. The effect of control deflection on the wing loading increases as the control size increases, as would be expected. As the angle of attack is increased, the effect of control deflection diminishes. The chordwise movement of the center of pressure of the control loading with angle of attack and control deflection is nonexistent. The changes due to the different configurations are in agreement with the movements of the centroids of area.

From consideration of the spanwise movements of the wing centers of pressure, it can be seen that the full-span configurations show no variations due to angle of attack and control deflection whereas the partial-span configurations exhibit changes similar to those previously noted for the chordwise centers of pressure. The magnitude of the movement depends on the relative position of the control centroid with respect to that of the wing. The spanwise center-of-pressure location for the control load remains constant with changes in angle of attack and control deflection and is in the neighborhood of the control centroid.

CONCLUSIONS

From the results, reported herein, of an experimental and theoretical investigation of several flap-type trailing-edge controls on a trapezoidal wing at Mach numbers of 1.61 and 2.01, the following primary conclusions may be reached.

Pressure Distributions

1. The pressure changes due to increasing the Mach number from 1.61 to 2.01 were in fair agreement with the changes predicted by the $1/\sqrt{M^2 - 1}$ relationship.

2. The effect of increasing the Reynolds number from 1.7×10^6 to 5.6×10^6 was negligible.

3. The effect on the pressures of increasing the hinge-line gap indicated flow through the gap in the direction from the control high-pressure surface to the control low-pressure surface.

4. Both shock-expansion theory and the semi-infinite line source and sink linear-theory method were accurate in predicting the pressures due to wing thickness.

5. Shock-expansion theory was most effective in predicting the pressures due to control deflection and trailing-edge thickness.

6. Linear-theory predictions of the wing-tip, control-tip, and control-parting-line effects were in most cases considerably in error because of crossflow and vortex formations encountered.

7. Viscous separation and/or shock detachment occurred ahead of the hinge line on the control high-pressure side and ahead of the trailing edge on the low-pressure side at the larger angles.

8. Detachment of the leading-edge shock and localized separation on the upper surface near the leading edge had a marked effect on the pressure distributions in this region of the wing at angles of attack.

Chordwise Loadings

1. The experimental loadings due to control deflection or angle of attack in the two-dimensional regions of the controls tended to be rectangular.

2. The experimental loadings due to angle of attack over the complete wing chord in the two-dimensional regions tended to be triangular.

3. The experimental loadings in the vicinity of the parting lines or wing tip had little resemblance to those predicted by linear theory.

Spanwise Loadings

1. Separation and/or shock detachment ahead of the hinge line had little effect on the control normal-force loadings, but caused increased wing normal-force loadings.

2. Increasing the trailing-edge thickness increased both the wing and control loadings.

3. In general, the experimental variations in loading across the span were linear and about 70 percent of the two-dimensional value predicted by linear theory, except for the wing normal-force loadings due to angle of attack, which agreed with linear theory.

4. The carryovers of loading from the control to the wing adjacent to a parting line were much less than the linear theory estimated and in many cases were negligible.

5. The experimental losses in loading from the two-dimensional regions on the control to the regions near the wing tip or parting lines were considerably less than predicted by linear theory.

Centers of Pressure

1. The movements of the centers of pressure of the wing load with angle of attack and control deflection were, in general, smooth.

2. The centers of pressure of the control loadings were located approximately at the control centroids and were unaffected by control deflection or angle of attack.

Langley Aeronautical Laboratory,
National Advisory Committee for Aeronautics,
Langley Field, Va., November 14, 1955.

REFERENCES

1. Lord, Douglas R., and Czarnecki, K. R.: Aerodynamic Characteristics of Several Flap-Type Trailing-Edge Controls on a Trapezoidal Wing at Mach Numbers of 1.61 and 2.01. NACA RM L54D19, 1954.

2. Lord, Douglas R., and Czarnecki, K. R.: Tabulated Pressure Data for Several Flap-Type Trailing-Edge Controls on a Trapezoidal Wing at Mach Numbers of 1.61 and 2.01. NACA RM L55J04, 1955.

3. Jones, Robert T.: Thin Oblique Airfoils at Supersonic Speed. NACA Rep. 851, 1946. (Supersedes NACA TN 1107.)

4. Harmon, Sidney M.: Theoretical Supersonic Wave Drag of Untapered Sweptback and Rectangular Wings at Zero Lift. NACA TN 1449, 1947.

5. Lagerstrom, P. A., and Graham, Martha E.: Linearized Theory of Supersonic Control Surfaces. Jour. Aero. Sci., vol. 16, no. 1, Jan. 1949, pp. 31-34.

6. Cohen, Doris: The Theoretical Lift of Flat Swept-Back Wings at Supersonic Speeds. NACA TN 1555, 1948.

7. Lagerstrom, P. A.: Linearized Supersonic Theory of Conical Wings (Corrected copy). NACA TN 1685, 1950.

8. Mager, Artus: Prediction of Shock-Induced Turbulent Boundary-Layer Separation. Jour. Aero. Sci. (Readers' Forum), vol. 22, no. 3, Mar. 1955, pp. 201-202.

9. Bogdonoff, S. M., and Kepler, C. E.: Separation of a Supersonic Turbulent Boundary Layer. Jour. Aero. Sci., vol. 22, no. 6, June 1955, pp. 414-424, 430.

10. Holder, D. W., Pearcey, H. H., and Gadd, G. E.: The Interaction Between Shock Waves and Boundary Layers, with a note on "The Effects of the Interaction on the Performance of Supersonic Intakes" By J. Seddon. C.P. No. 180, British A.R.C., 1955.

11. Czarnecki, K. R., and Mueller, James N.: Investigation at Supersonic Speeds of Some of the Factors Affecting the Flow Over a Rectangular Wing With Symmetrical Circular-Arc Section and 30-Percent-Chord Trailing-Edge Flap. NACA RM L50J18, 1951.

12. Ulmann, Edward F., and Lord, Douglas R.: An Investigation of Flow Characteristics at Mach Number 4.04 Over 6- and 9-Percent-Thick Symmetrical Circular-Arc Airfoils Having 30-Percent-Chord Trailing-Edge Flaps. NACA RM L51D30, 1951.

13. Cheng, H. K.: Aerodynamics of a Rectangular Plate With Vortex Separation in Supersonic Flow. Jour. Aero. Sci., vol. 22, no. 4, Apr. 1955, pp. 217-226.

14. Czarnecki, K. R., and Lord, Douglas R.: Simplified Procedures for Estimating Flap-Control Loads at Supersonic Speeds. NACA RM L55E12, 1955.

TABLE I

CHORDWISE LOCATIONS OF ORIFICES

[Station spanwise locations shown in figure 2]

Orifices ahead of hinge line:
(orifice locations identical on upper and lower surfaces).

Stations	1	3	4	7	8
$\frac{x}{c_R}$	0.034	0.157	0.275	0.394	0.469
	.093	.203	.308	.414	.482
	.162	.260	.354	.449	.509
	.260	.342	.420	.499	.549
	.358	.423	.485	.548	.588
	.456	.505	.551	.598	.628
	.554	.586	.617	.648	.667
	.603	.627	.650	.673	.687
	.652	.667	.682	.697	.707
	.701	.708	.715	.722	.727
	.737	.737	.737	.737	.737

Orifices behind hinge lines:
(orifices located on upper surface only for configurations 1, 2, 3, and 4; orifice locations identical on upper and lower surfaces for configurations 5 and 6).

Stations	1	2	3	4	5	6	7	8
$\frac{x}{c_R}$	0.757	0.751	0.751	0.750	0.749	0.749	0.748	0.747
	.774	.770	.769	.764	.762	.762	.760	.756
	.838	.825	.822	.807	.798	.798	.792	.782
	.902	.879	.875	.850	.835	.835	.824	.808
	.976	.940	.934	.893	.870	.870	.852	.826

Additional orifices located: On wing inside hinge-line gap at stations 1, 3, 4, 7, and 8 and on control leading edge at stations 3, 4, 5, 7, 8 where applicable.

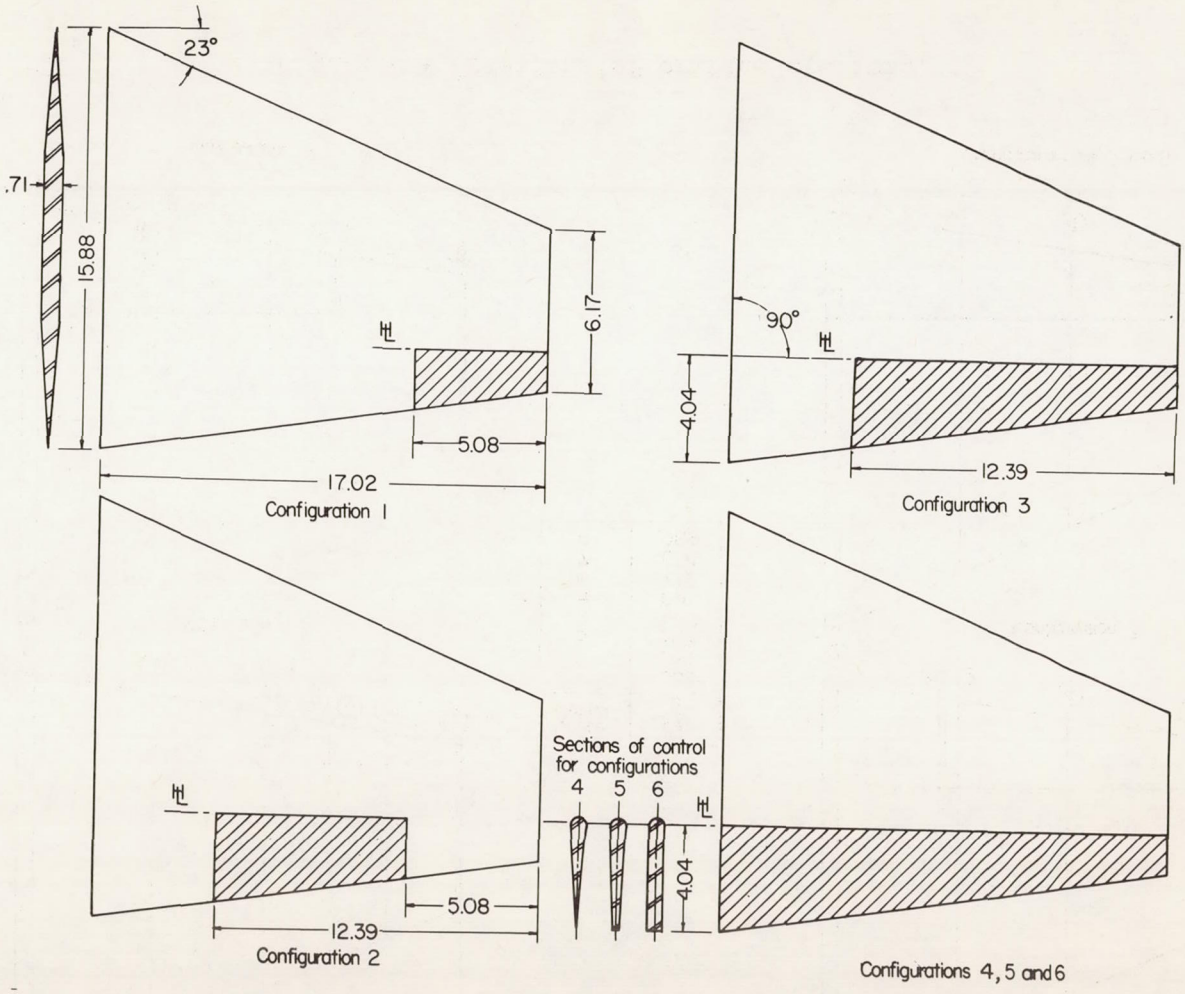

Figure 1.- Sketches of model configurations tested. (All dimensions in inches.)

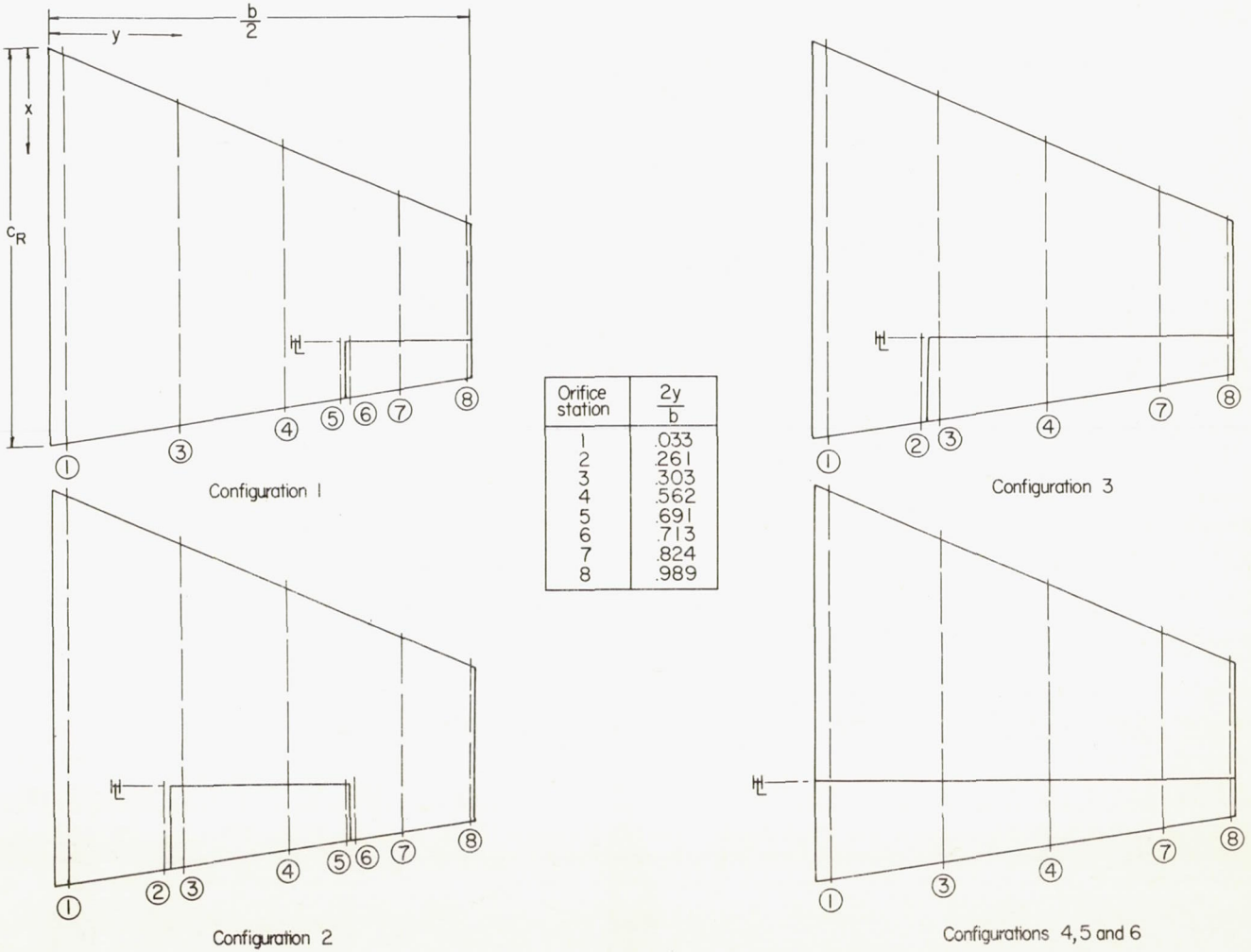

Orifice station	2y/b
1	.033
2	.261
3	.303
4	.562
5	.691
6	.713
7	.824
8	.989

Figure 2.- Locations of orifice stations.

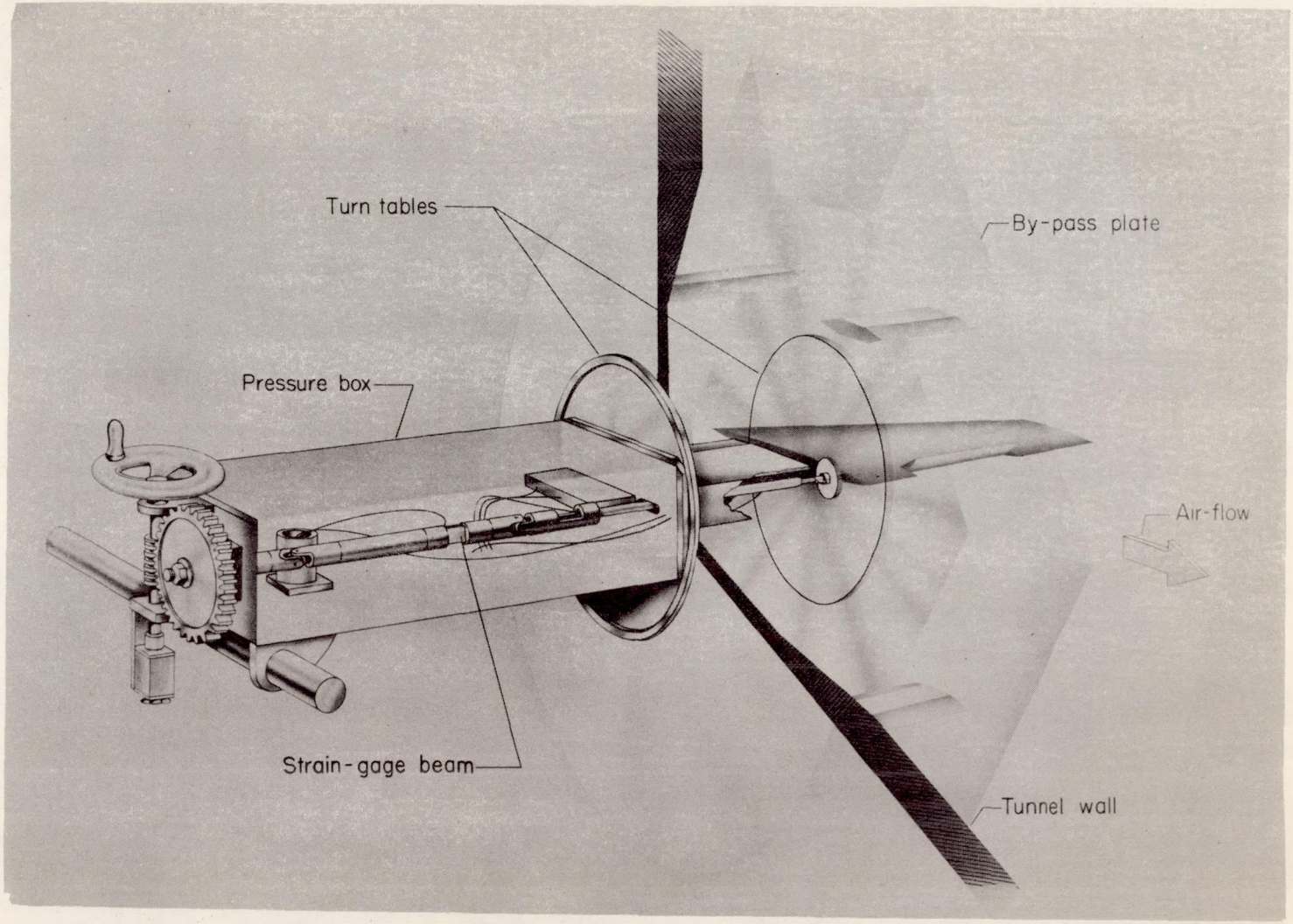

Figure 3.- Sketch of test setup.

L-83645

L-79384

Figure 4.- Photograph of model configuration 2 mounted on the bypass plate.

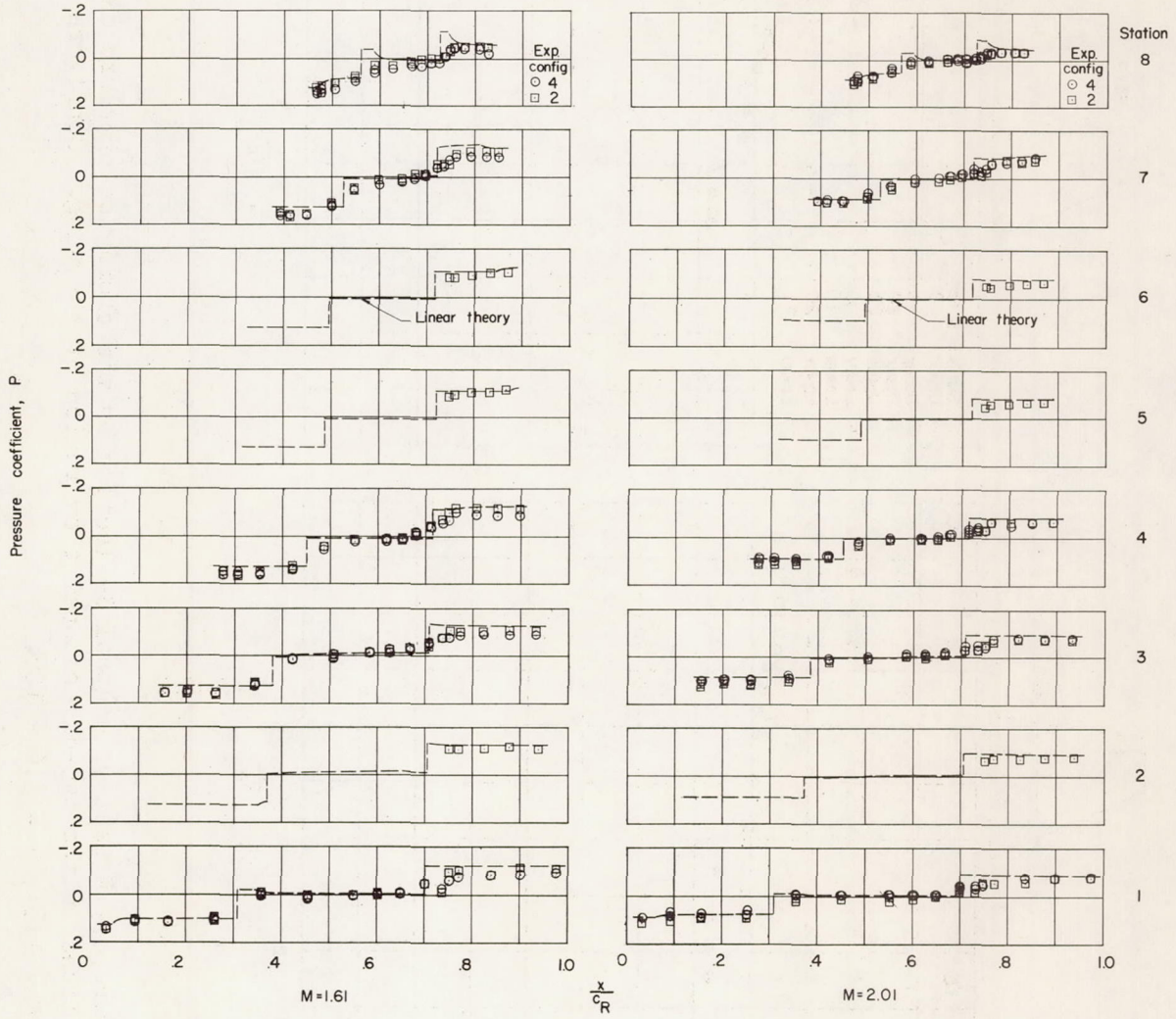

Figure 5.- Comparison of experimental and theoretical thickness pressures for two typical configurations. $R = 3.6 \times 10^6$; $\alpha = 0^\circ$; $\delta = 0^\circ$.

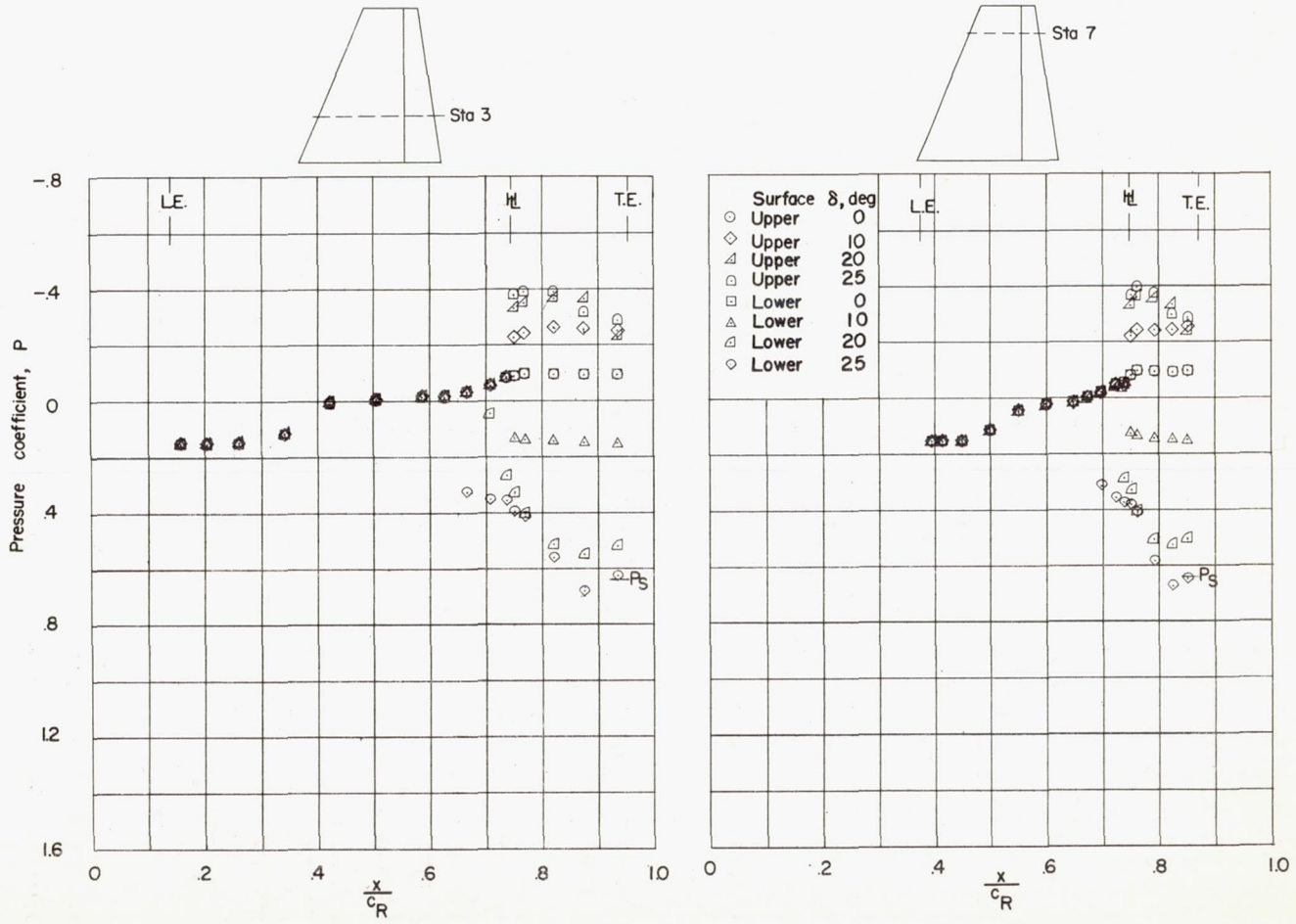

(a) $\alpha = 0^{\circ}$.

Figure 6.- Effect of control deflection on the chordwise pressure distributions in the two-dimensional flow region of the wing. Configuration 4; M = 1.61; R = 3.6×10^6.

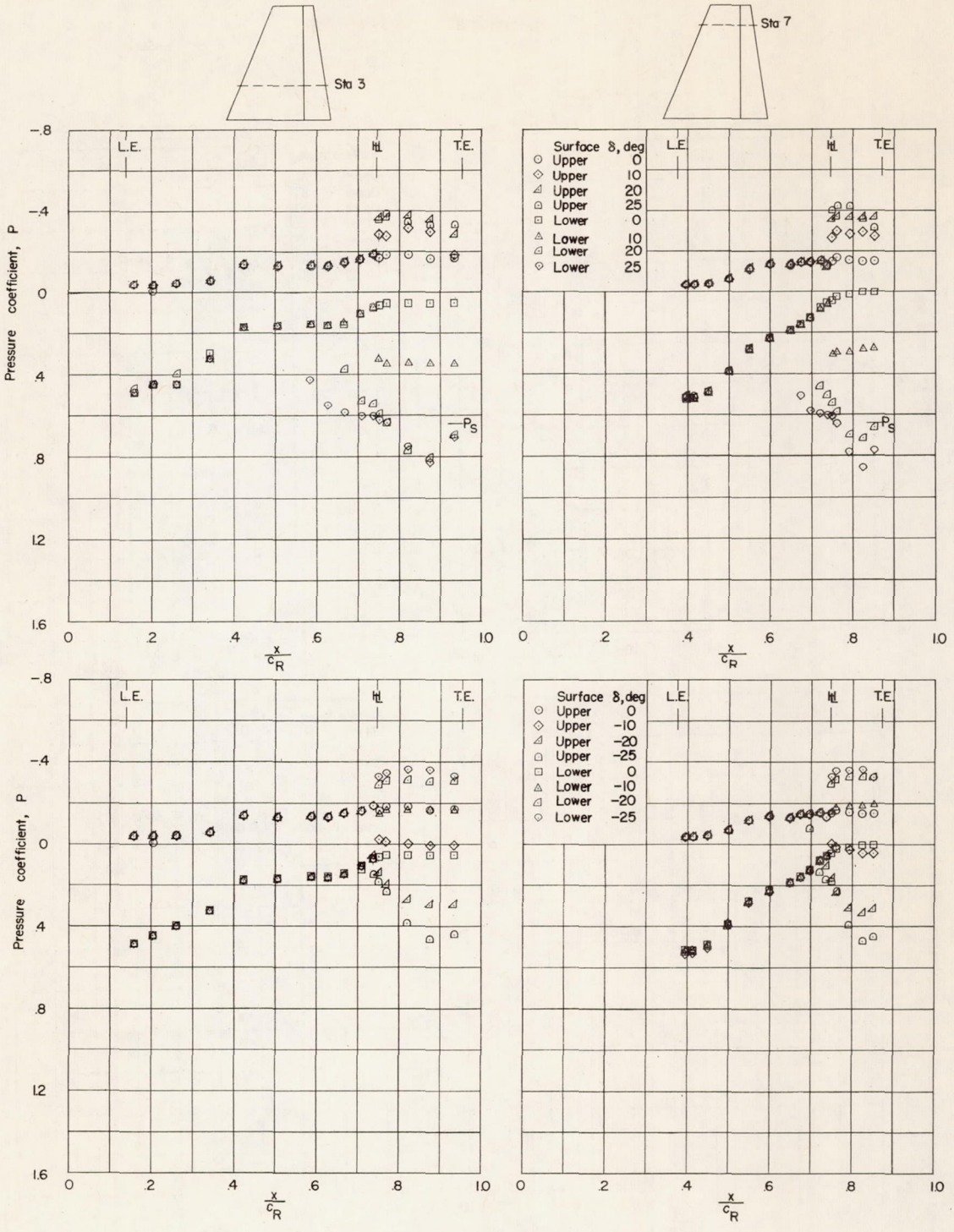

(b) $\alpha = 6^{\circ}$.

Figure 6.- Continued.

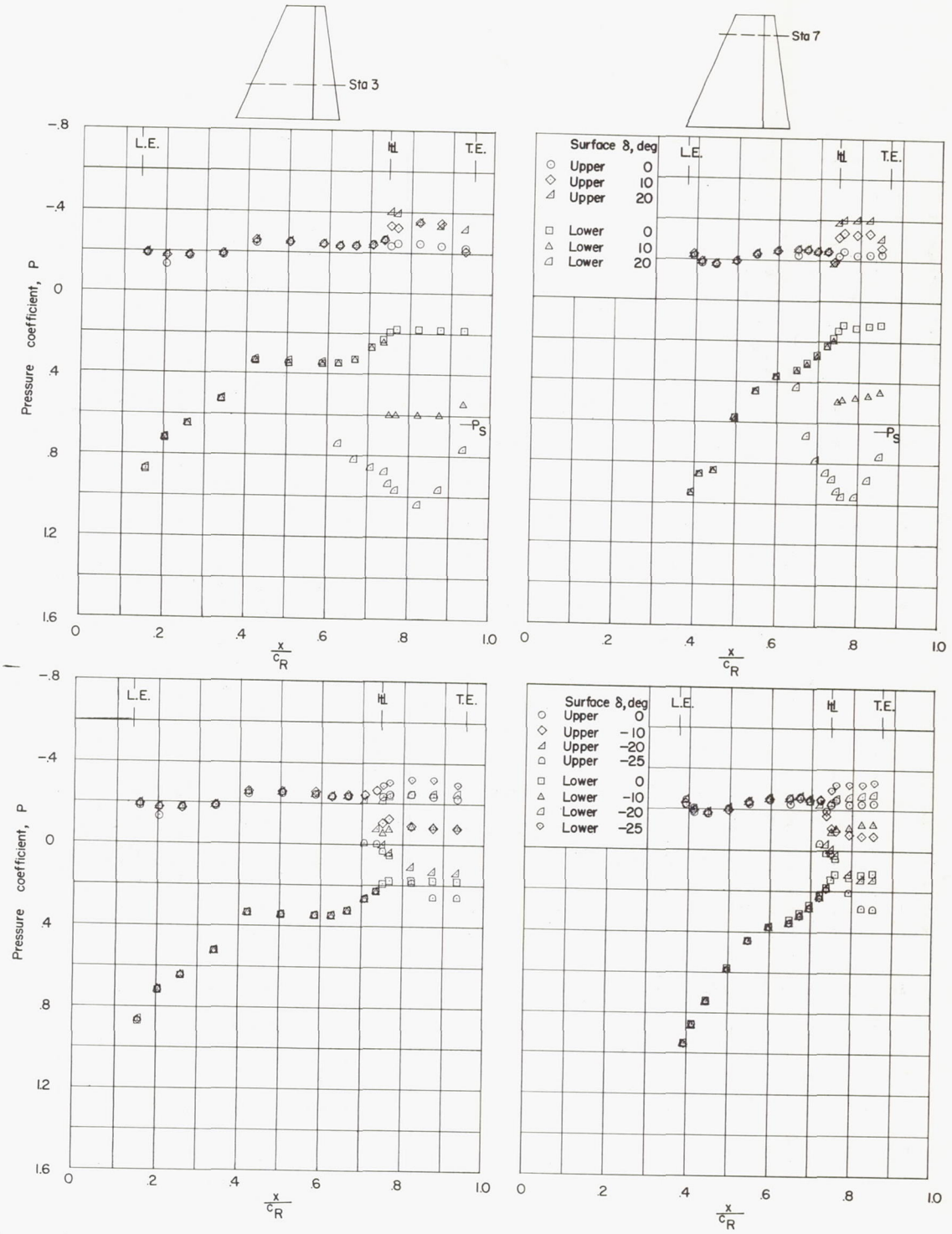

(c) $\alpha = 12^{\circ}$.

Figure 6.- Concluded.

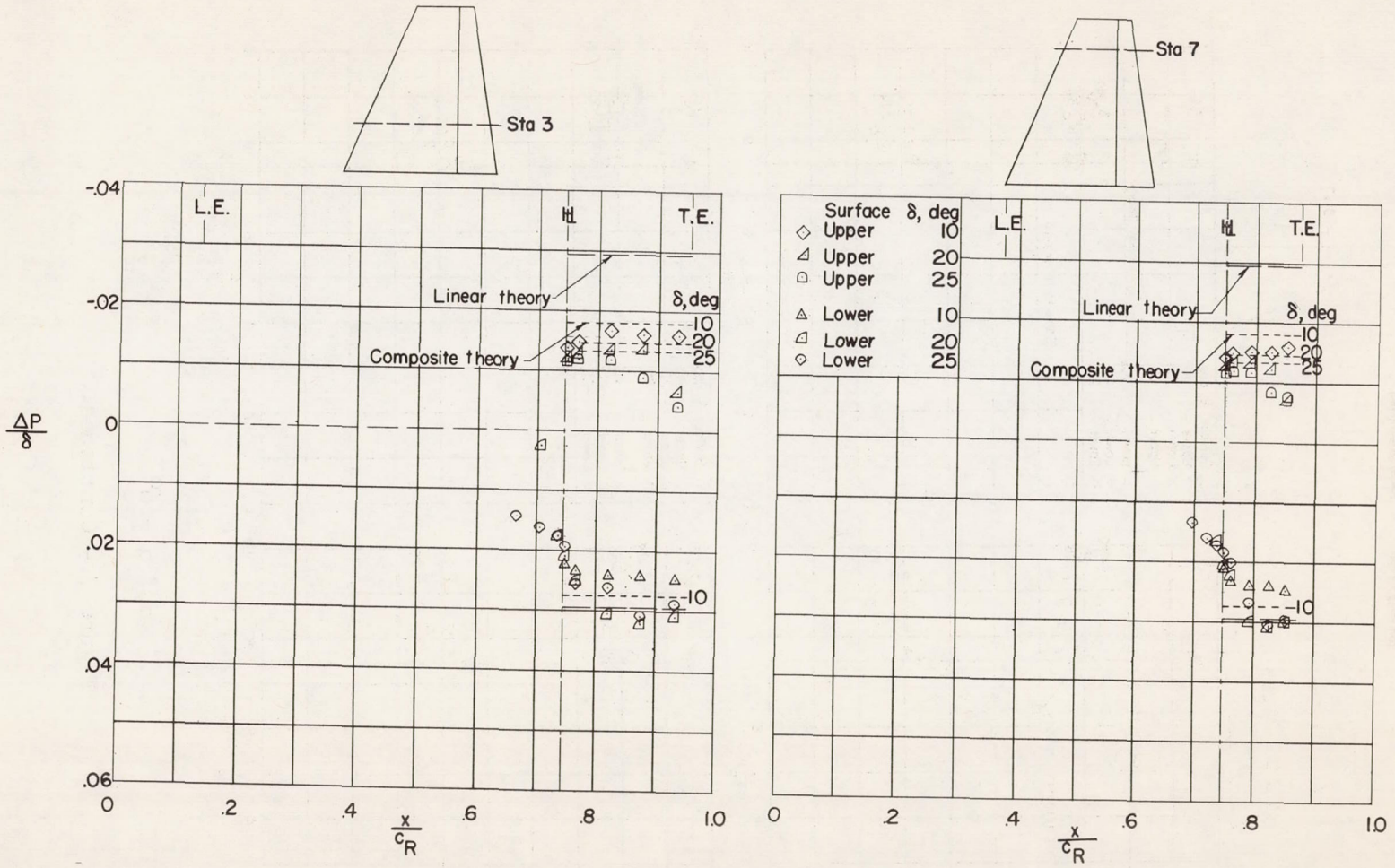

(a) $\alpha = 0^{\circ}$.

Figure 7.- Comparison of experimental and theoretical incremental pressures due to control deflection in the two-dimensional flow region of the wing. Configuration 4; M = 1.61; R = 3.6×10^6.

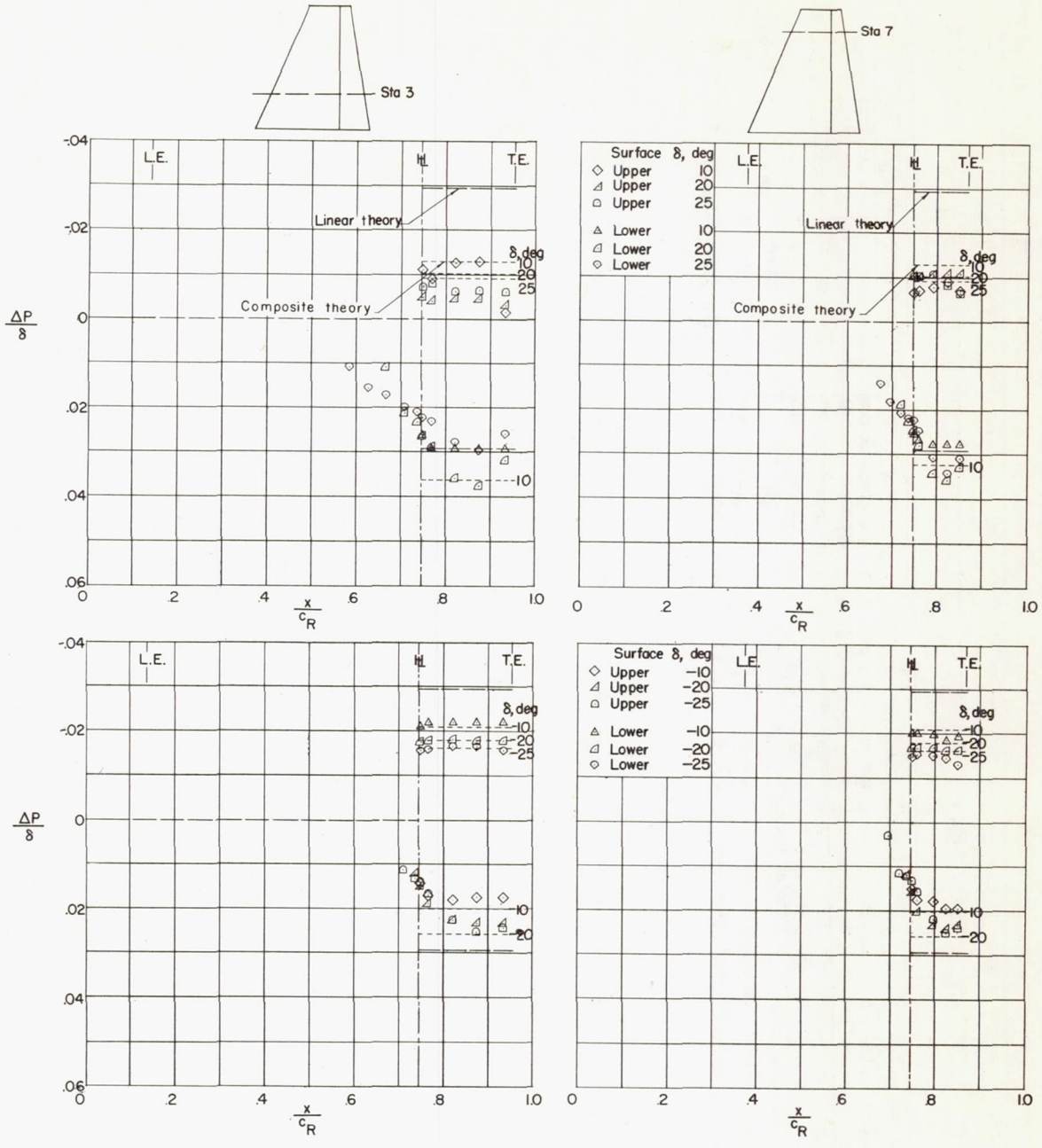

(b) $\alpha = 6^{\circ}$.

Figure 7.- Continued.

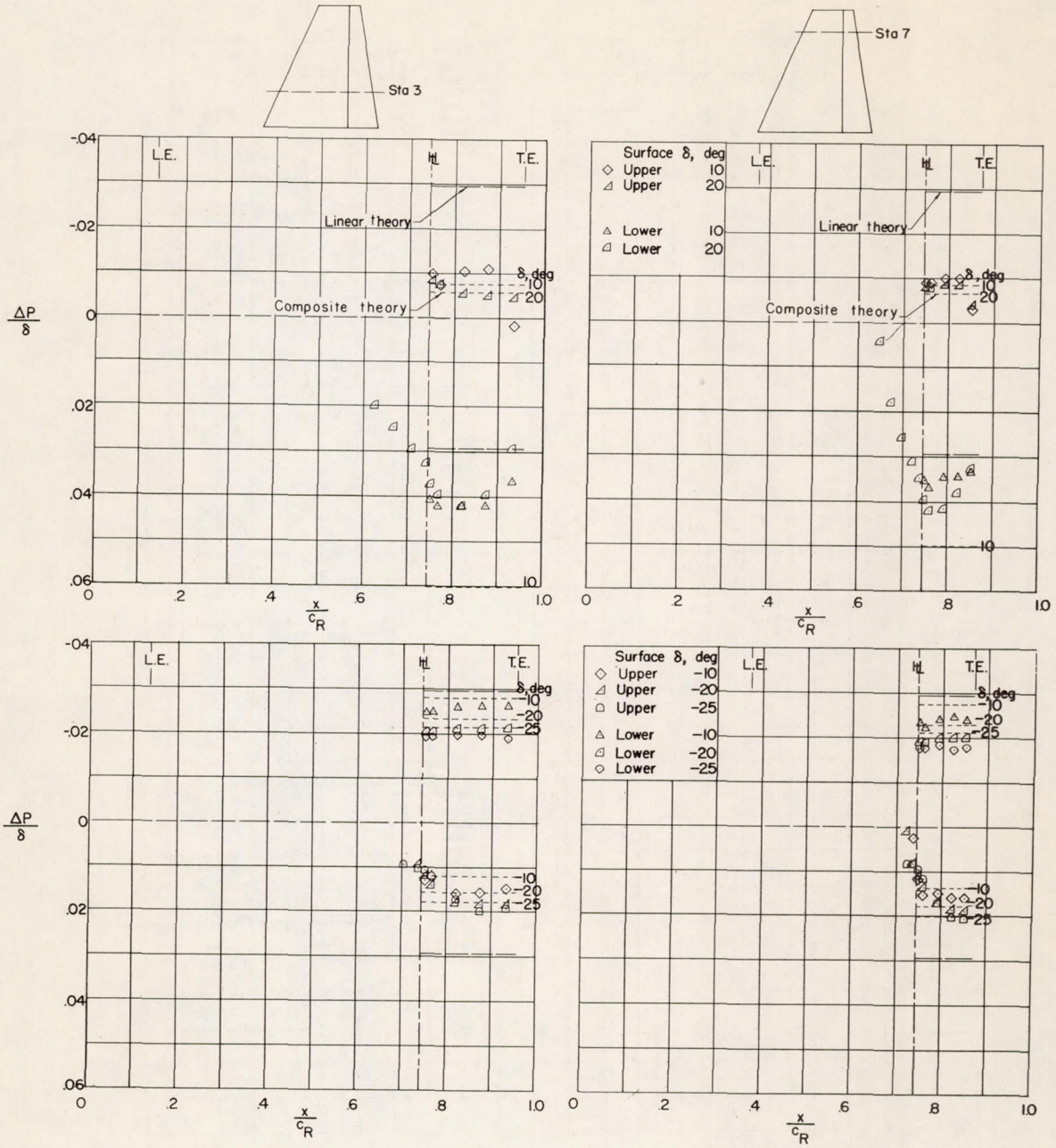

(c) $\alpha = 12^{\circ}$.

Figure 7.- Concluded.

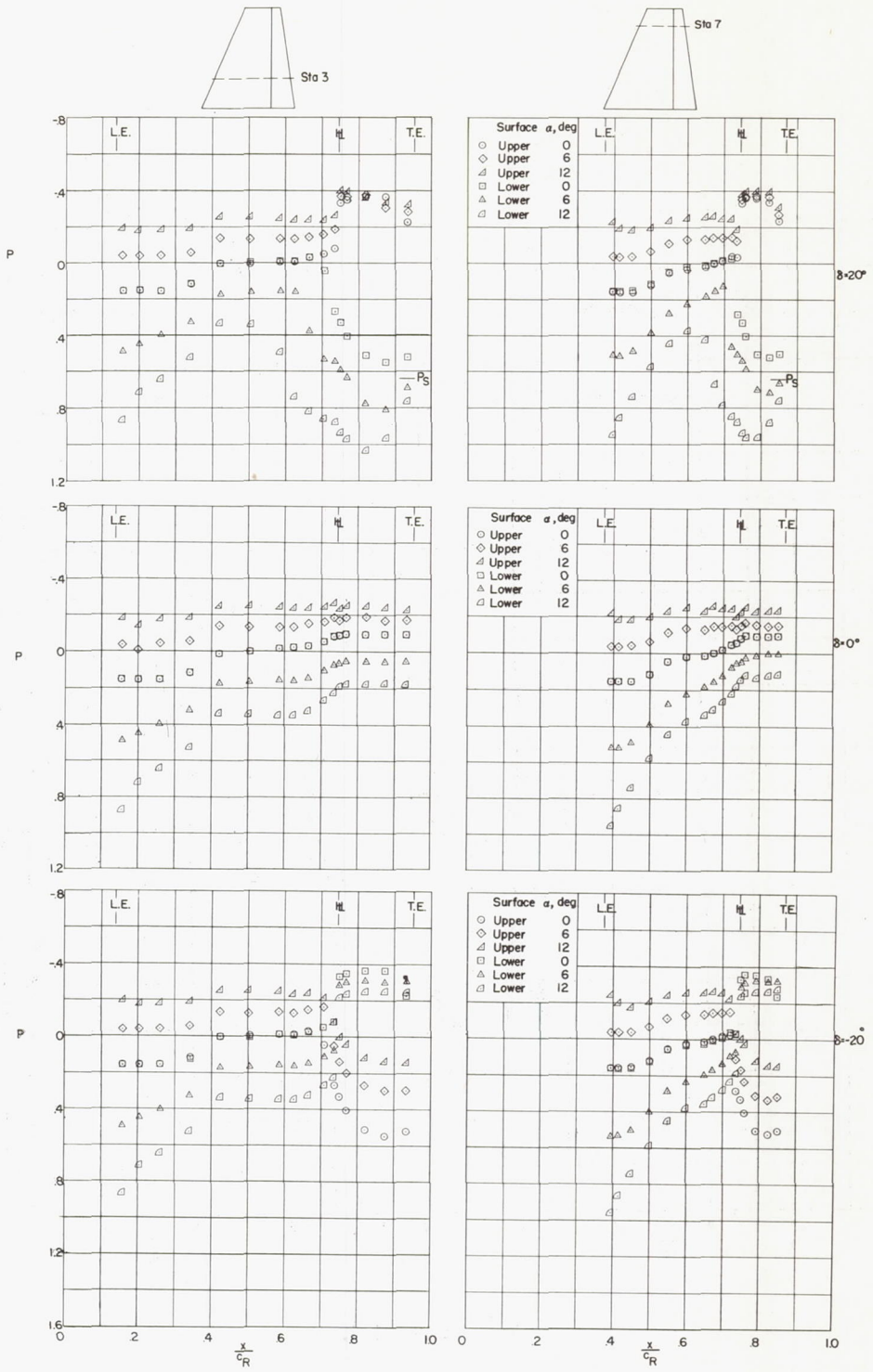

Figure 8.- Effect of angle of attack on the chordwise pressure distributions at two spanwise stations. Configuration 4; M = 1.61; R = 3.6×10^6.

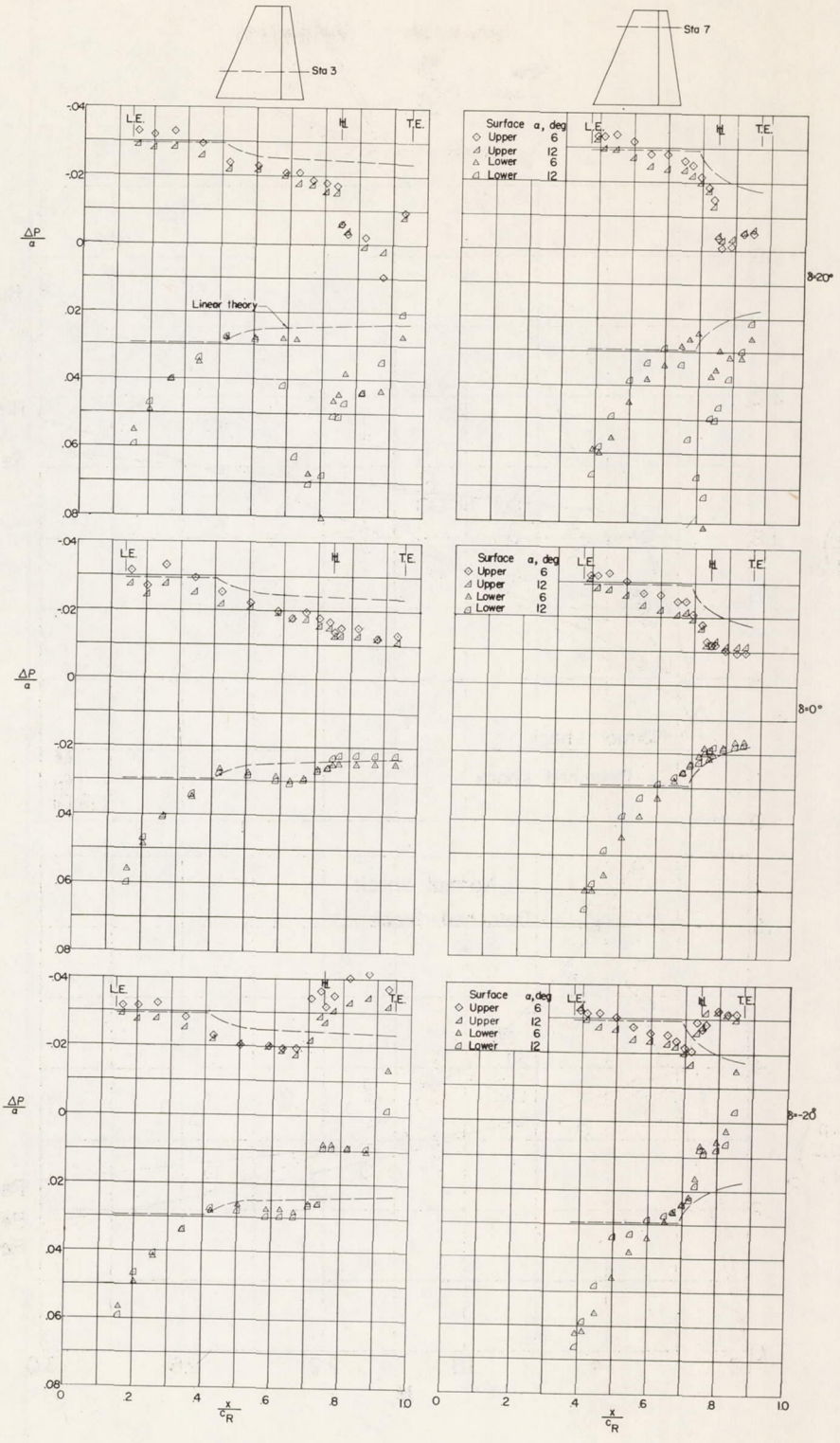

Figure 9.- Comparison of experimental and theoretical incremental pressures due to angle of attack at two spanwise stations. Configuration 4; M = 1.61; R = 3.6×10^6.

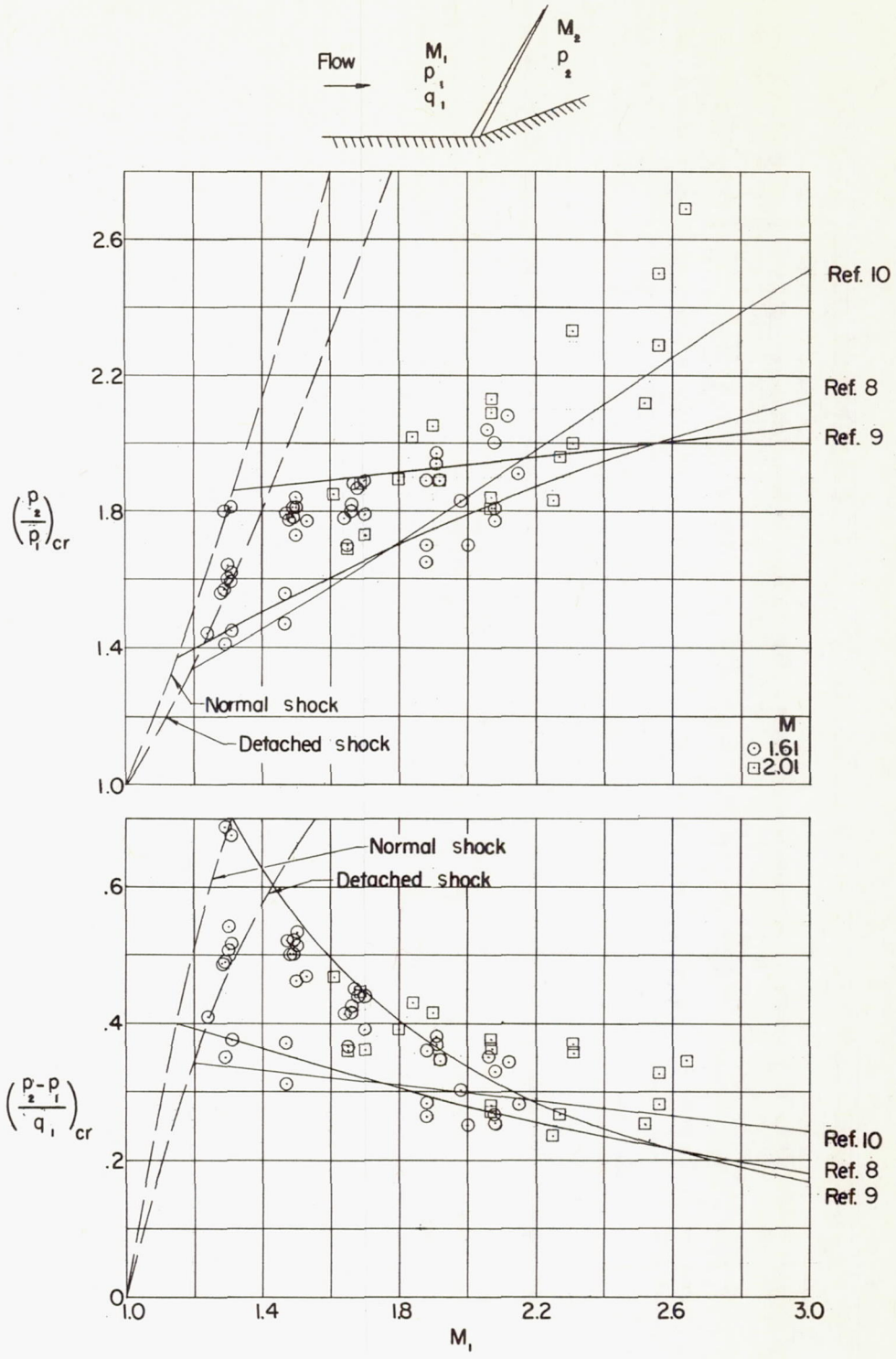

Figure 10.- Variation of critical-pressure ratios for separation ahead of hinge line with local surface Mach number. Configurations 4, 5, and 6; $R = 3.6 \times 10^6$.

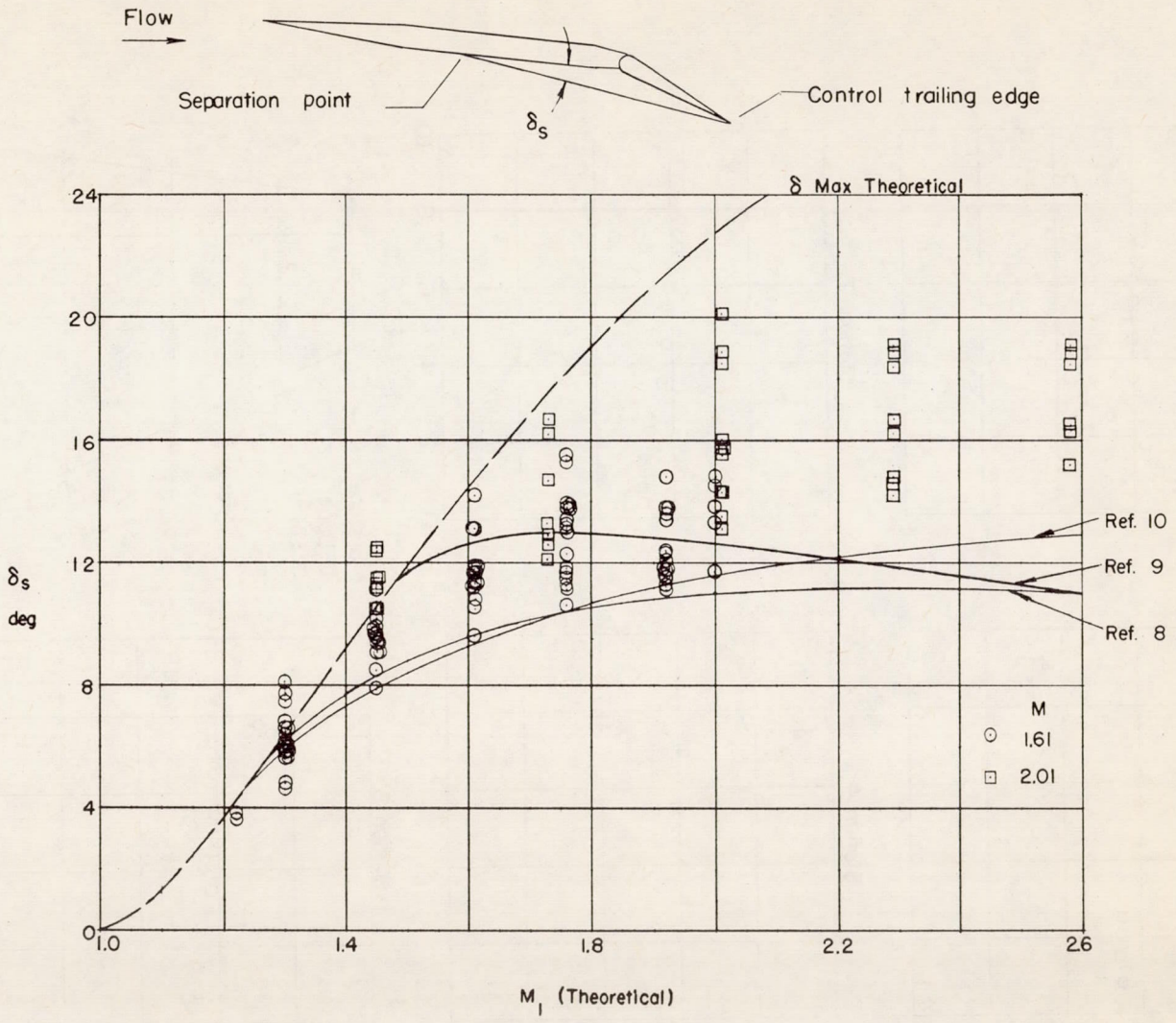

Figure 11.- Variation of effective separation angle with theoretical local surface Mach number. Configurations 4, 5, and 6; $R = 3.6 \times 10^6$.

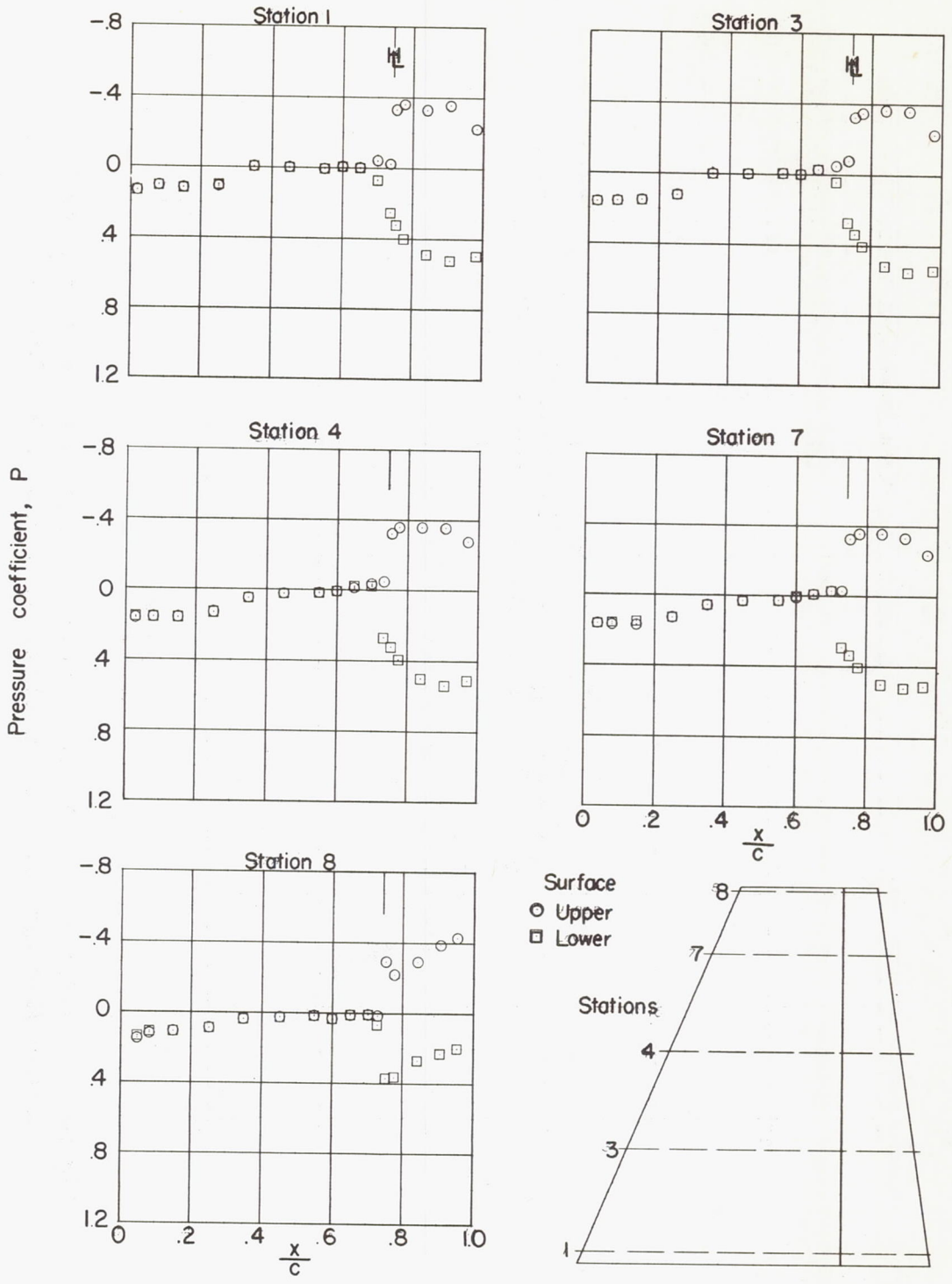

(a) $\alpha = 0^{\circ}$; $\delta = 20^{\circ}$.

Figure 12.- Chordwise pressure distributions at five spanwise stations on configuration 4. $M = 1.61$; $R = 3.6 \times 10^{6}$.

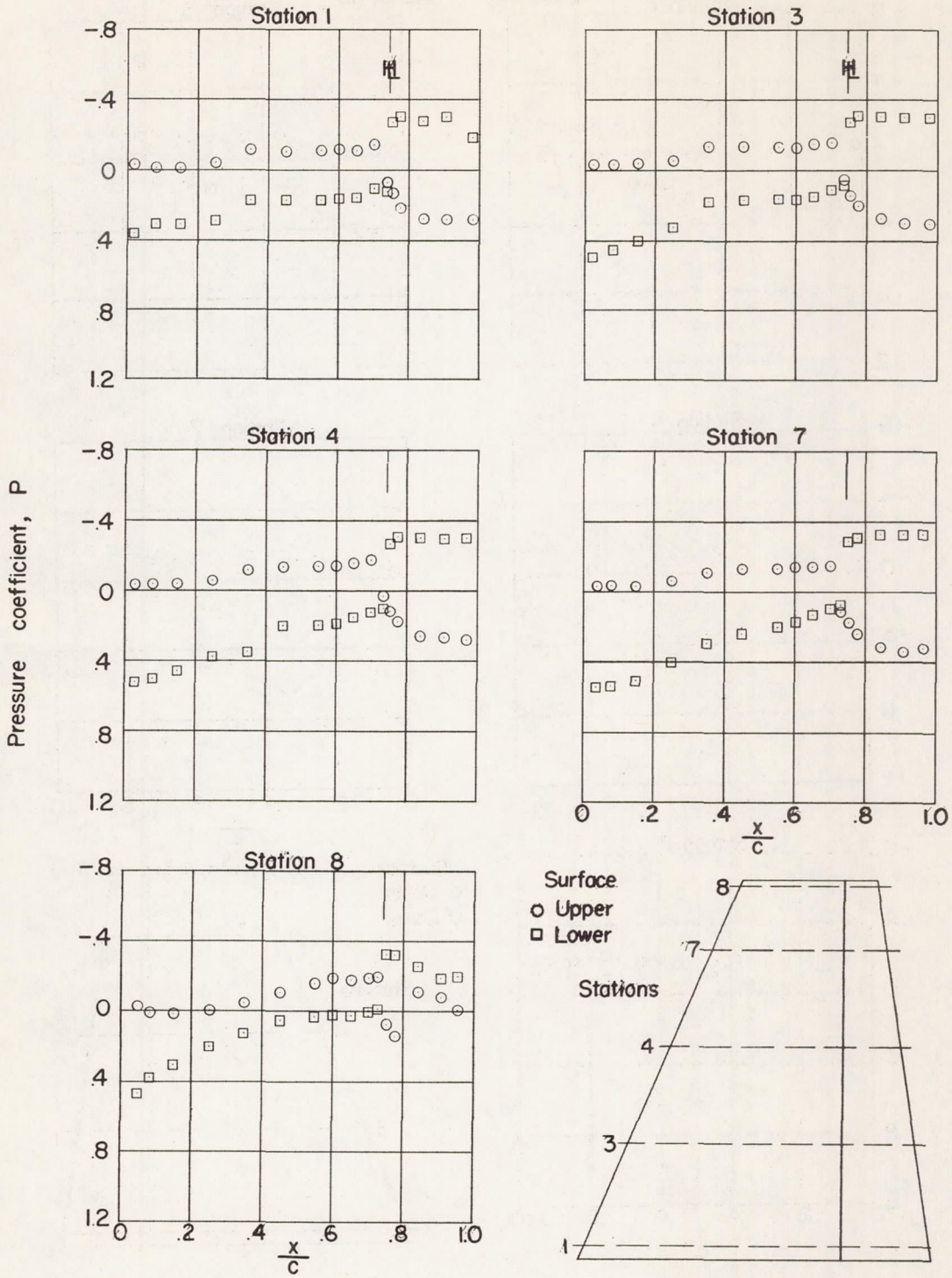

(b) $\alpha = 6^{\circ}$; $\delta = -20^{\circ}$.

Figure 12.- Continued.

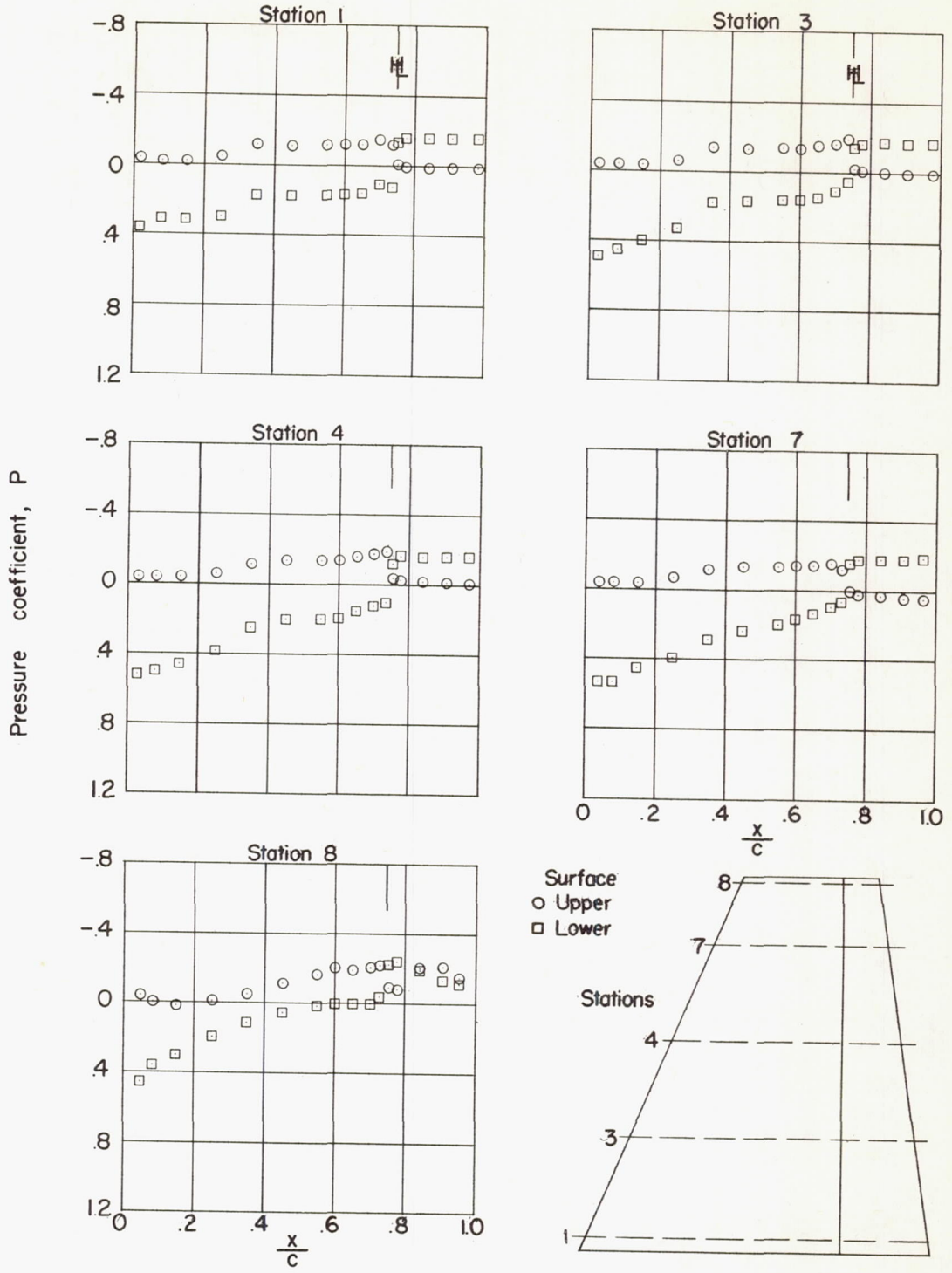

(c) $\alpha = 6^{\circ}$; $\delta = -10^{\circ}$.

Figure 12.- Continued.

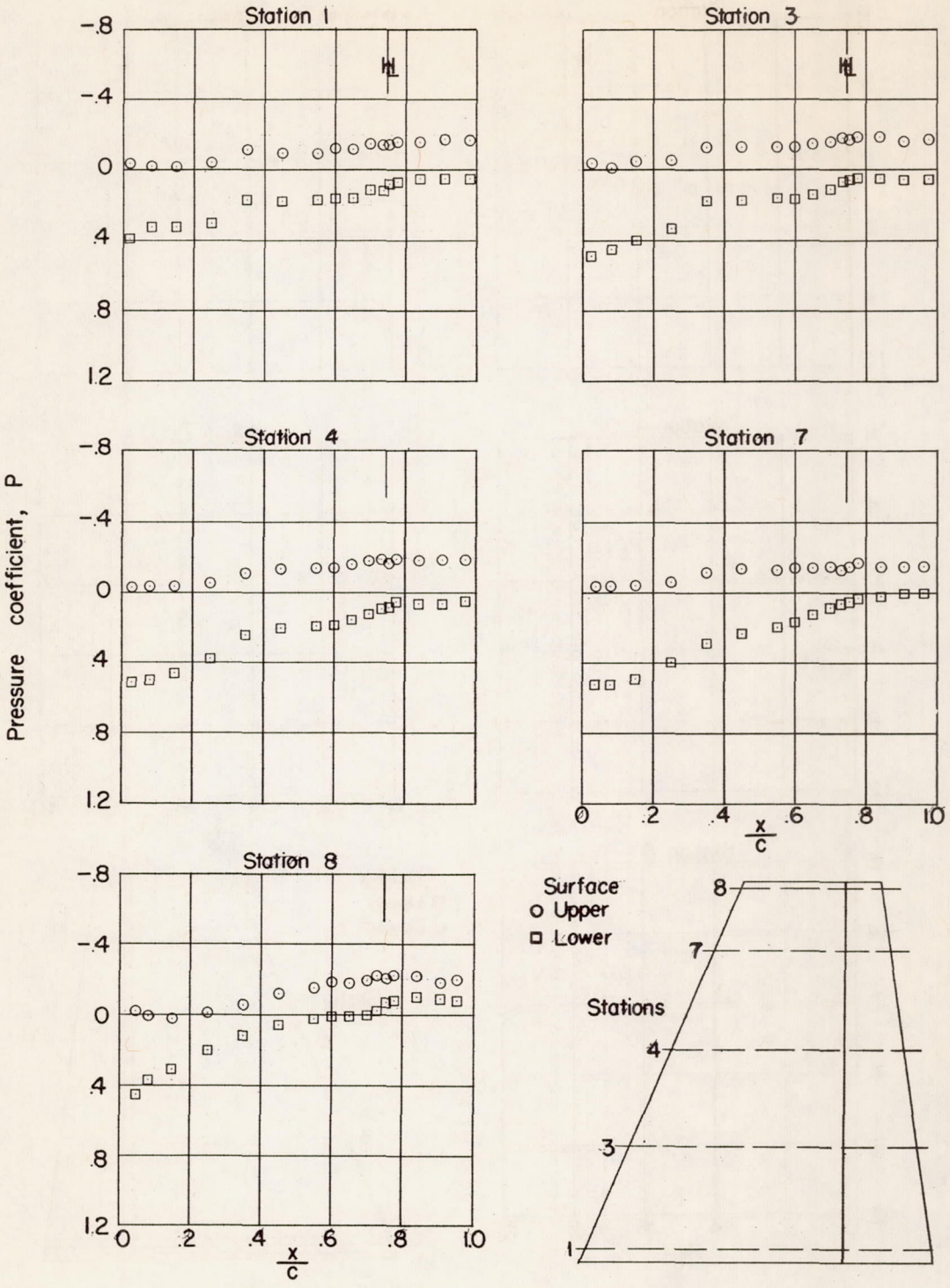

(d) $\alpha = 6^{\circ}$; $\delta = 0^{\circ}$.

Figure 12.- Continued.

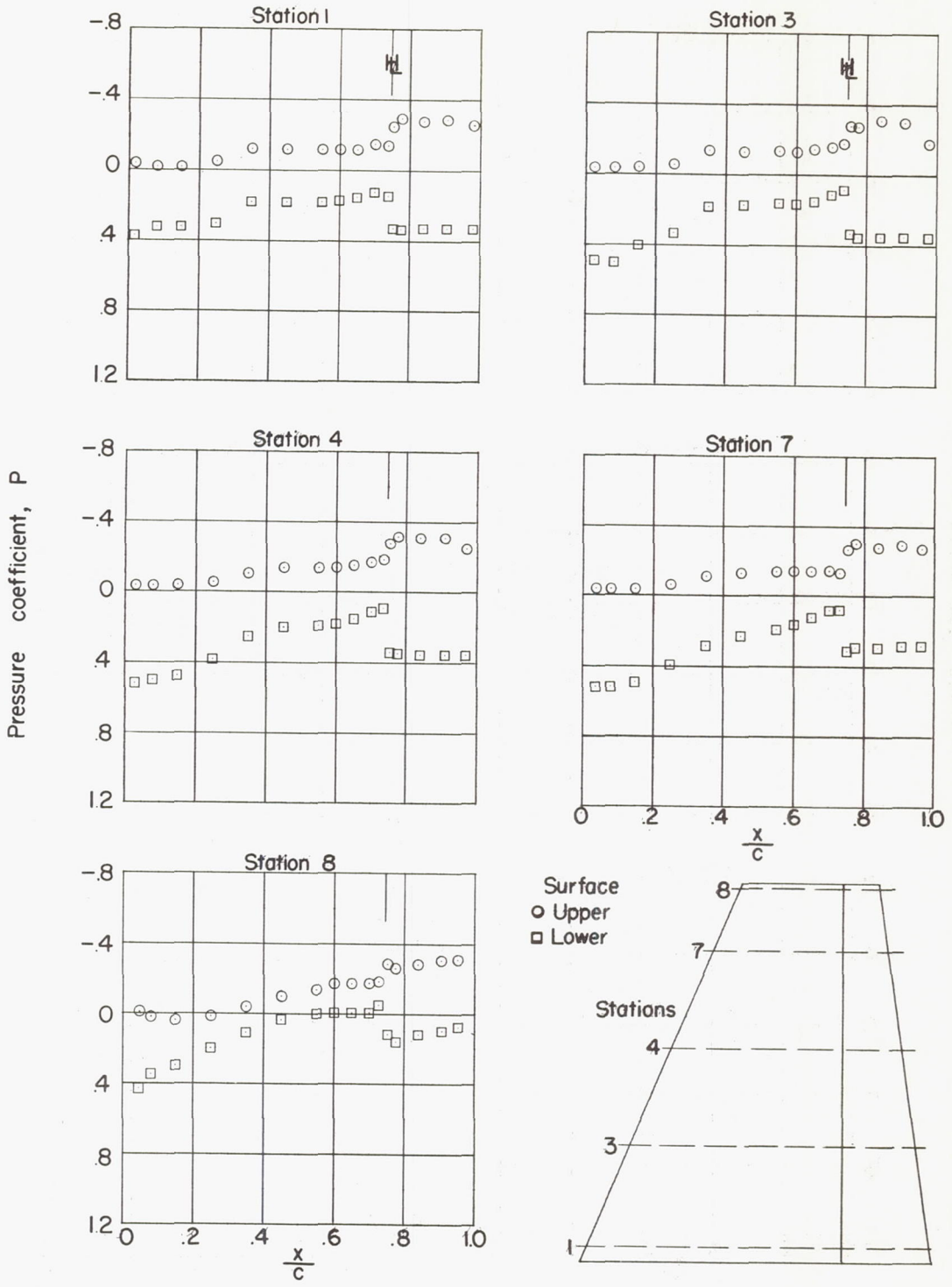

(e) $\alpha = 6^{\circ}$; $\delta = 10^{\circ}$.

Figure 12.- Continued.

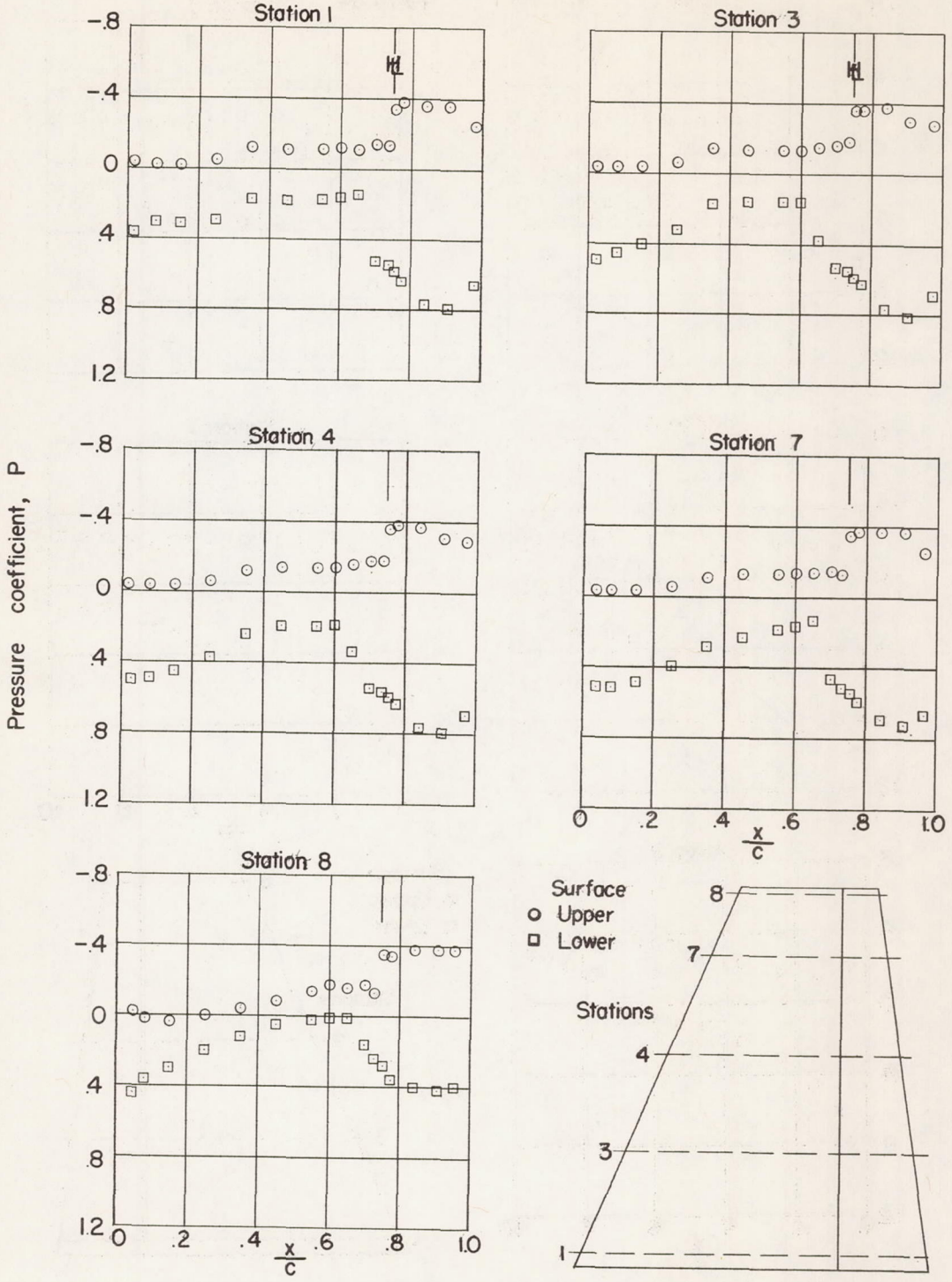

(f) $\alpha = 6^{\circ}$; $\delta = 20^{\circ}$.

Figure 12.- Continued.

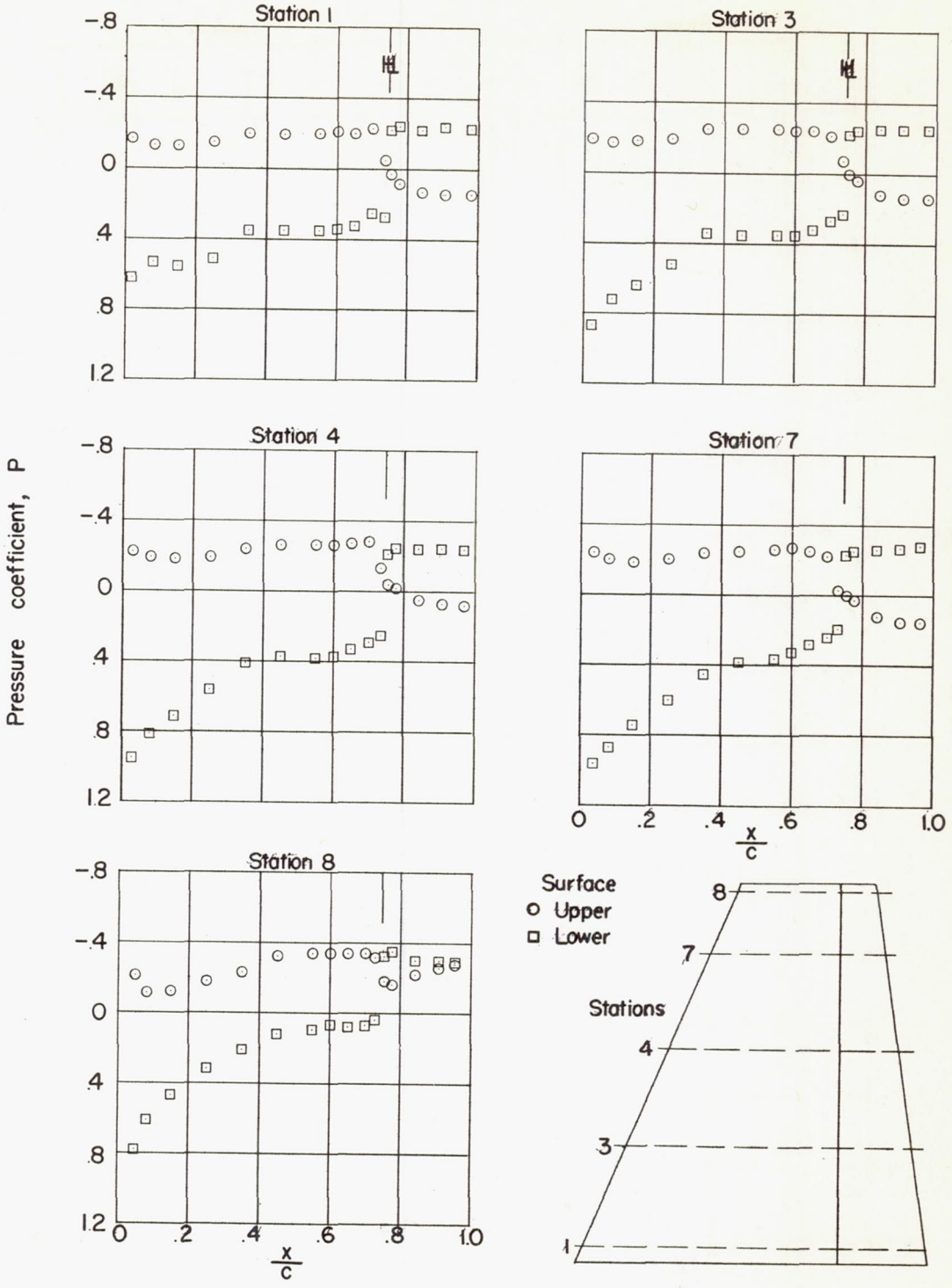

(g) $\alpha = 12^{\circ}$; $\delta = -20^{\circ}$.

Figure 12.- Continued.

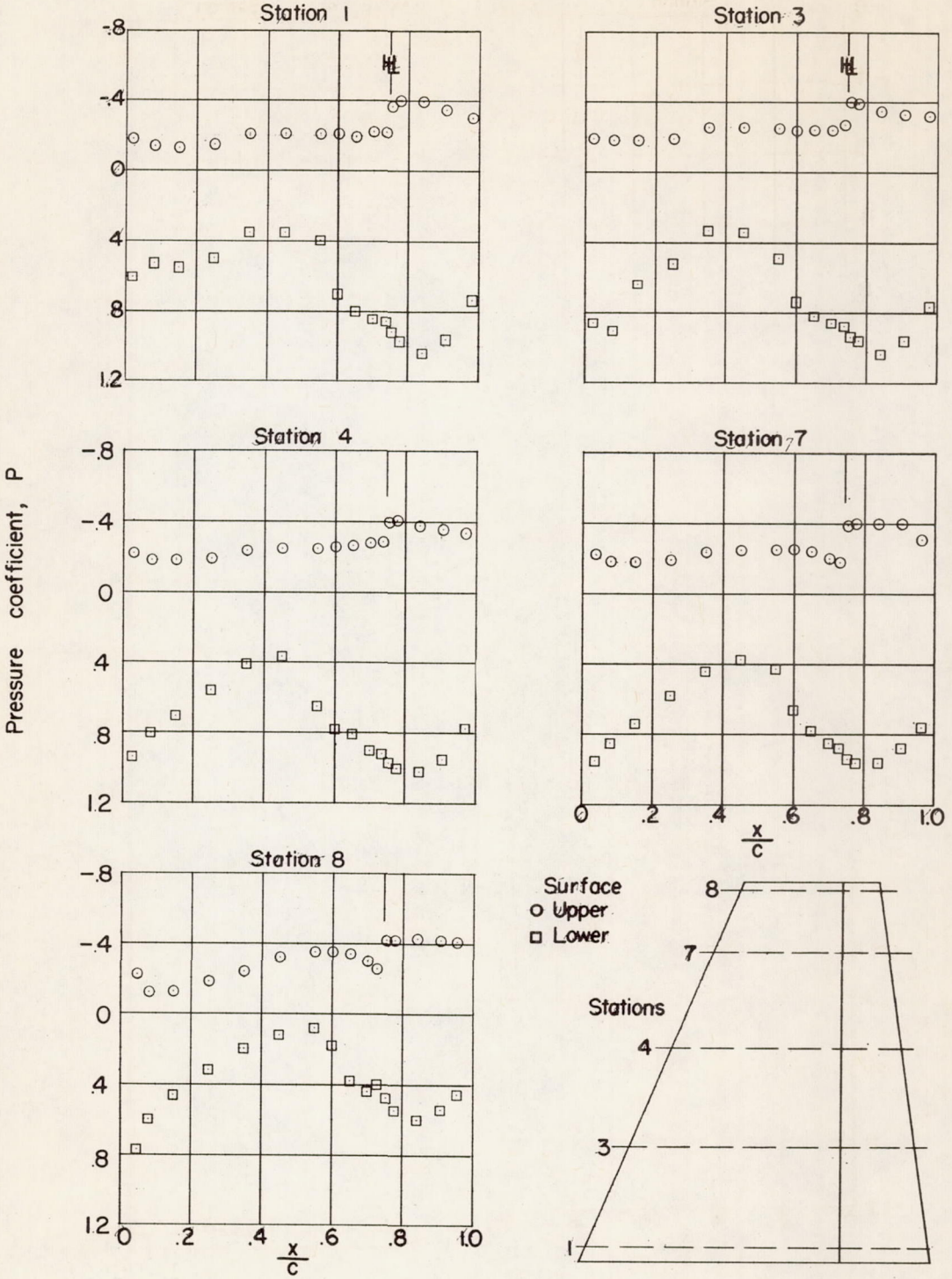

(h) $\alpha = 12^{\circ}$; $\delta = 20^{\circ}$.

Figure 12.- Concluded.

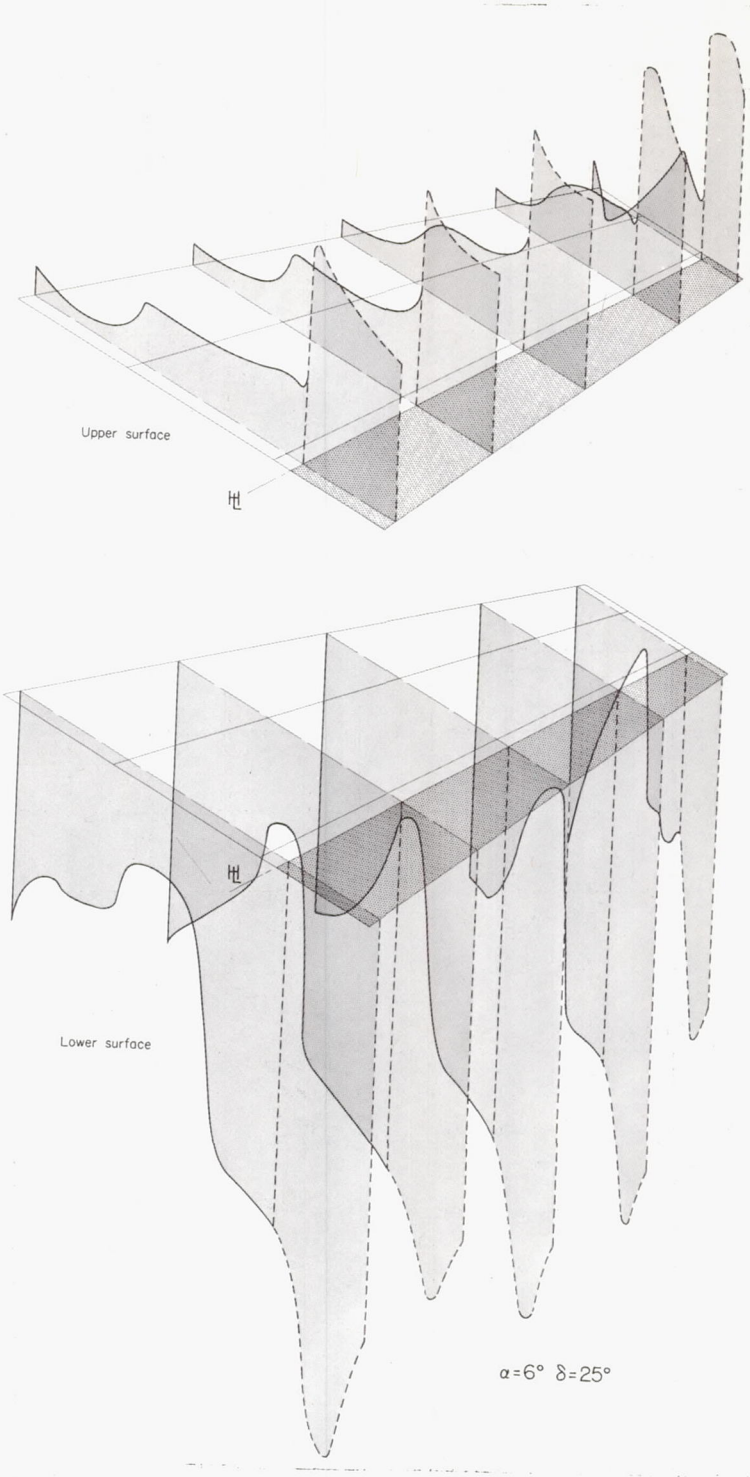

L-90506

Figure 13.- Chordwise pressure distributions on upper and lower surfaces across the span of configuration 4. Height of shaded area indicates the magnitude of the pressure coefficient, negative above the surface and positive below. M = 1.61; R = 3.6×10^6.

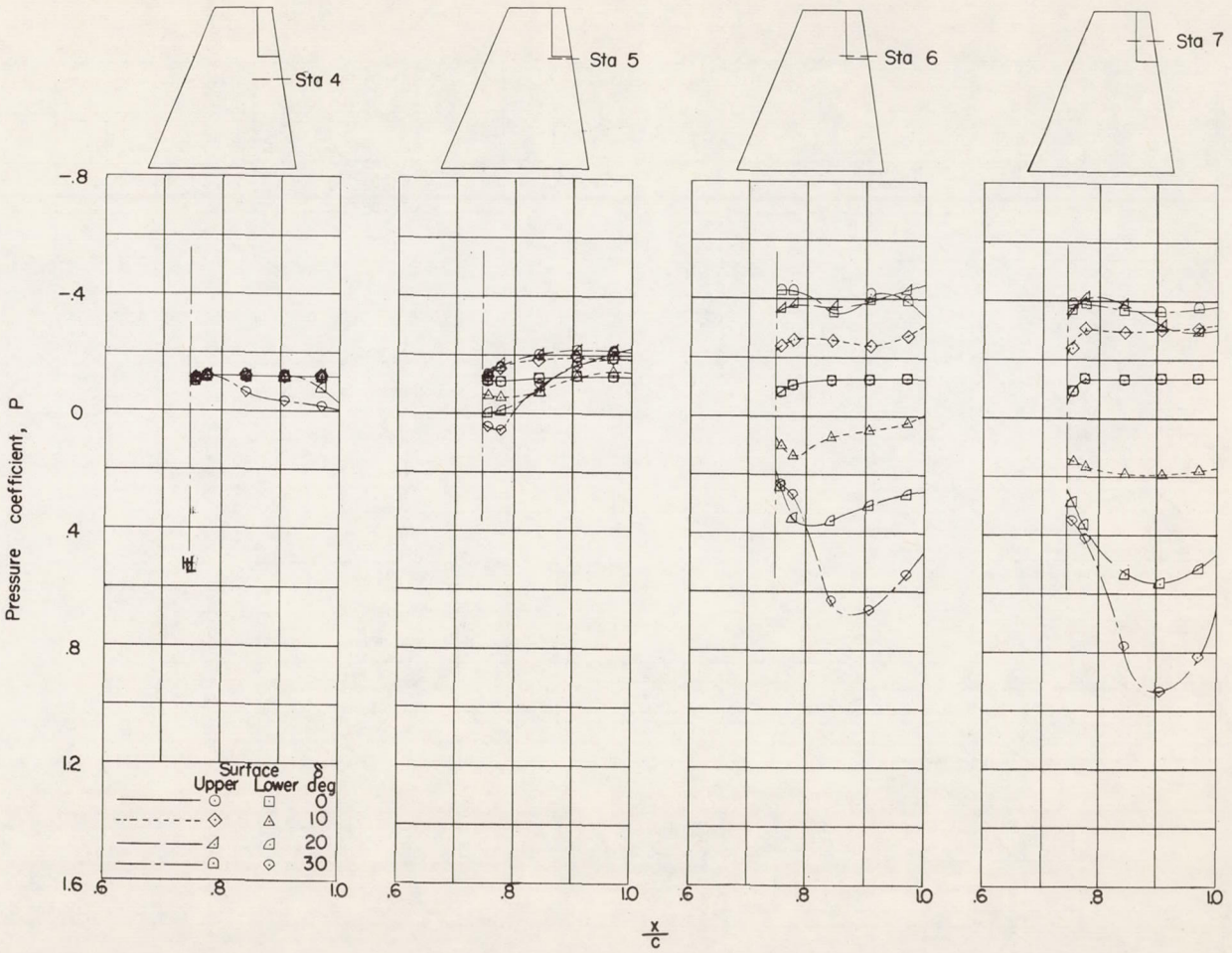

(a) $\alpha = 0^{\circ}$.

Figure 14.- Effect of control deflection on chordwise pressure distributions in the vicinity of the wing-control parting line. Configuration 1; M = 1.61; R = 3.6×10^6.

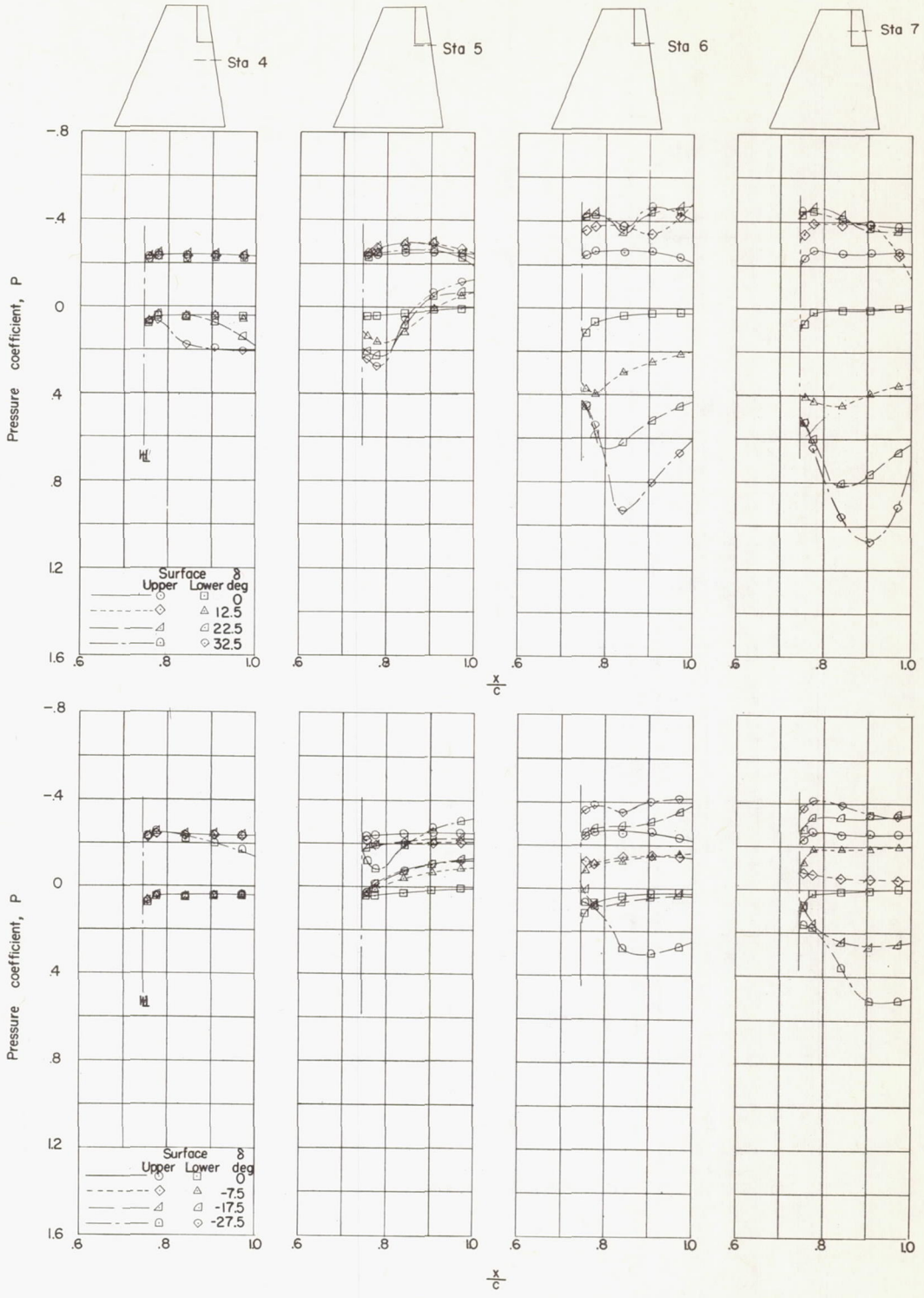

(b) $\alpha = 6^{\circ}$.

Figure 14.- Continued.

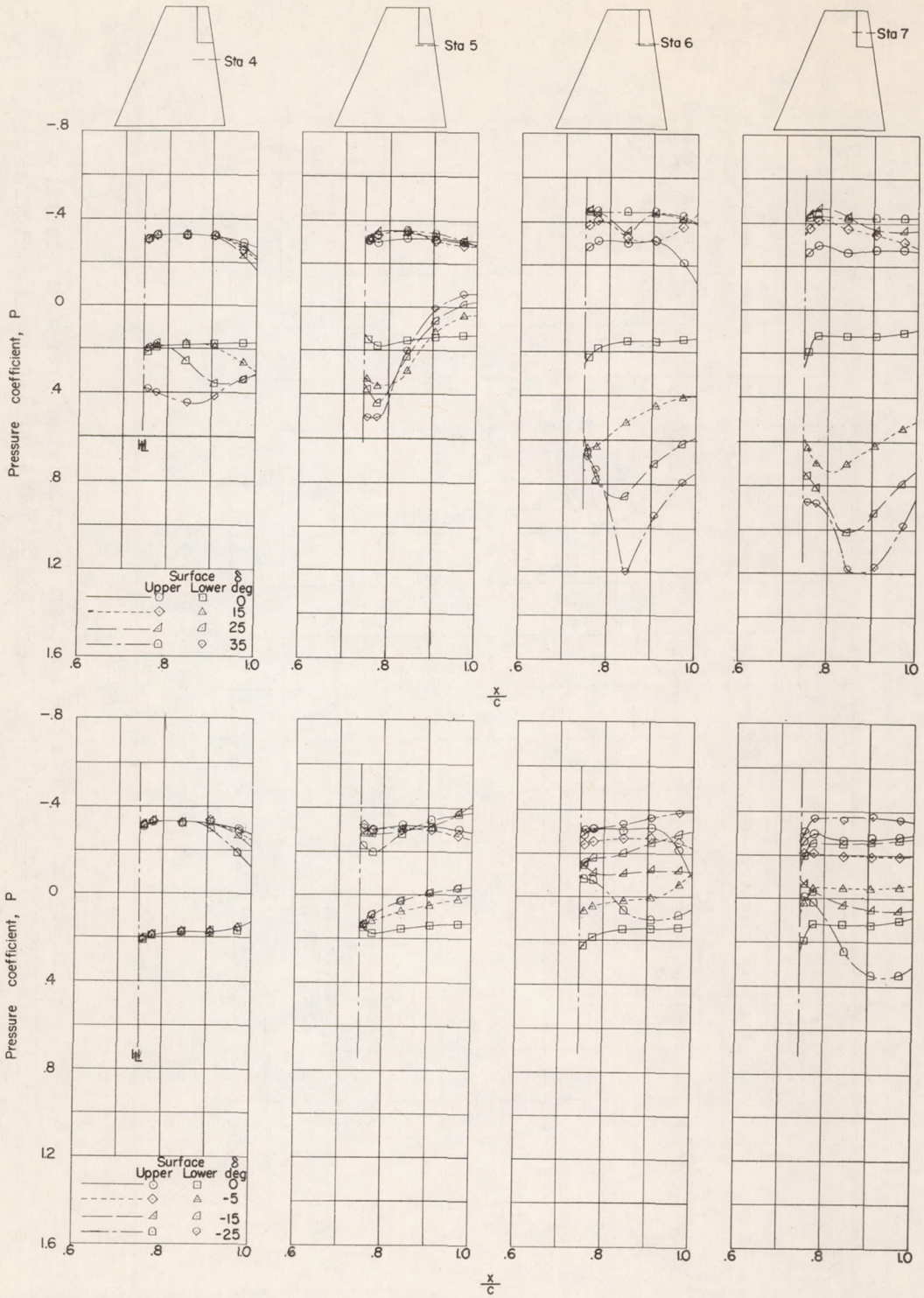

(c) $\alpha = 12^{\circ}$.

Figure 14.- Concluded.

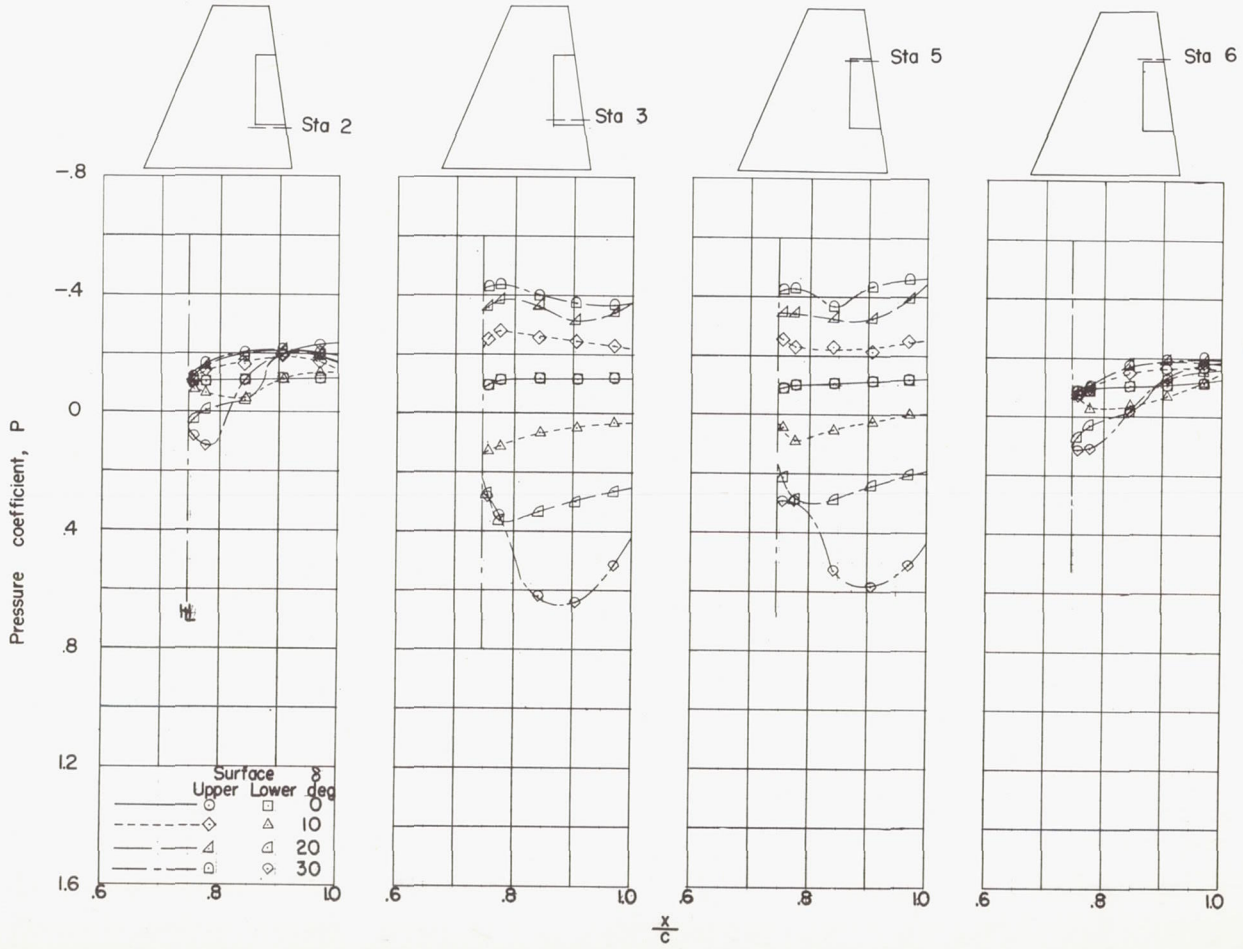

(a) $\alpha = 0^{\circ}$.

Figure 15.- Effect of control deflection on chordwise pressure distributions in the vicinity of the wing-control parting lines. Configuration 2; M = 1.61; R = 3.6×10^6.

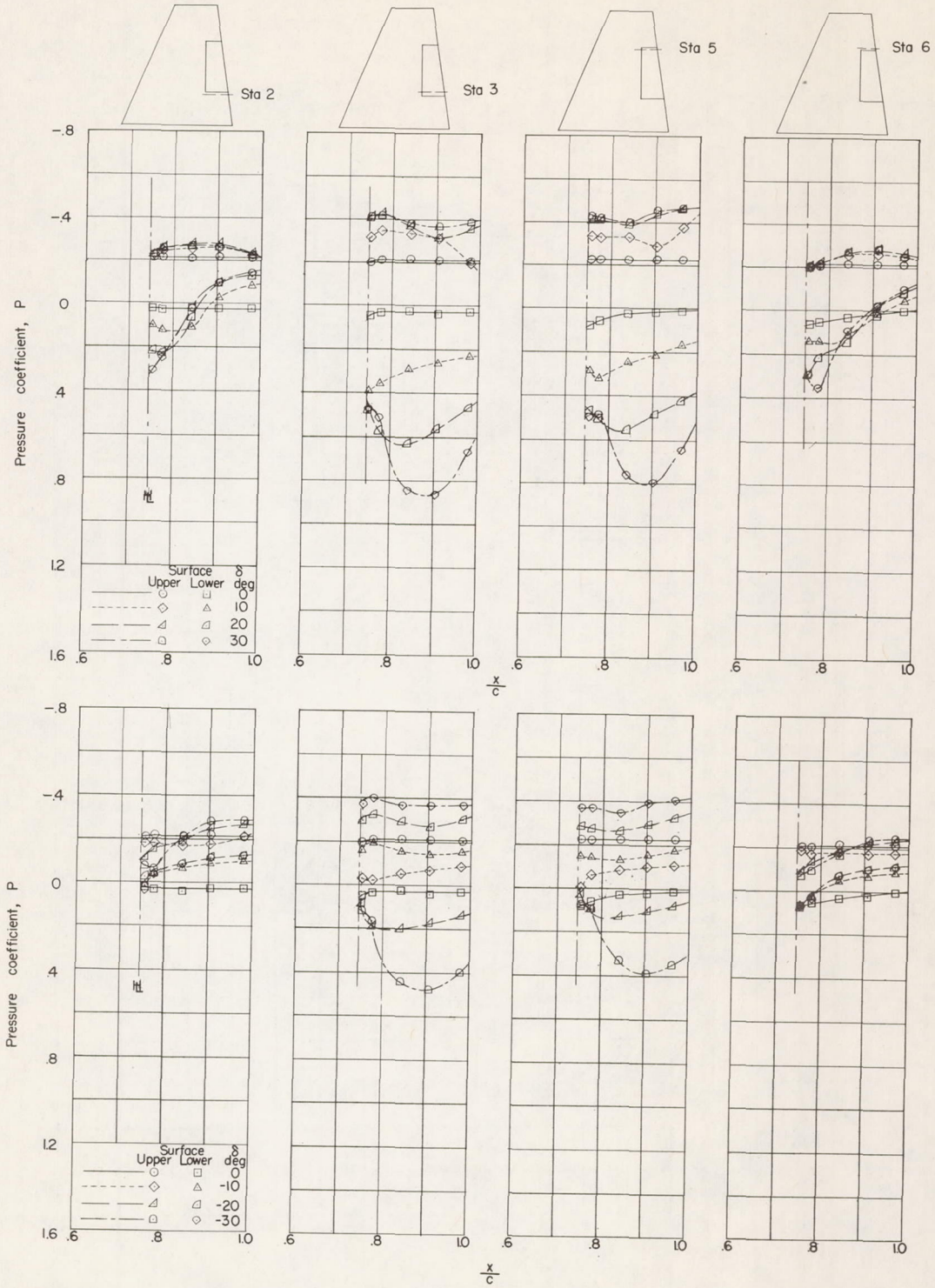

(b) $\alpha = 6°$.

Figure 15.- Continued.

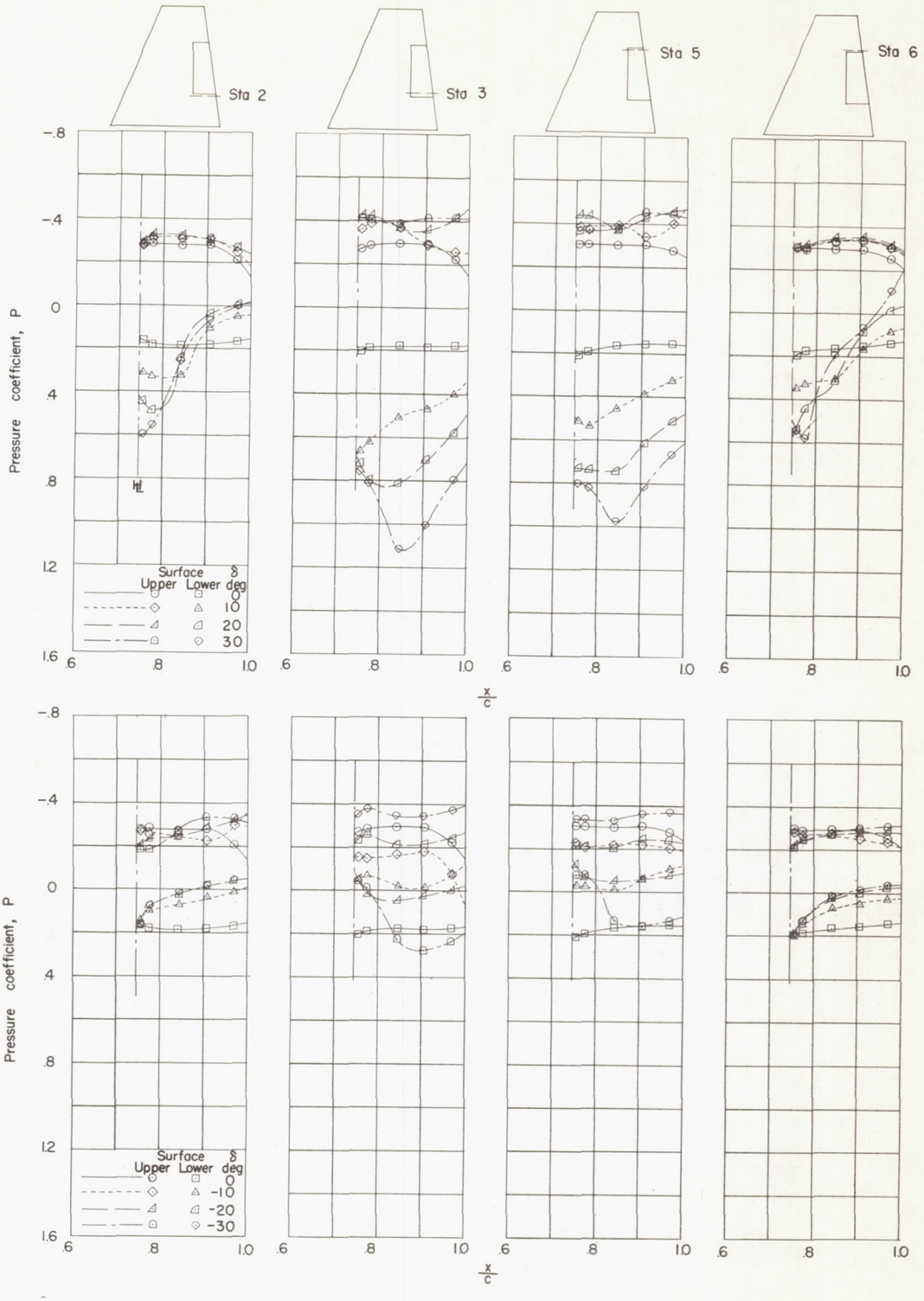

(c) $\alpha = 12^{\circ}$.

Figure 15.- Concluded.

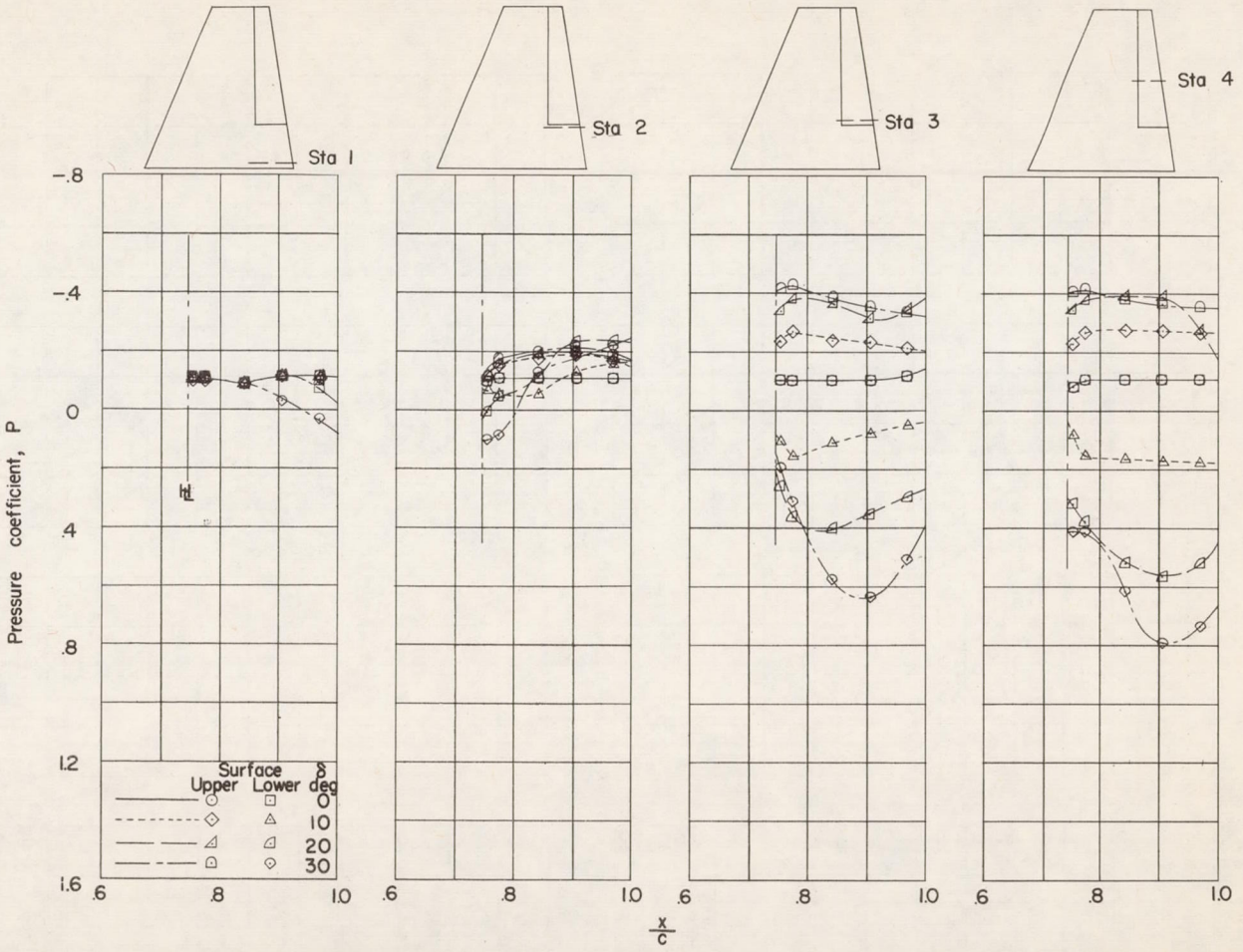

(a) $\alpha = 0^{\circ}$.

Figure 16.- Effect of control deflection on chordwise pressure distributions in the vicinity of the wing-control parting line. Configuration 3; M = 1.61; R = 3.6×10^6.

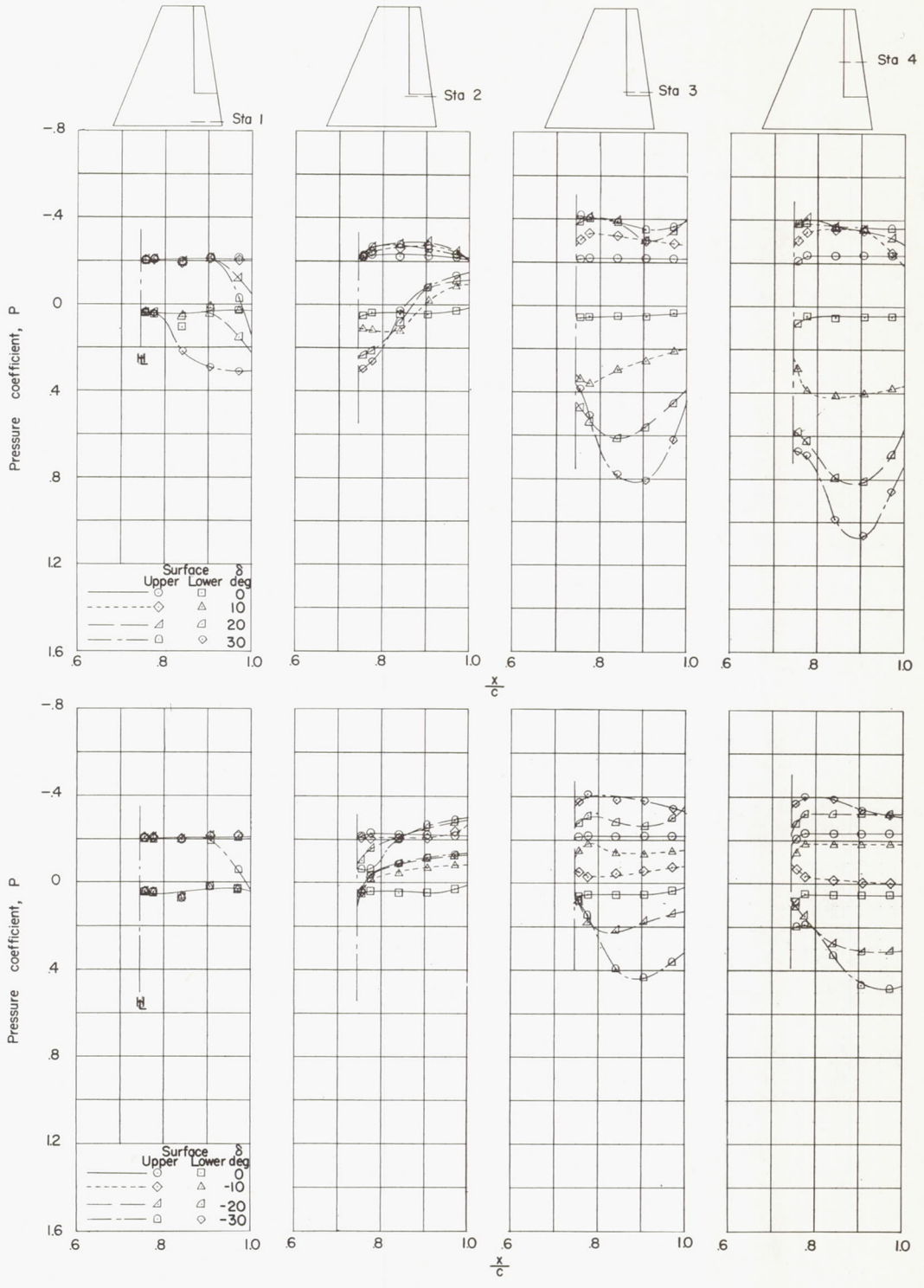

(b) $\alpha = 6^{\circ}$.

Figure 16.- Continued.

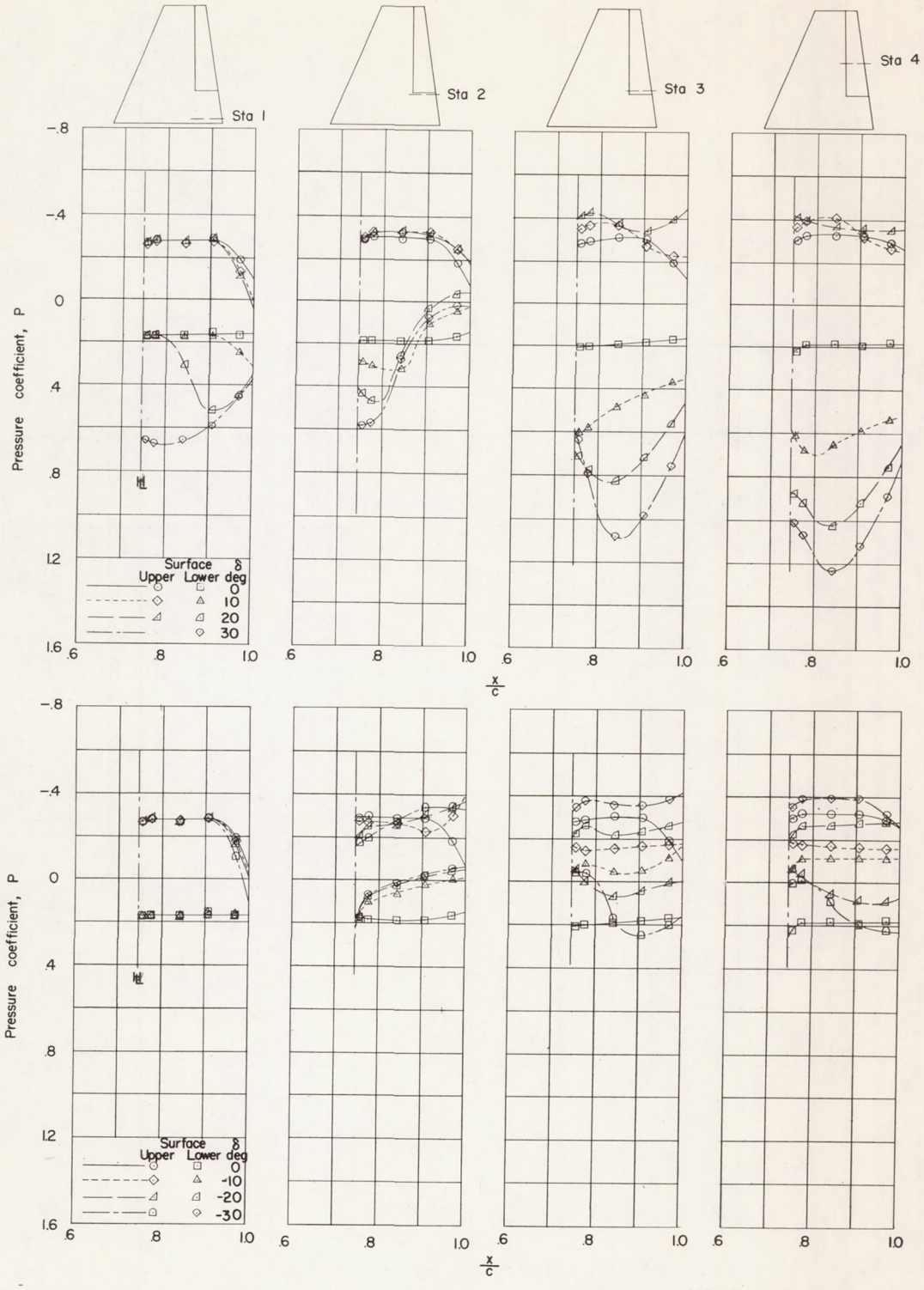

(c) $\alpha = 12^{\circ}$.

Figure 16.- Concluded.

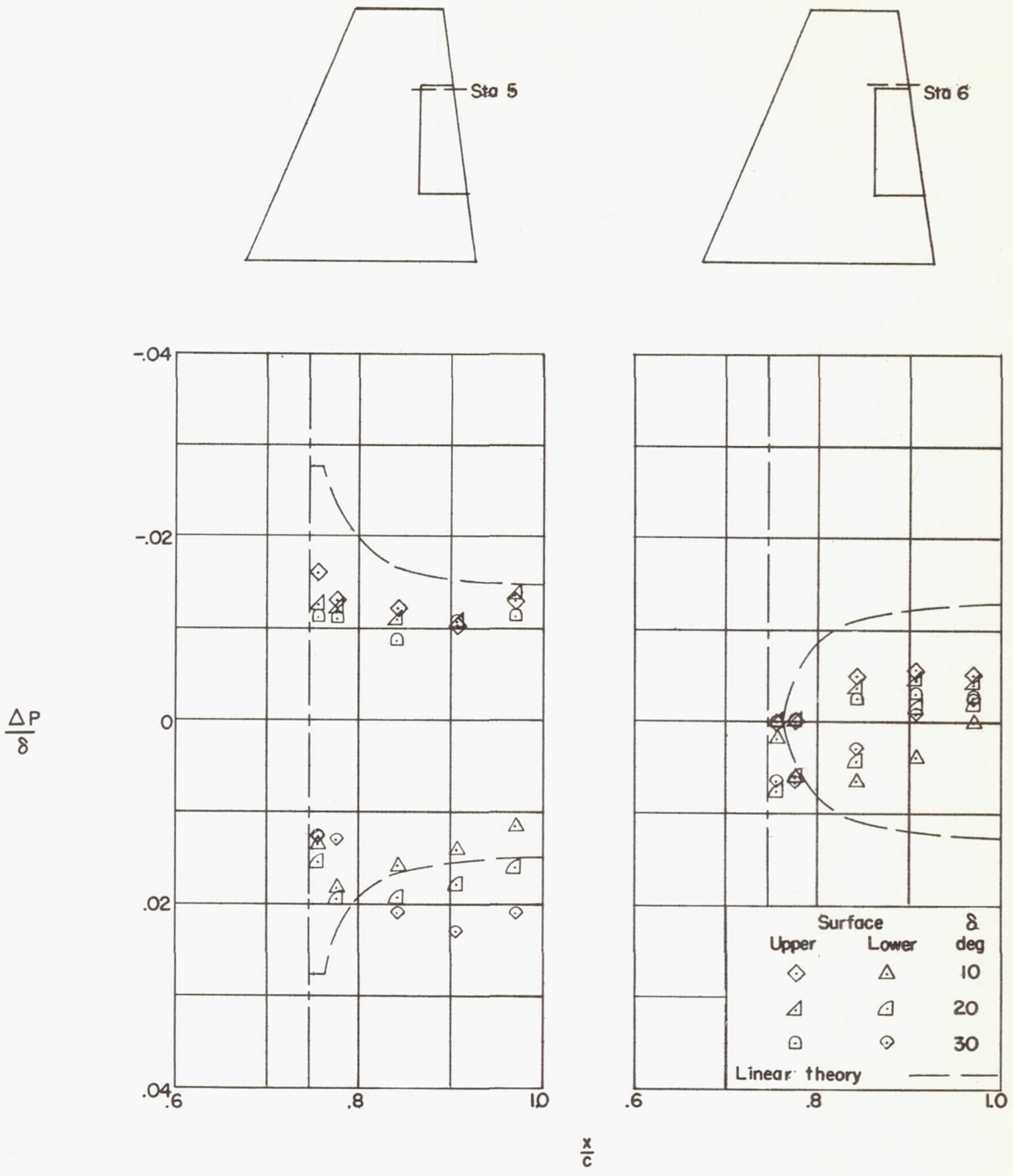

(a) $\alpha = 0^{\circ}$.

Figure 17.- Comparison of experimental and theoretical incremental pressure distributions adjacent to a typical wing-control parting line. Configuration 2; M = 1.61; R = 3.6×10^6.

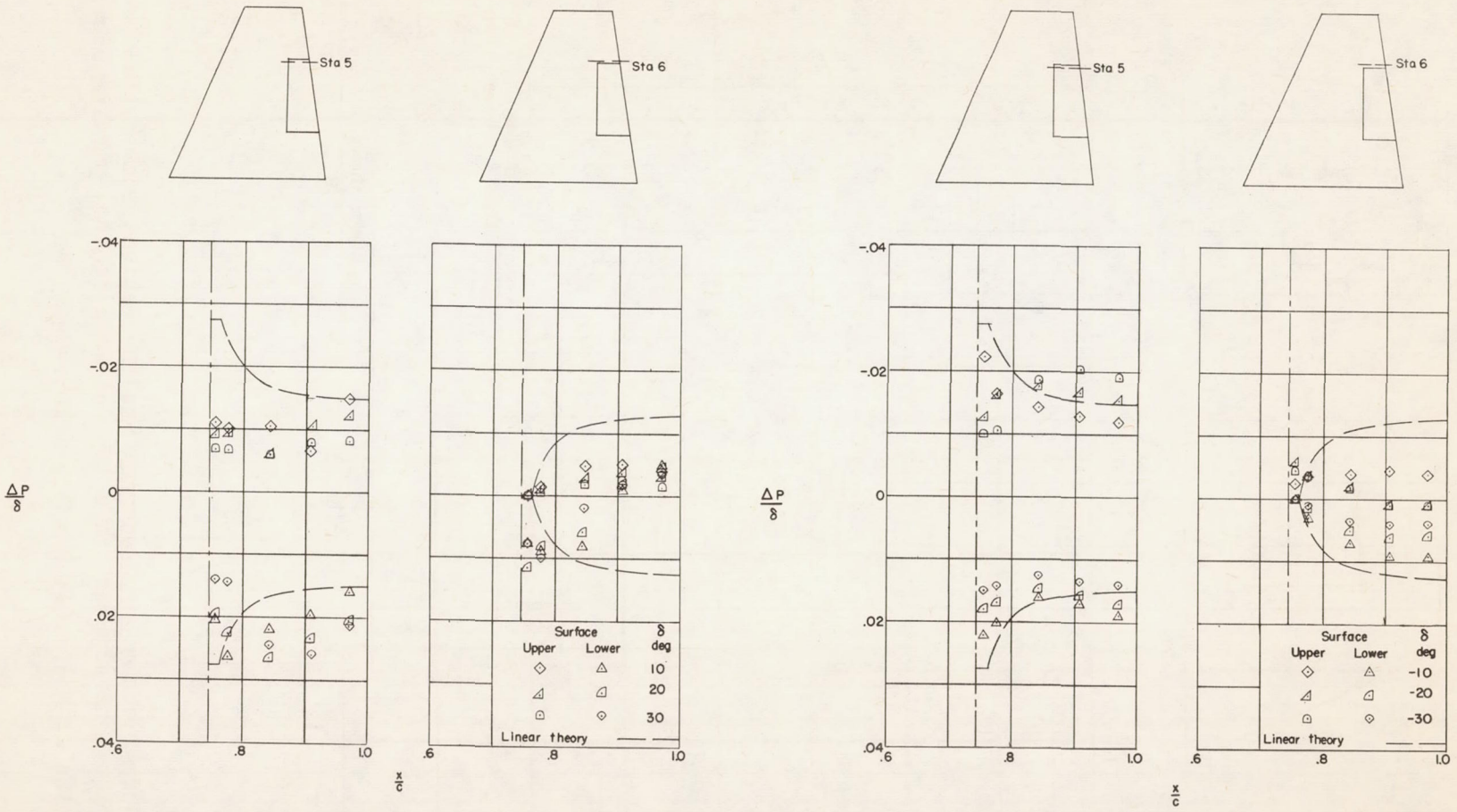

(b) $\alpha = 6^{\circ}$.

Figure 17.- Continued.

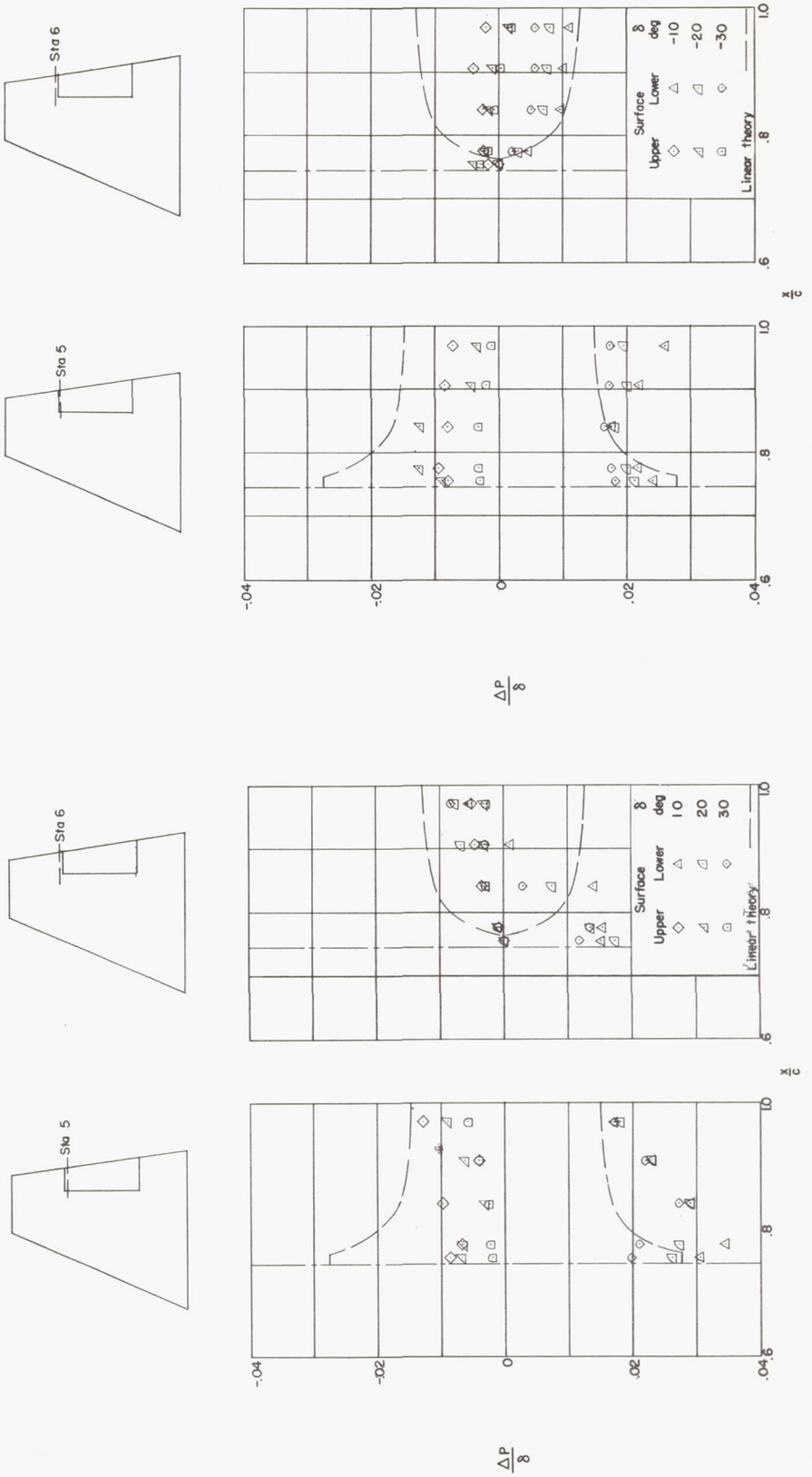

(c) $\alpha = 12^{\circ}$.

Figure 17.- Concluded.

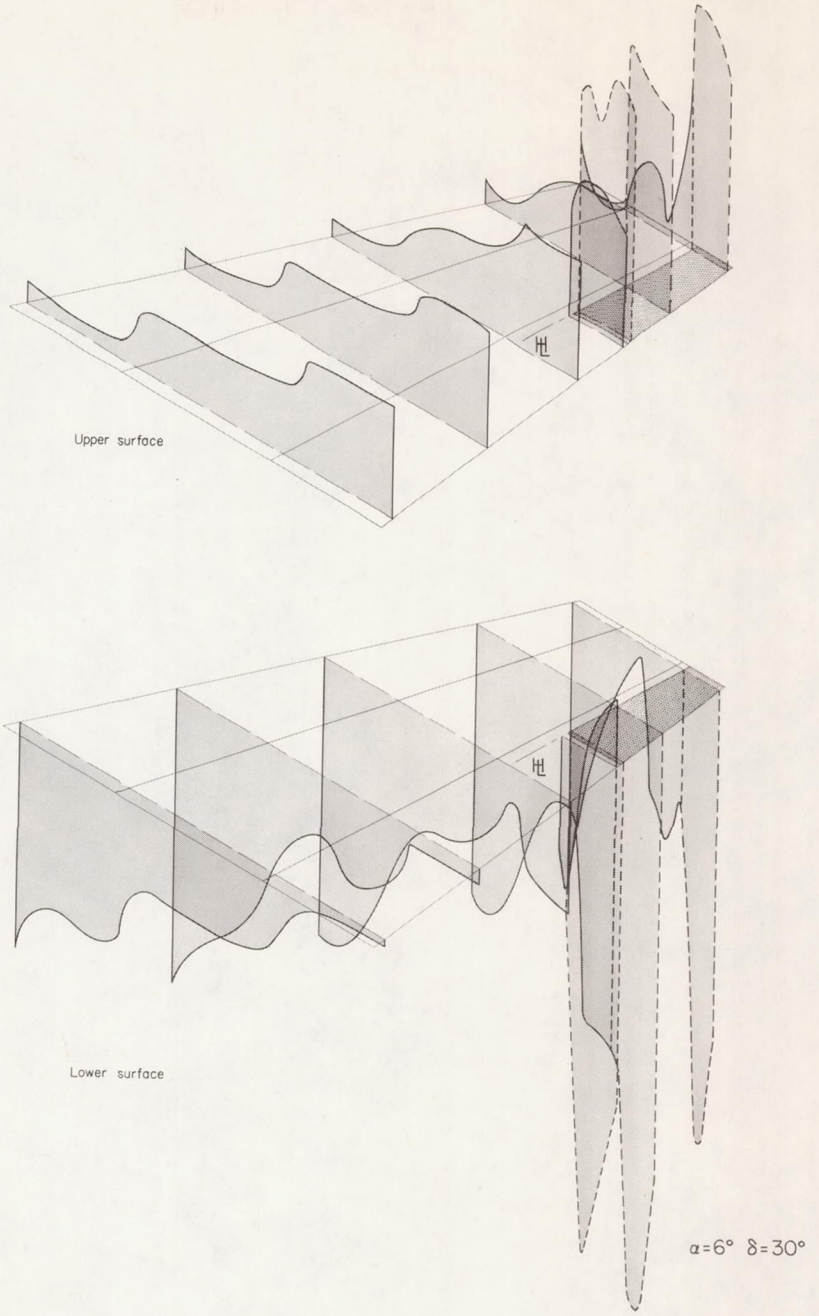

(a) Configuration 1. L-90507

Figure 18.- Chordwise pressure distributions on upper and lower surfaces across the span of the partial-span control configurations. Height of shaded area indicates the magnitude of the pressure coefficient, negative above the surface and positive below. M = 1.61; R = 3.6×10^6.

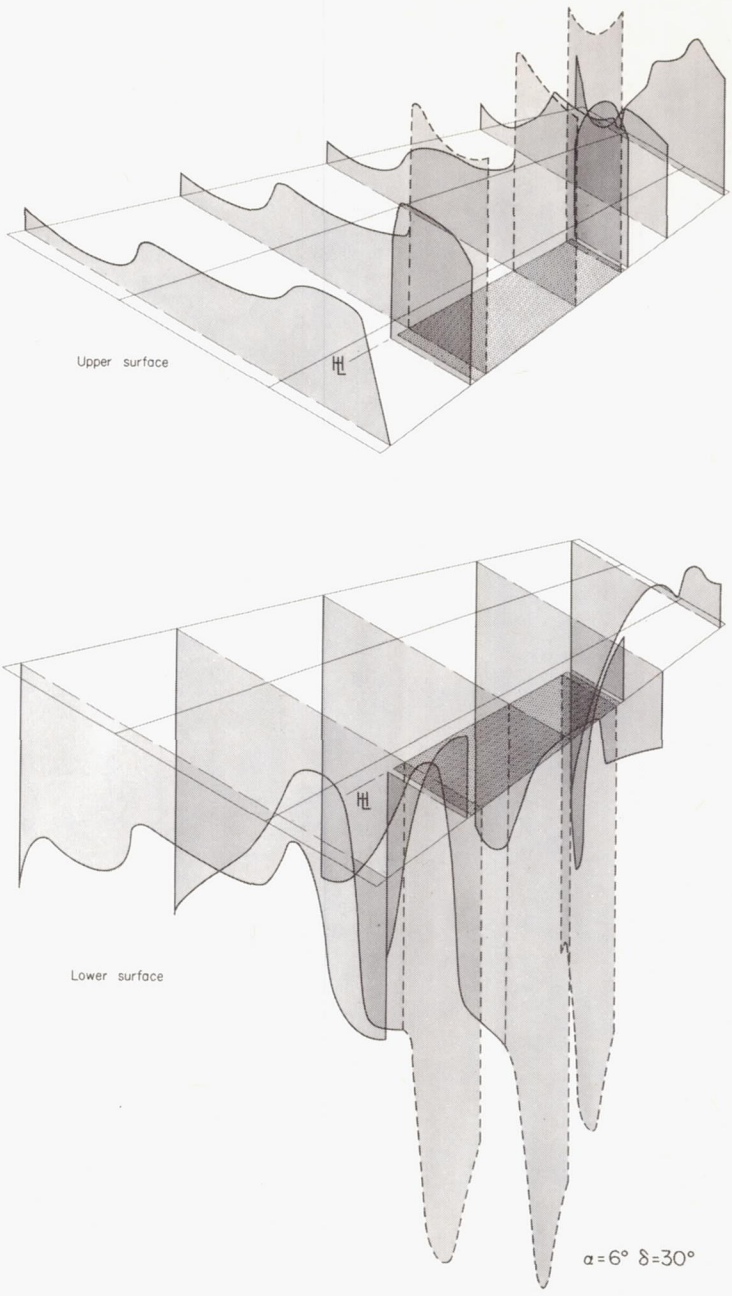

L-90508

(b) Configuration 2.

Figure 18.- Continued.

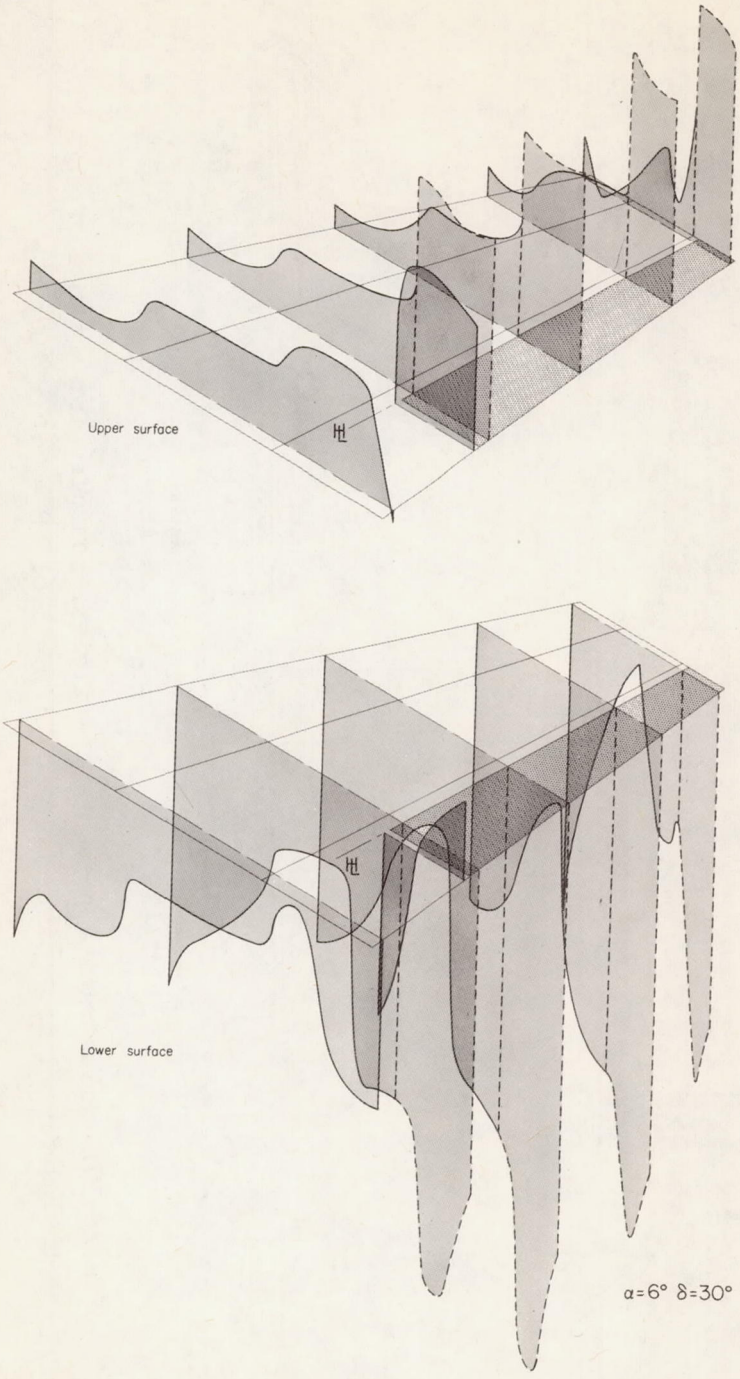

(c) Configuration 3. L-90509

Figure 18.- Concluded.

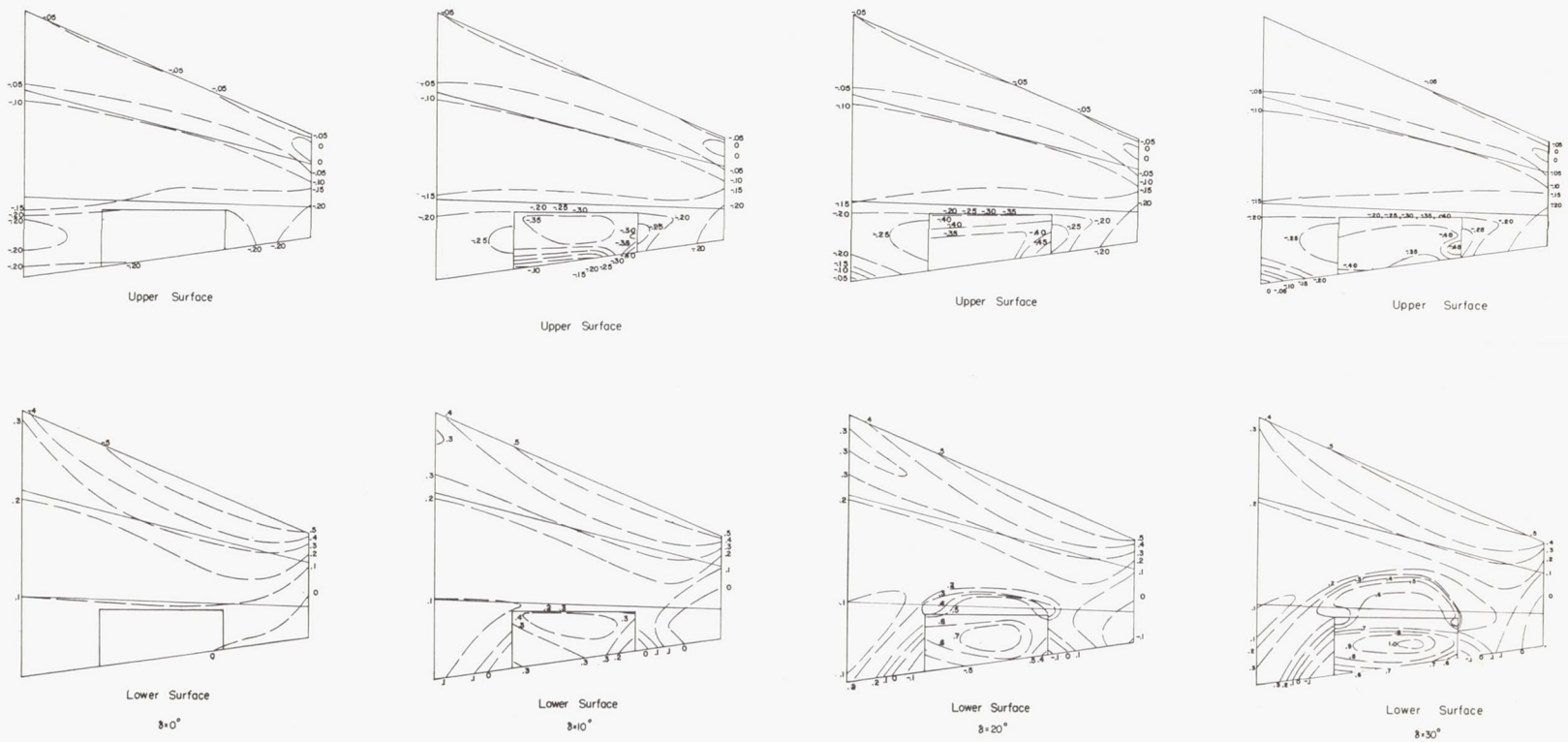

Figure 19.- Illustrative pressure-coefficient contours for a range of control deflections. Configuration 2; M = 1.61; R = 3.6×10^6; $\alpha = 6^\circ$.

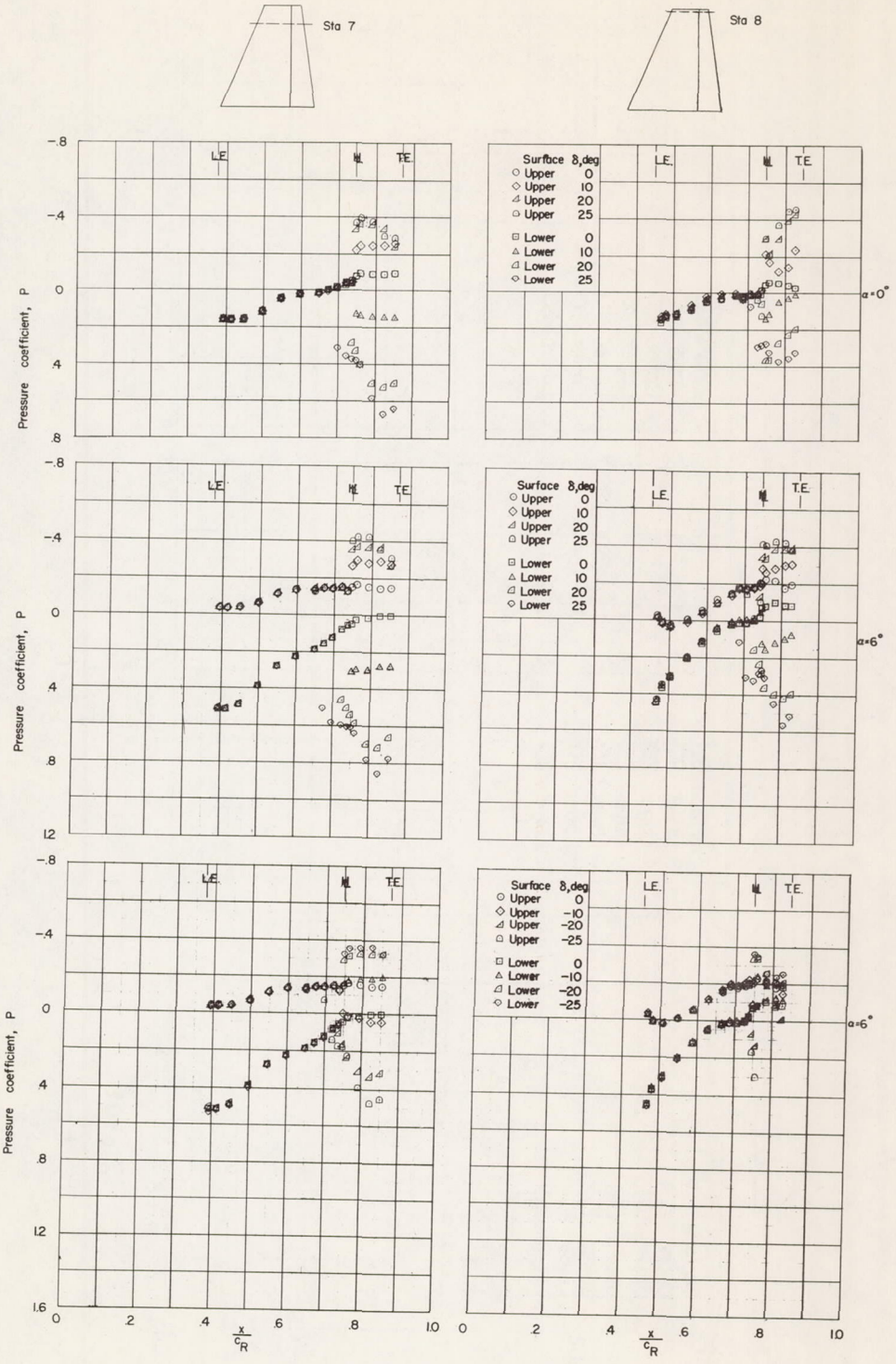

Figure 20.- Variation of chordwise pressure distributions in the vicinity of the wing tip with control deflection. Configuration 4; M = 1.61; $R = 3.6 \times 10^6$.

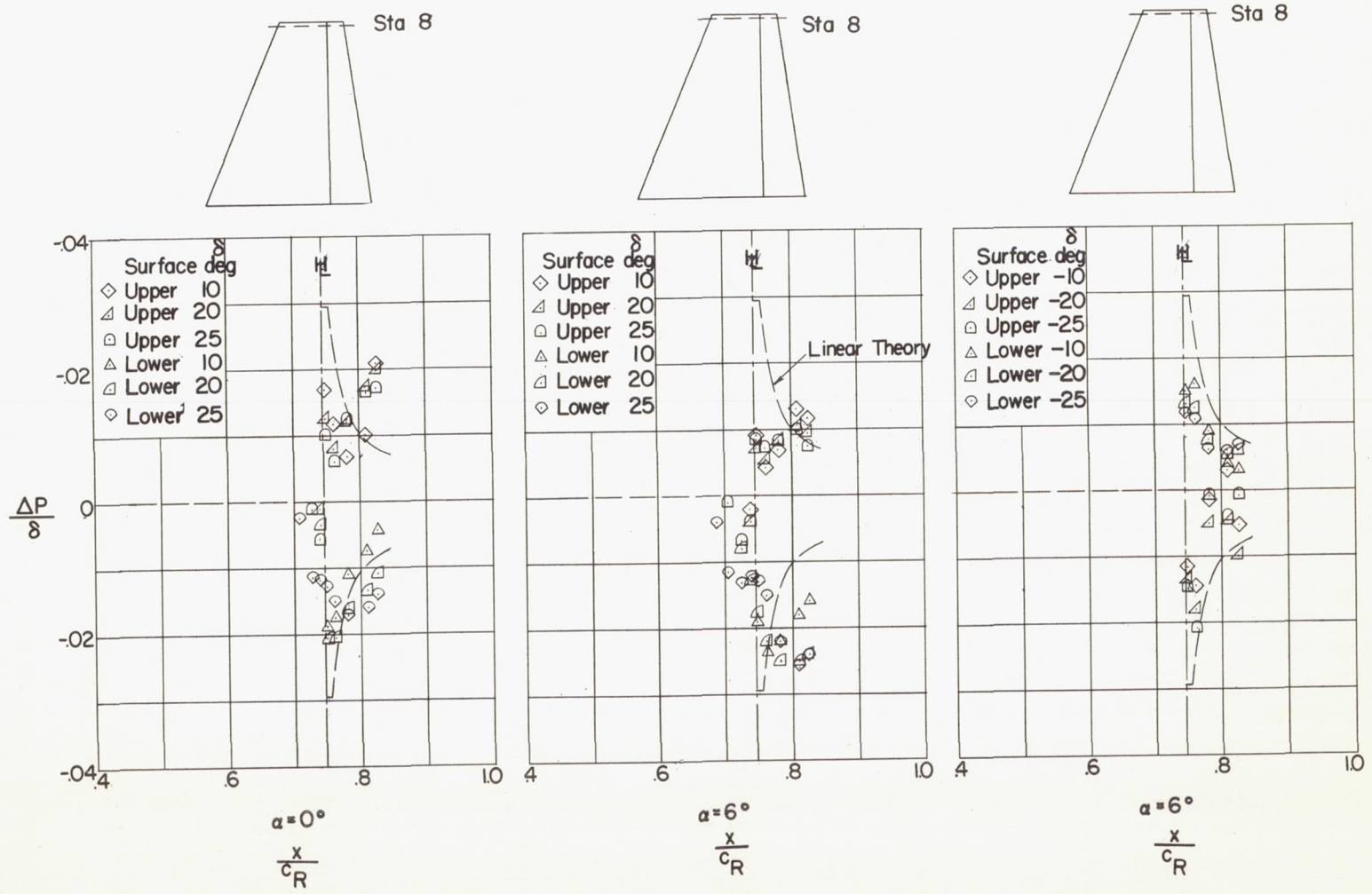

Figure 21.- Comparison of experimental and theoretical incremental pressure distributions in the vicinity of the wing tip due to control deflection. Configuration 4; M = 1.61; R = 3.6×10^6.

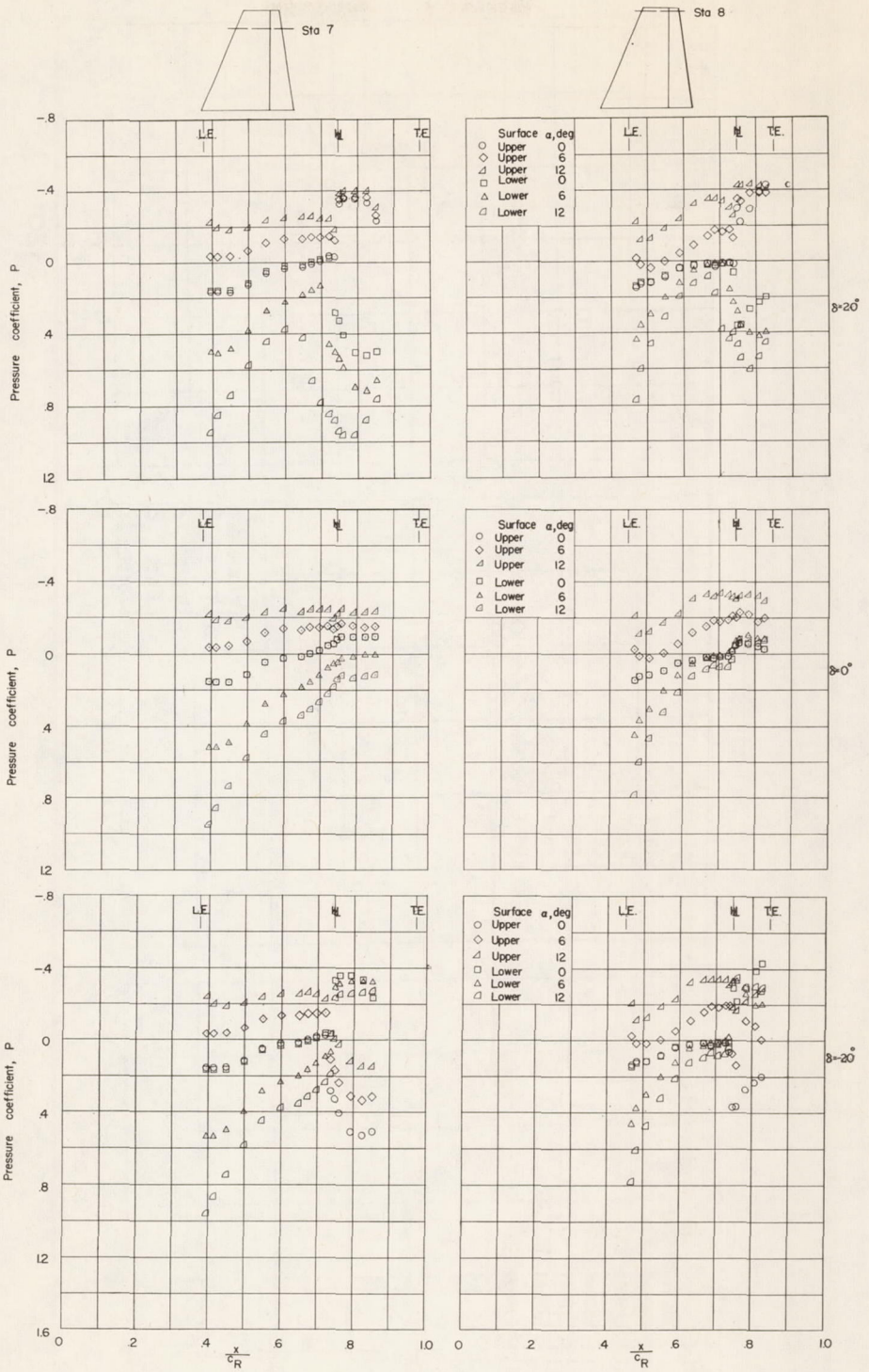

Figure 22.- Variation of chordwise pressure distributions in the vicinity of the wing tip with angle of attack. Configuration 4; M = 1.61; R = 3.6×10^6.

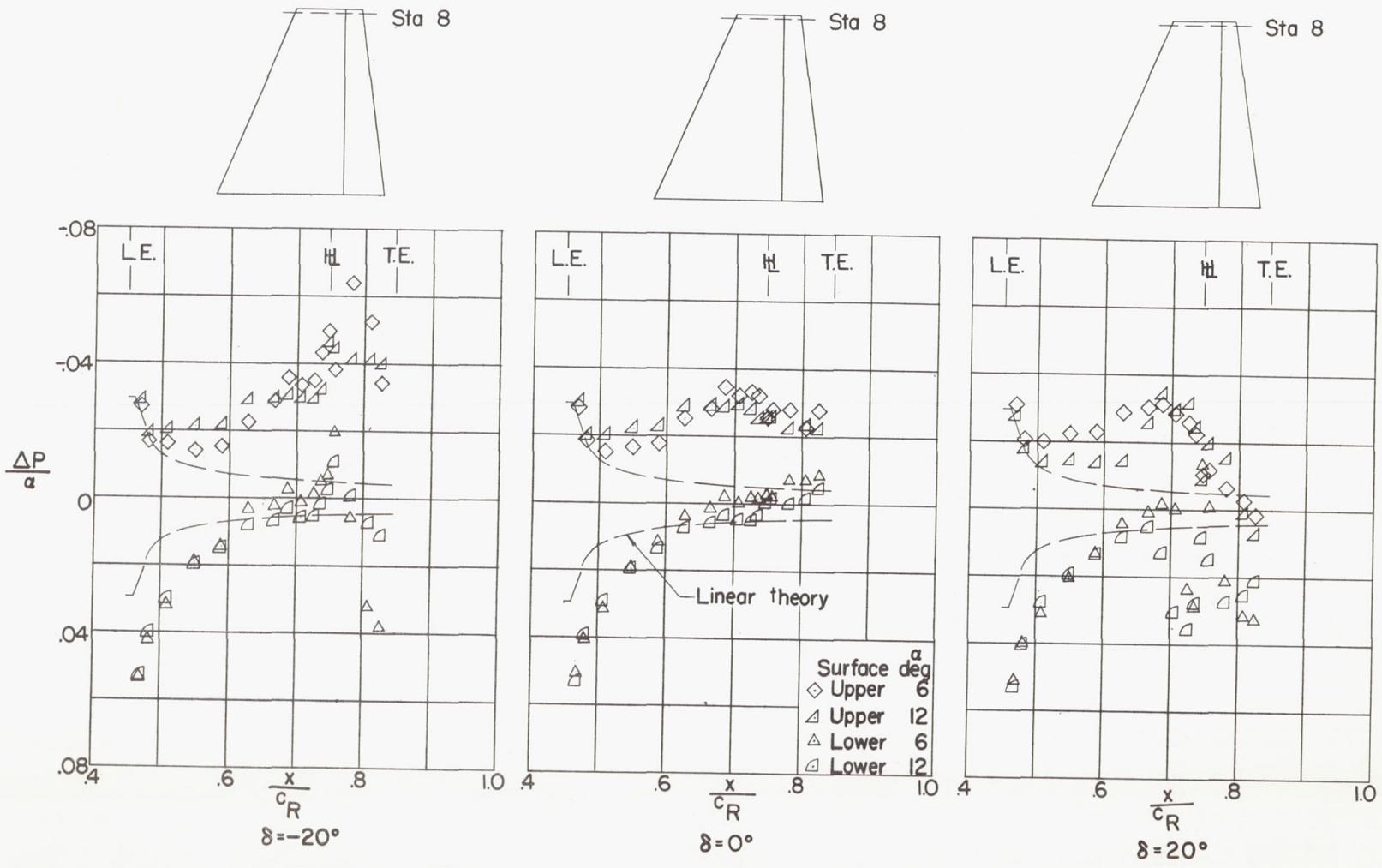

Figure 23.- Comparison of experimental and theoretical incremental pressure distributions in the vicinity of the wing tip due to angle of attack. Configuration 4; M = 1.61; R = 3.6×10^6.

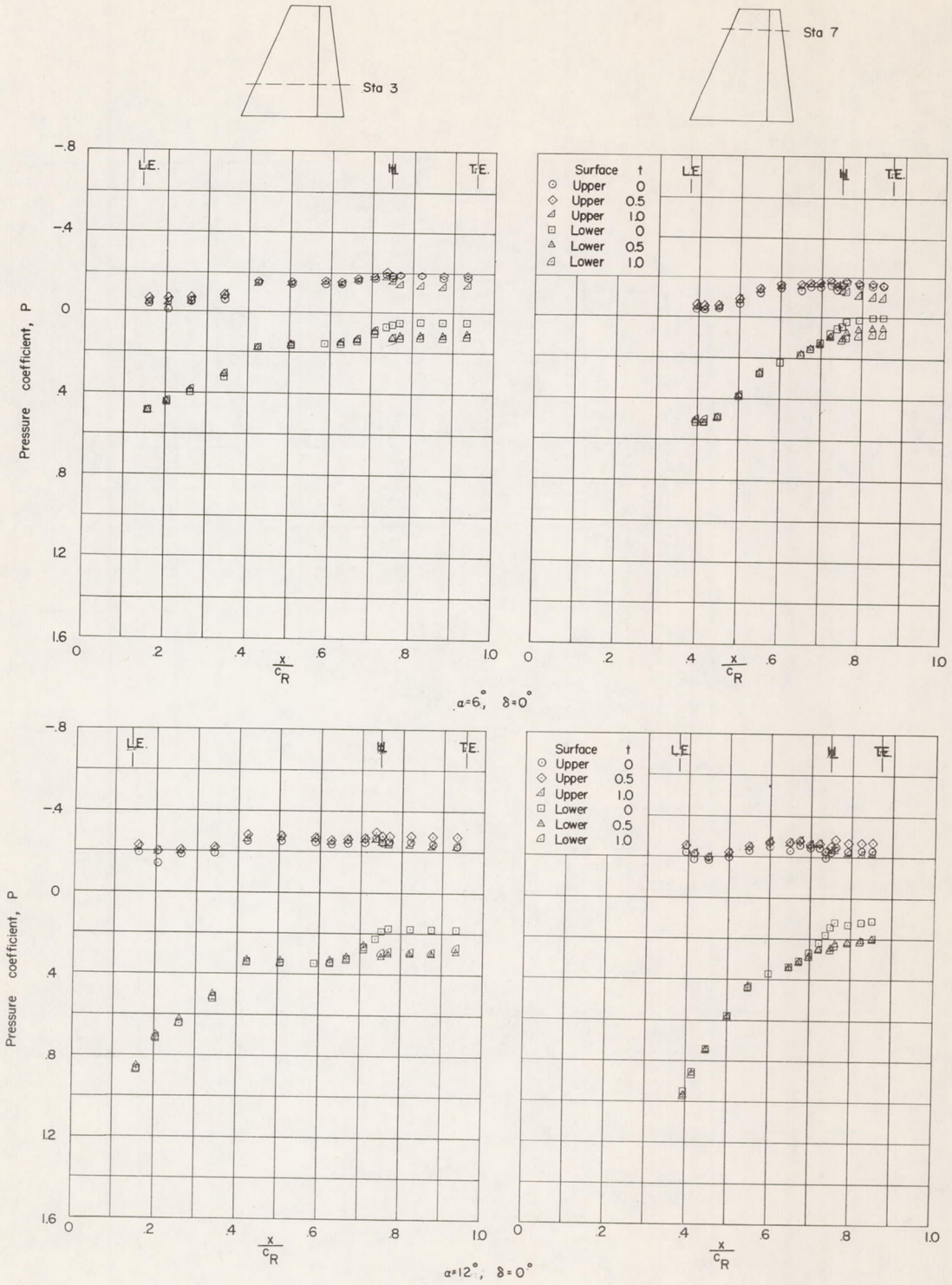

Figure 24.- Effect of control trailing-edge thickness on the chordwise pressure distributions at two spanwise stations. M = 1.61; R = 3.6×10^6.

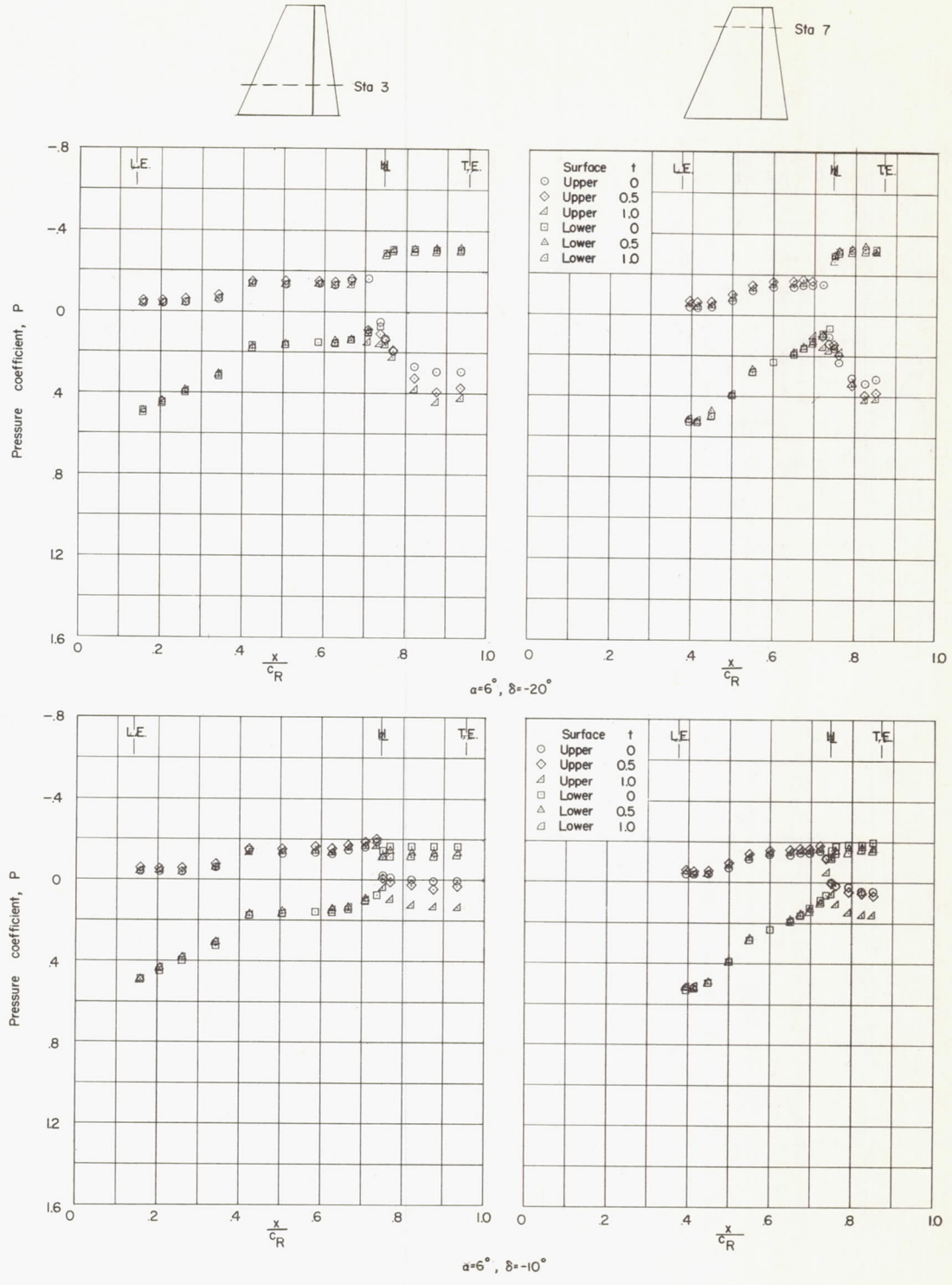

Figure 24.- Continued.

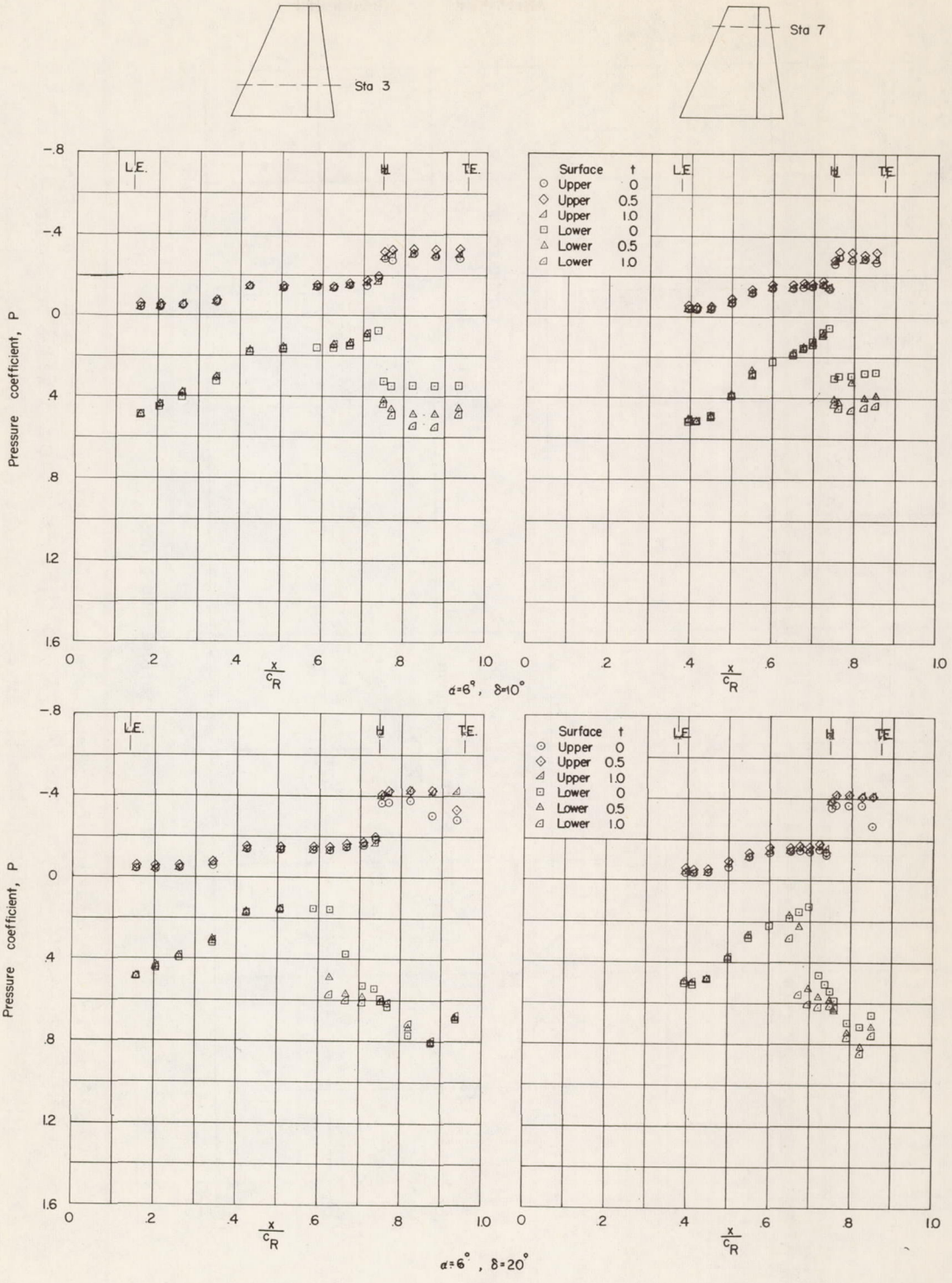

Figure 24.- Concluded.

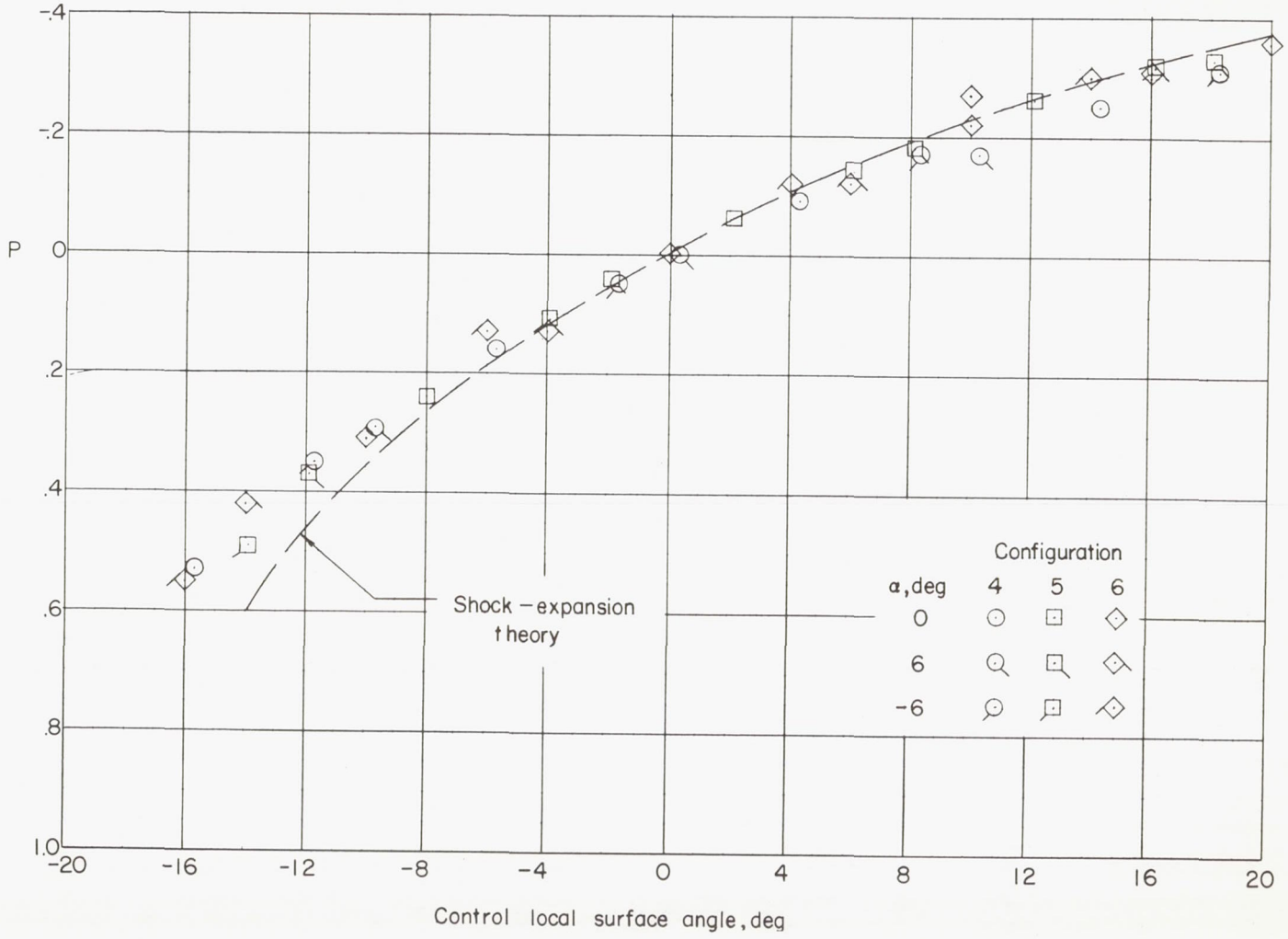

Figure 25.- Correlation of final pressure coefficients attained on upper surface of configurations 4, 5, and 6, at station 3 with those predicted by shock-expansion theory. M = 1.61; R = 3.6×10^6.

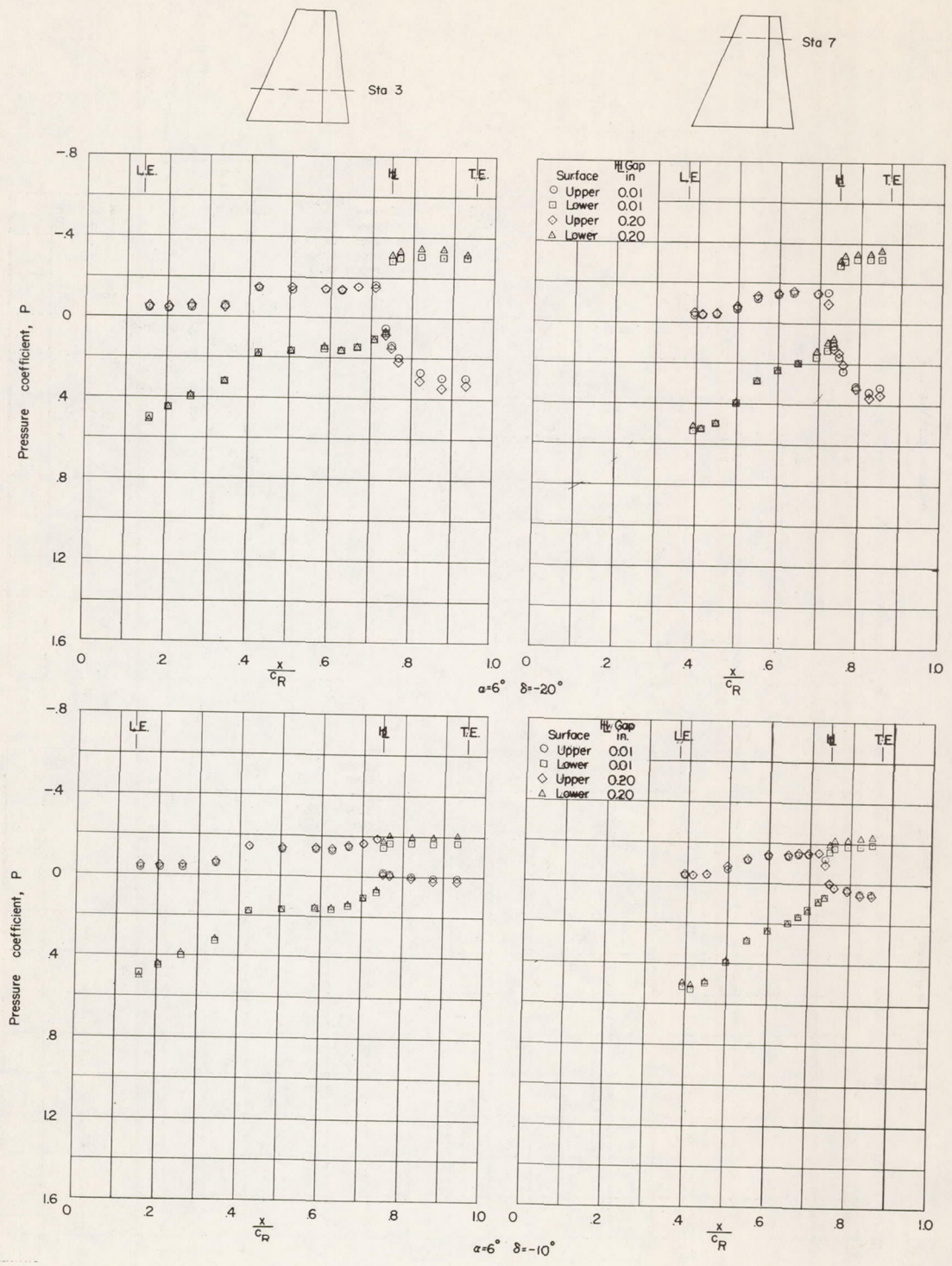

Figure 26.- Effect of increasing the hinge-line gap from 0.01 to 0.20 inch on the chordwise pressure distributions at two spanwise stations. Configuration 4; M = 1.61; R = 3.6×10^6.

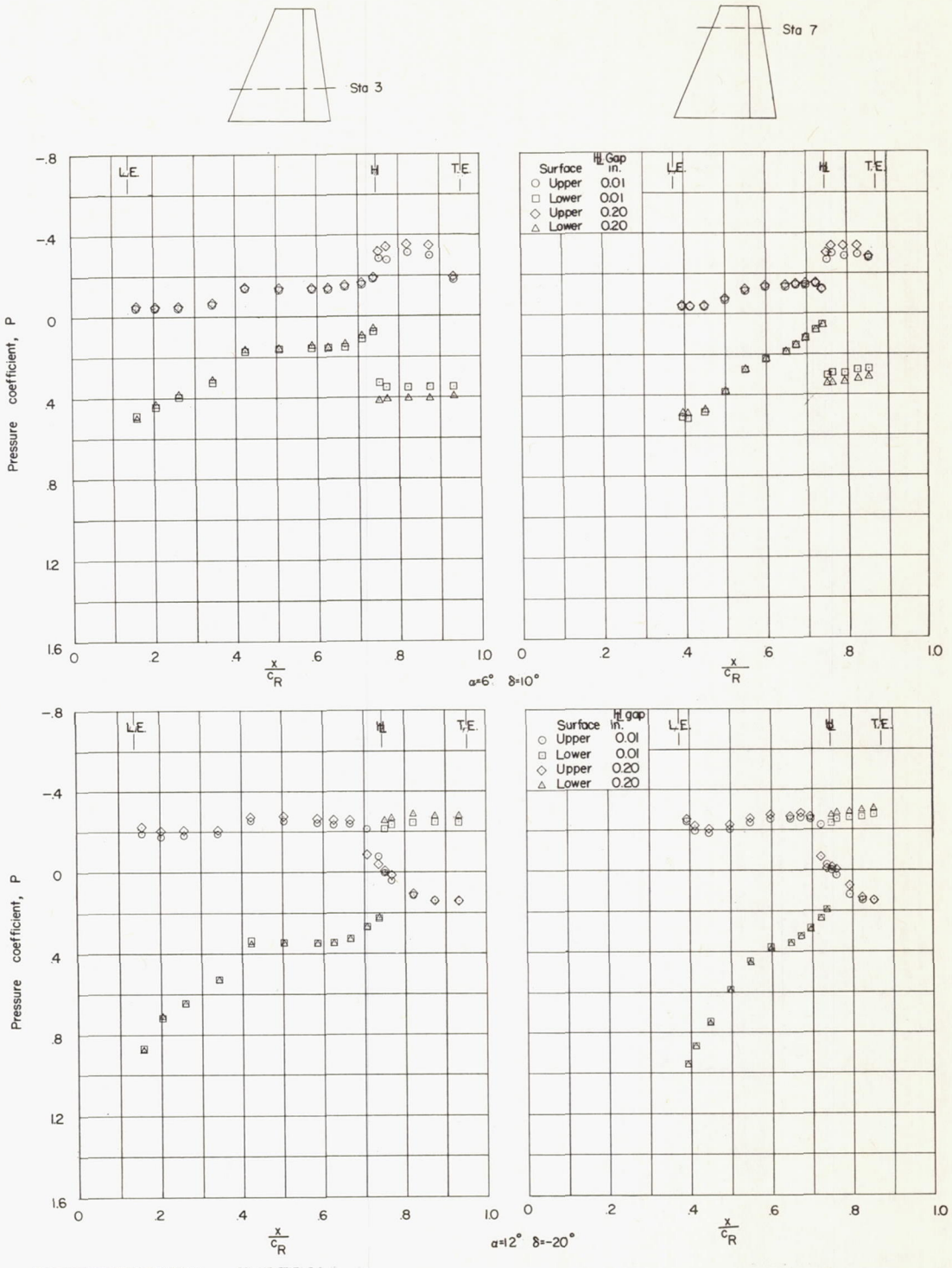

Figure 26.- Continued.

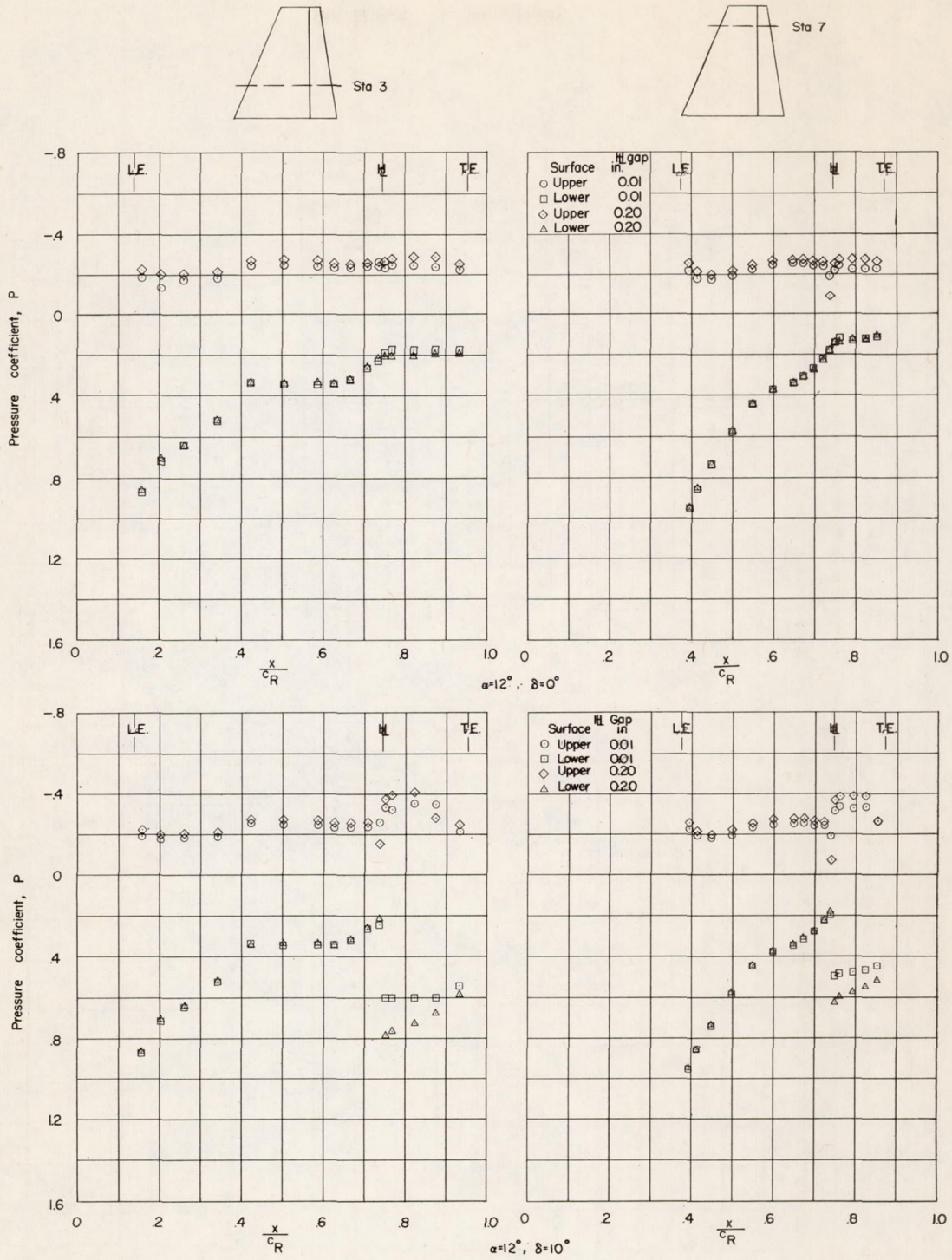

Figure 26.- Concluded.

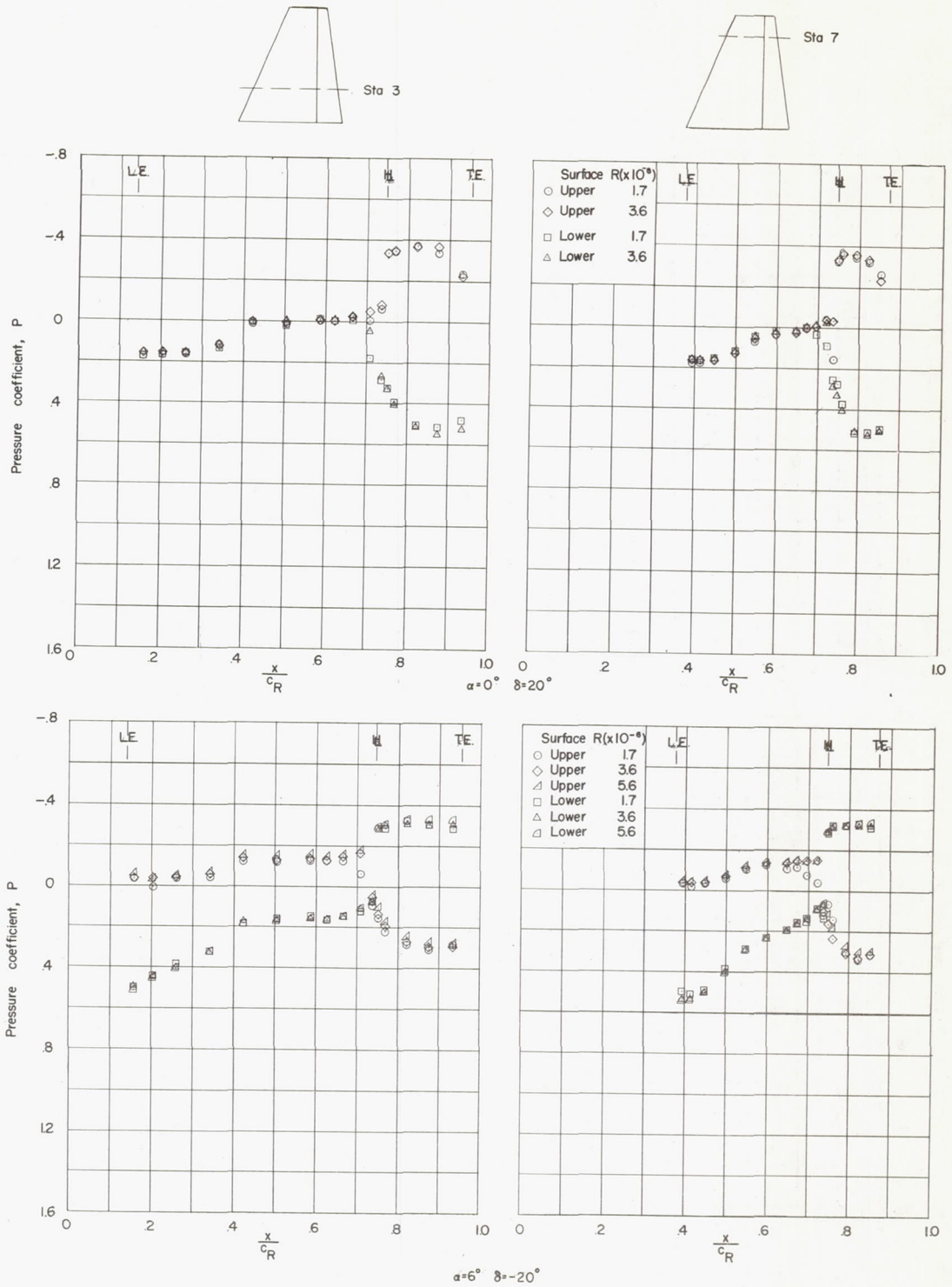

Figure 27.- Effect of Reynolds number on the chordwise pressure distributions at two spanwise stations. Configuration 4; M = 1.61.

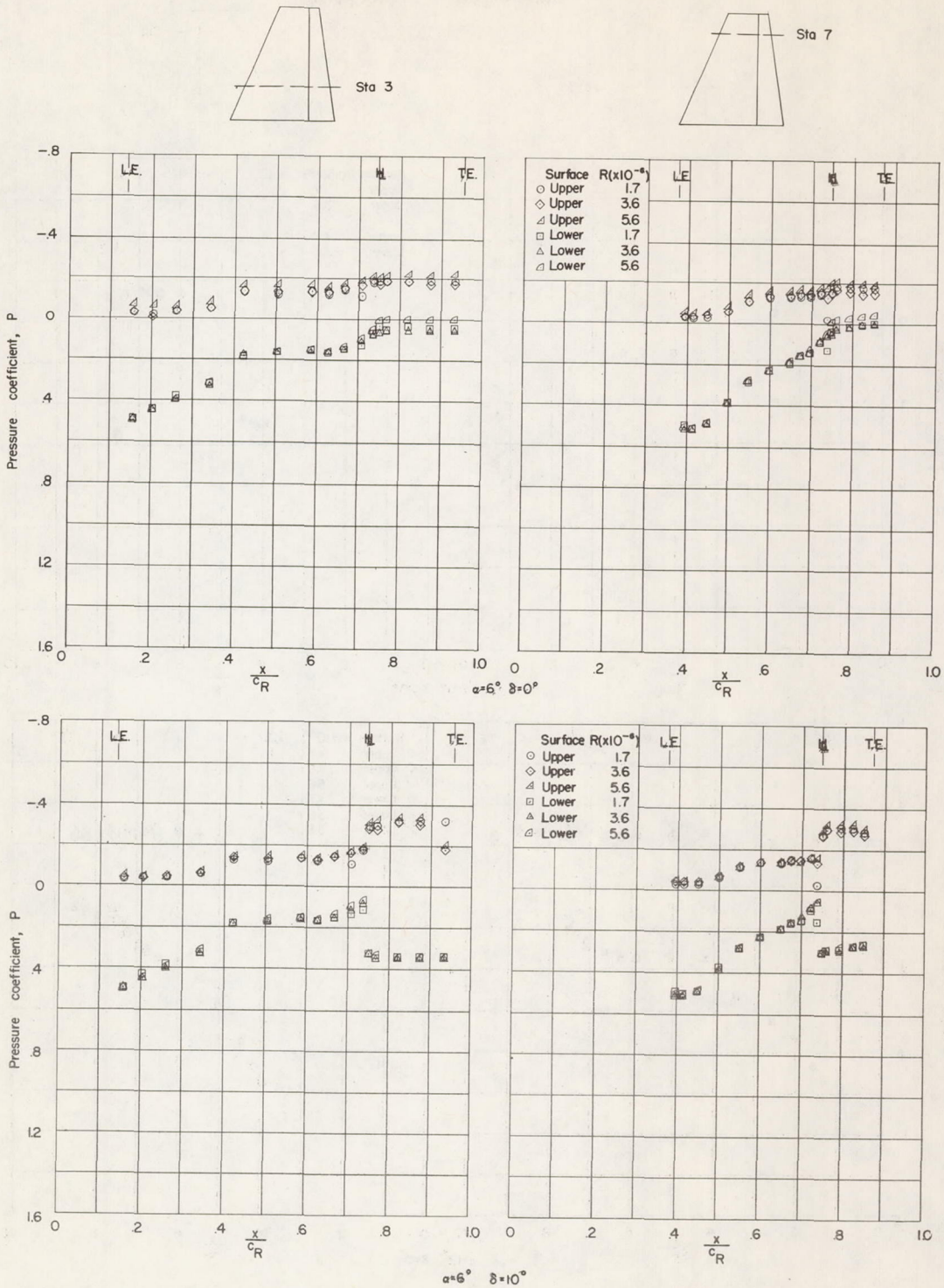

Figure 27.- Continued.

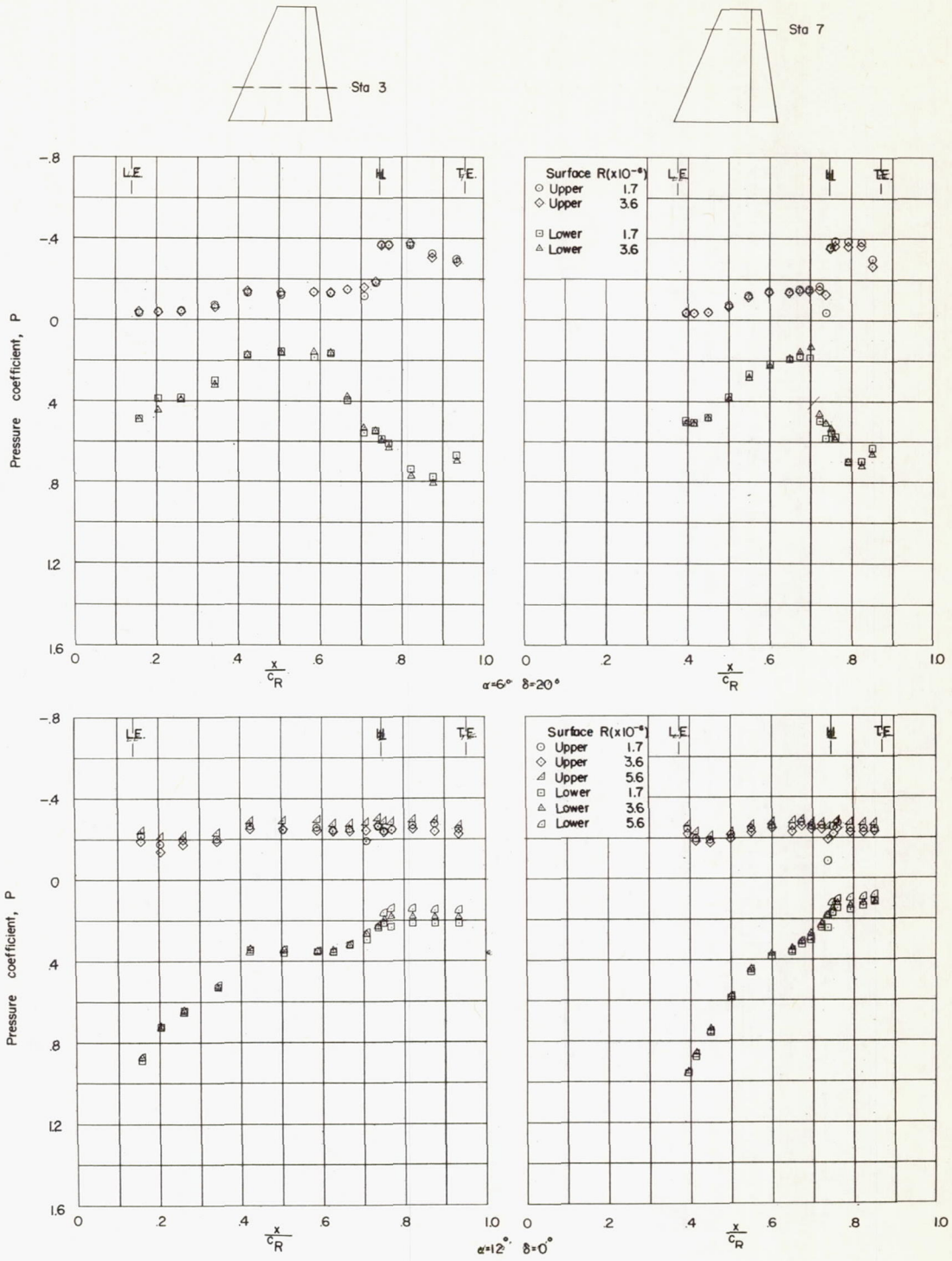

Figure 27.- Concluded.

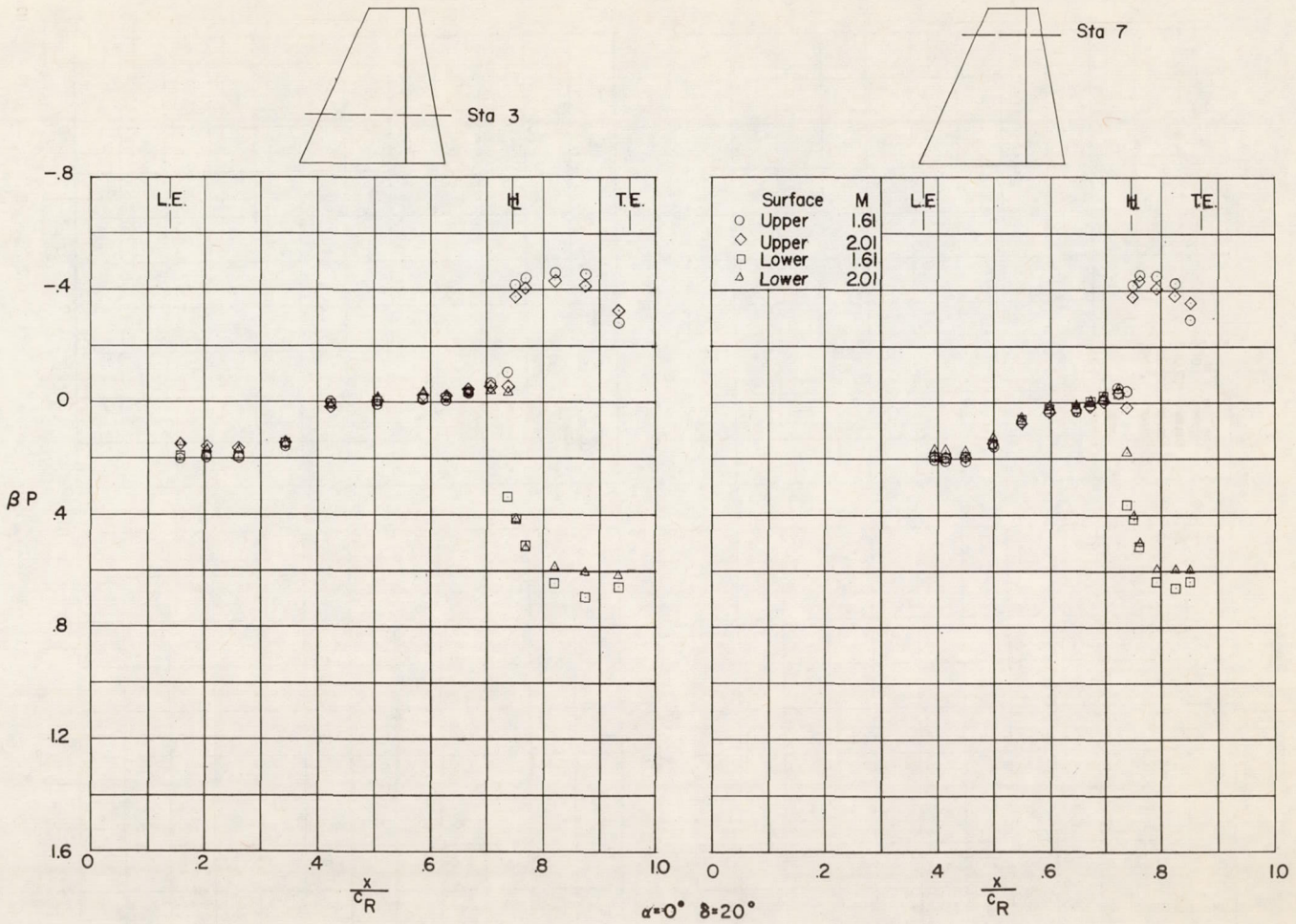

Figure 28.- Effect of Mach number on the chordwise pressure distributions at two spanwise stations. Configuration 4; R = 3.6×10^6.

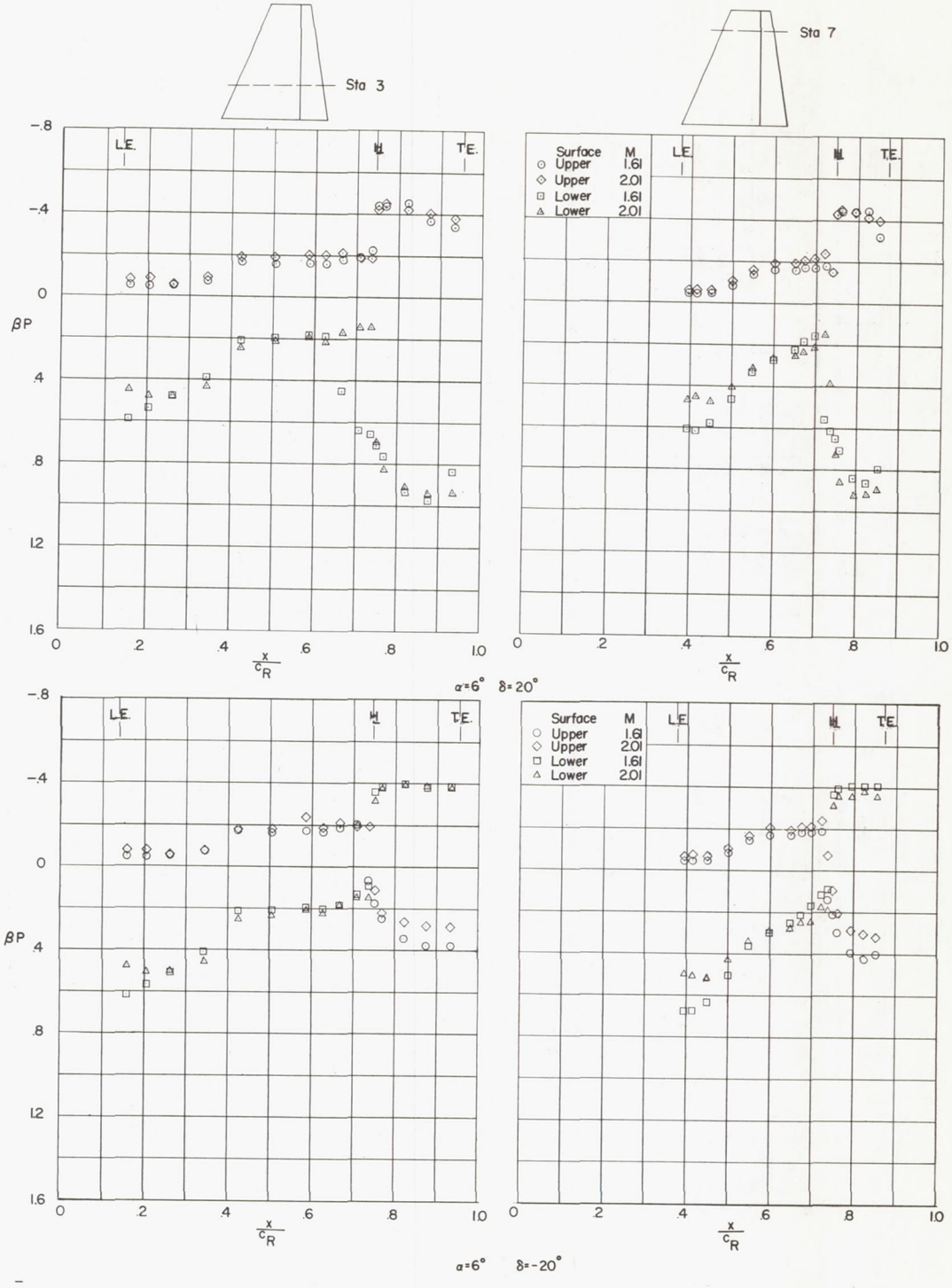

Figure 28.- Continued.

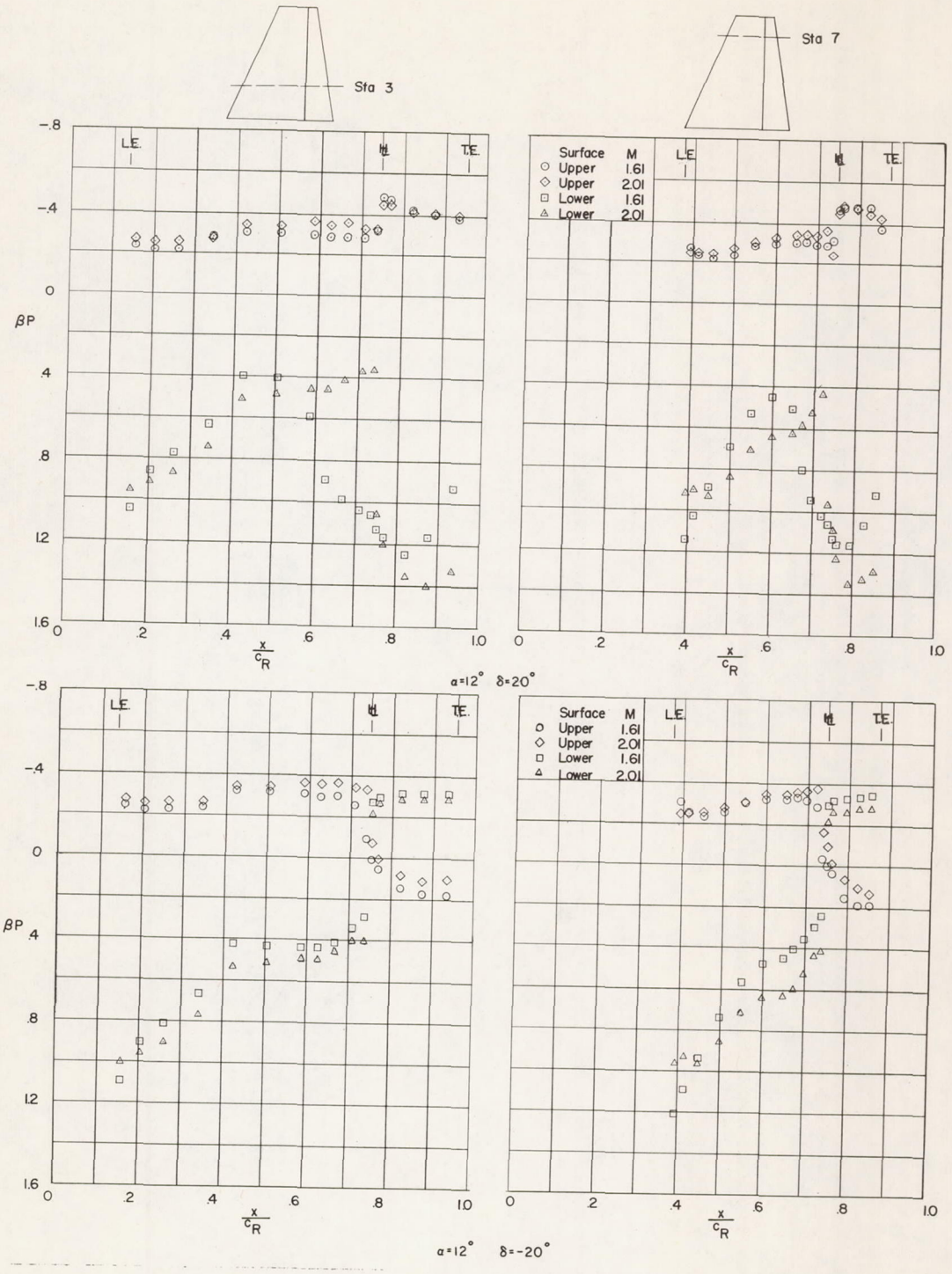

Figure 28.- Concluded.

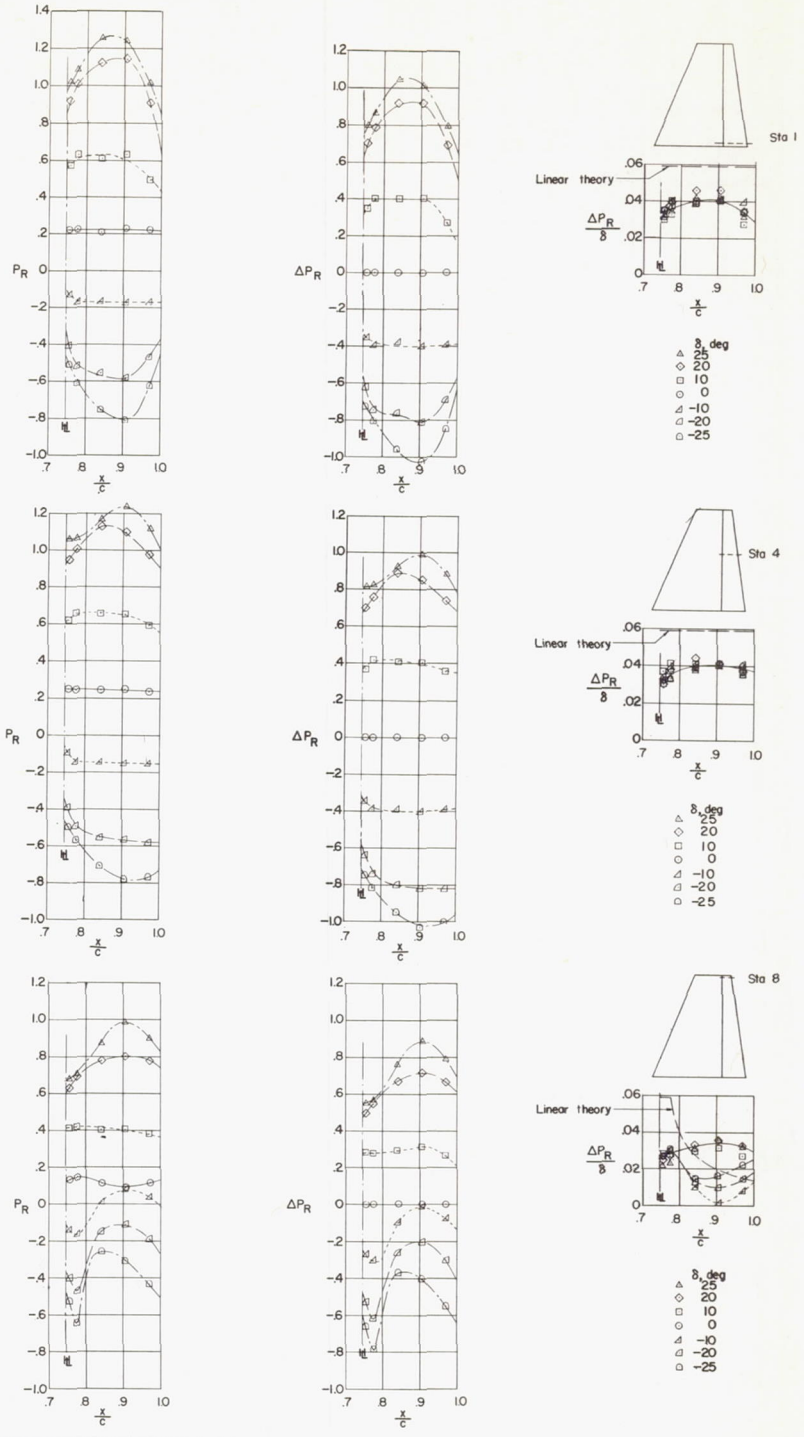

Figure 29.- Chordwise loadings due to control deflection for three spanwise stations. Configuration 4; M = 1.61; R = 3.6×10^6; $\alpha = 6^\circ$.

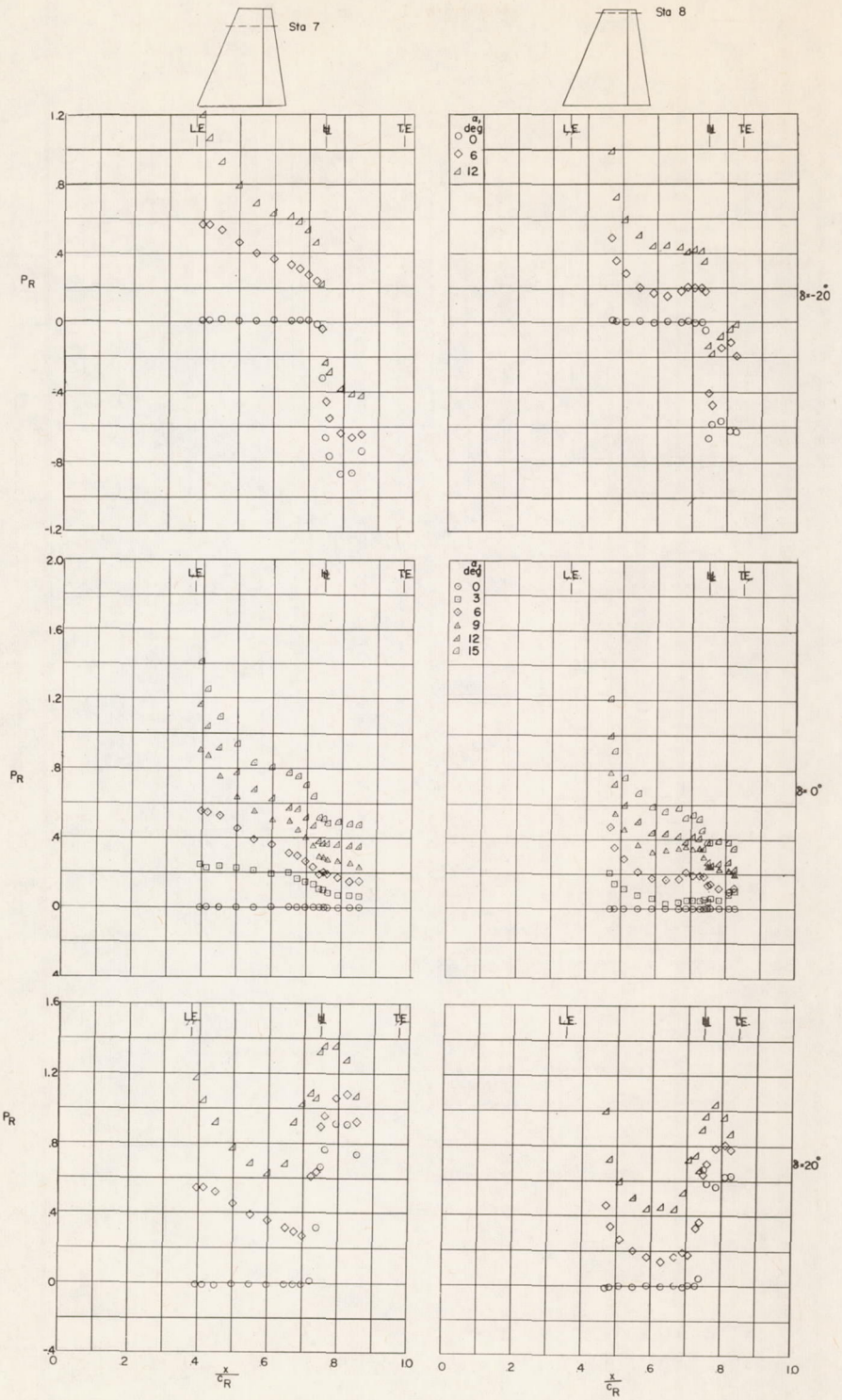

Figure 30.- Variation of the chordwise loadings near the wing tip with angle of attack. Configuration 4; M = 1.61; R = 3.6×10^6.

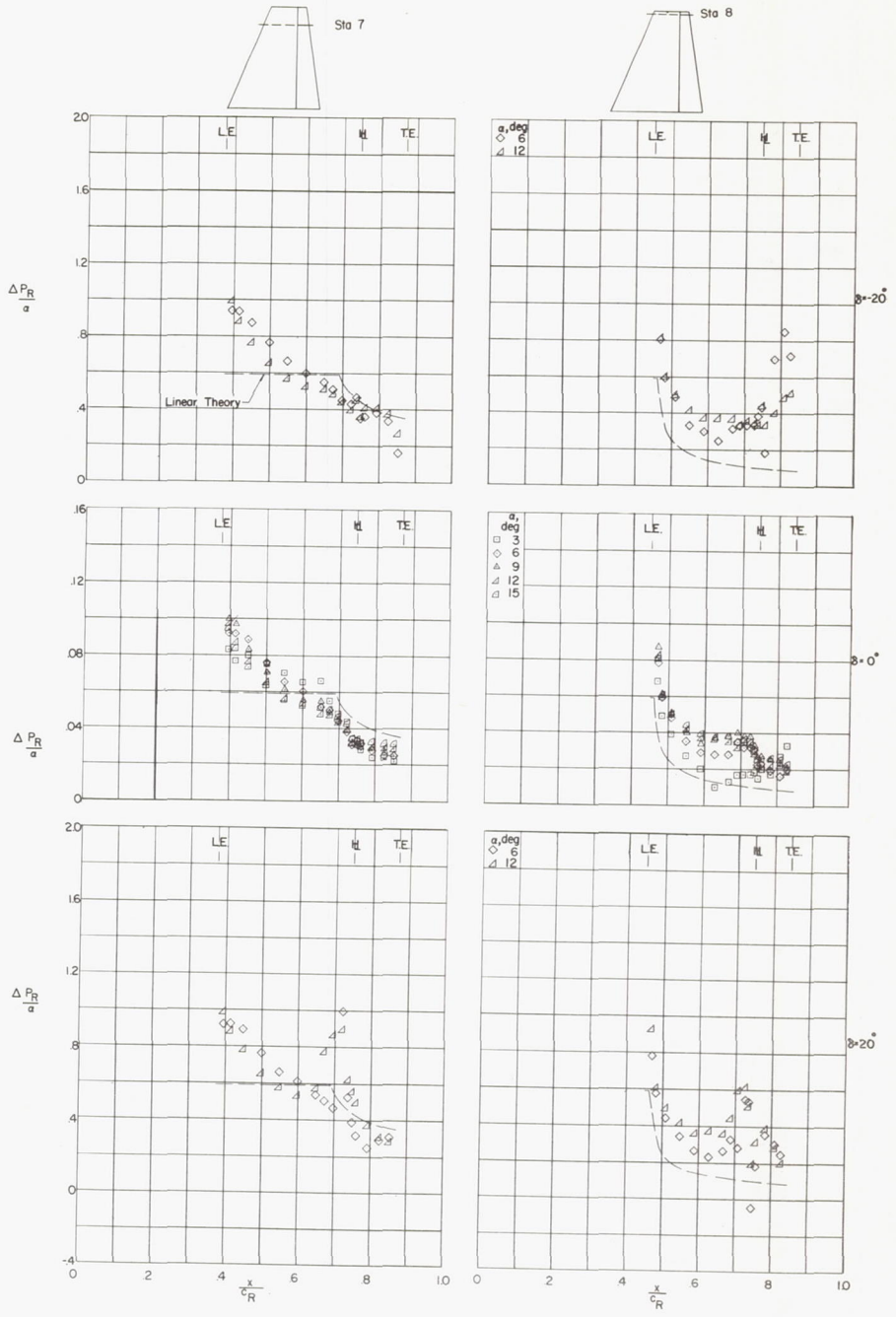

Figure 31.- Variation of the chordwise loadings due to angle of attack near the wing tip with angle of attack. Configuration 4; M = 1.61; R = 3.6×10^6.

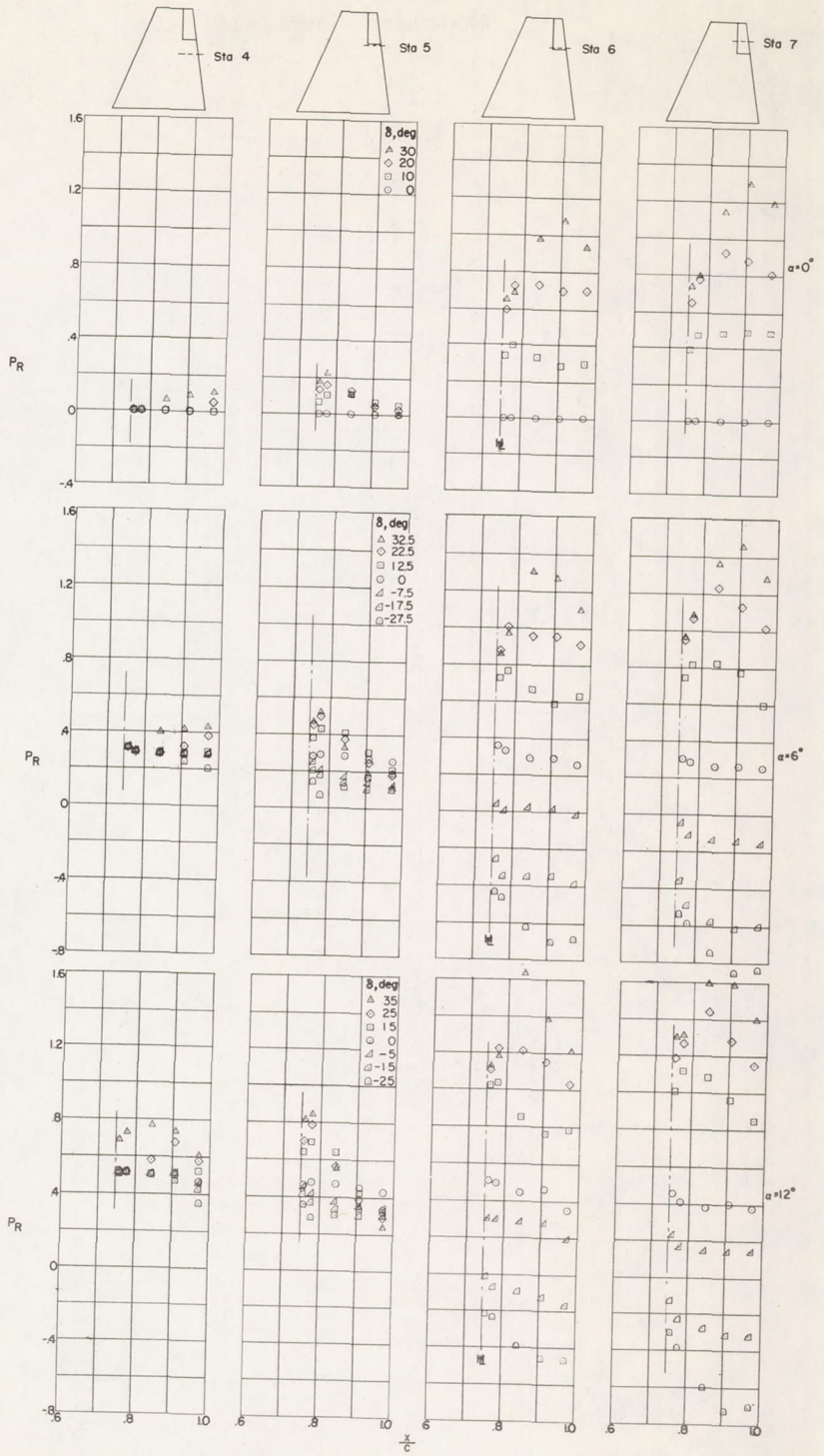

Figure 32.- Effect of control deflection on the chordwise loadings in the vicinity of the wing-control parting line. Configuration 1; M = 1.61; R = 3.6×10^6.

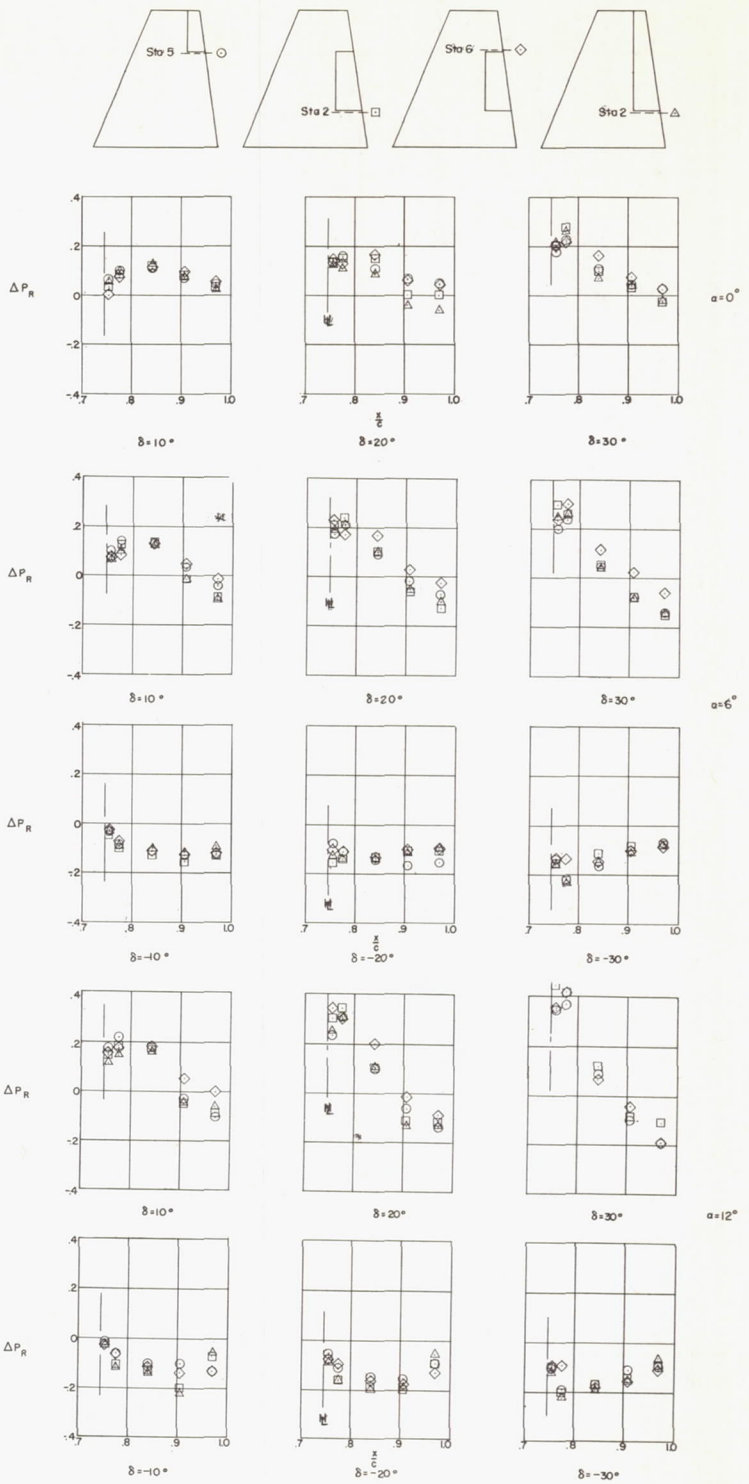

Figure 33.- Effect of control deflection and angle of attack on the incremental chordwise-loading carryovers adjacent to the wing-control parting lines due to control deflection. $M = 1.61$; $R = 3.6 \times 10^6$.

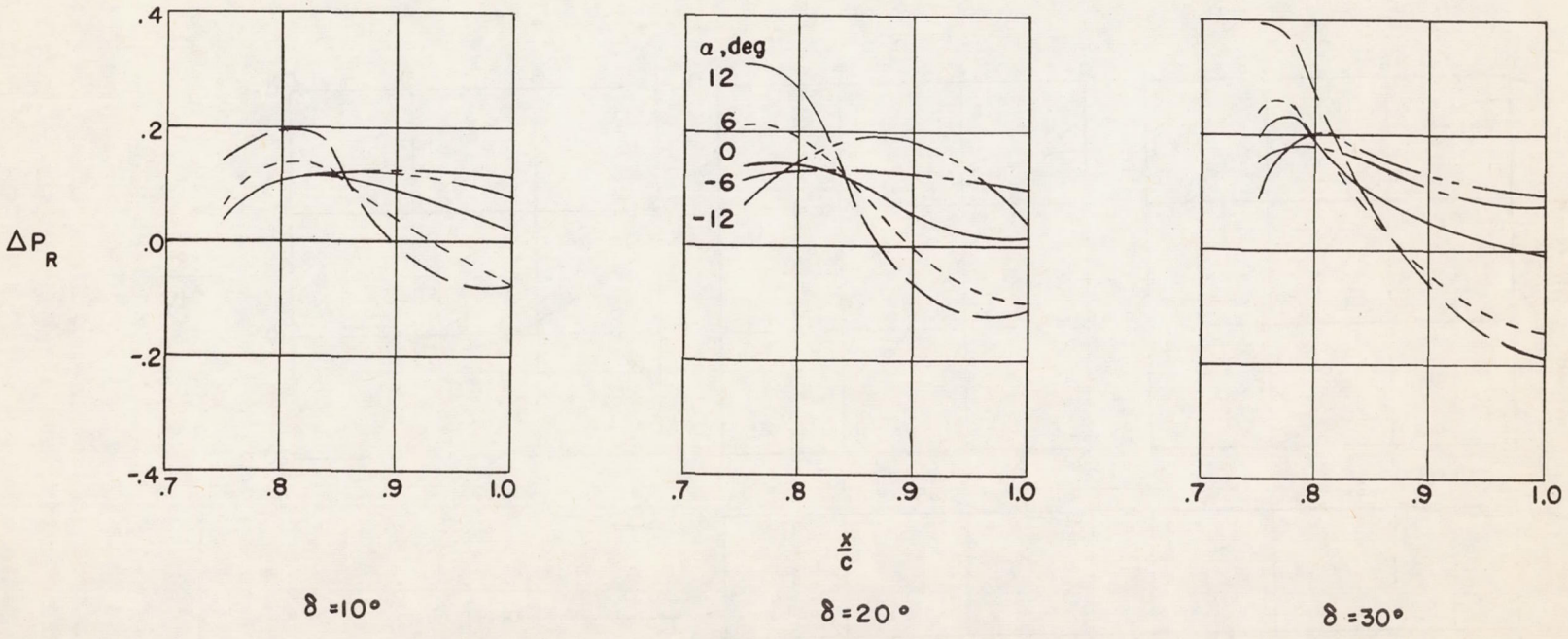

Figure 34.- Variation of average incremental chordwise-loading carryovers due to control deflection with angle of attack. Configurations 1, 2, and 3; M = 1.61; R = 3.6×10^6.

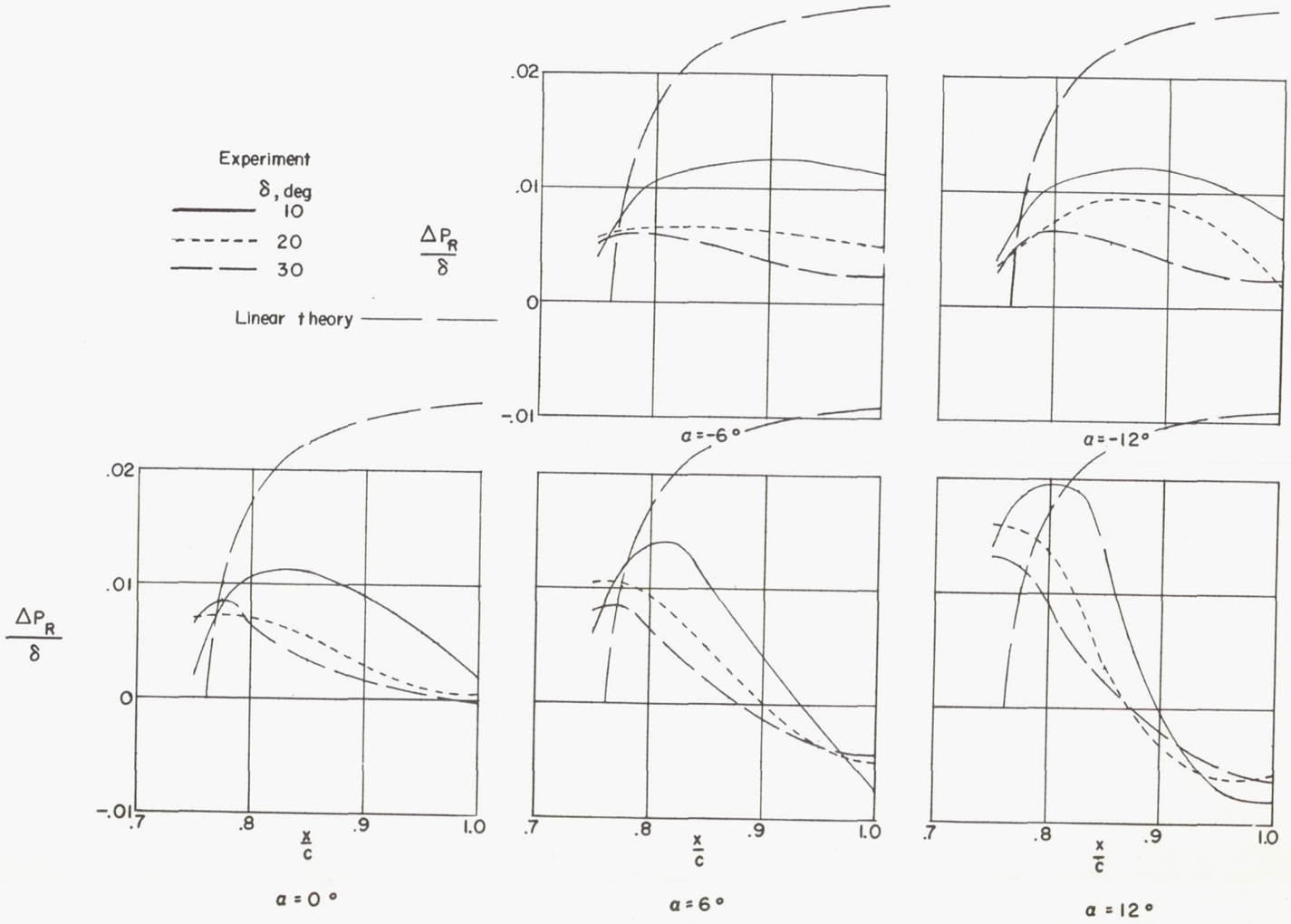

Figure 35.- Variation of normalized incremental loading carryovers with control deflection. Configurations 1, 2, and 3; M = 1.61; R = 3.6×10^6.

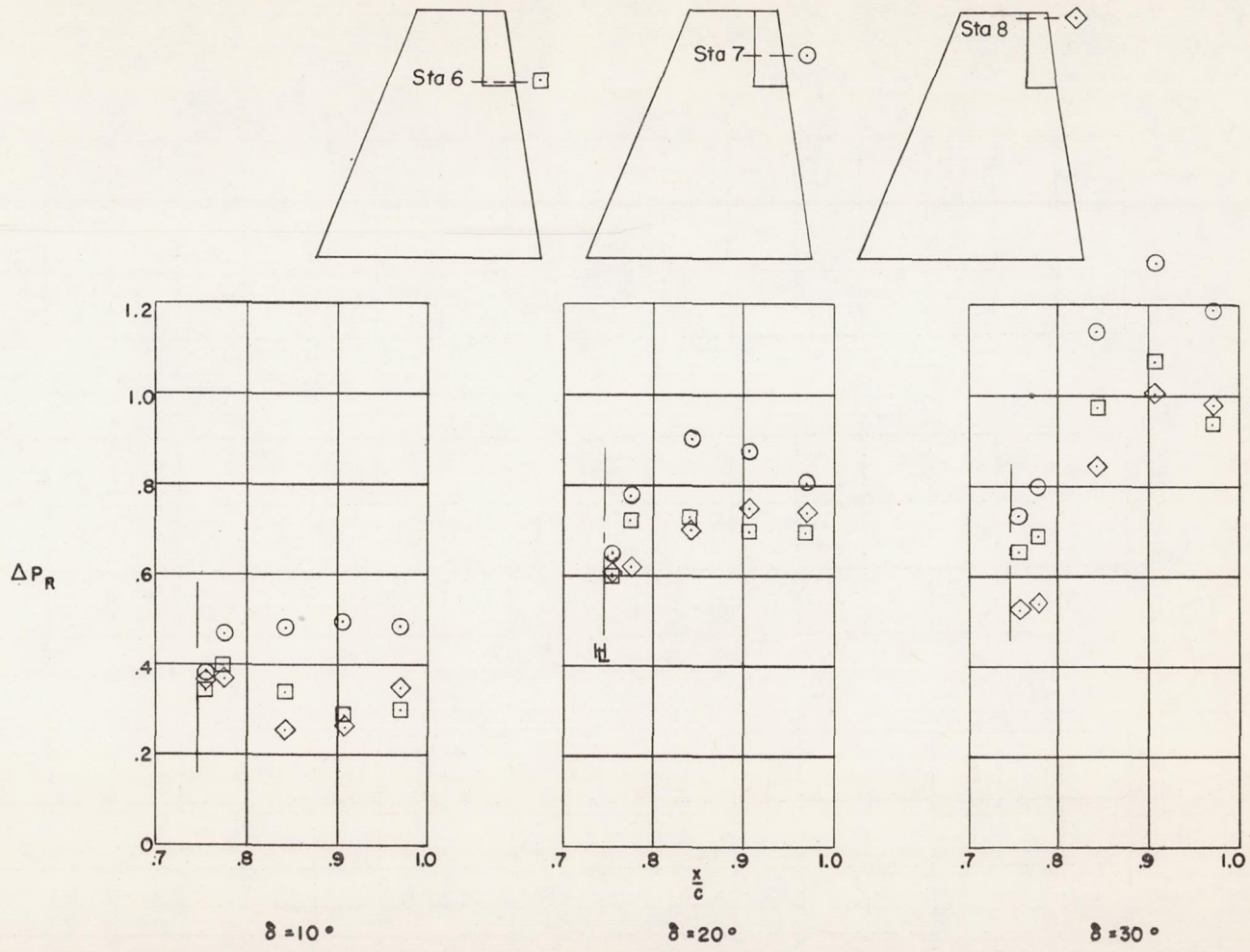

(a) $\alpha = 0^{\circ}$.

Figure 36.- Incremental chordwise loadings across span of control.
Configuration 1; M = 1.61; R = 3.6×10^6.

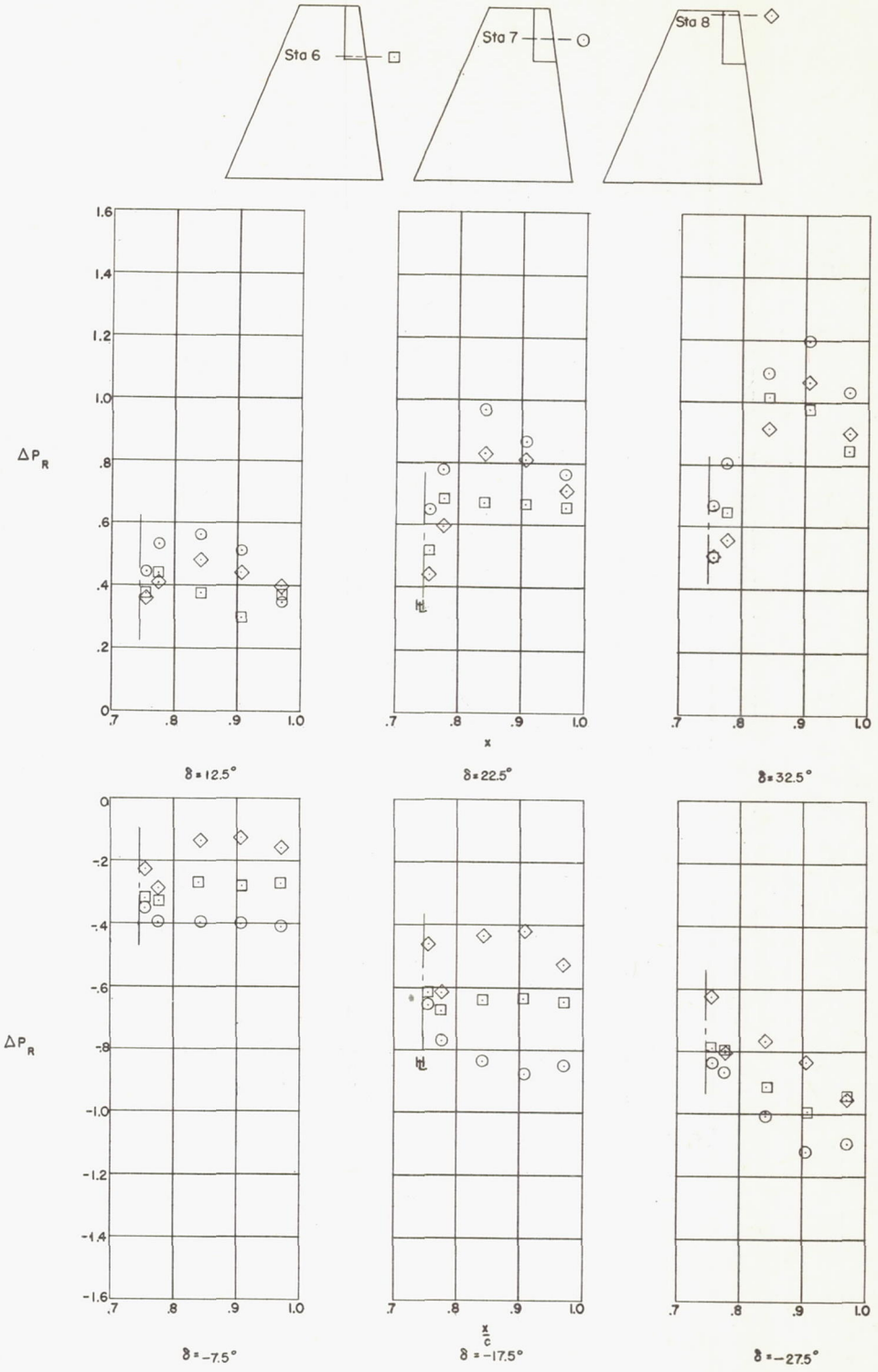

(b) $\alpha = 6°$.

Figure 36.- Continued.

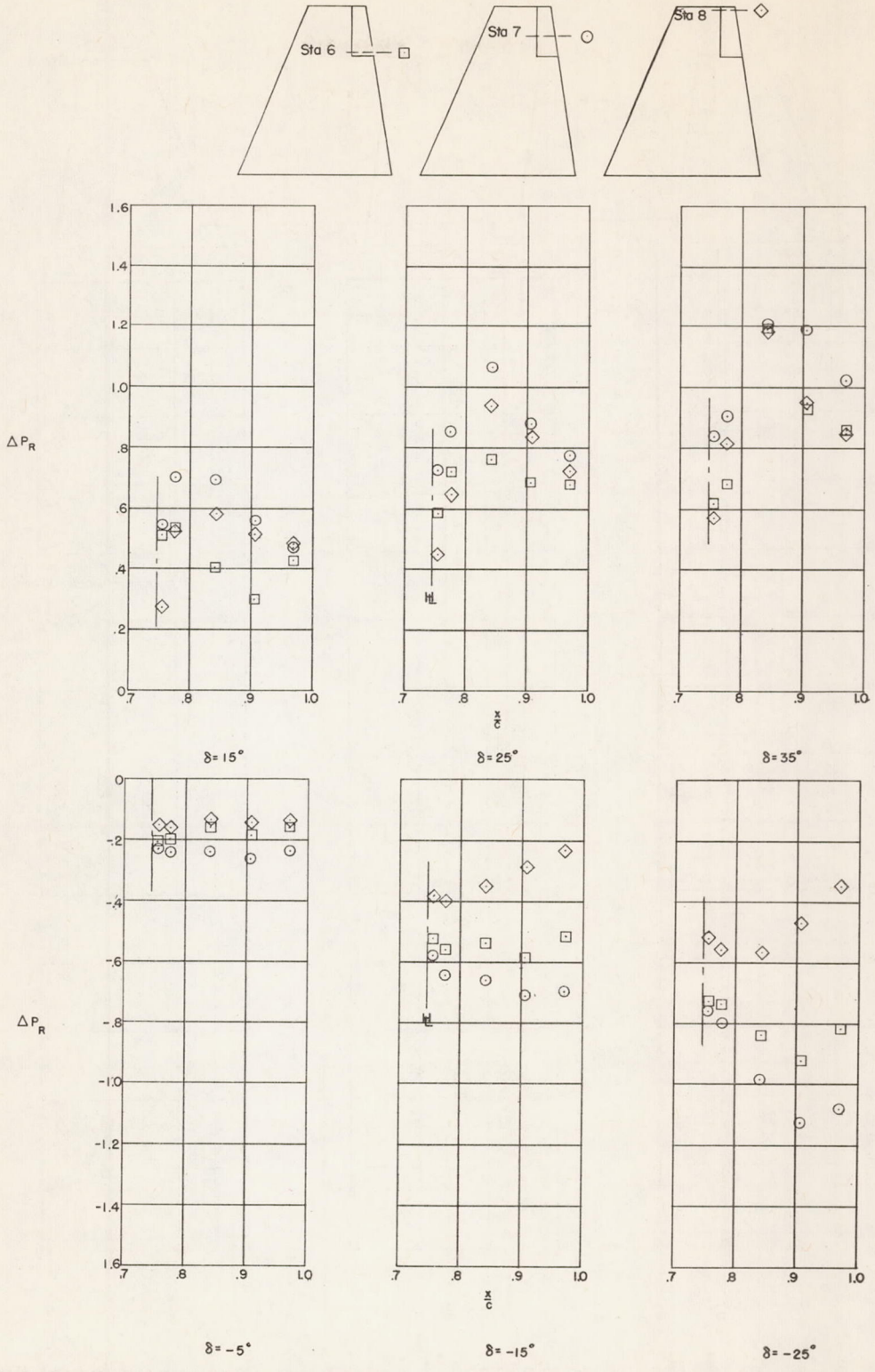

(c) $\alpha = 12^{\circ}$.

Figure 36.- Concluded.

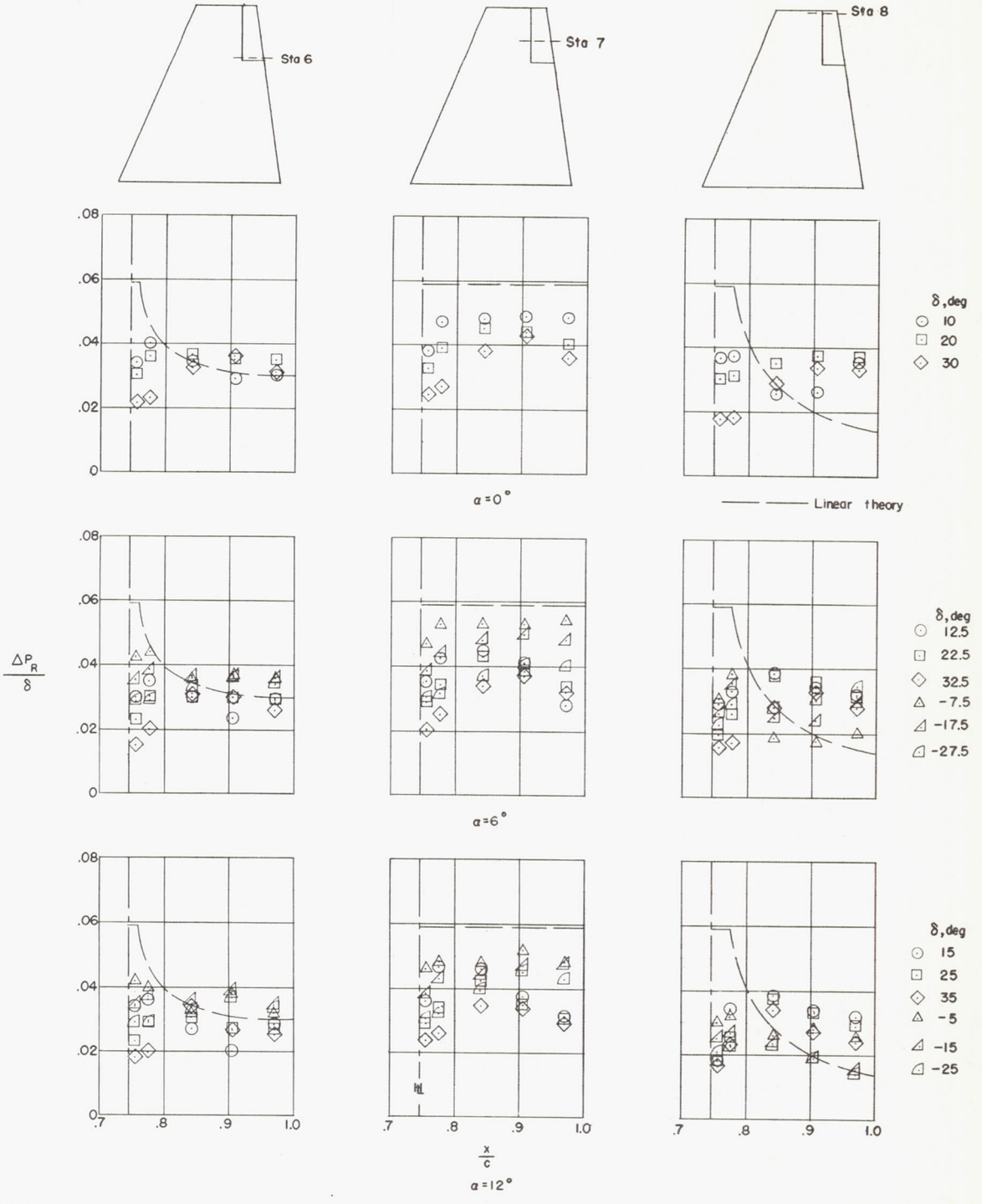

Figure 37.- Variation of normalized incremental loadings across span of control. Configuration 1; M = 1.61; R = 3.6×10^6.

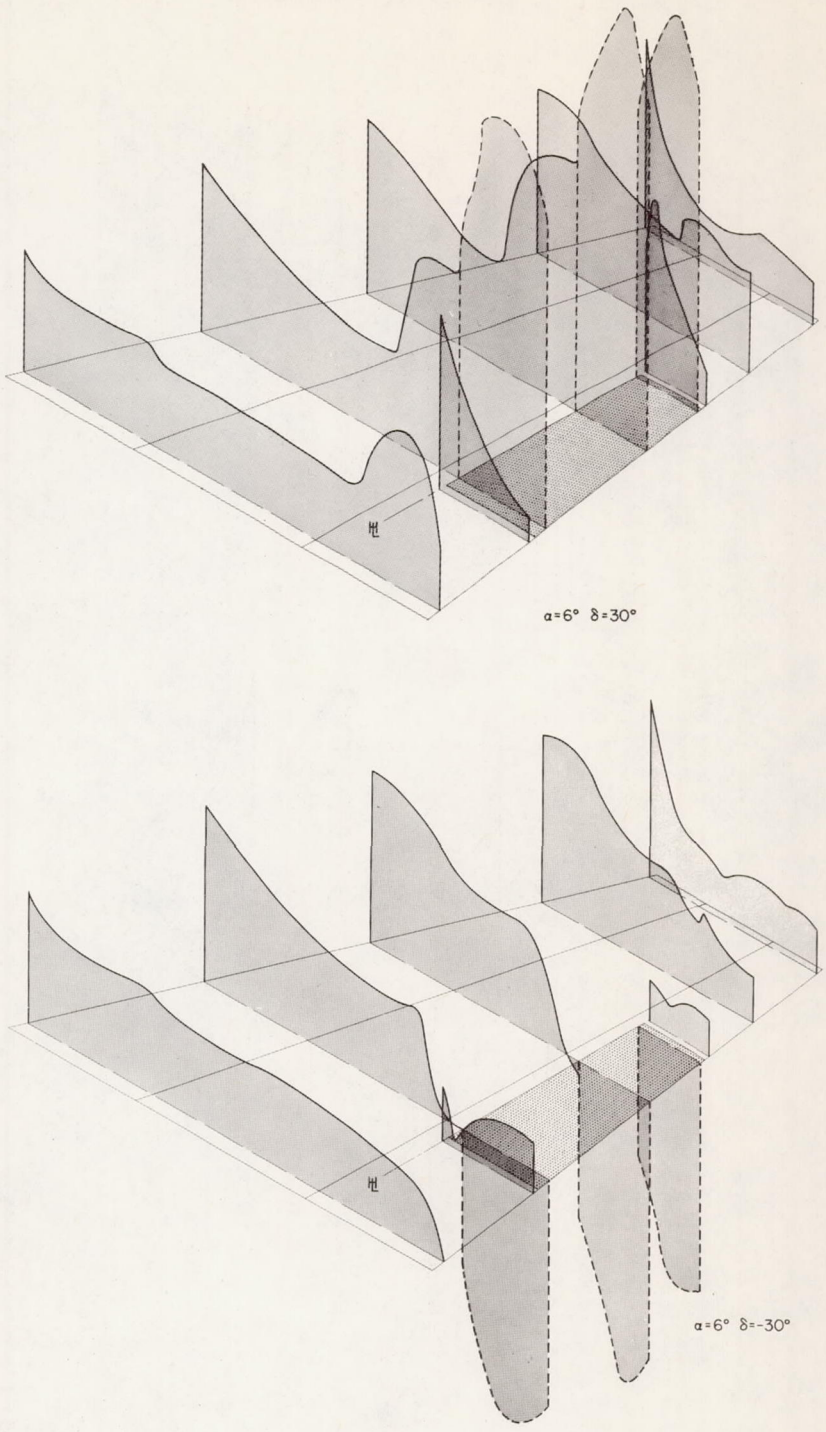

(a) Configuration 2.

L-90510

Figure 38.- Illustrative diagrams showing the spanwise variation of the chordwise loadings on two typical configurations. M = 1.61; R = 3.6×10^6.

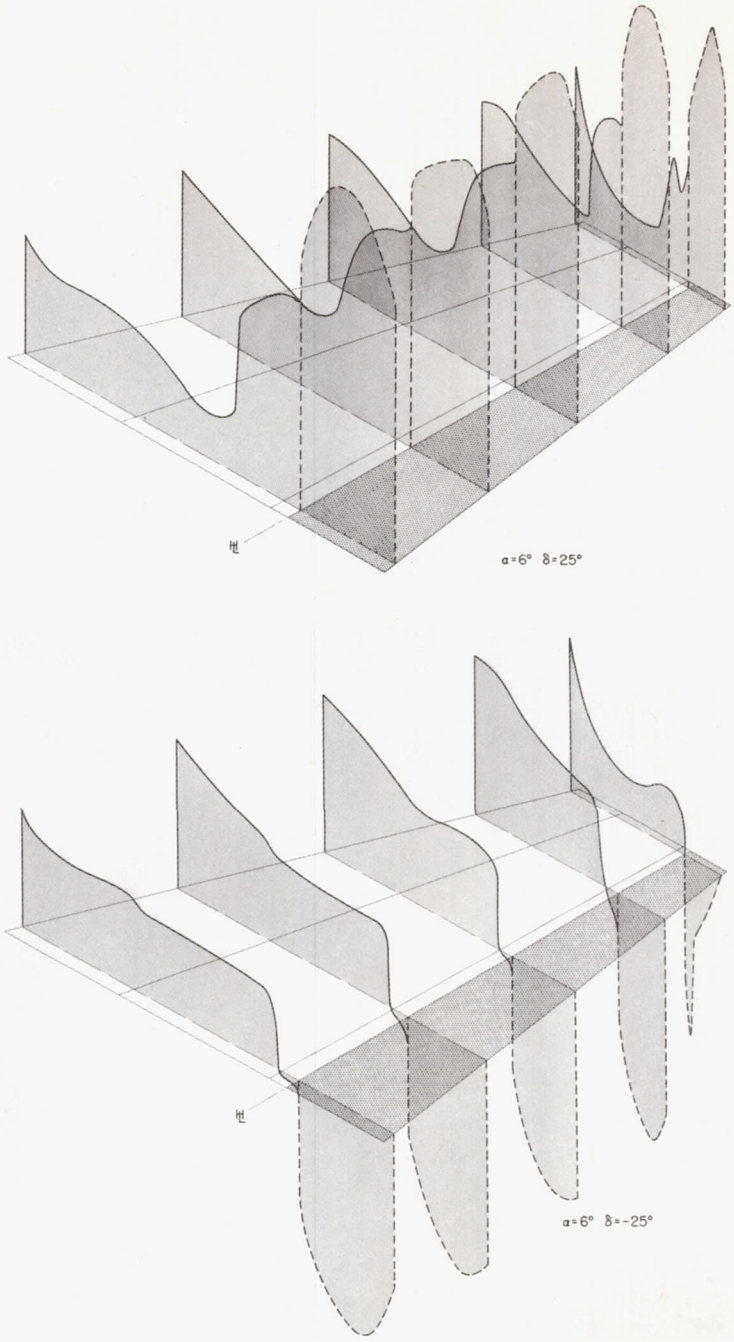

L-90511

(b) Configuration 4.

Figure 38.- Concluded.

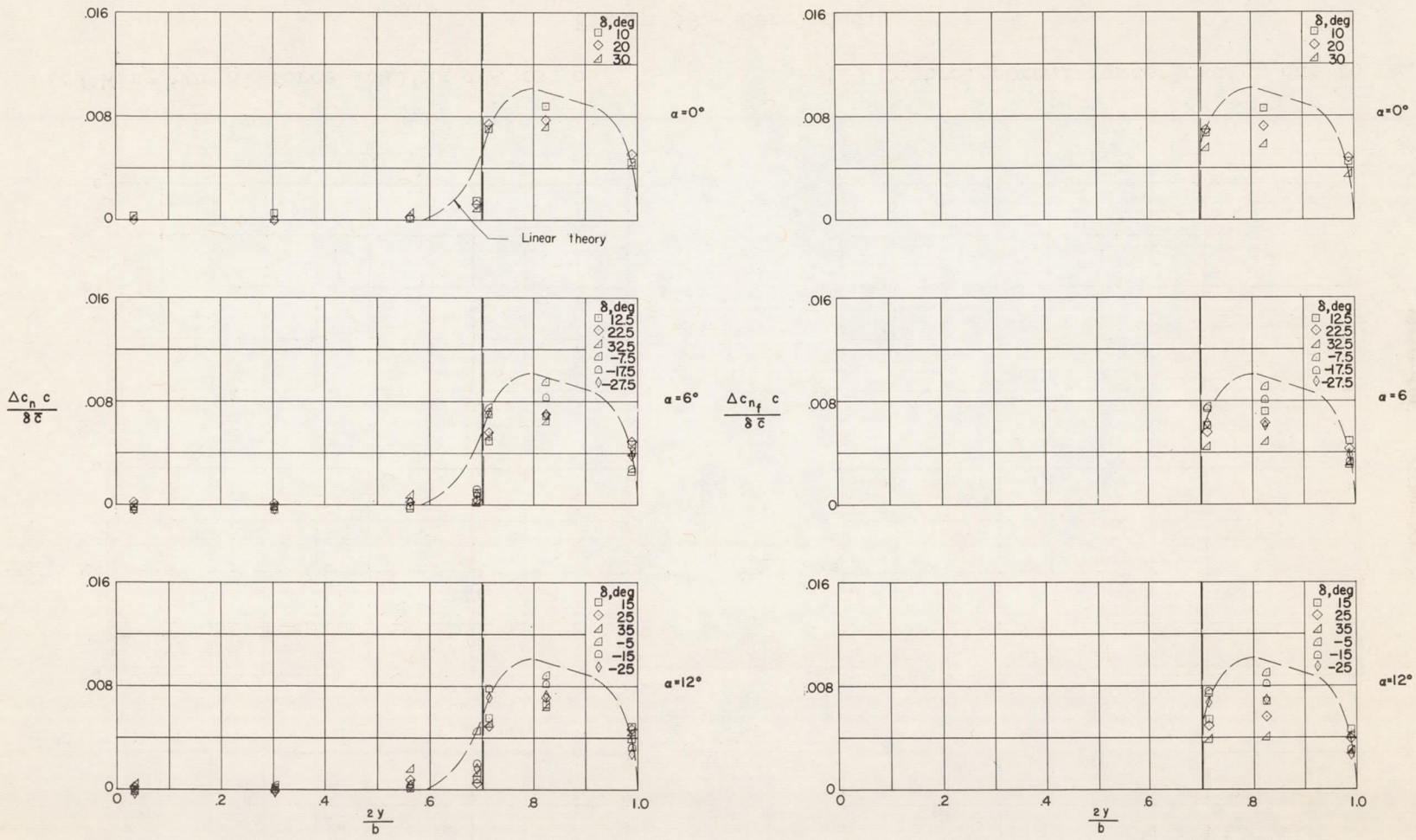

(a) Wing normal-force loading due to δ.

(b) Control normal-force loading due to δ.

Figure 39.- Spanwise normal-force loading distributions for configuration 1. M = 1.61; R = 3.6×10^6.

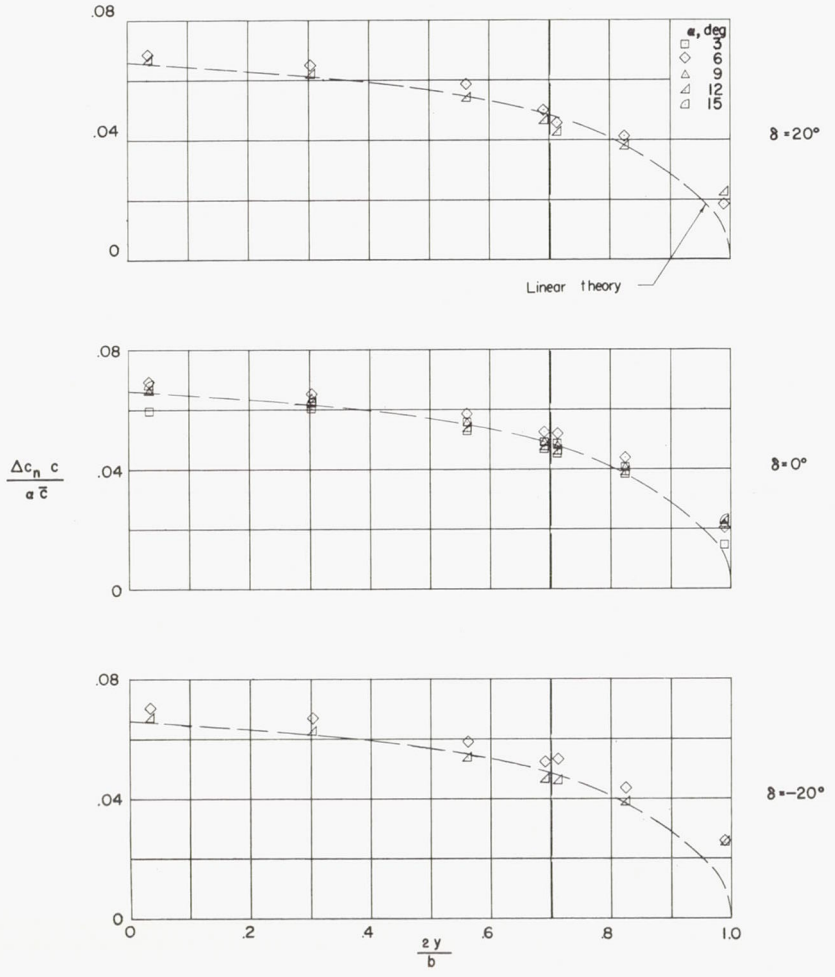

(c) Wing normal-force loading due to α.

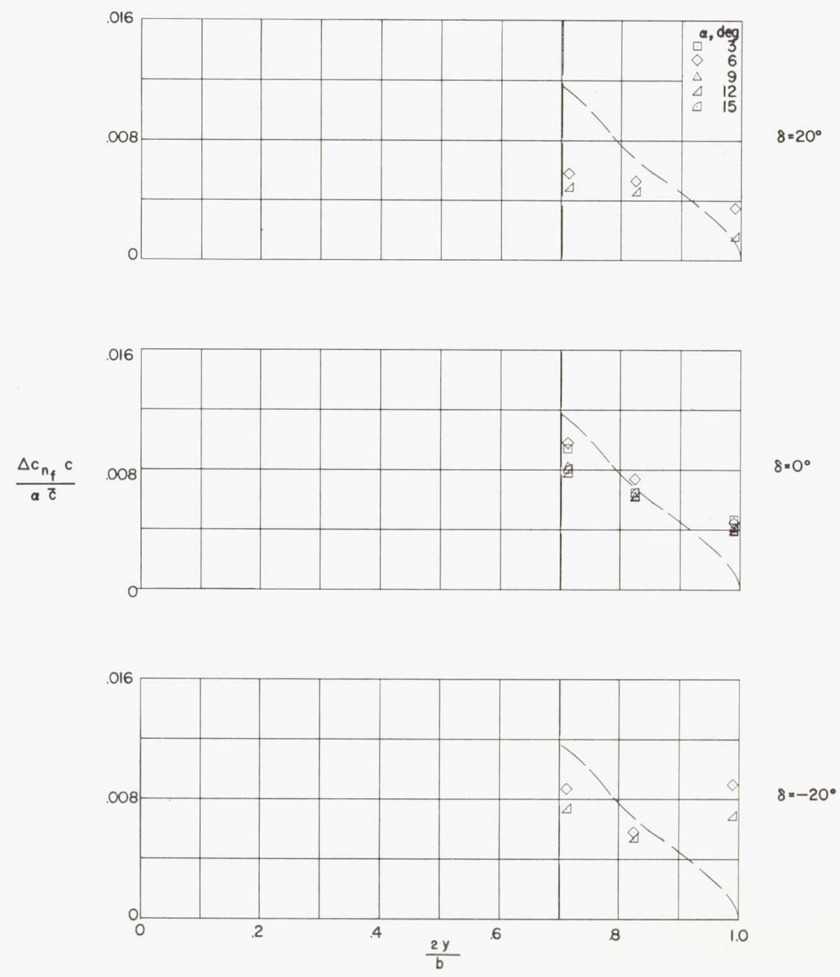

(d) Control normal-force loading due to α.

Figure 39.- Concluded.

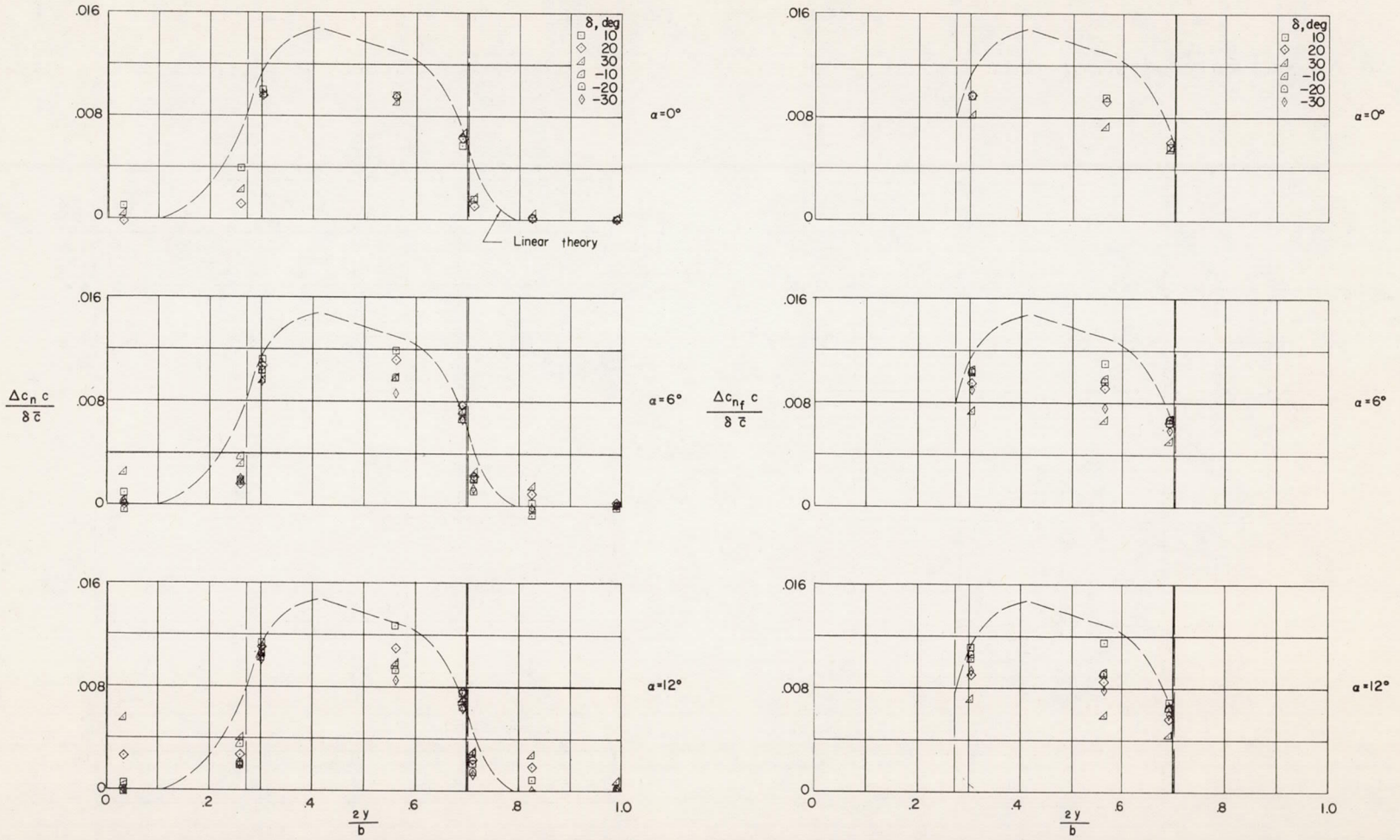

(a) Wing normal-force loading due to δ.

(b) Control normal-force loading due to δ.

Figure 40.- Spanwise normal-force loading distributions for configuration 2. M = 1.61; R = 3.6×10^6.

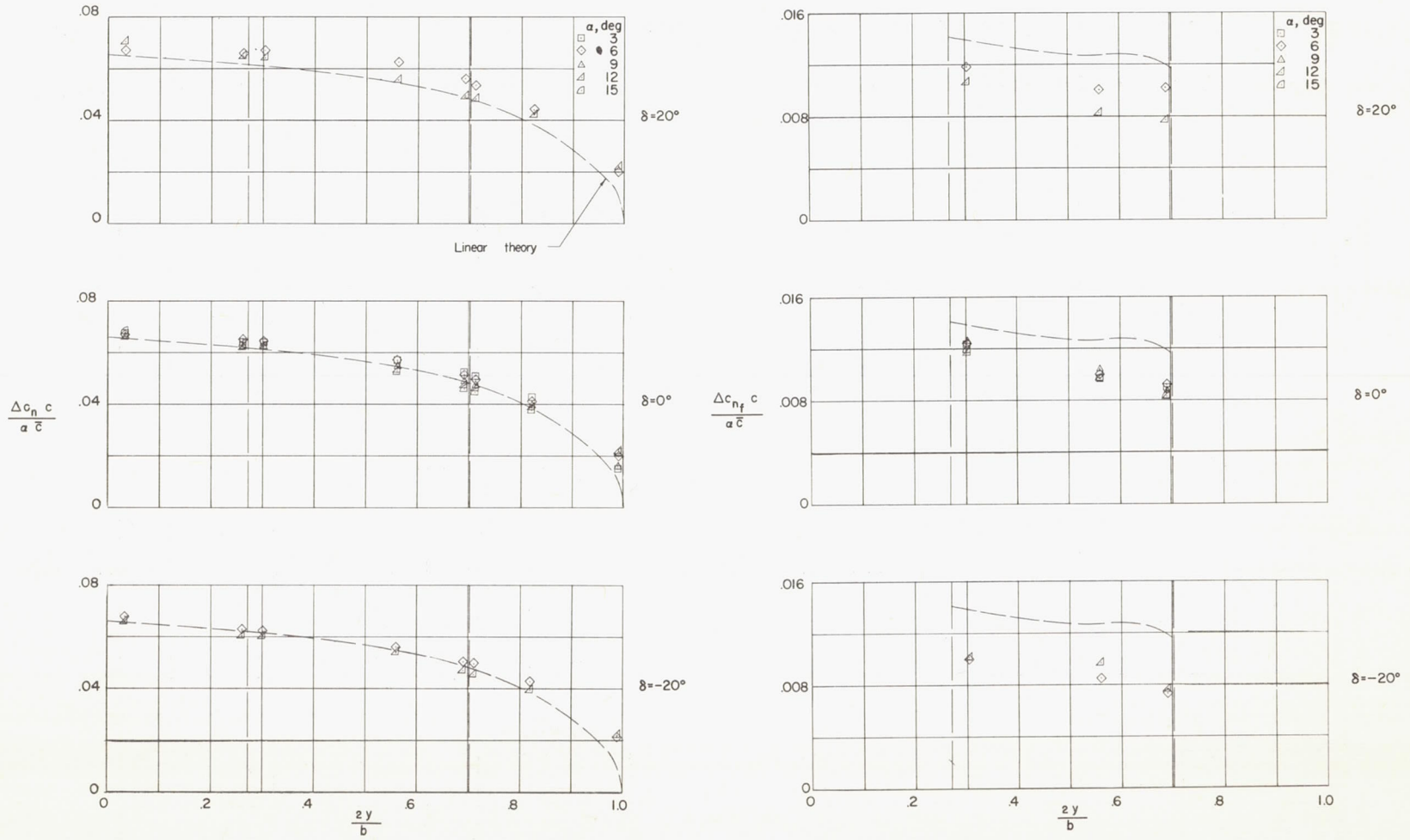

(c) Wing normal-force loading due to α.

(d) Control normal-force loading due to α.

Figure 40.- Concluded.

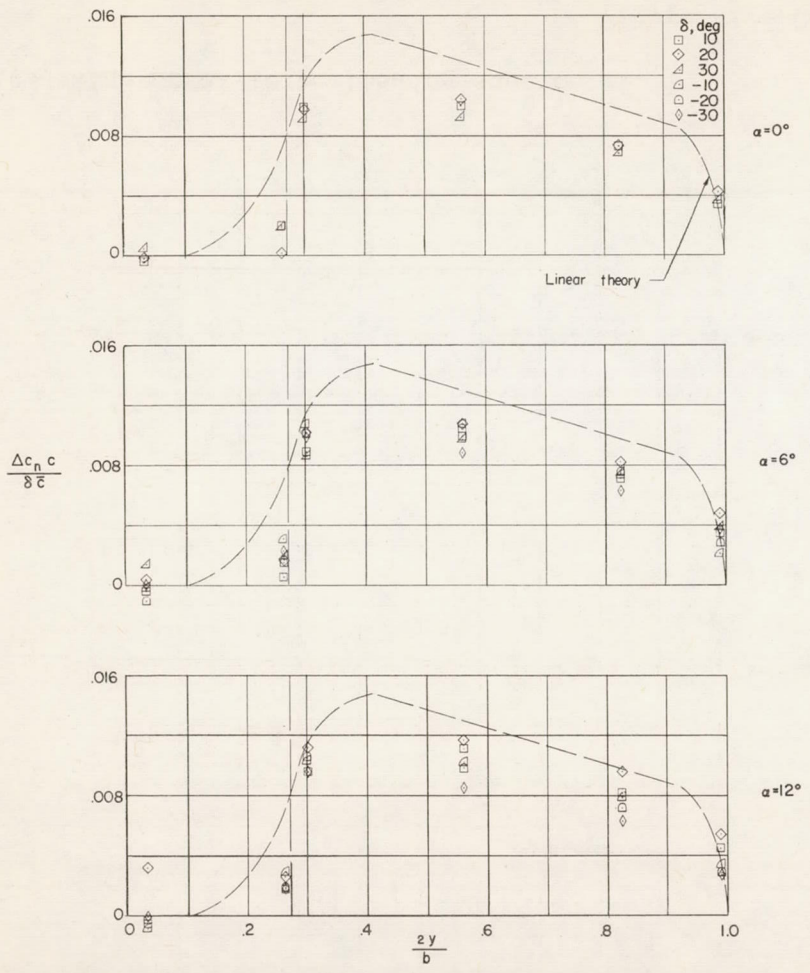

(a) Wing normal-force loading due to δ.

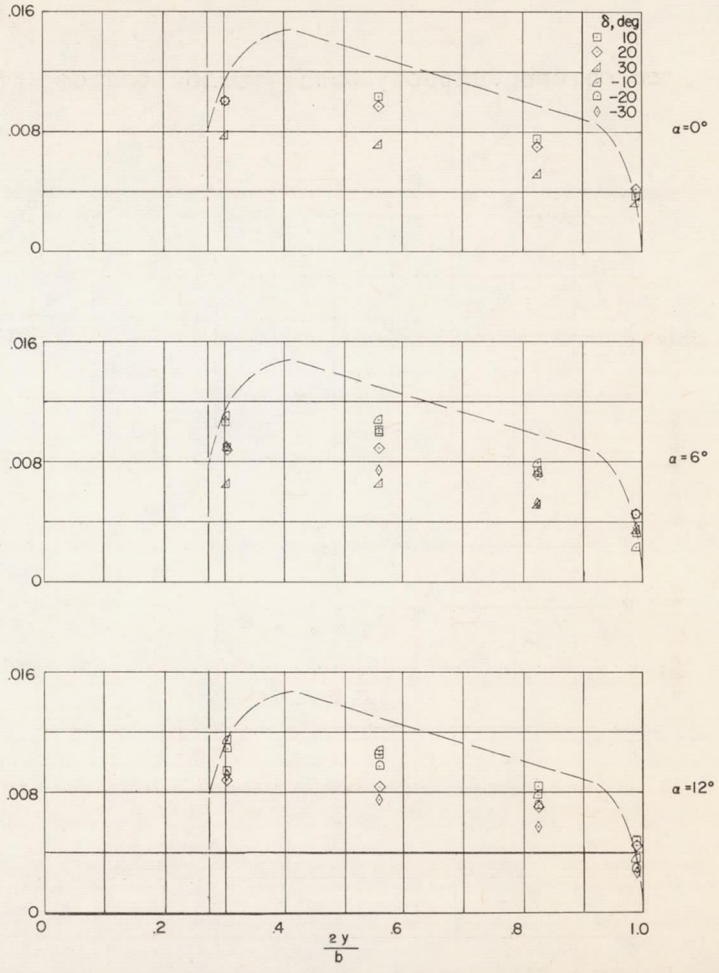

(b) Control normal-force loading due to δ.

Figure 41.- Spanwise normal-force loading distributions for configuration 3. M = 1.61; R = 3.6×10^6.

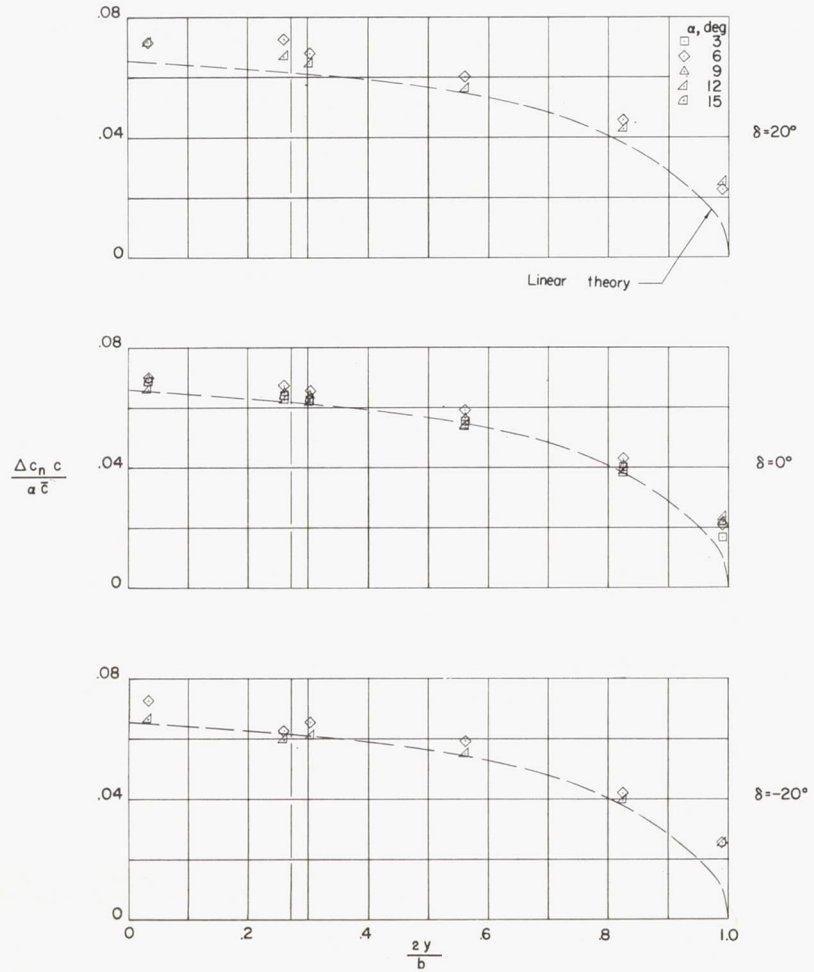

(c) Wing normal-force loading due to α.

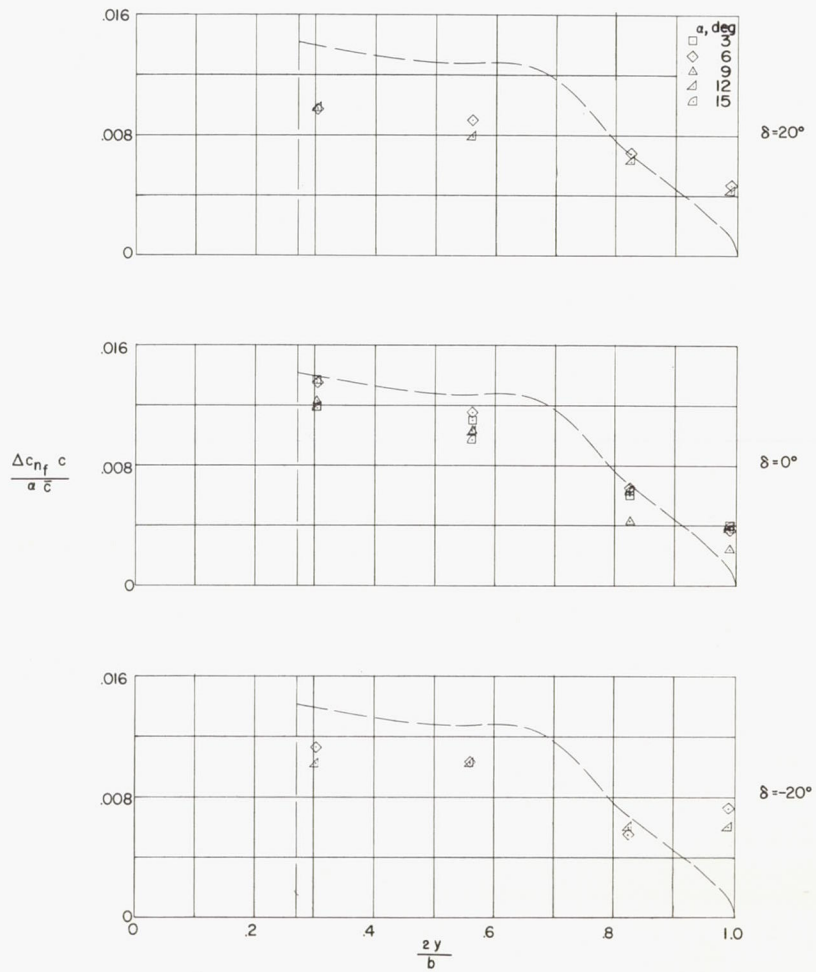

(d) Control normal-force loading due to α.

Figure 41.- Concluded.

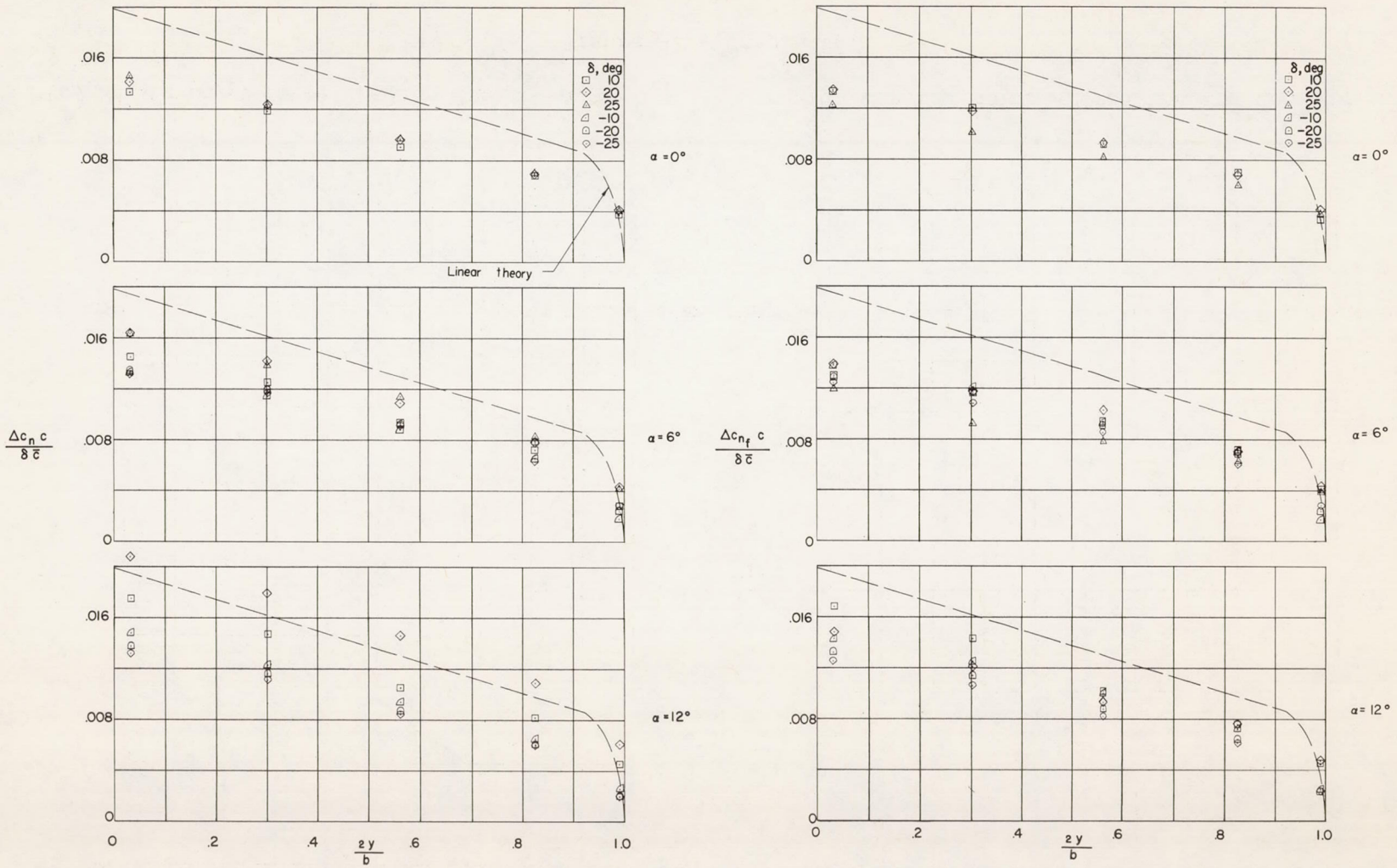

(a) Wing normal-force loading due to δ.

(b) Control normal-force loading due to δ.

Figure 42.- Spanwise normal-force loading distributions for configuration 4. M = 1.61; R = 3.6×10^6.

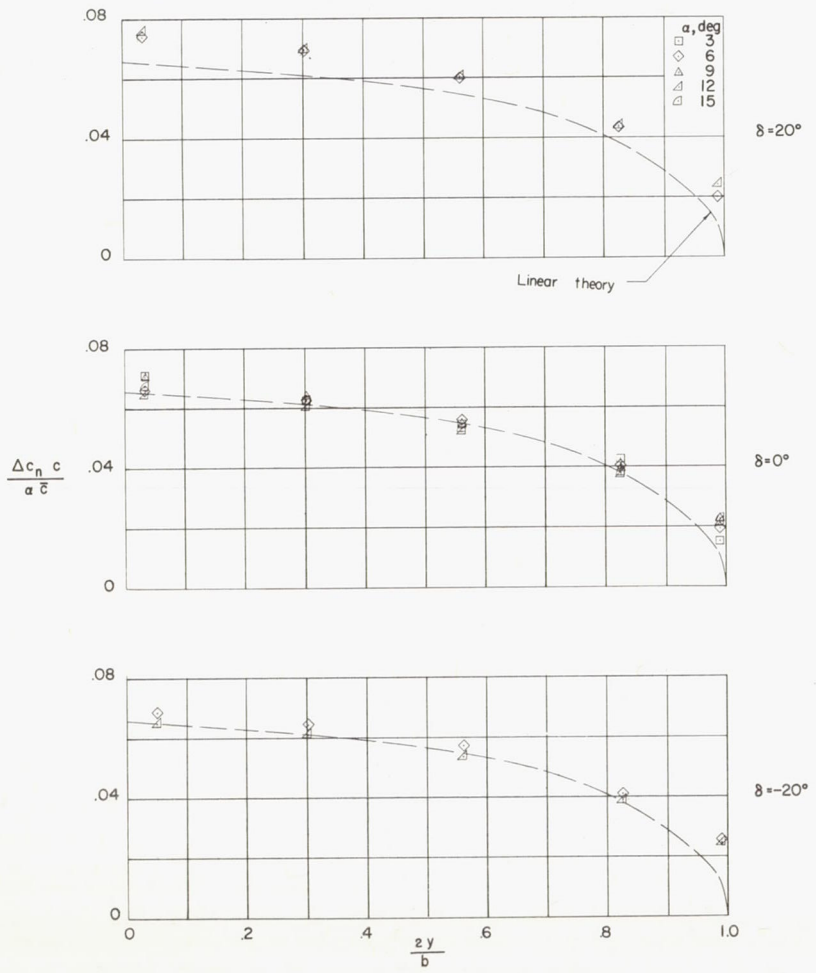

(c) Wing normal-force loading due to α.

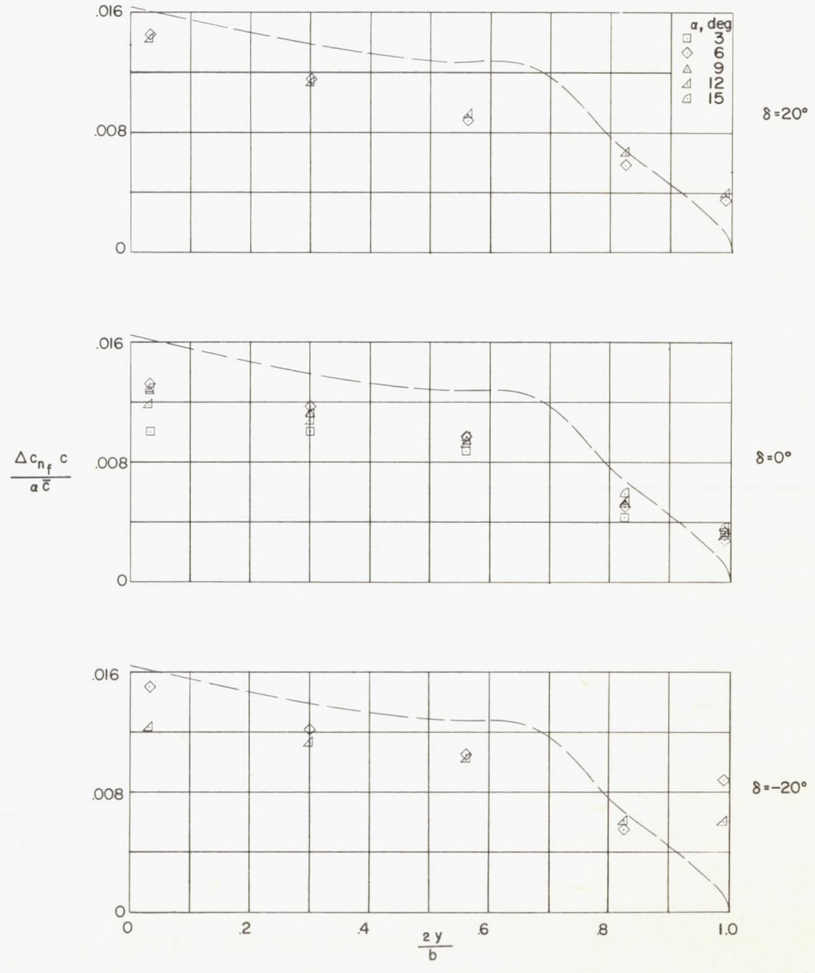

(d) Control normal-force loading due to α.

Figure 42.- Concluded.

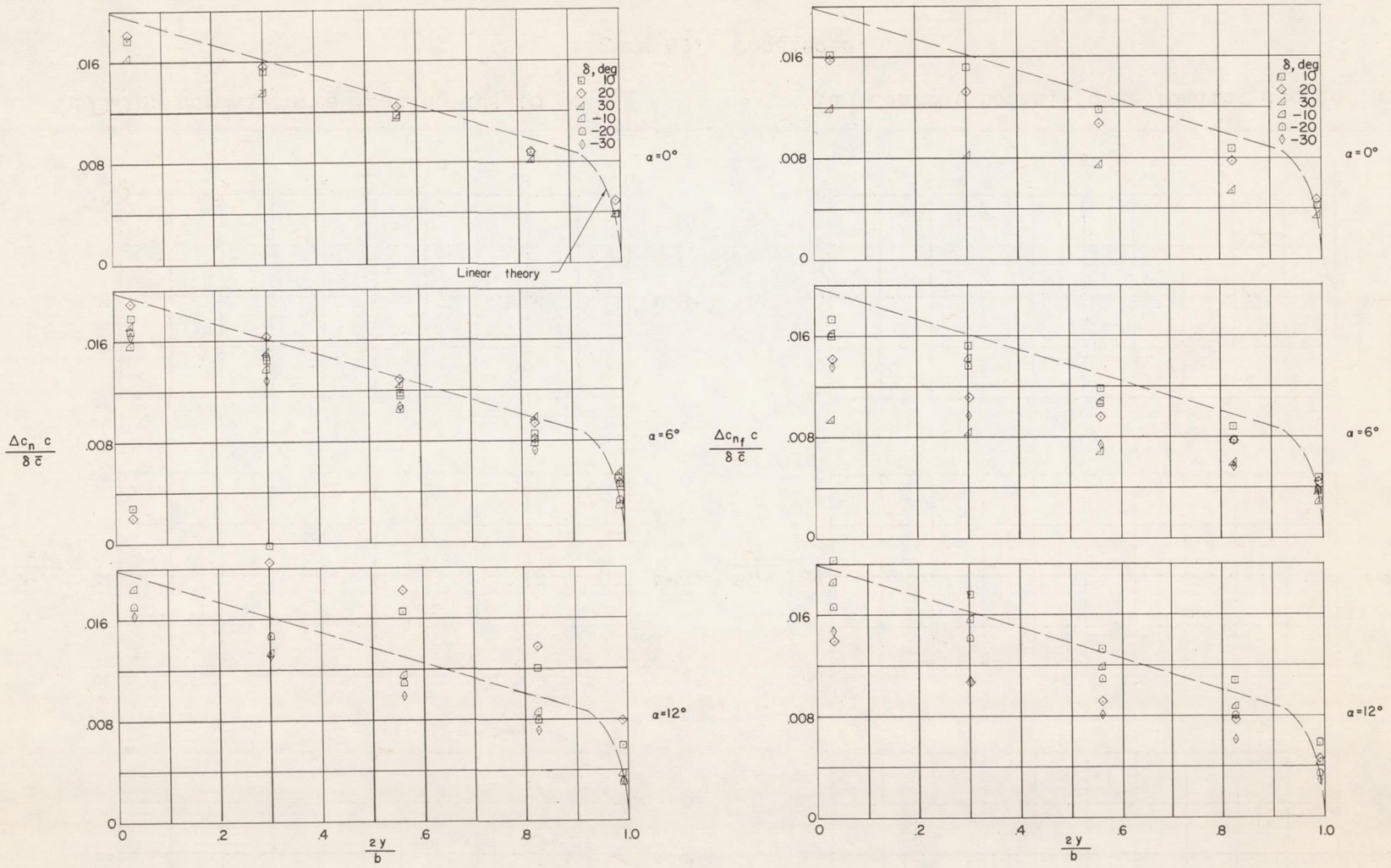

(a) Wing normal-force loading due to δ.

(b) Control normal-force loading due to δ.

Figure 43.- Spanwise normal-force loading distributions for configuration 5. M = 1.61; R = 3.6×10^6.

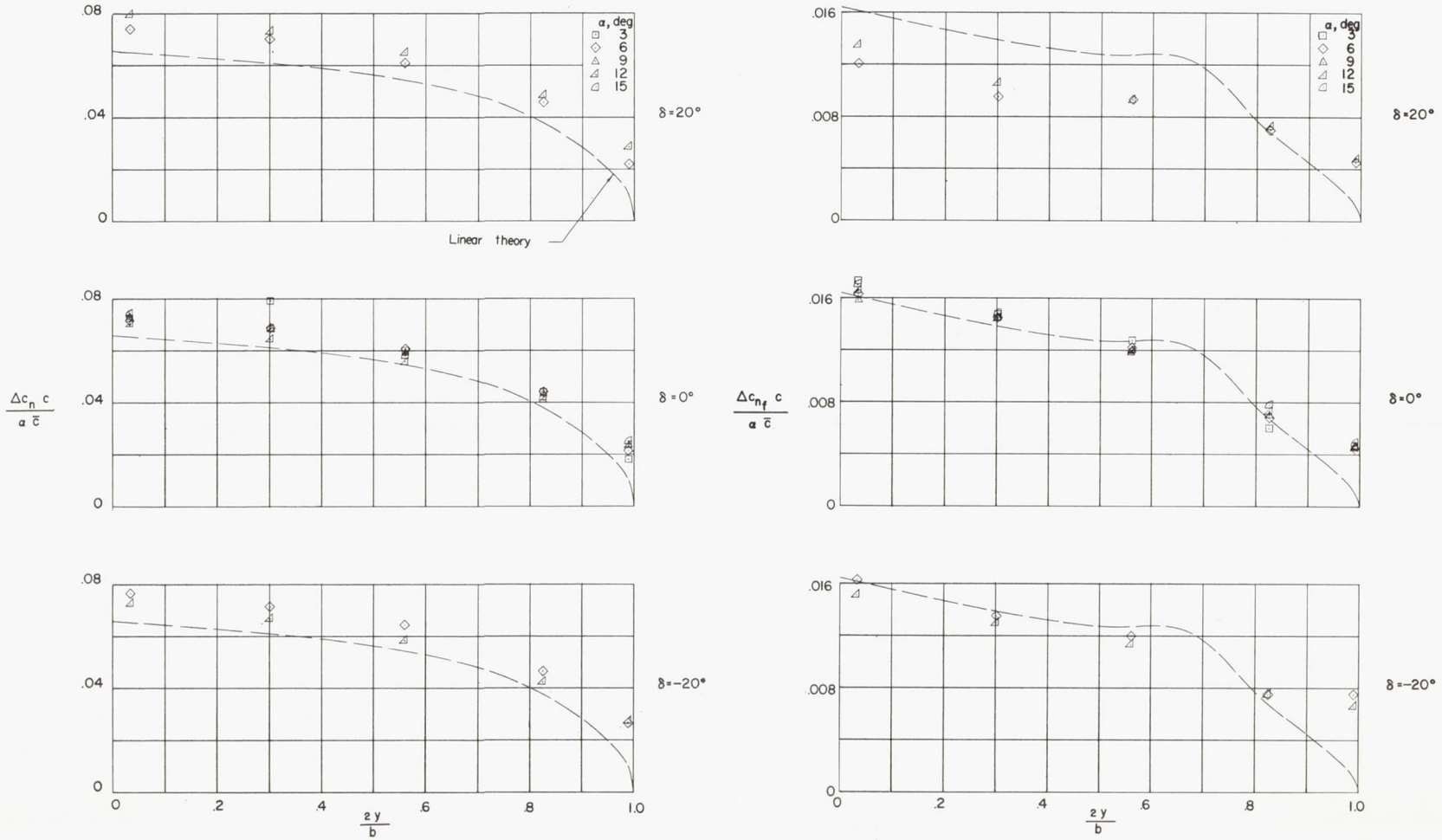

(c) Wing normal-force loading due to α.

(d) Control normal-force loading due to α.

Figure 43.- Concluded.

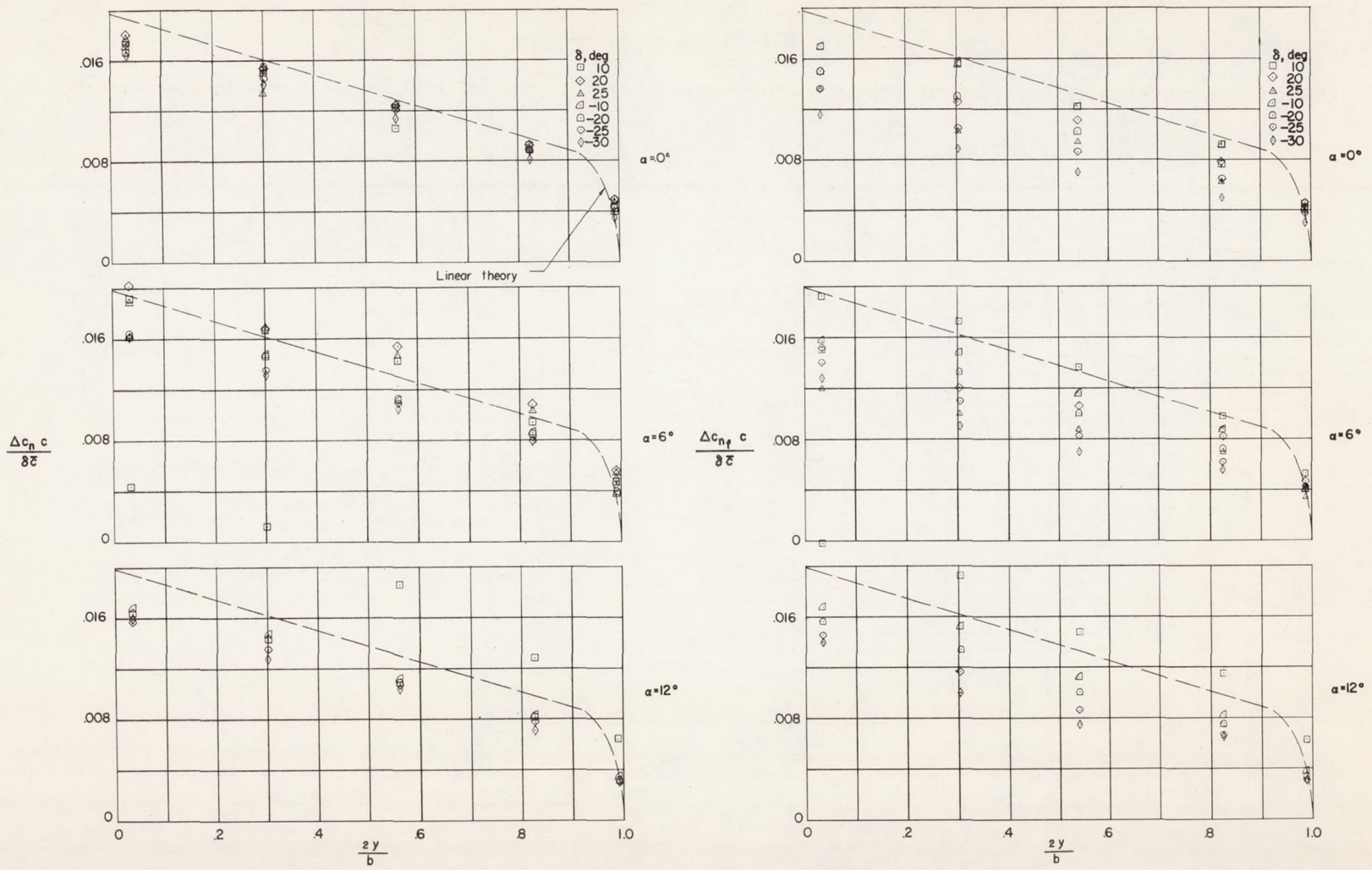

(a) Wing normal-force loading due to δ.

(b) Control normal-force loading due to δ.

Figure 44.- Spanwise normal-force loading distributions for configuration 6. M = 1.61; R = 3.6×10^6.

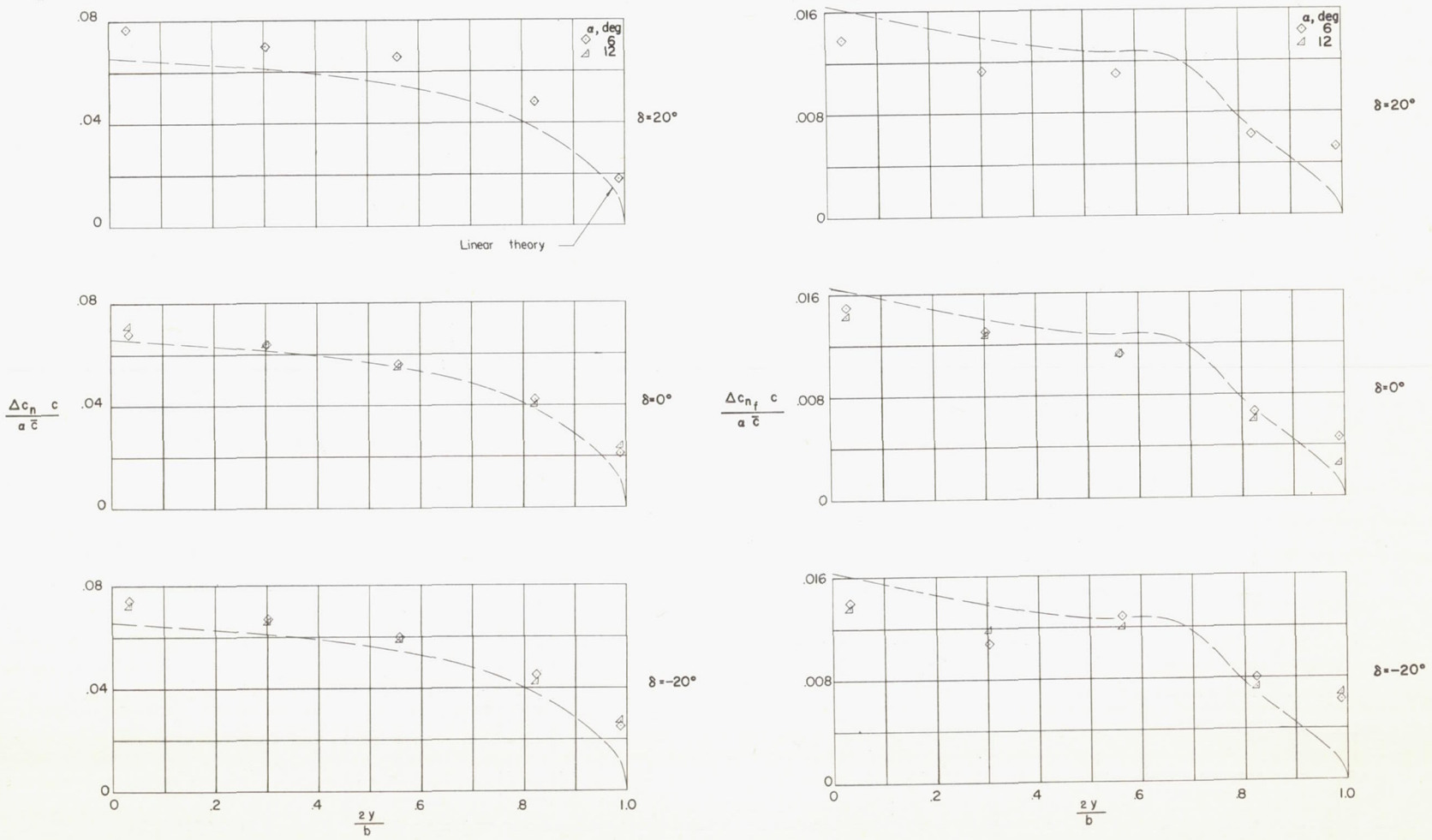

(c) Wing normal-force loading due to α.

(d) Control normal-force loading due to α.

Figure 44.- Concluded.

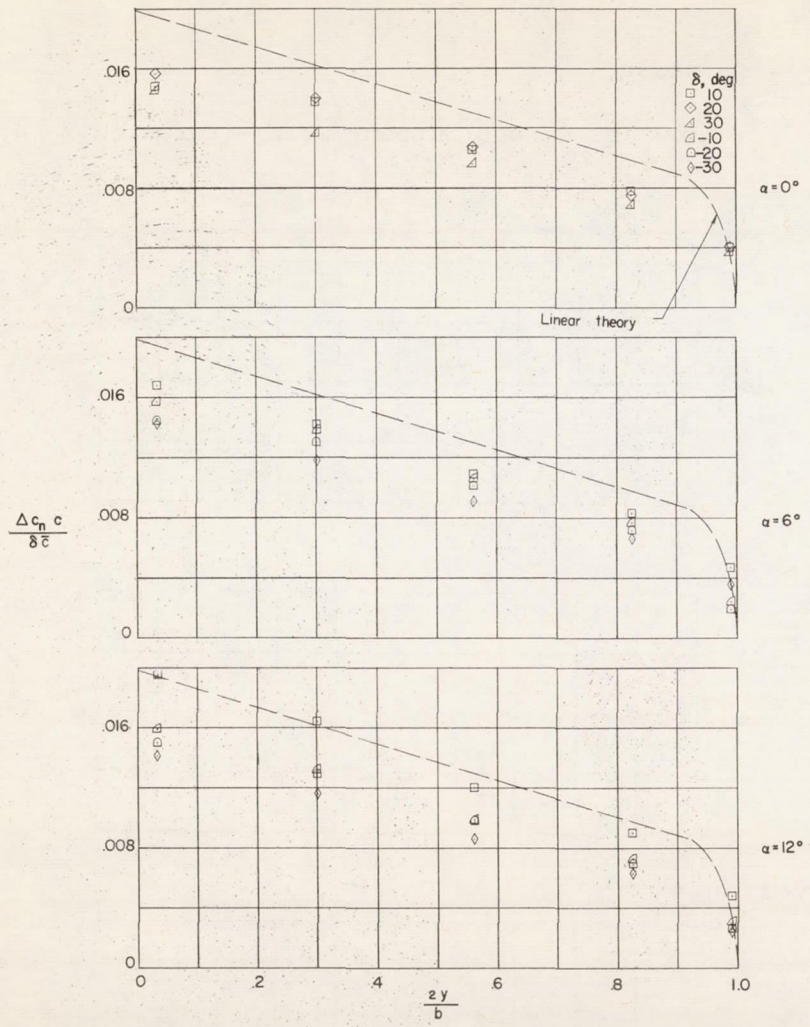

(a) Wing normal-force loading due to δ.

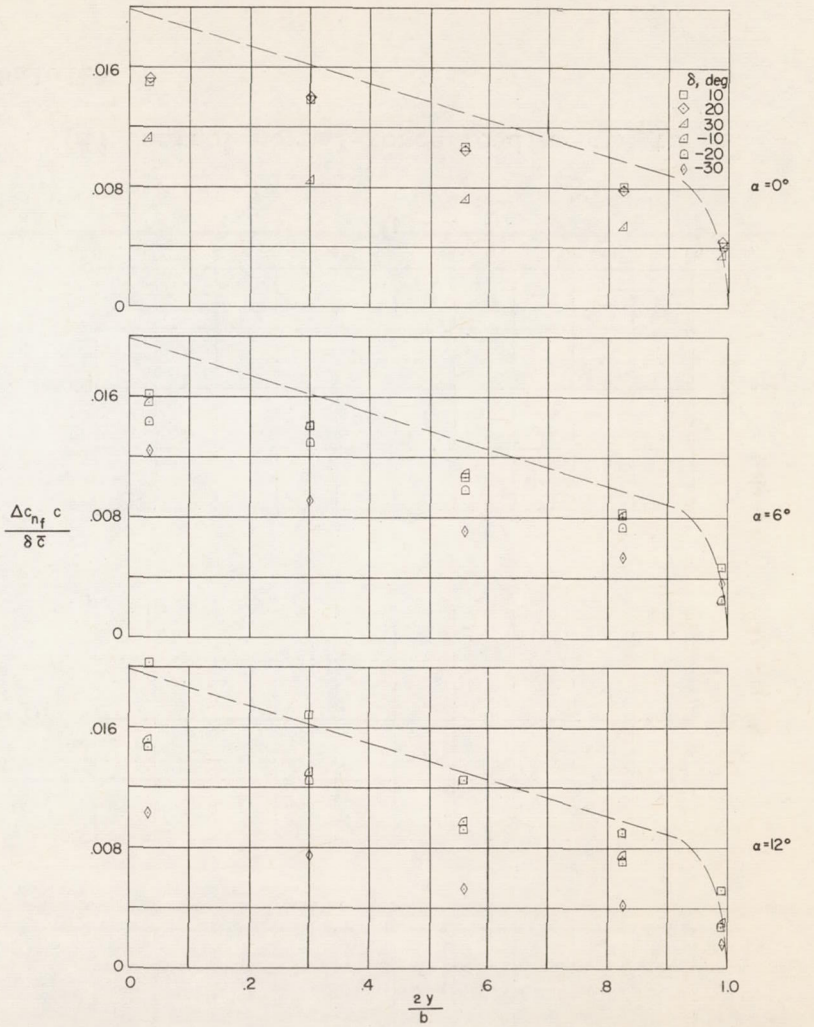

(b) Control normal-force loading due to δ.

Figure 45.- Spanwise normal-force loading distributions for configuration 4 with 0.20-inch hinge-line gap. M = 1.61; R = 3.6×10^6.

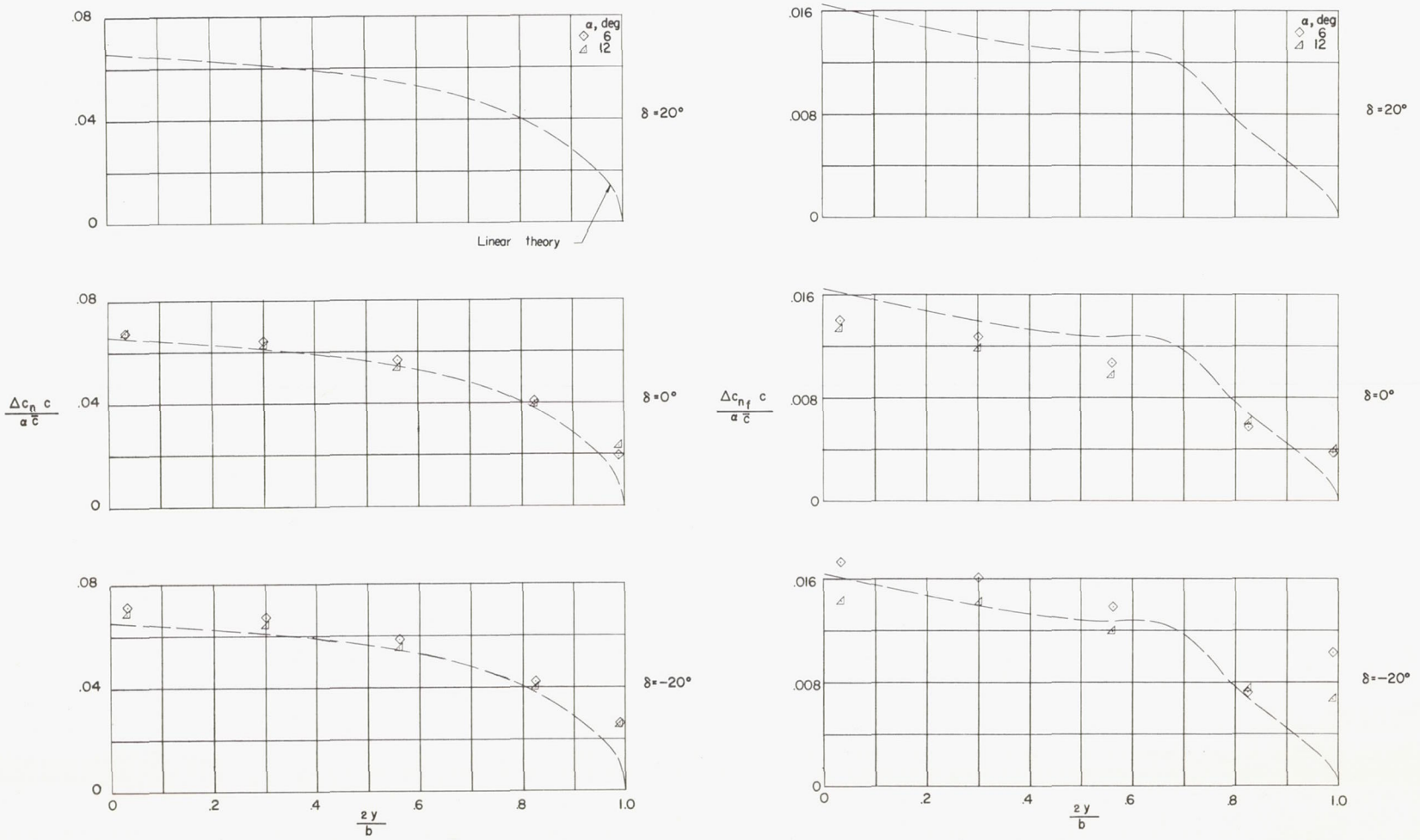

(c) Wing normal-force loading due to α.

(d) Control normal-force loading due to α.

Figure 45.- Concluded.

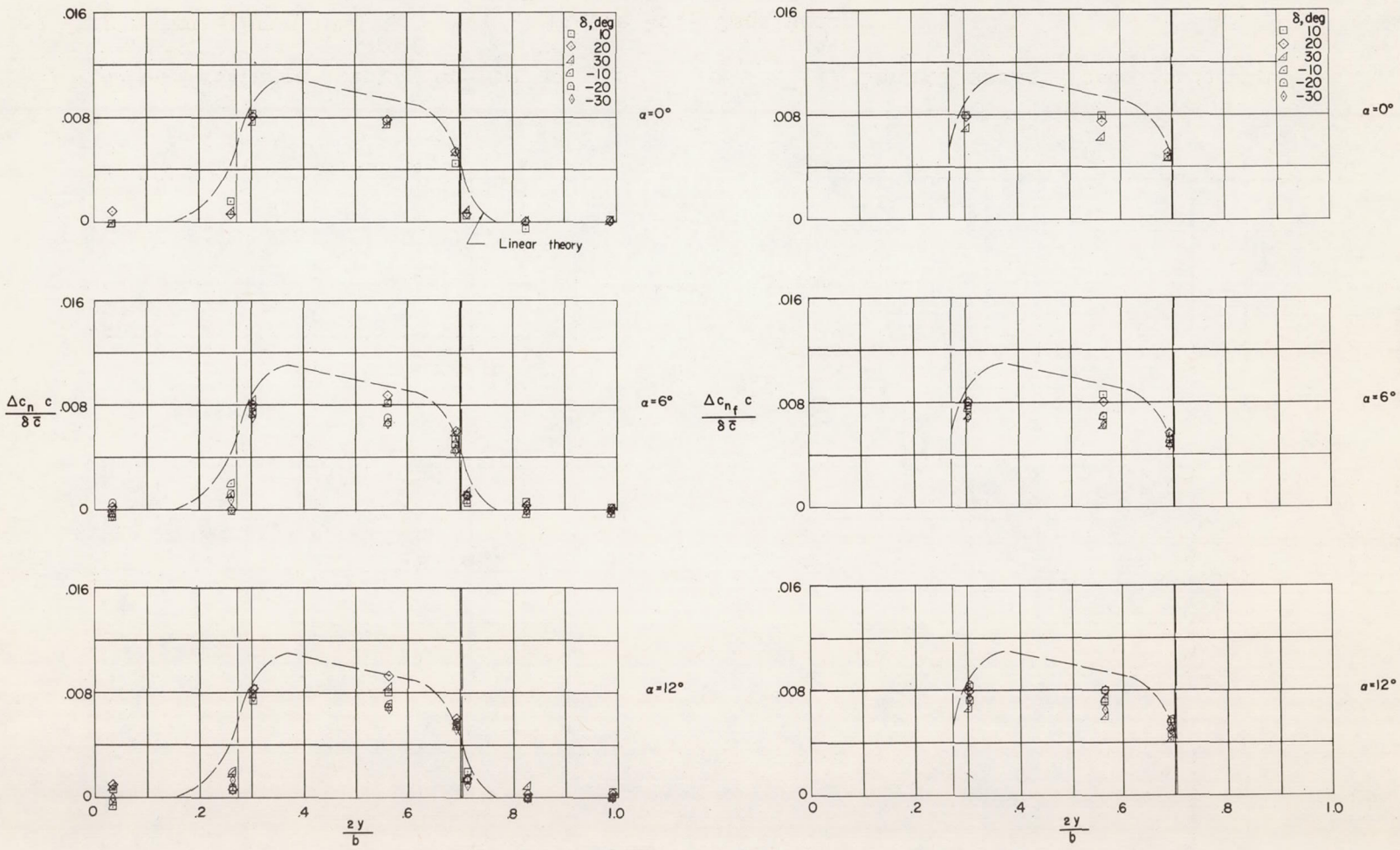

(a) Wing normal-force loading due to δ.

(b) Control normal-force loading due to δ.

Figure 46.- Spanwise normal-force loading distributions for configuration 2. $M = 2.01$; $R = 3.6 \times 10^6$.

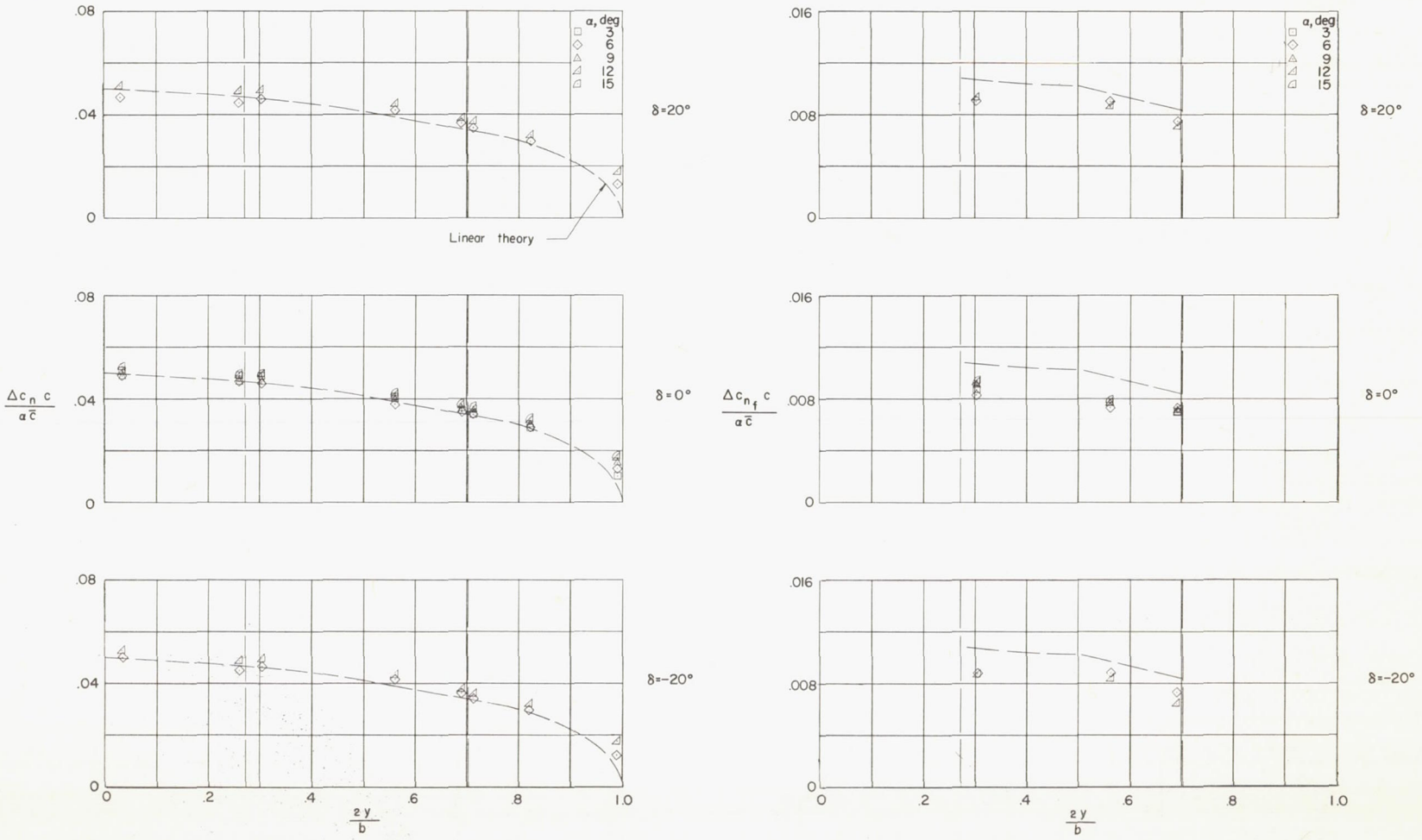

(c) Wing normal-force loading due to α.

(d) Control normal-force loading due to α.

Figure 46.- Concluded.

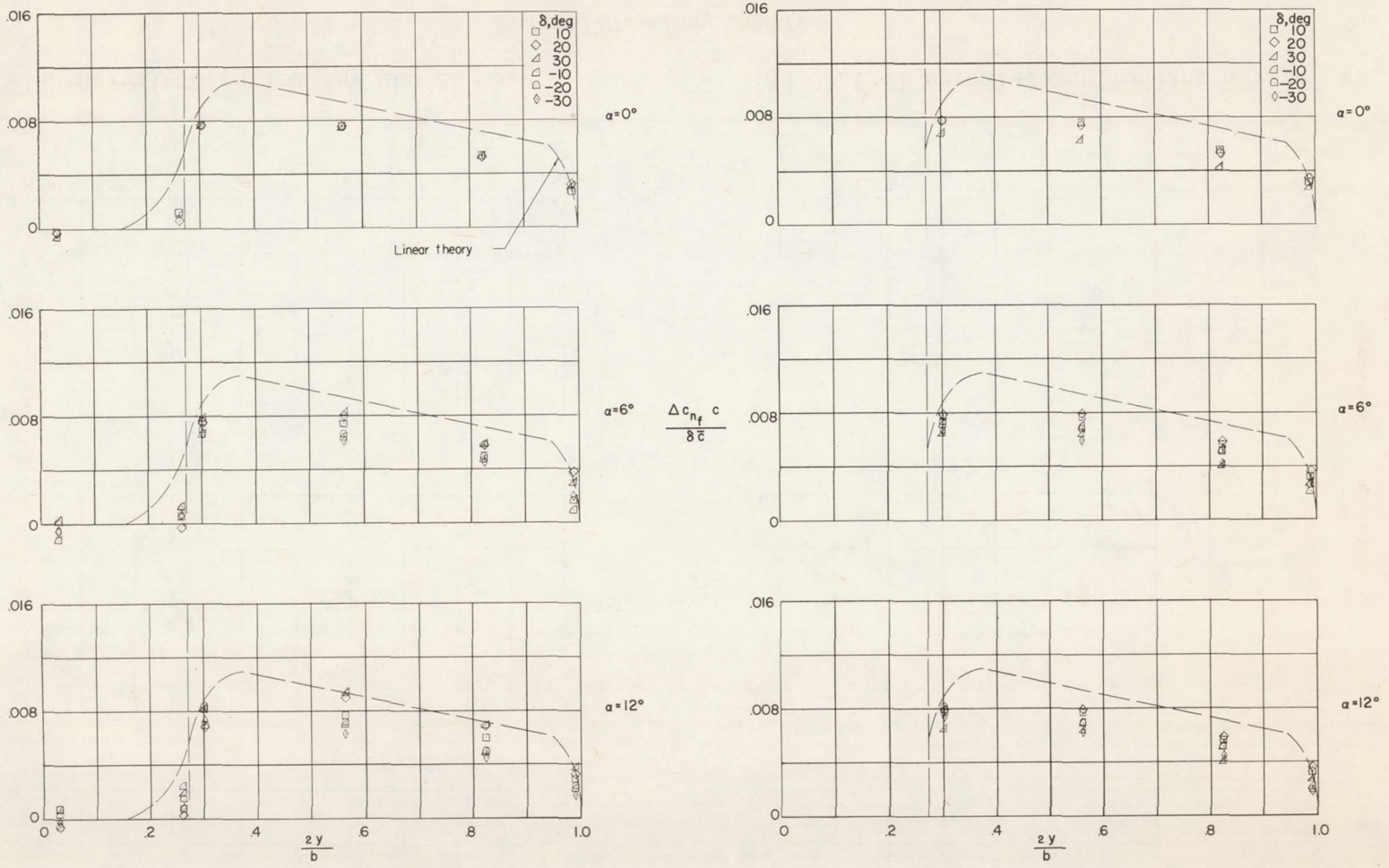

(a) Wing normal-force loading due to δ.

(b) Control normal-force loading due to δ.

Figure 47.- Spanwise normal-force loading distributions for configuration 3. M = 2.01; R = 3.6×10^6.

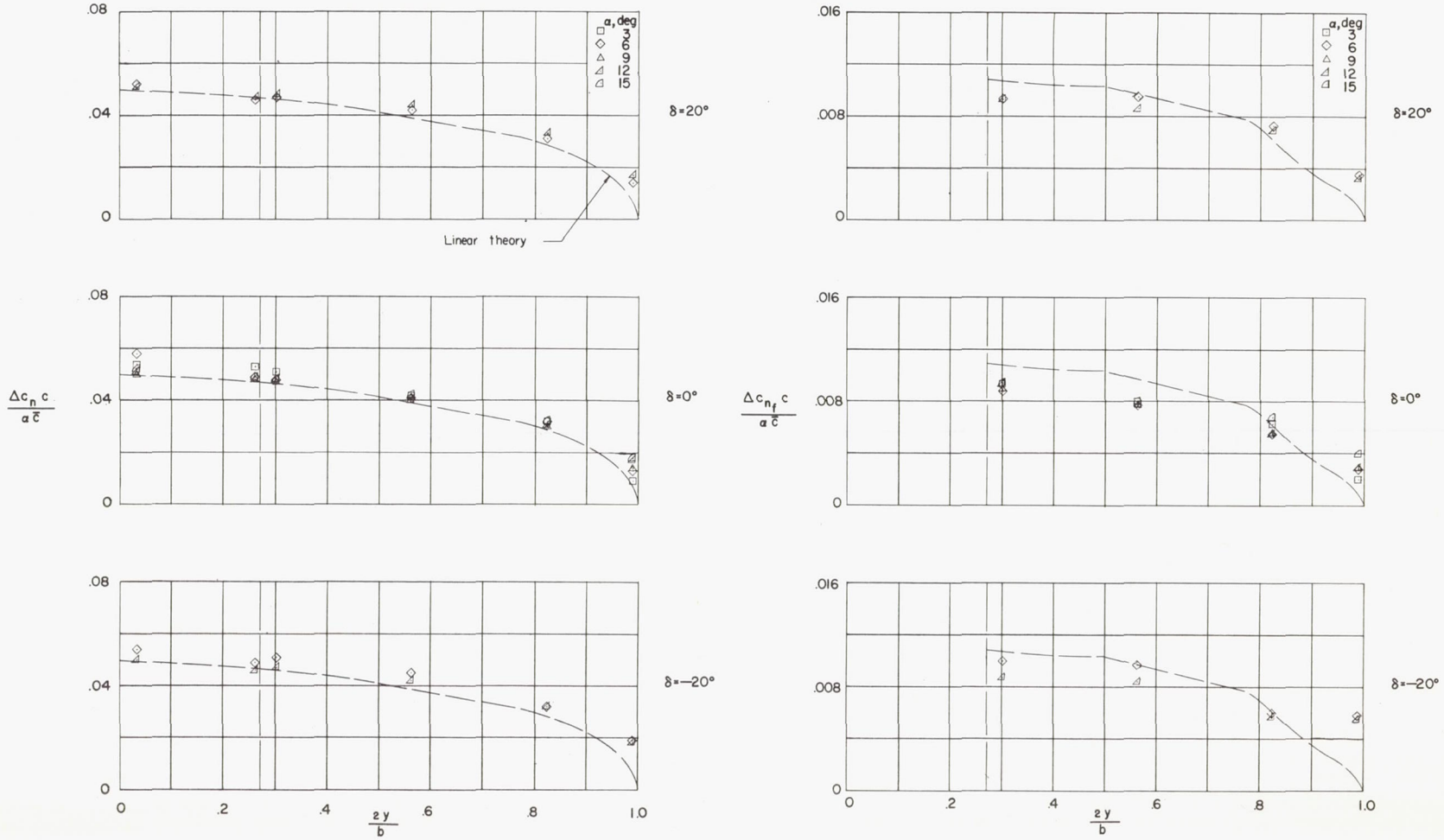

(c) Wing normal-force loading due to α.

(d) Control normal-force loading due to α.

Figure 47.- Concluded.

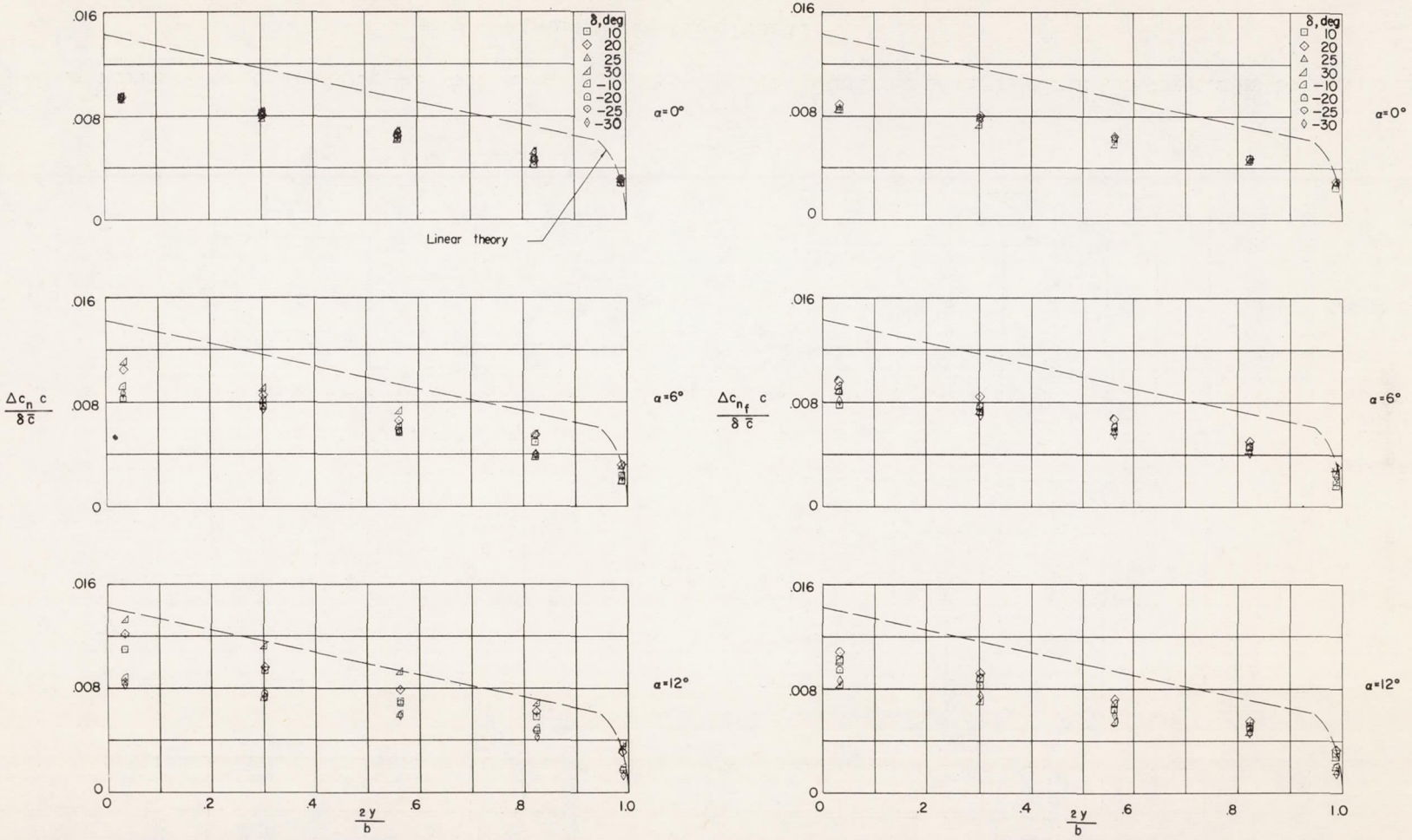

(a) Wing normal-force loading due to δ.

(b) Control normal-force loading due to δ.

Figure 48.- Spanwise normal-force loading distributions for configuration 4. M = 2.01; R = 3.6×10^6.

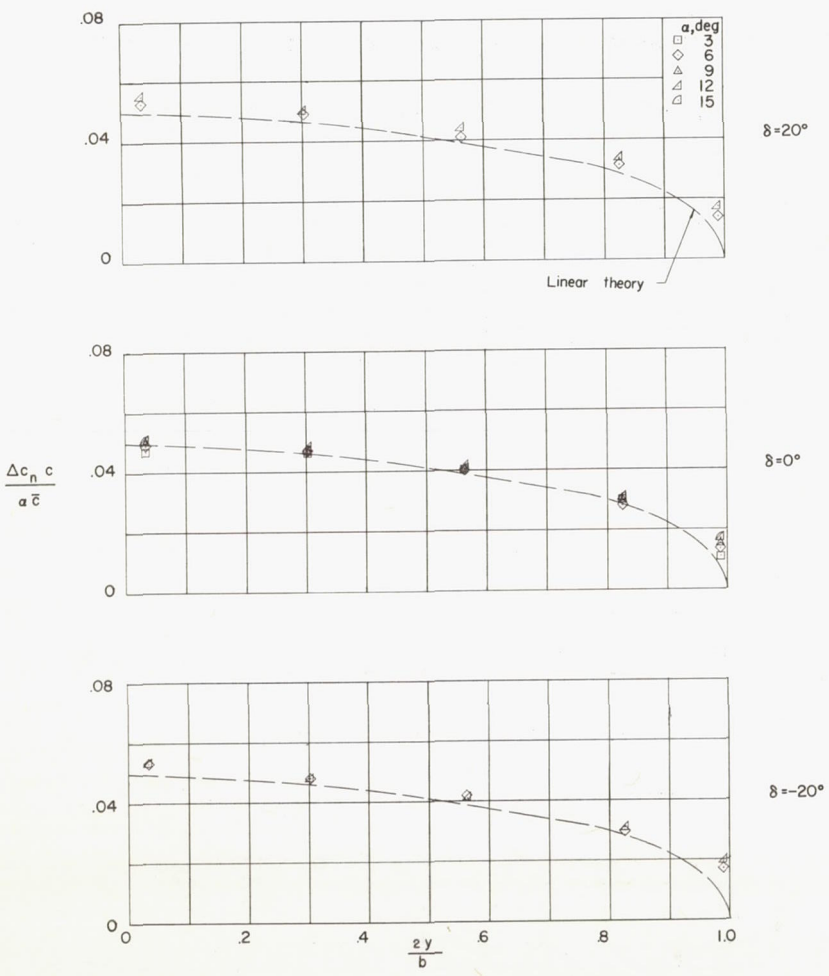

(c) Wing normal-force loading due to α.

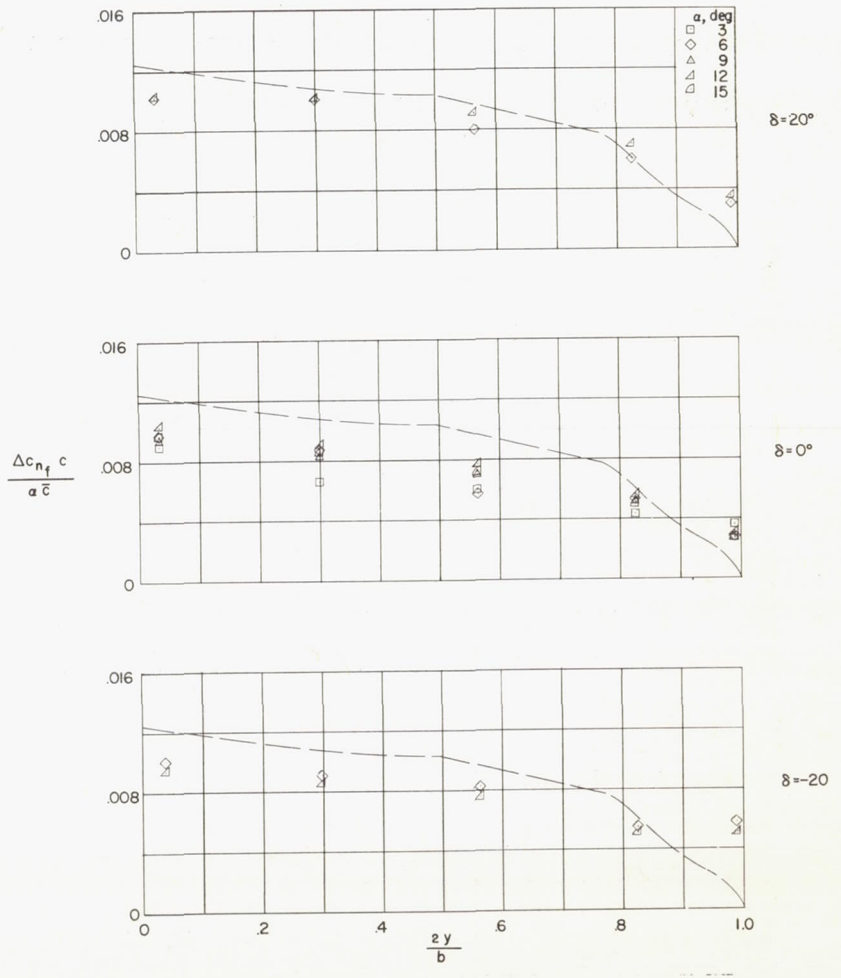

(d) Control normal-force loading due to α.

Figure 48.- Concluded.

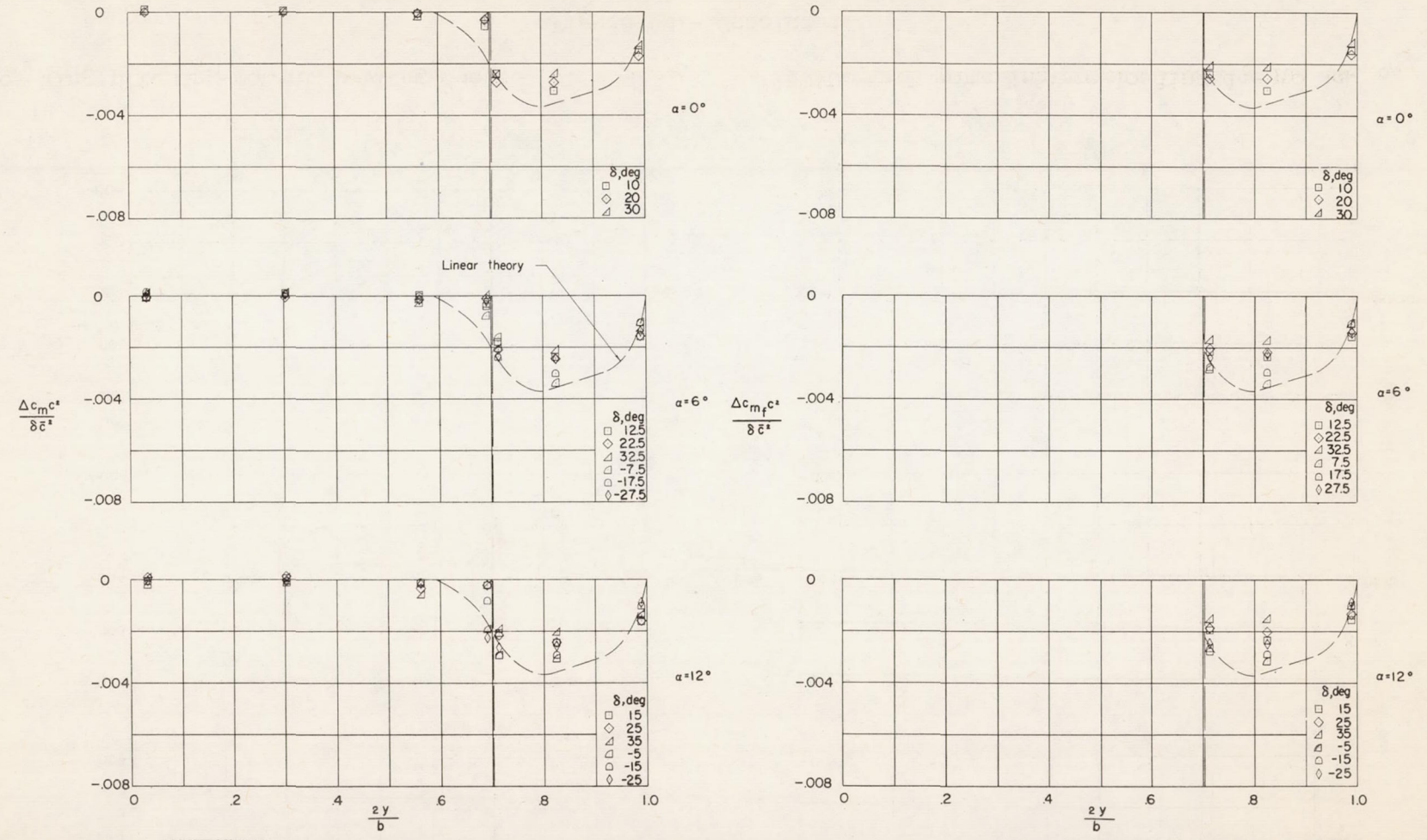

(a) Wing pitching-moment loading due to δ.

(b) Control pitching-moment loading due to δ.

Figure 49.- Spanwise pitching-moment loading distributions for configuration 1. M = 1.61; R = 3.6 × 10⁶.

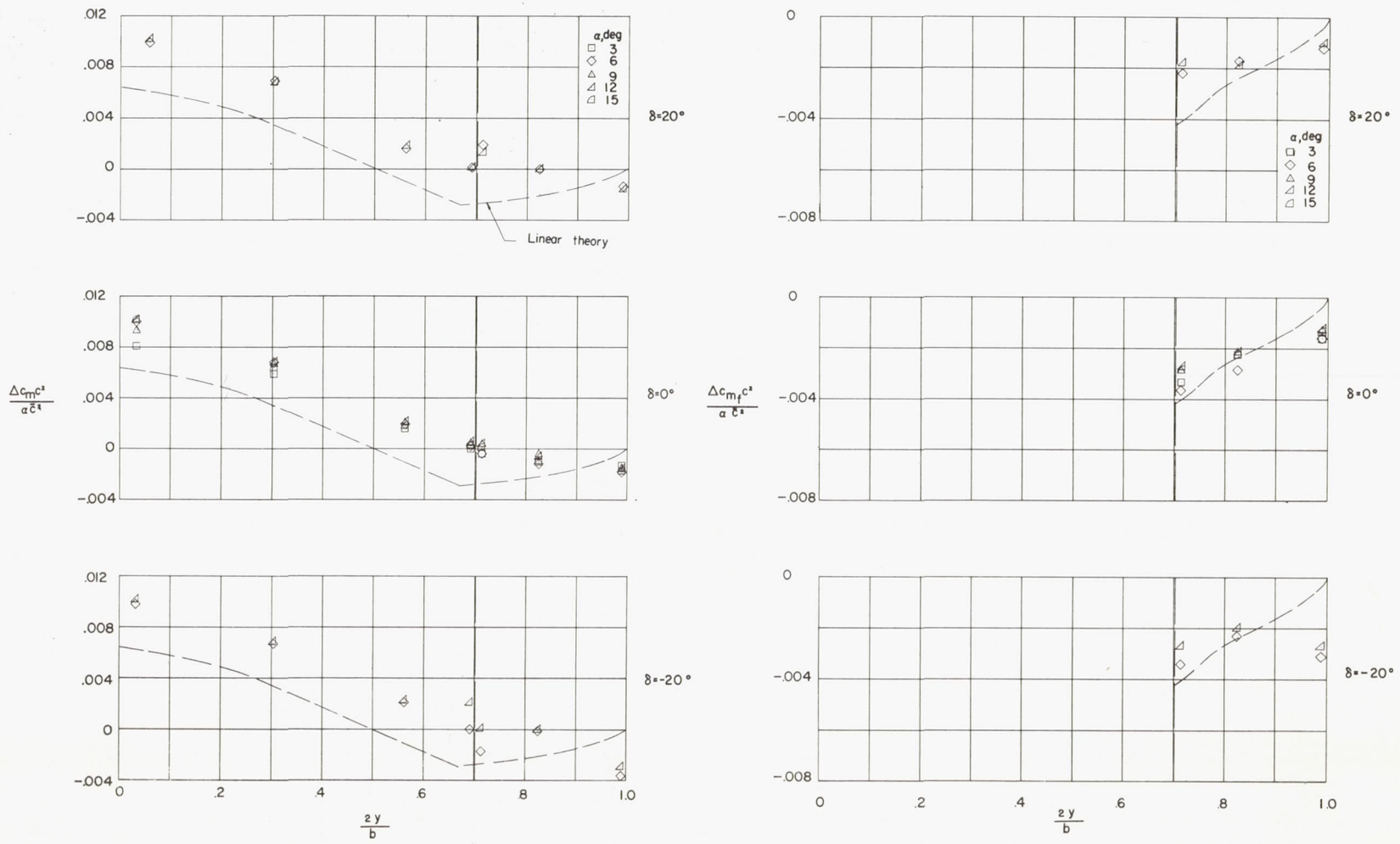

(c) Wing pitching-moment loading due to α.

(d) Control pitching-moment loading due to α.

Figure 49.- Concluded.

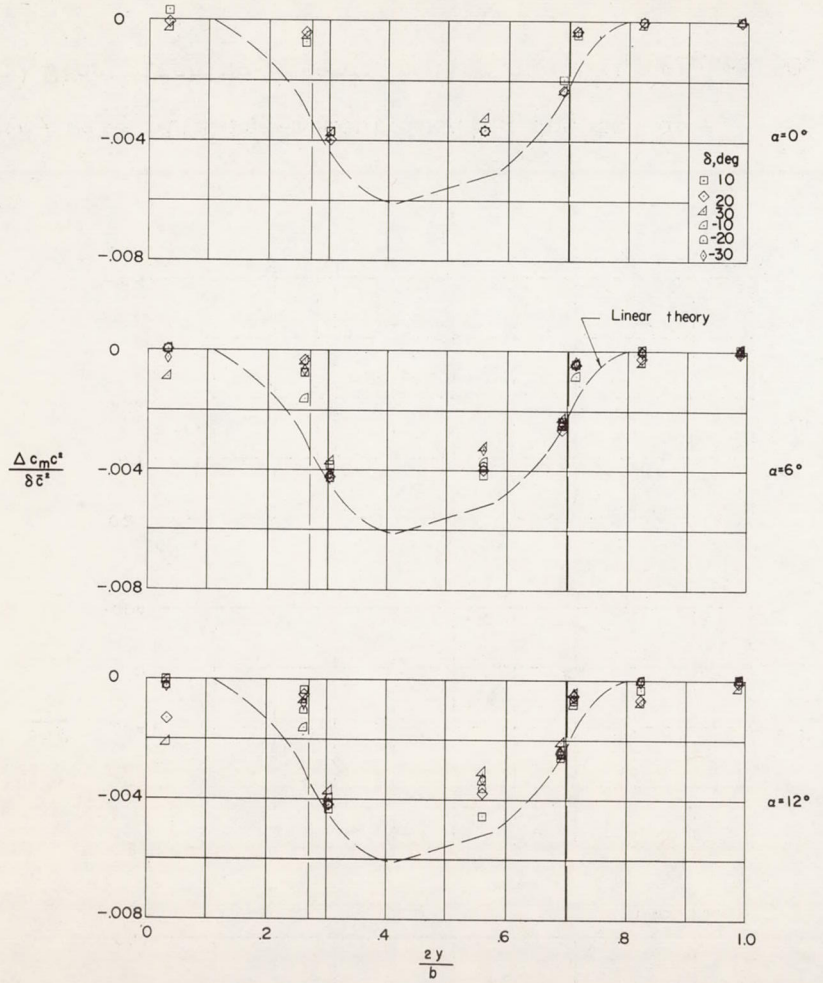

(a) Wing pitching-moment loading due to δ.

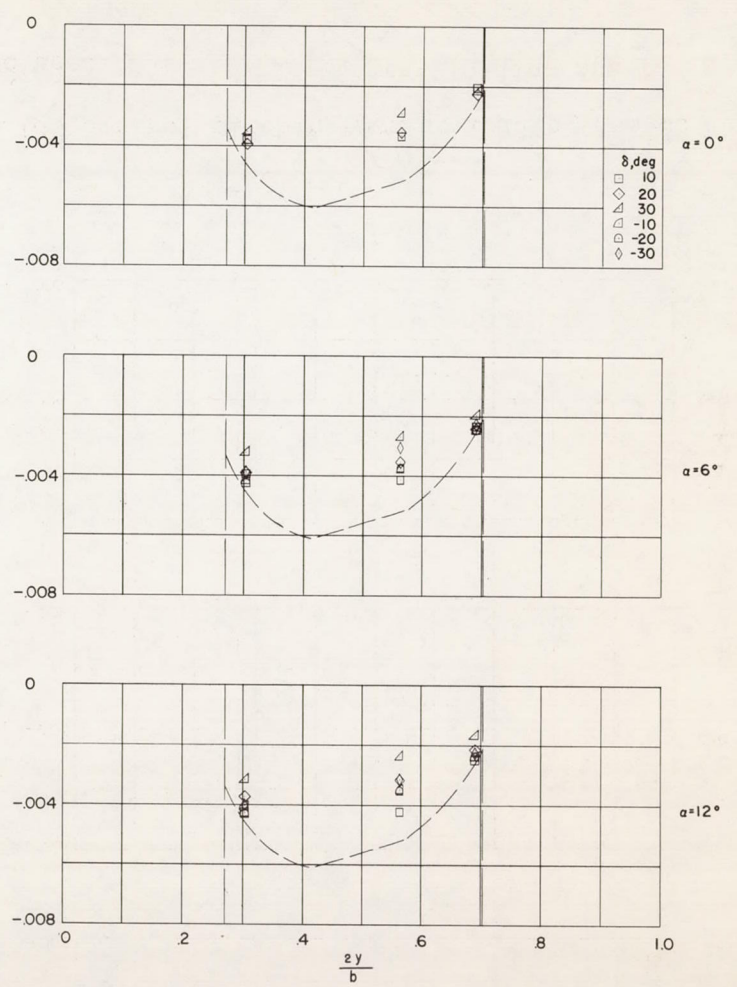

(b) Control pitching-moment loading due to δ.

Figure 50.- Spanwise pitching-moment loading distributions for configuration 2. M = 1.61; $R = 3.6 \times 10^6$.

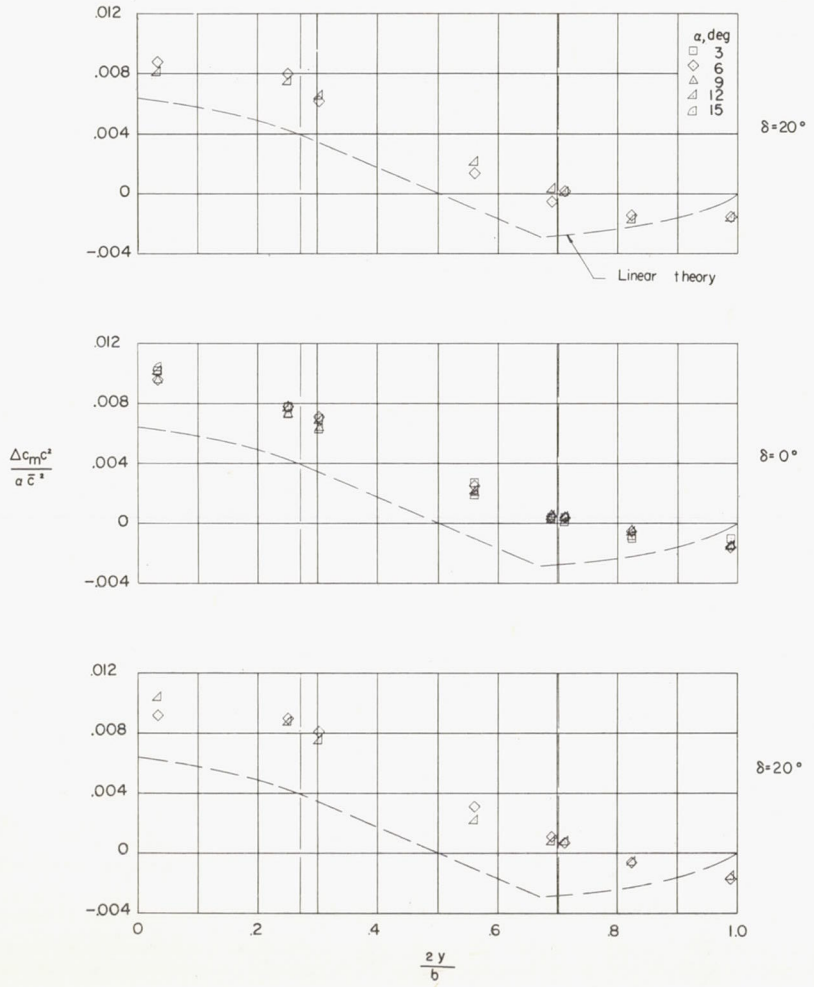

(c) Wing pitching-moment loading due to α.

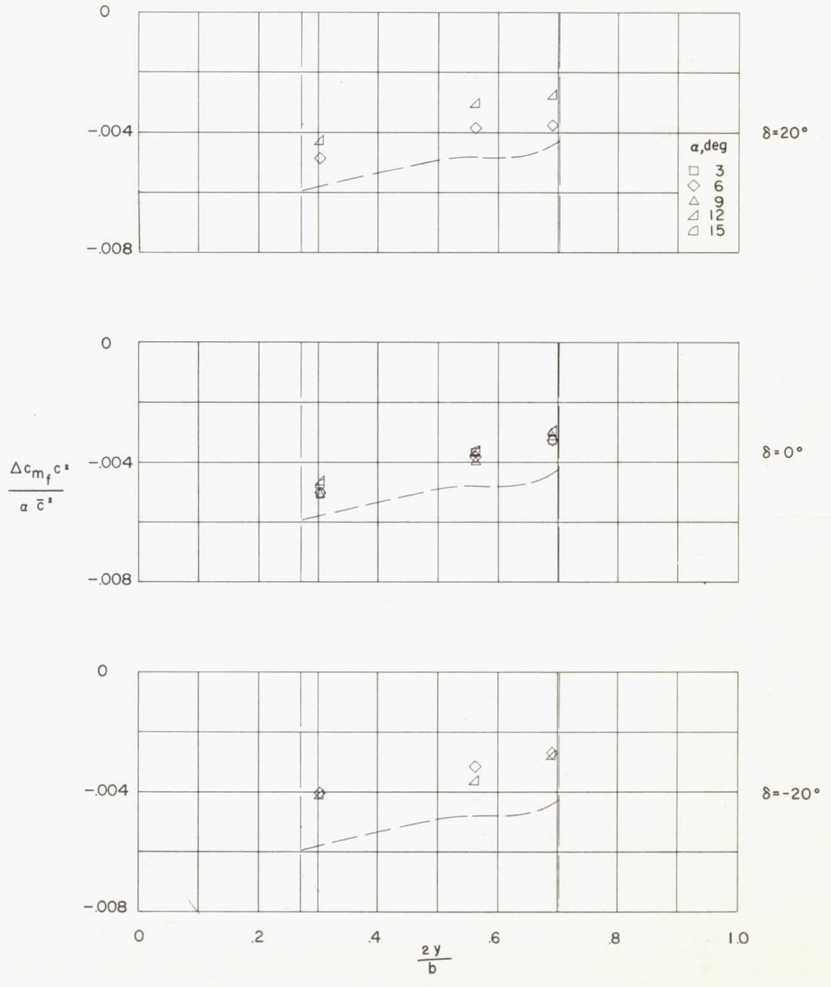

(d) Control pitching-moment loading due to α.

Figure 50.- Concluded.

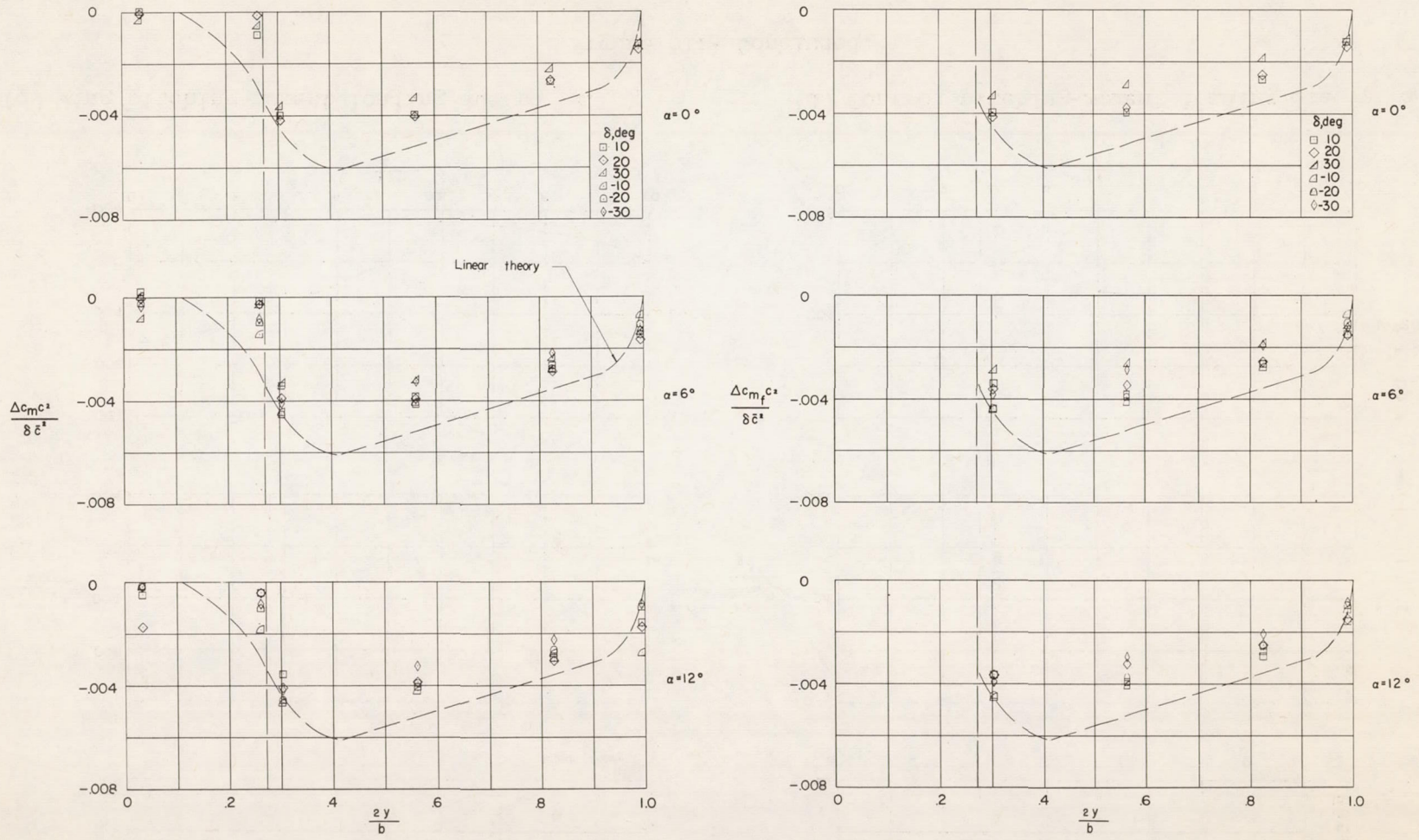

(a) Wing pitching-moment loading due to δ.

(b) Control pitching-moment loading due to δ.

Figure 51.- Spanwise pitching-moment loading distributions for configuration 3. M = 1.61; $R = 3.6 \times 10^6$.

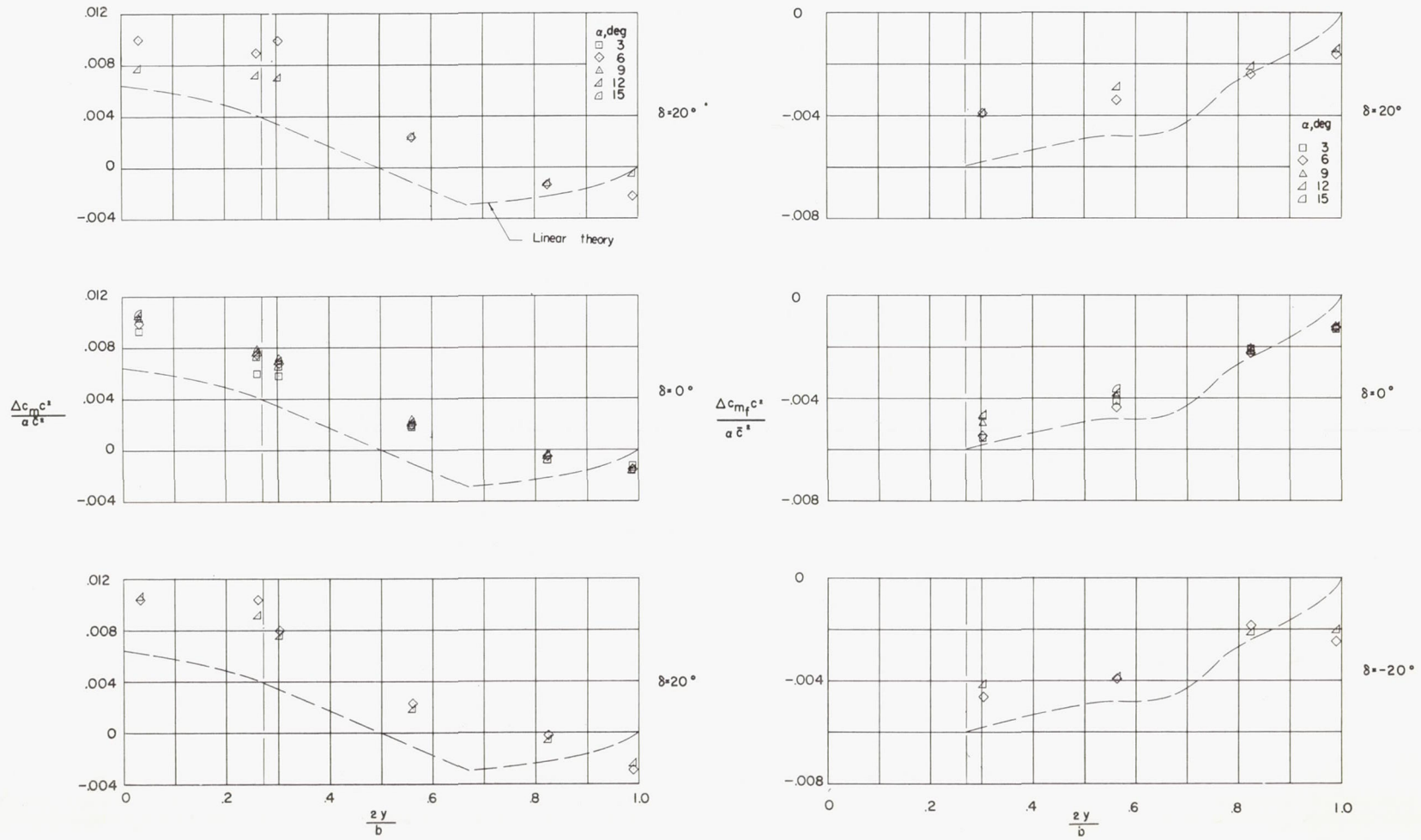

(c) Wing pitching-moment loading due to α.

(d) Control pitching-moment loading due to α.

Figure 51.- Concluded.

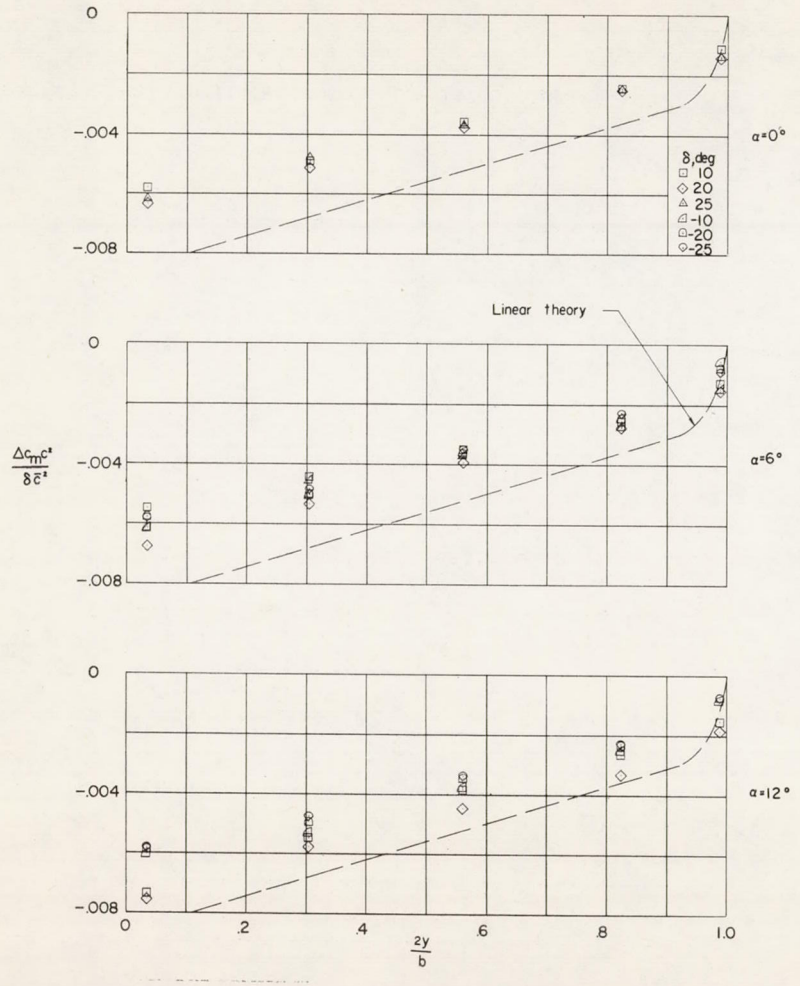

(a) Wing pitching-moment loading due to δ.

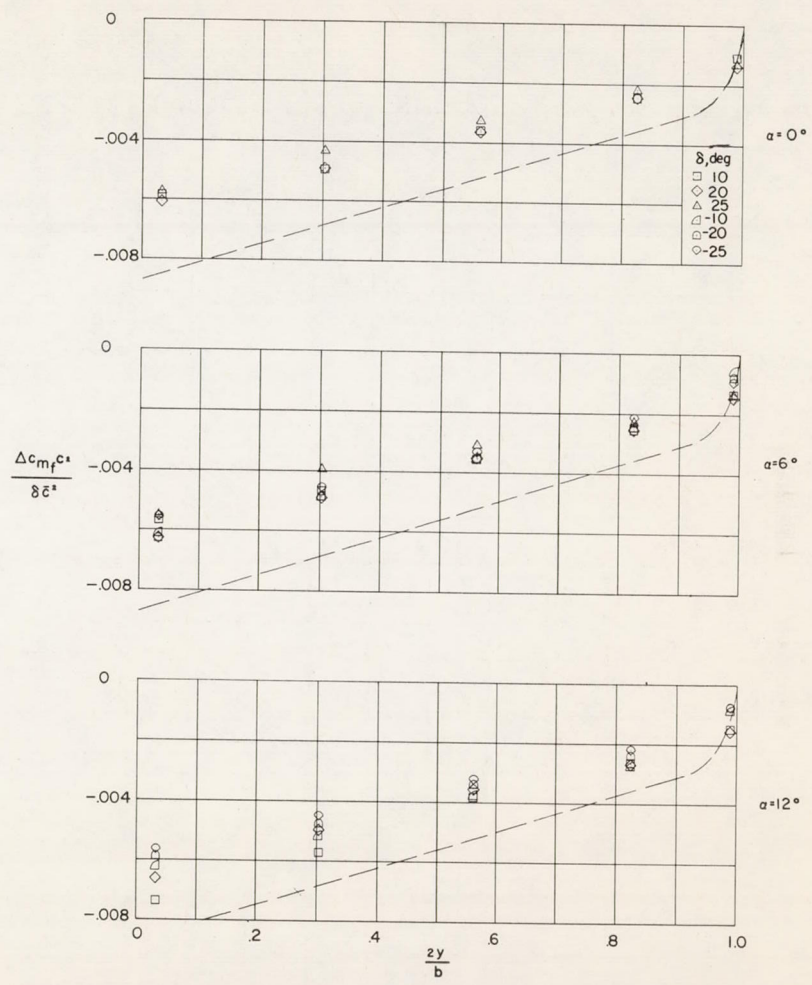

(b) Control pitching-moment loading due to δ.

Figure 52.- Spanwise pitching-moment loading distributions for configuration 4. M = 1.61; R = 3.6×10^6.

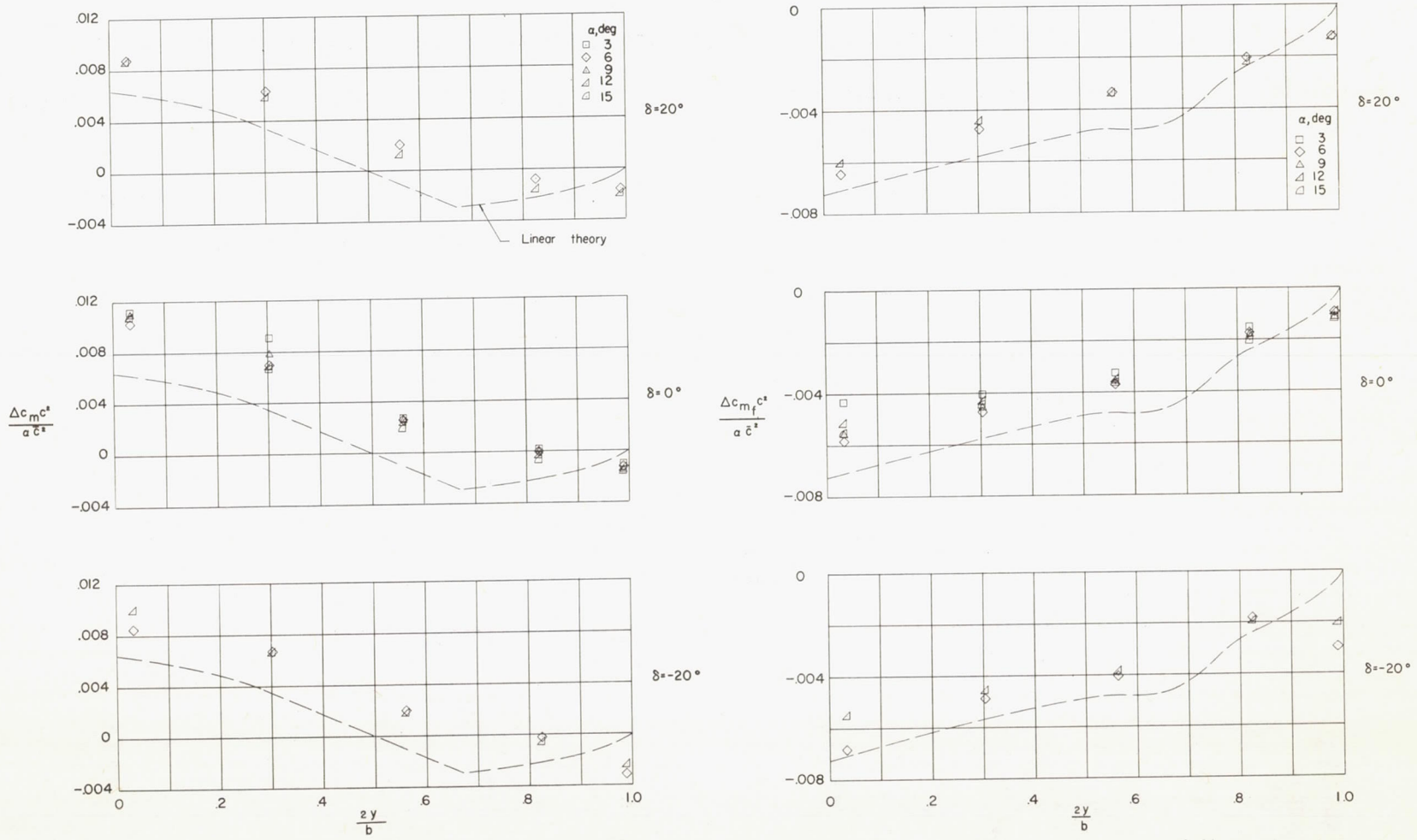

(c) Wing pitching-moment loading due to α.

(d) Control pitching-moment loading due to α.

Figure 52.- Concluded.

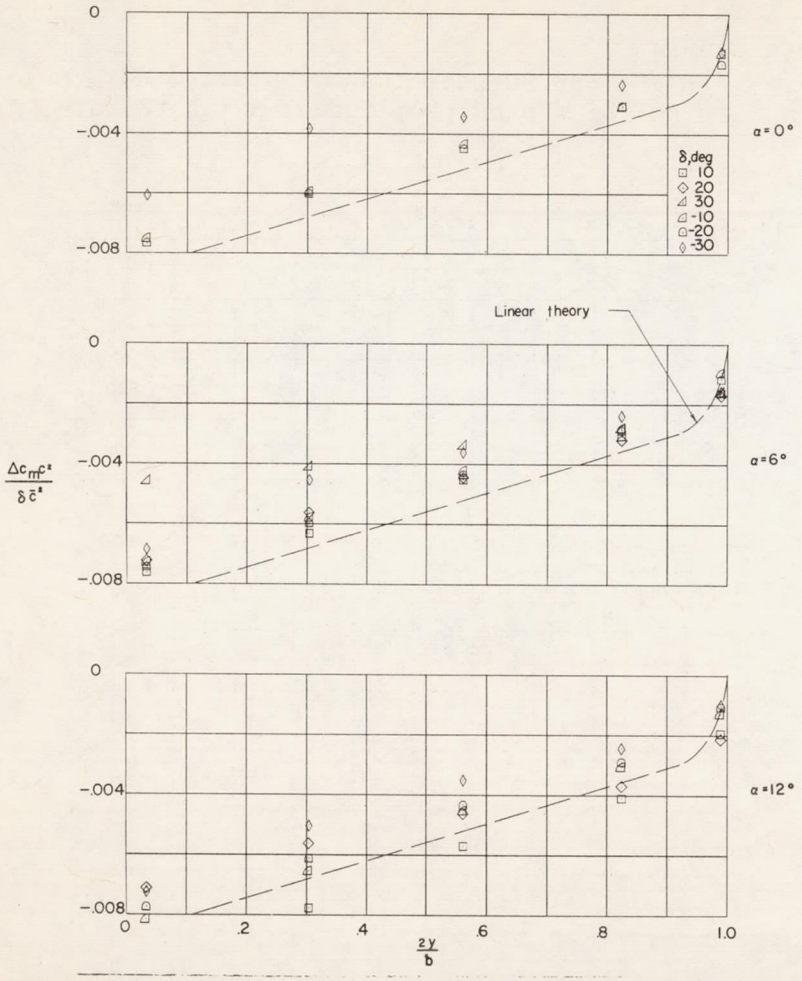

(a) Wing pitching-moment loading due to δ.

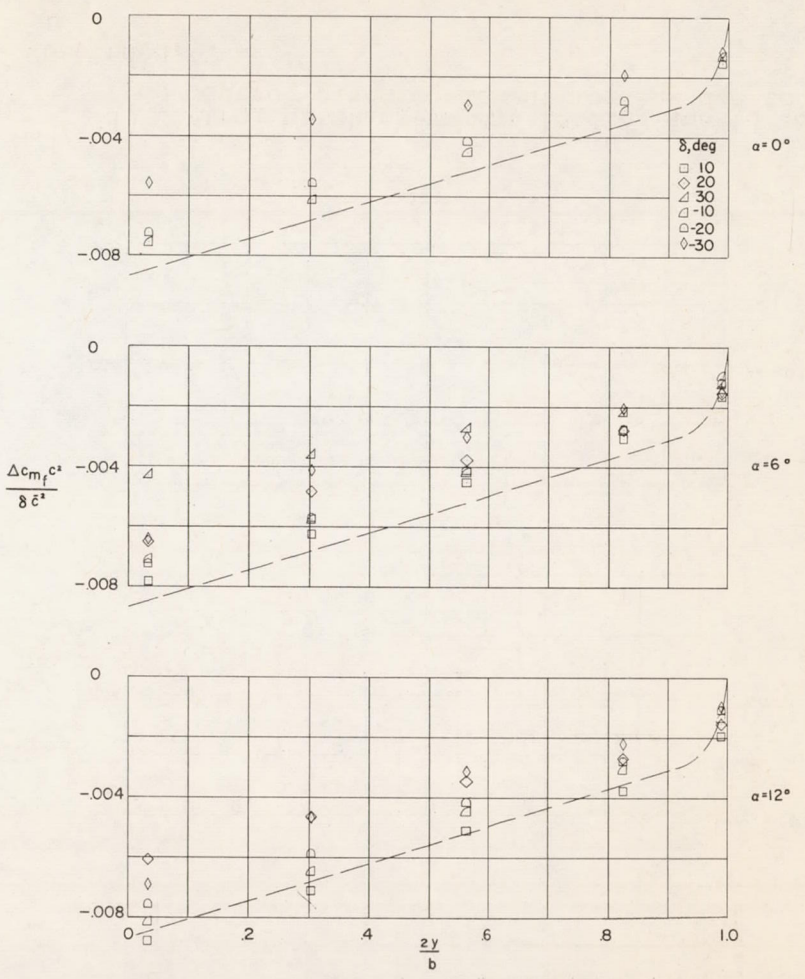

(b) Control pitching-moment loading due to δ.

Figure 53.- Spanwise pitching-moment loading distributions for configuration 5. M = 1.61; $R = 3.6 \times 10^6$.

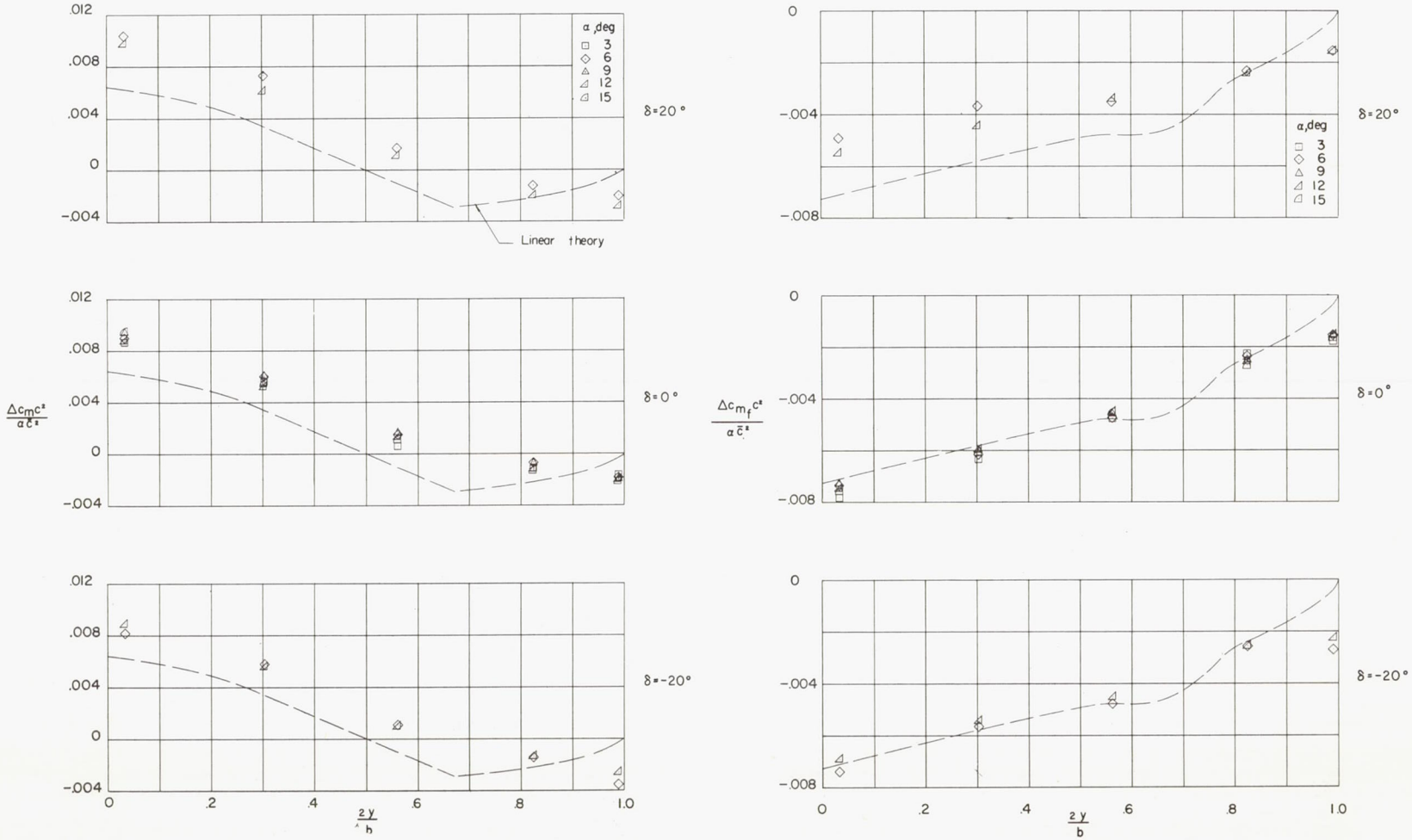

(c) Wing pitching-moment loading due to α.

(d) Control pitching-moment loading due to α.

Figure 53.- Concluded.

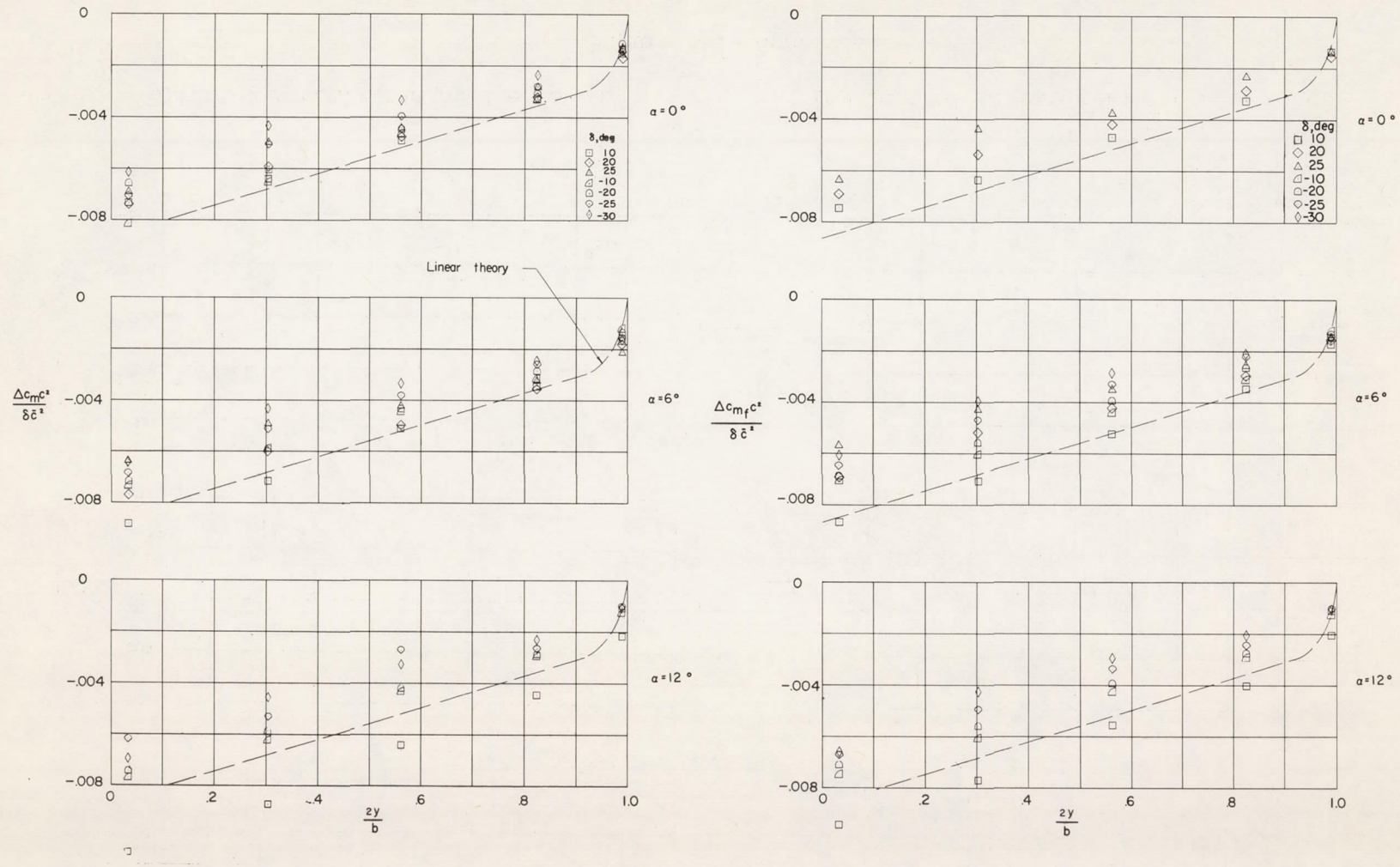

(a) Wing pitching-moment loading due to δ.

(b) Control pitching-moment loading due to δ.

Figure 54.- Spanwise pitching-moment loading distributions for configuration 6. M = 1.61; R = 3.6×10^6.

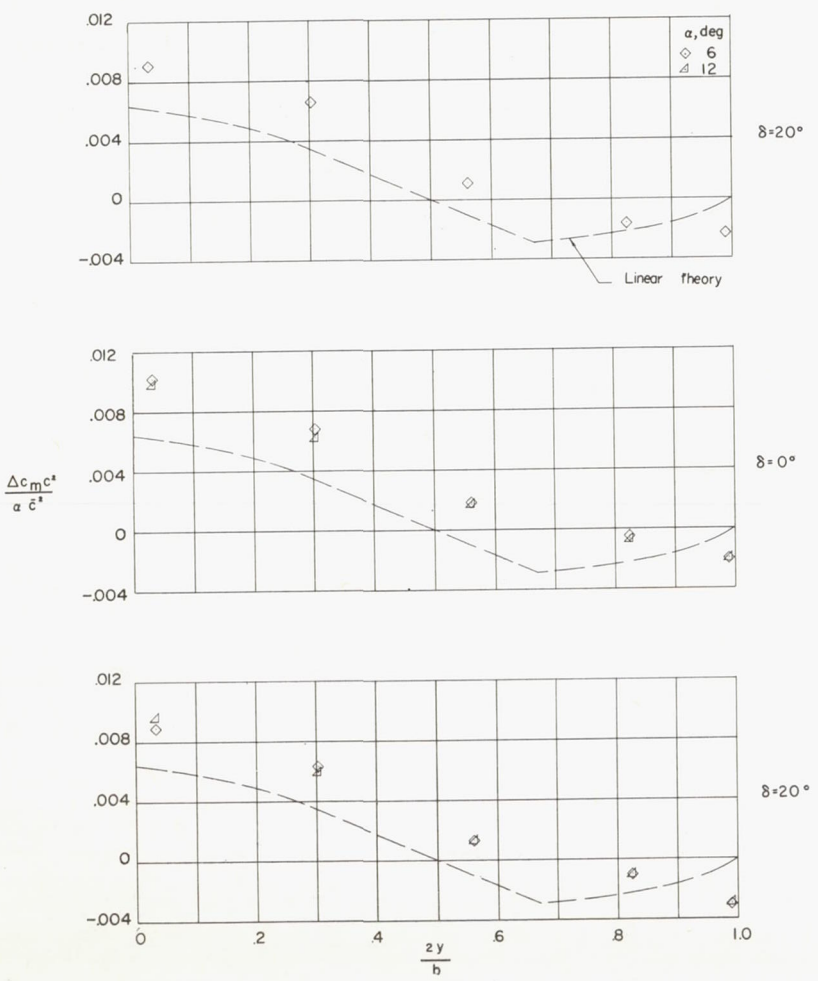

(c) Wing pitching-moment loading due to α.

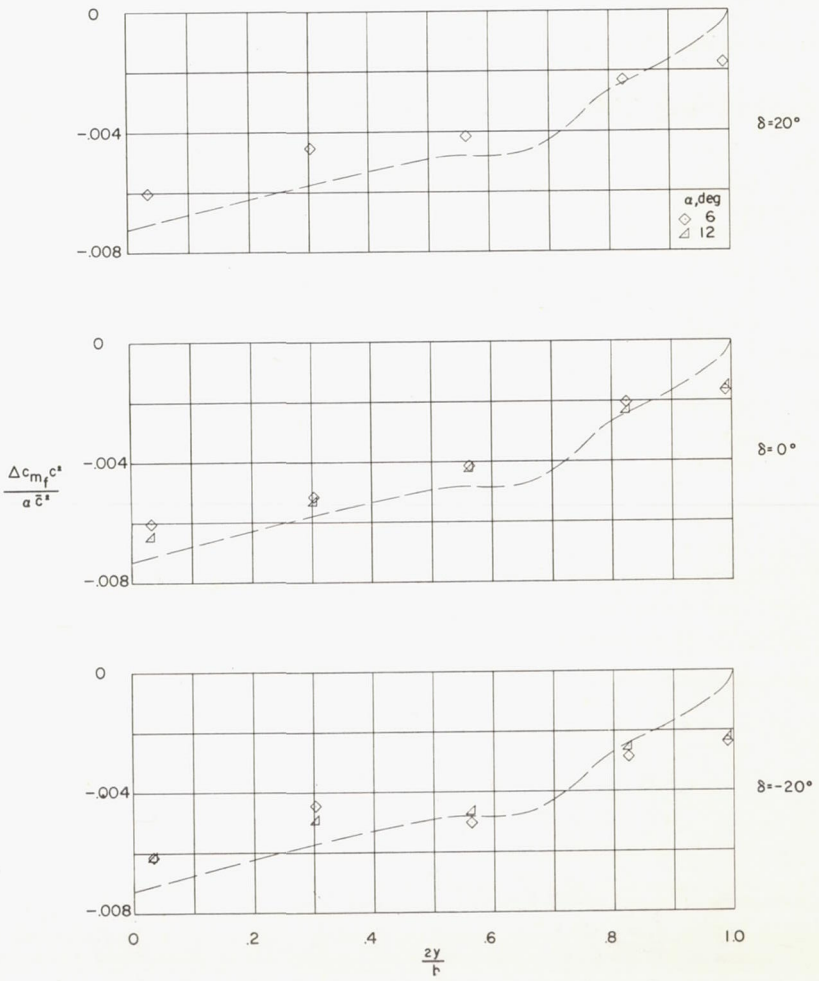

(d) Control pitching-moment loading due to α.

Figure 54.- Concluded.

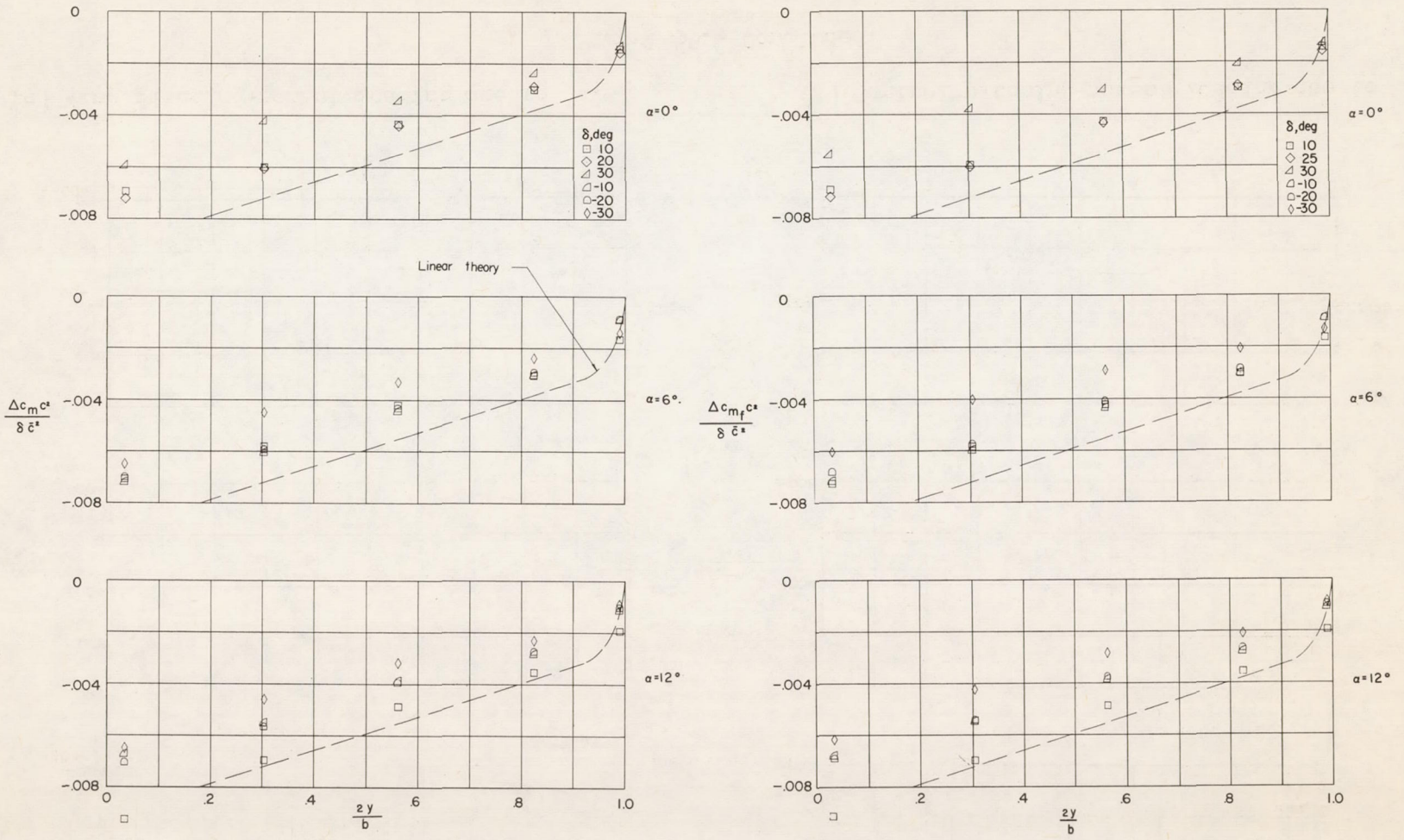

(a) Wing pitching-moment loading due to δ.

(b) Control pitching-moment loading due to δ.

Figure 55.- Spanwise pitching-moment loading distributions for configuration 4 with 0.20-inch hinge-line gap. M = 1.61; R = 3.6×10^6.

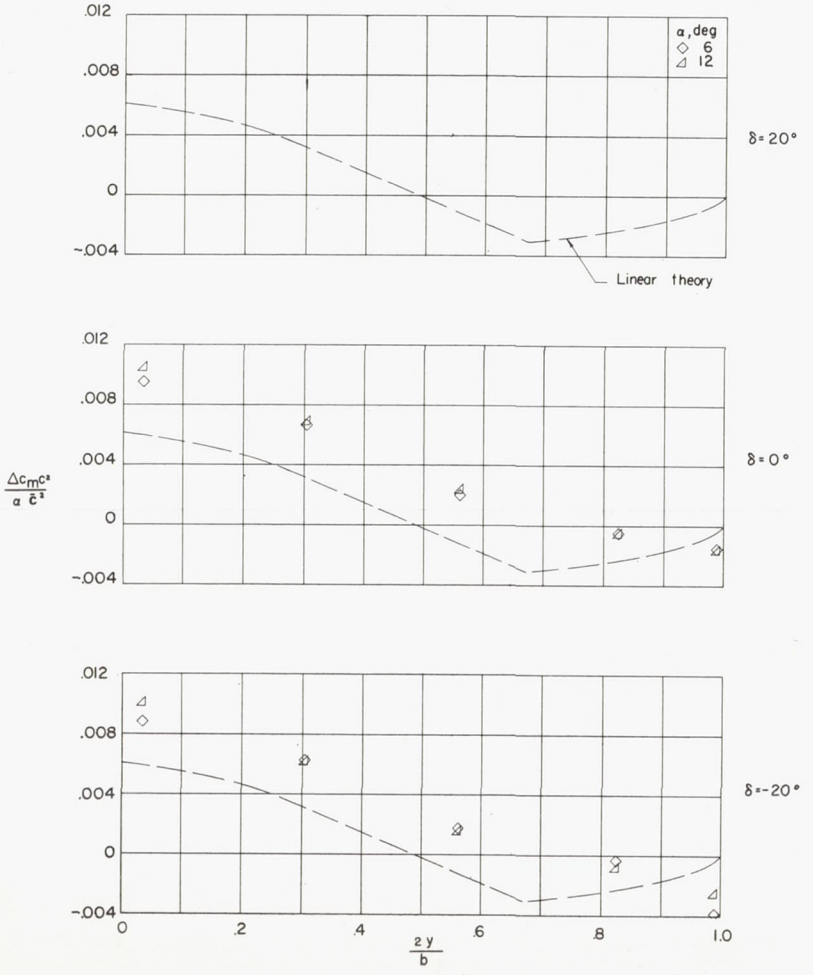

(c) Wing pitching-moment loading due to α.

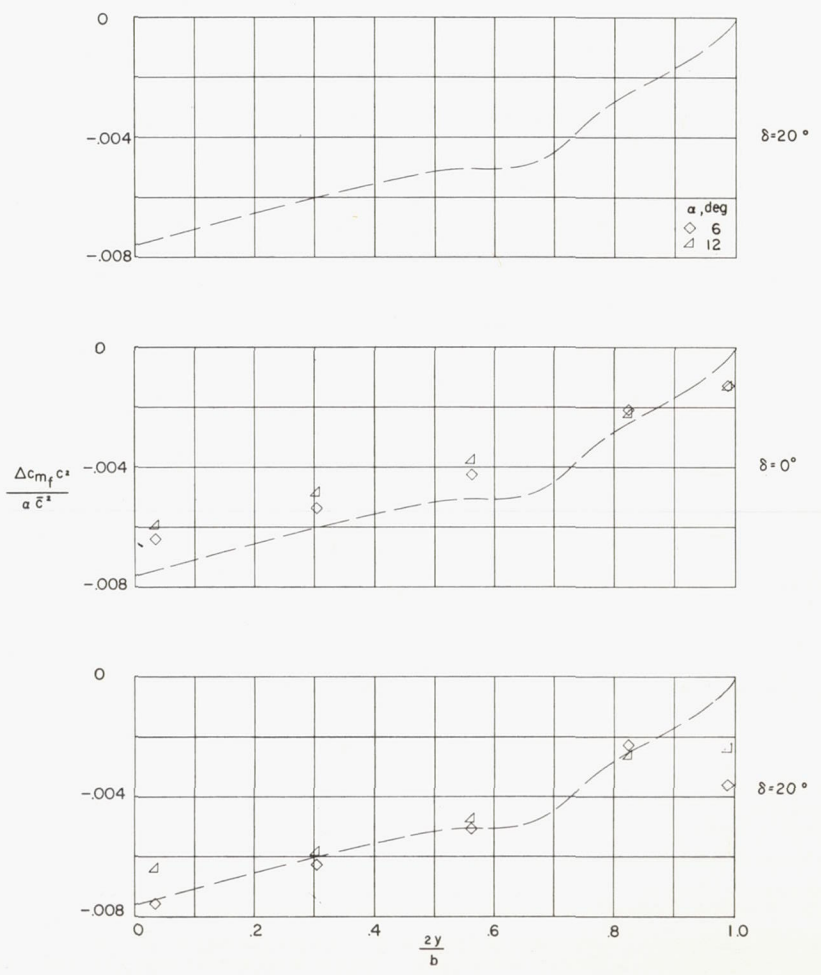

(d) Control pitching-moment loading due to α.

Figure 55.- Concluded.

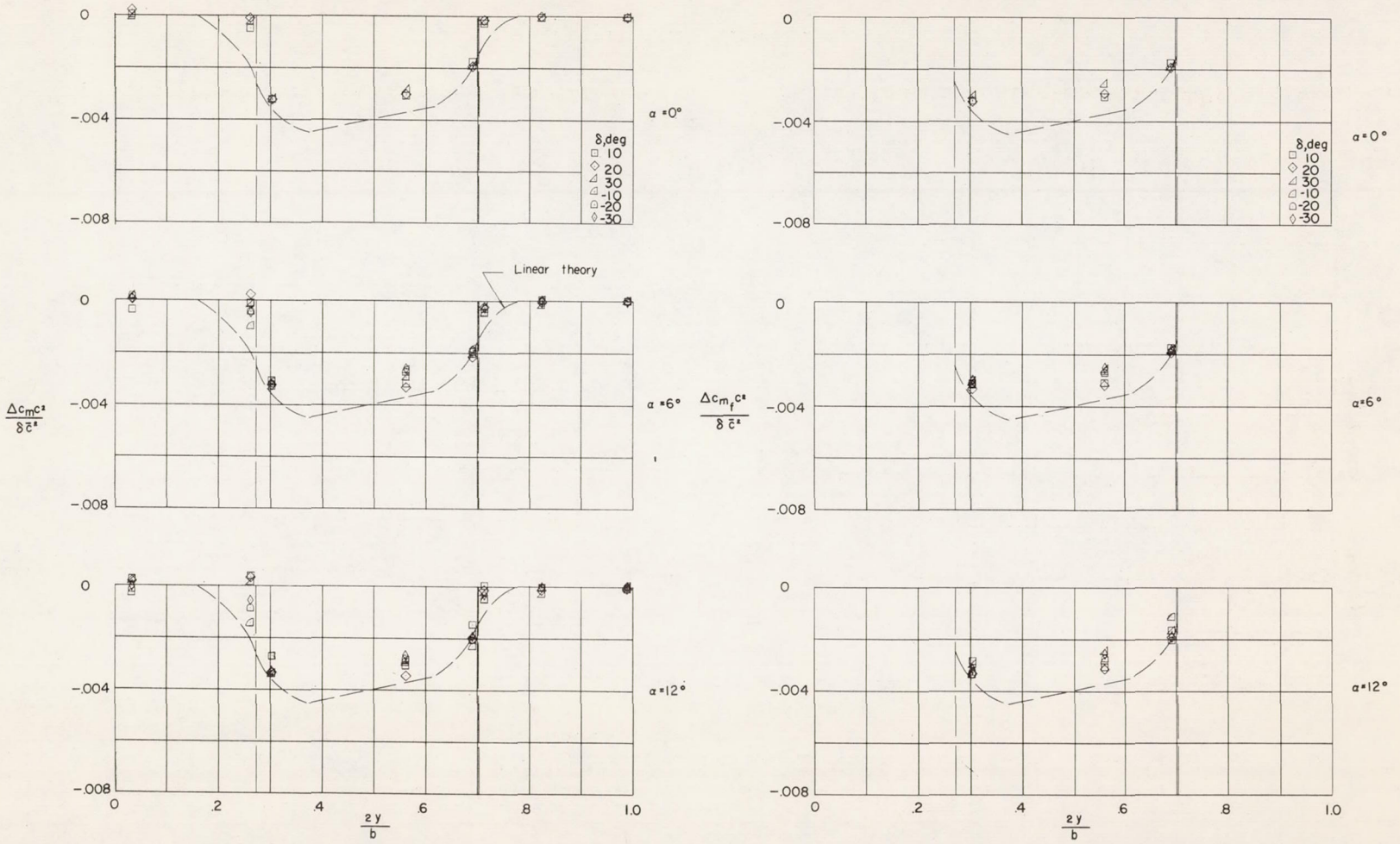

(a) Wing pitching-moment loading due to δ. (b) Control pitching-moment loading due to δ.

Figure 56.- Spanwise pitching-moment loading distributions for configuration 2. M = 2.01; R = 3.6×10^6.

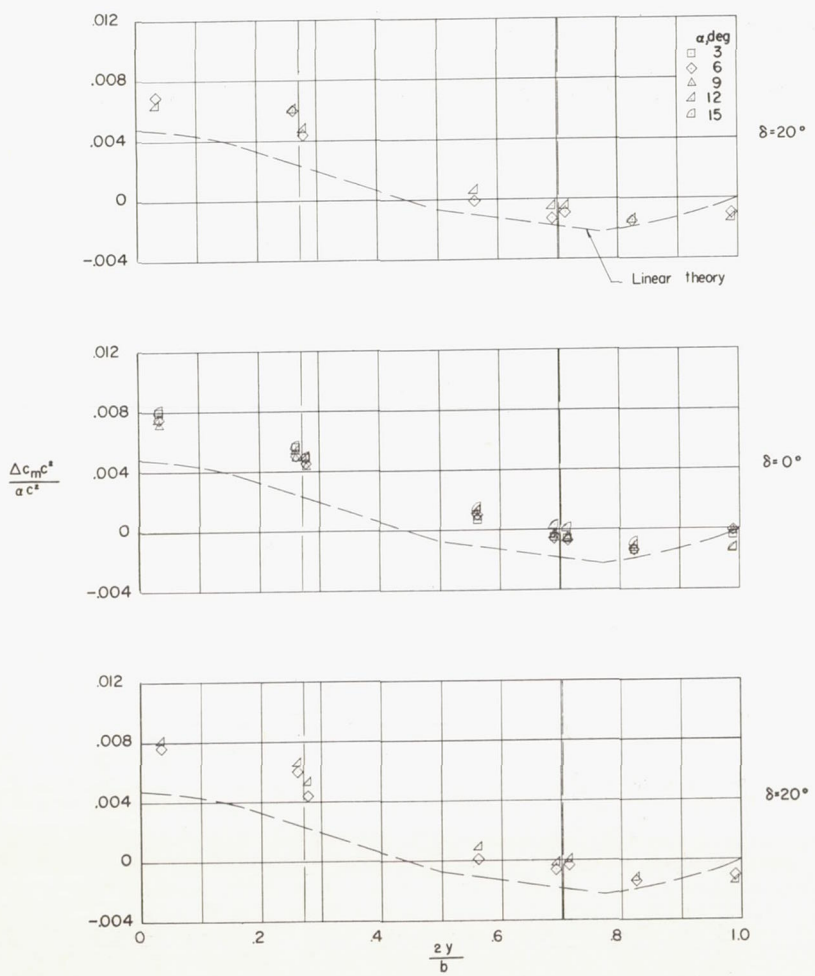

(c) Wing pitching-moment loading due to α.

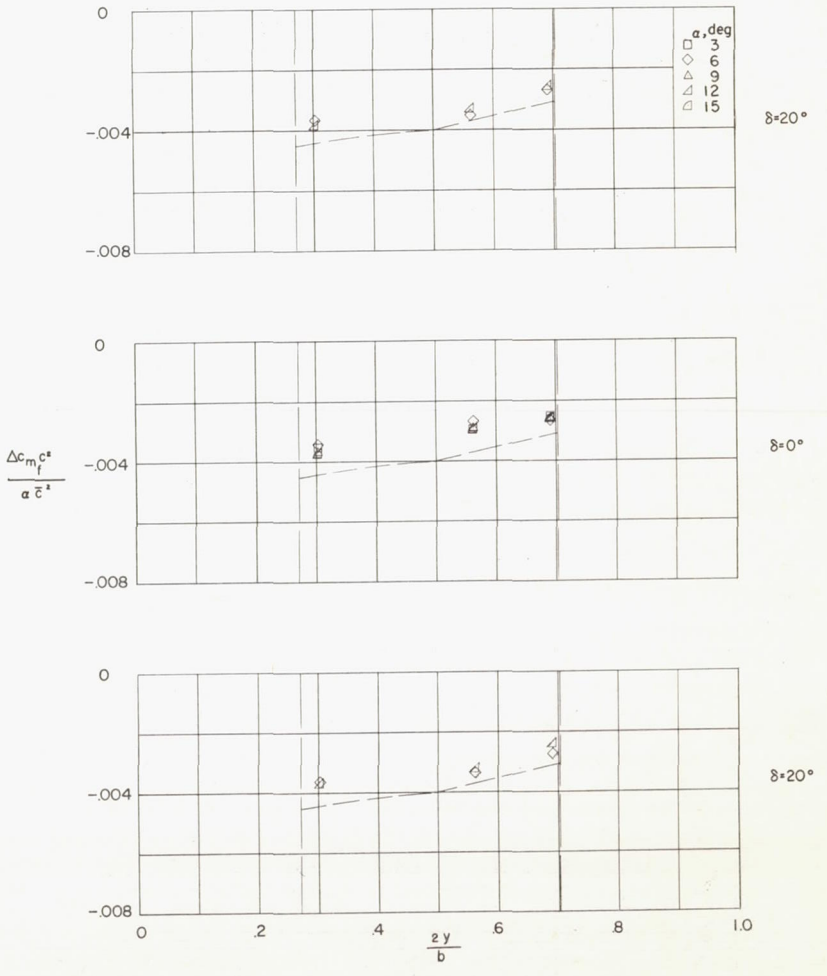

(d) Control pitching-moment loading due to α.

Figure 56.- Concluded.

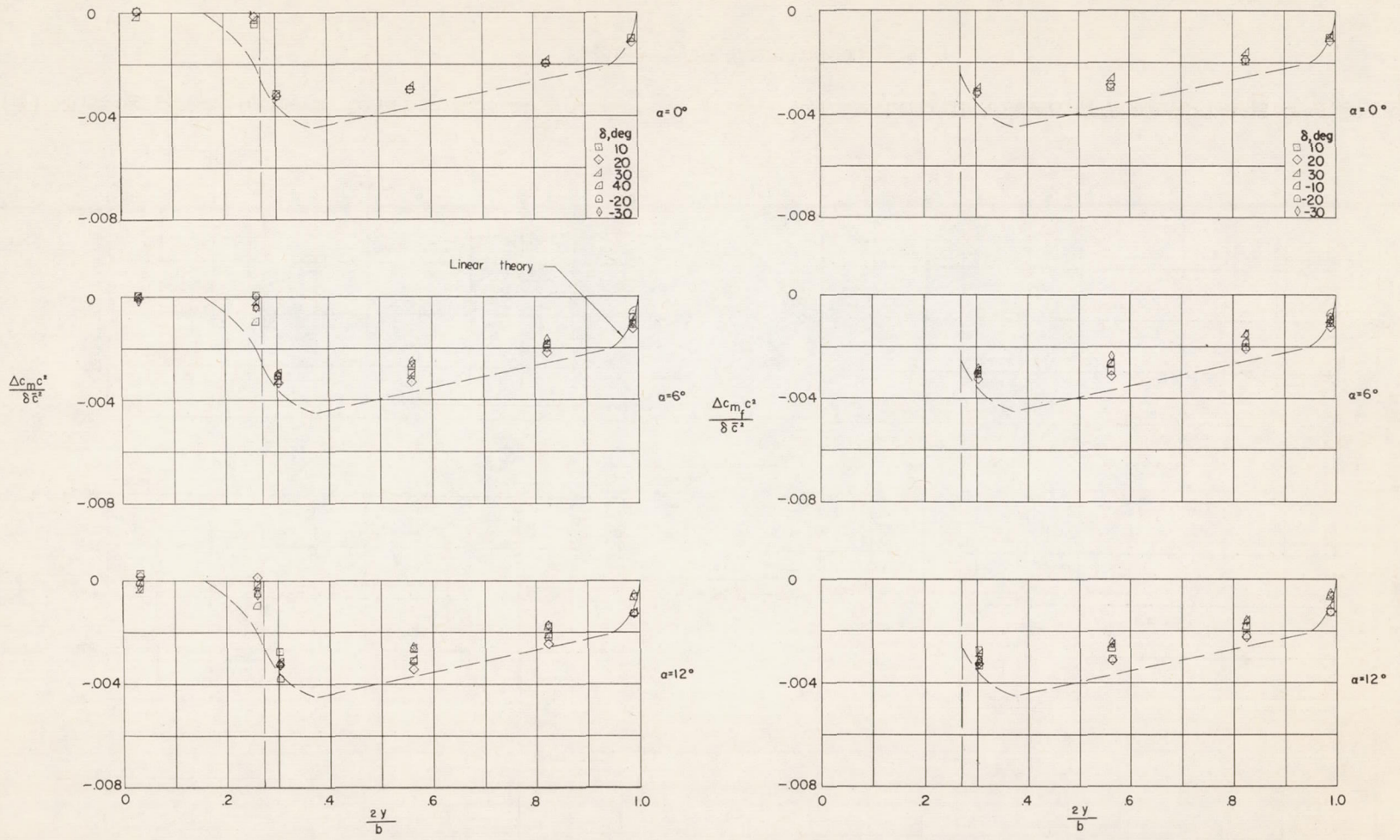

(a) Wing pitching-moment loading due to δ.

(b) Control pitching-moment loading due to δ.

Figure 57.- Spanwise pitching-moment loading distributions for configuration 3.
$M = 2.01$; $R = 3.6 \times 10^6$.

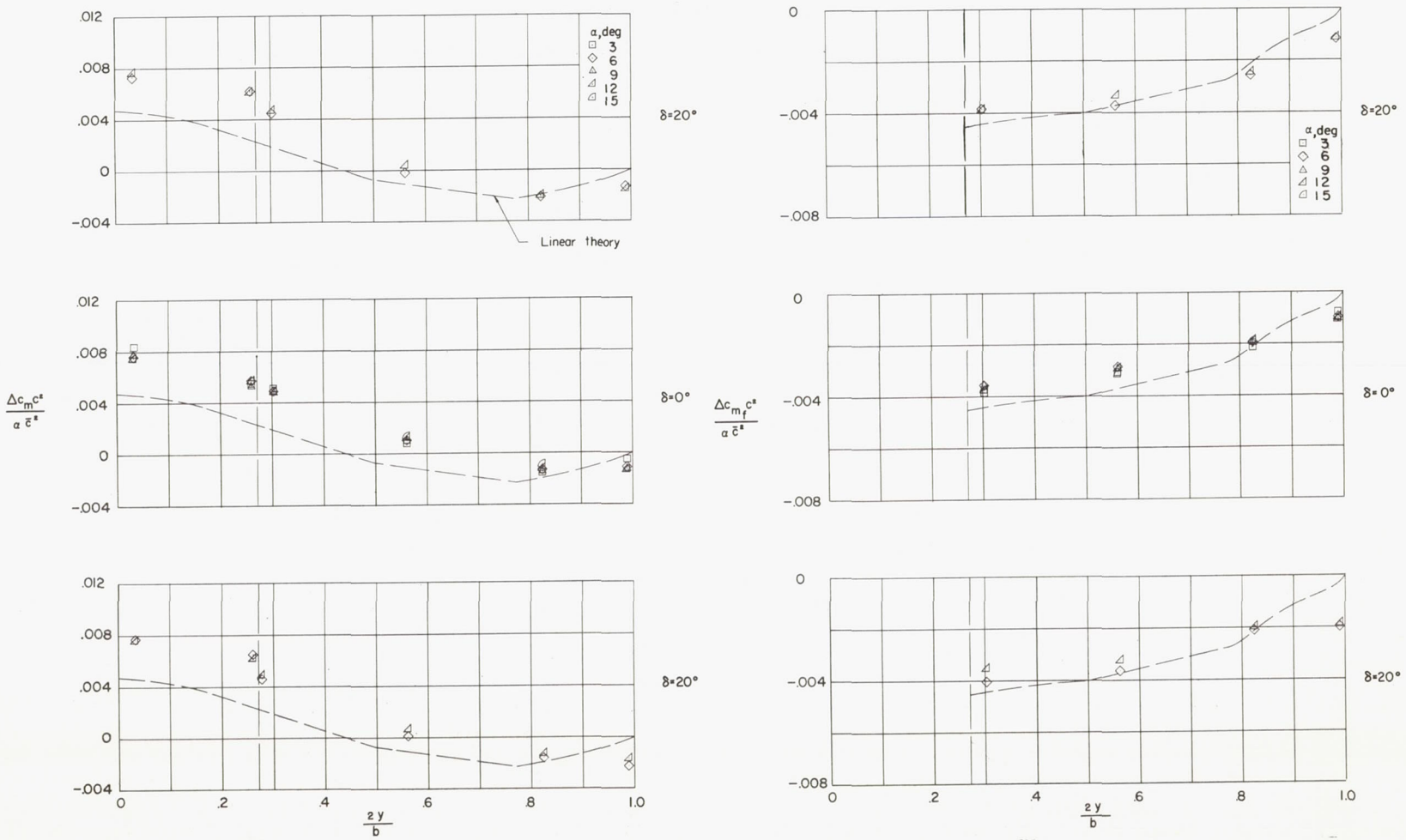

(c) Wing pitching-moment loading due to α.

(d) Control pitching-moment loading due to α.

Figure 57.- Concluded.

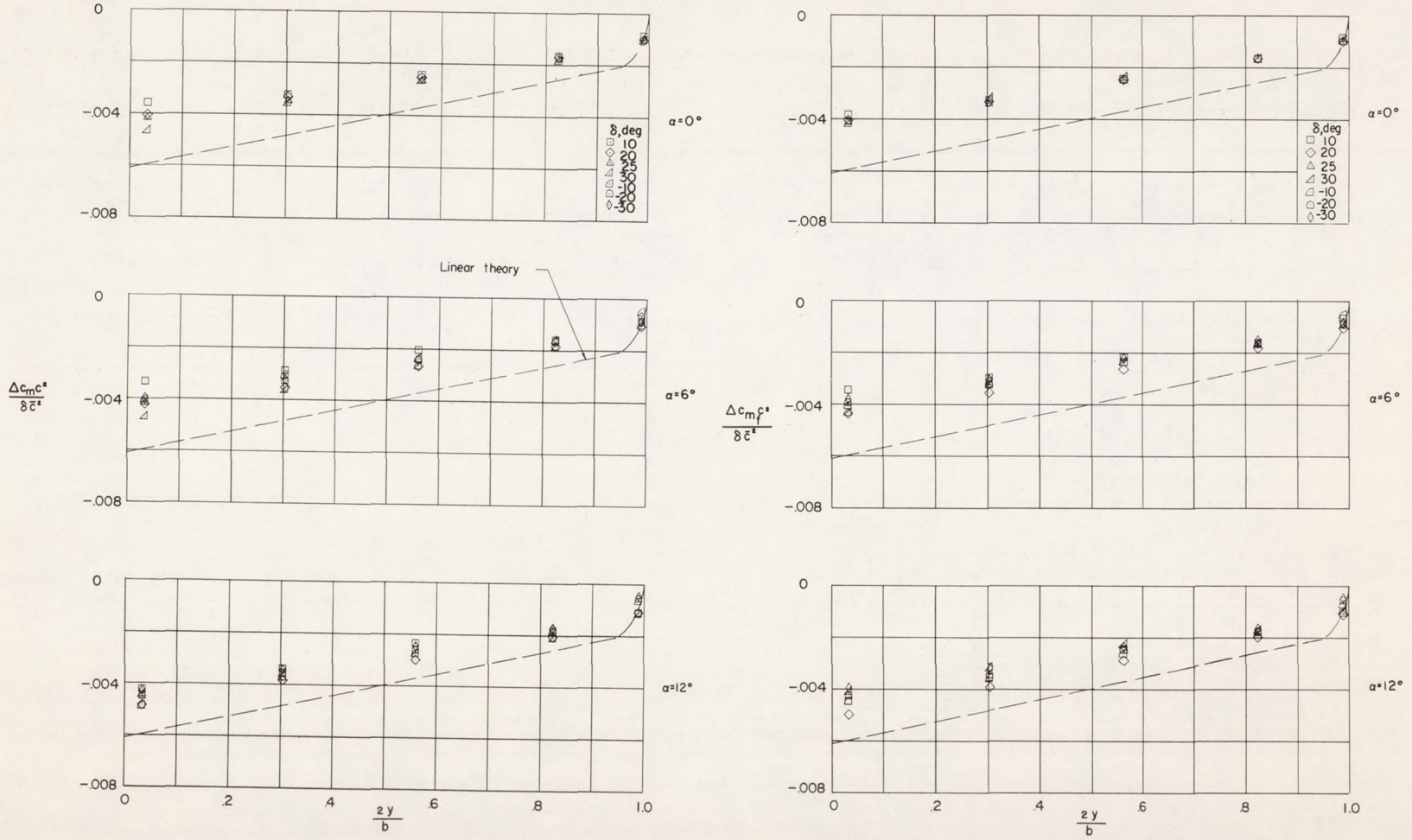

(a) Wing pitching-moment loading due to δ.

(b) Control pitching-moment loading due to δ.

Figure 58.- Spanwise pitching-moment loading distributions for configuration 4.
$M = 2.01$; $R = 3.6 \times 10^6$.

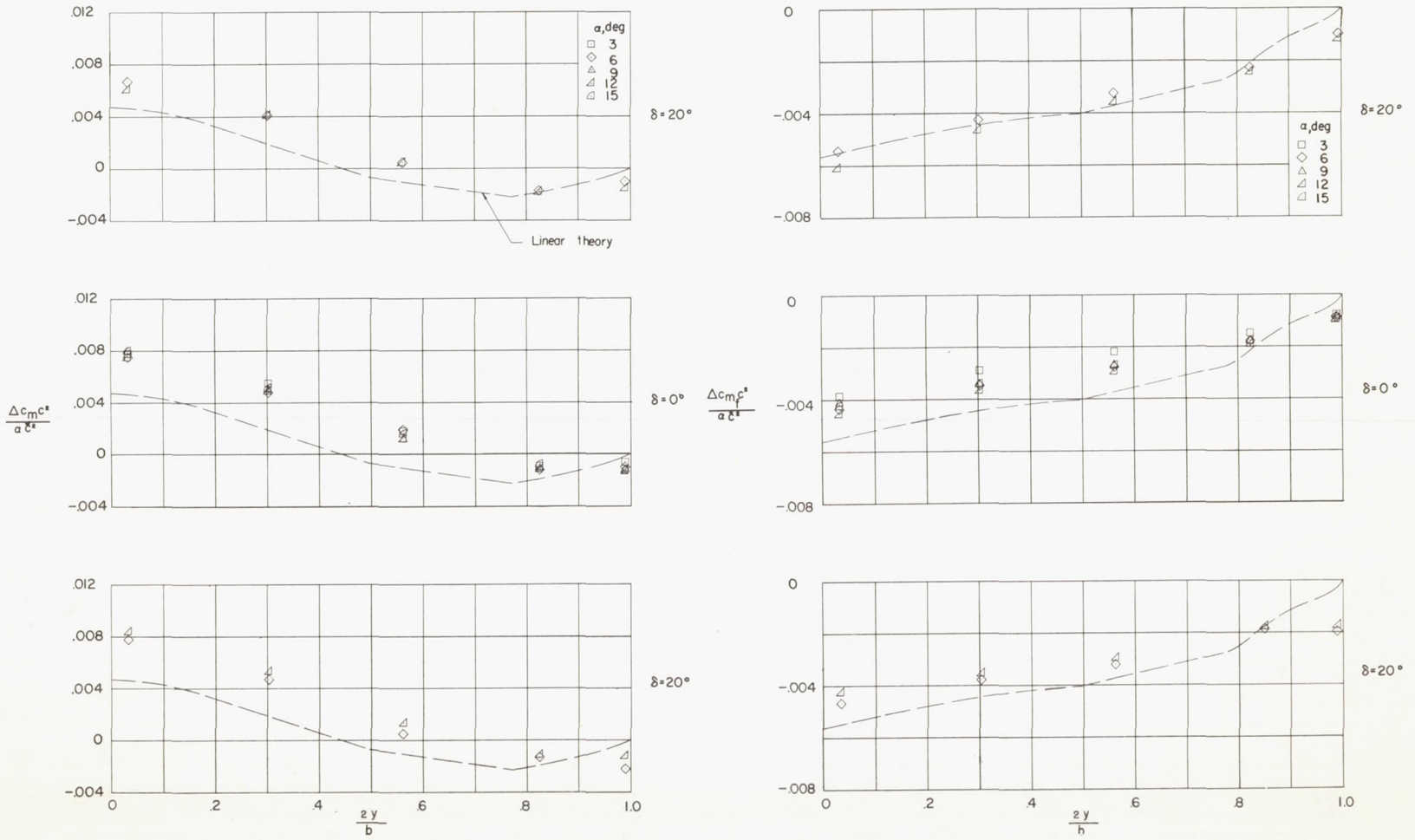

(c) Wing pitching-moment loading due to α.

(d) Control pitching-moment loading due to α.

Figure 58.- Concluded.

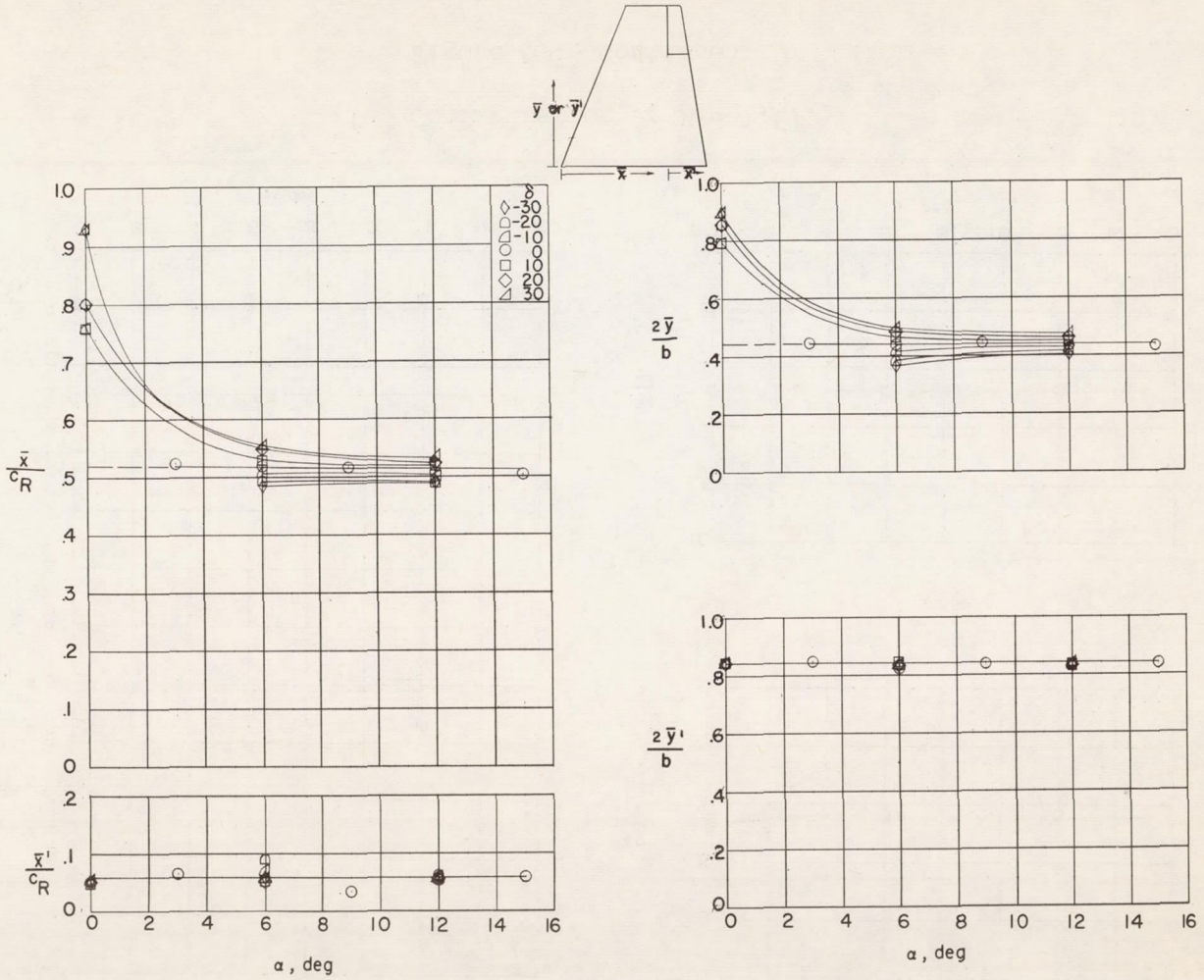

(a) Configuration 1; M = 1.61.

Figure 59.- Variation of chordwise and spanwise locations of wing and control-load center of pressures with angle of attack. R = 3.6×10^6.

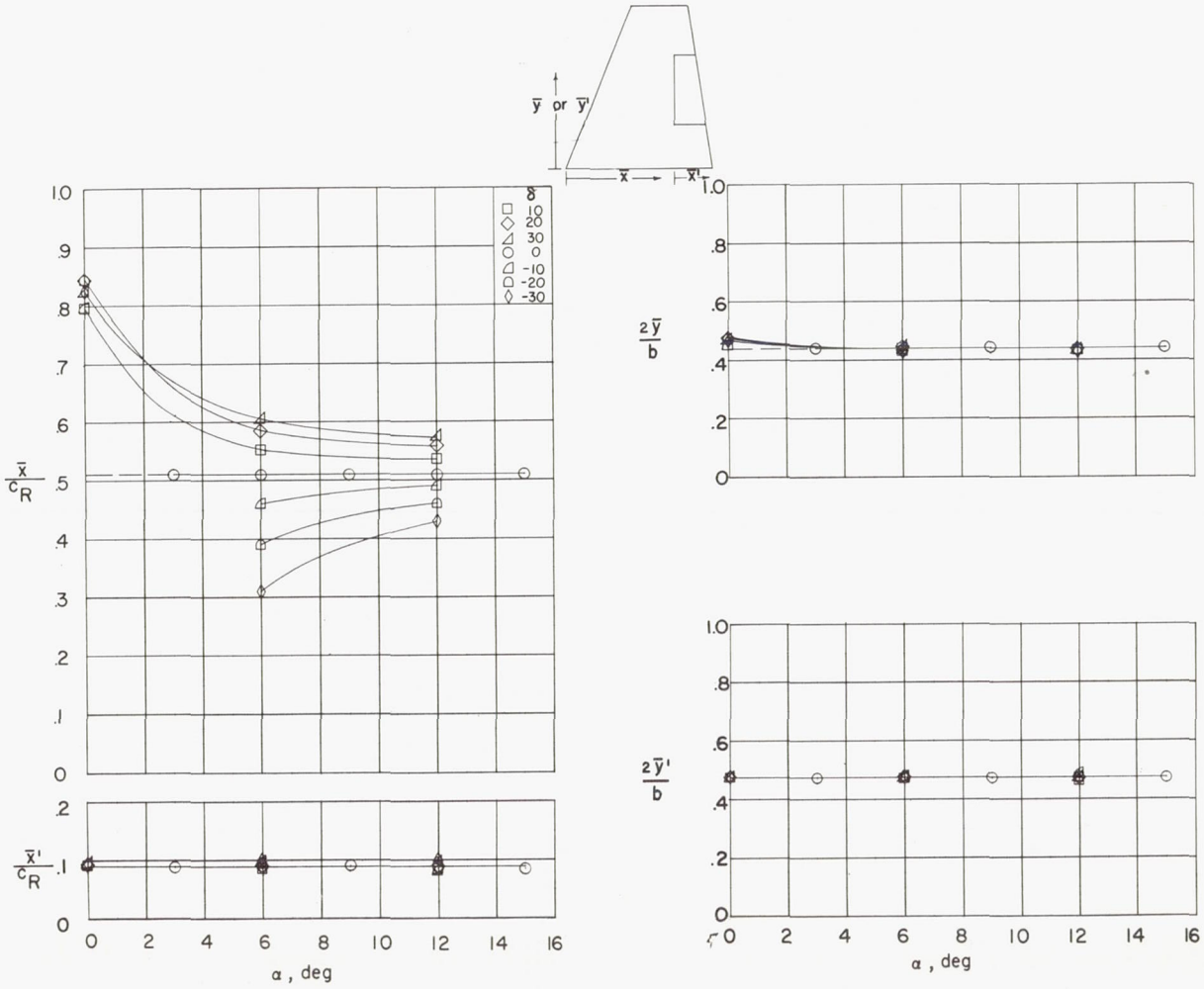

(b) Configuration 2; M = 1.61.

Figure 59.- Continued.

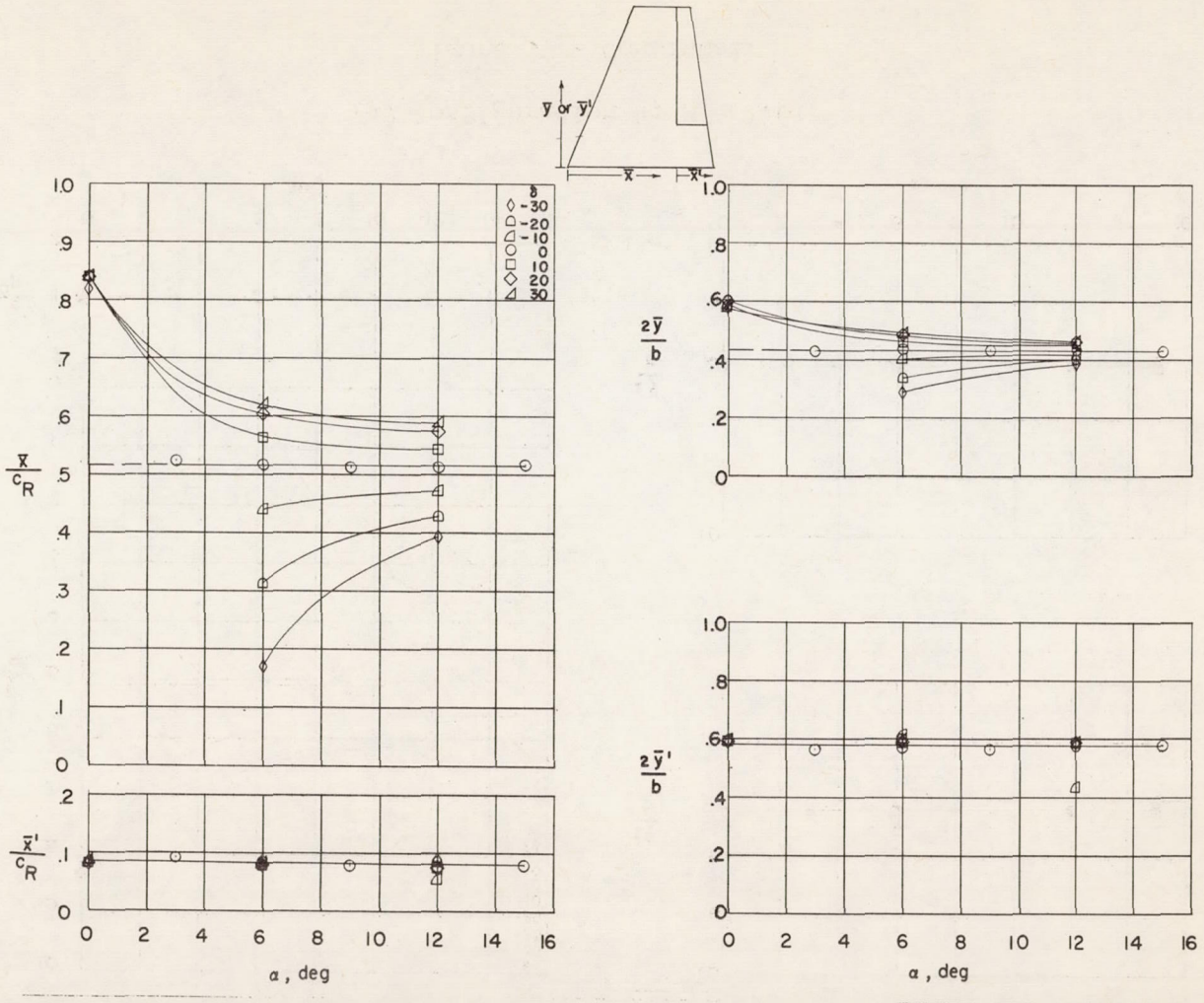

(c) Configuration 3; M = 1.61.

Figure 59.- Continued.

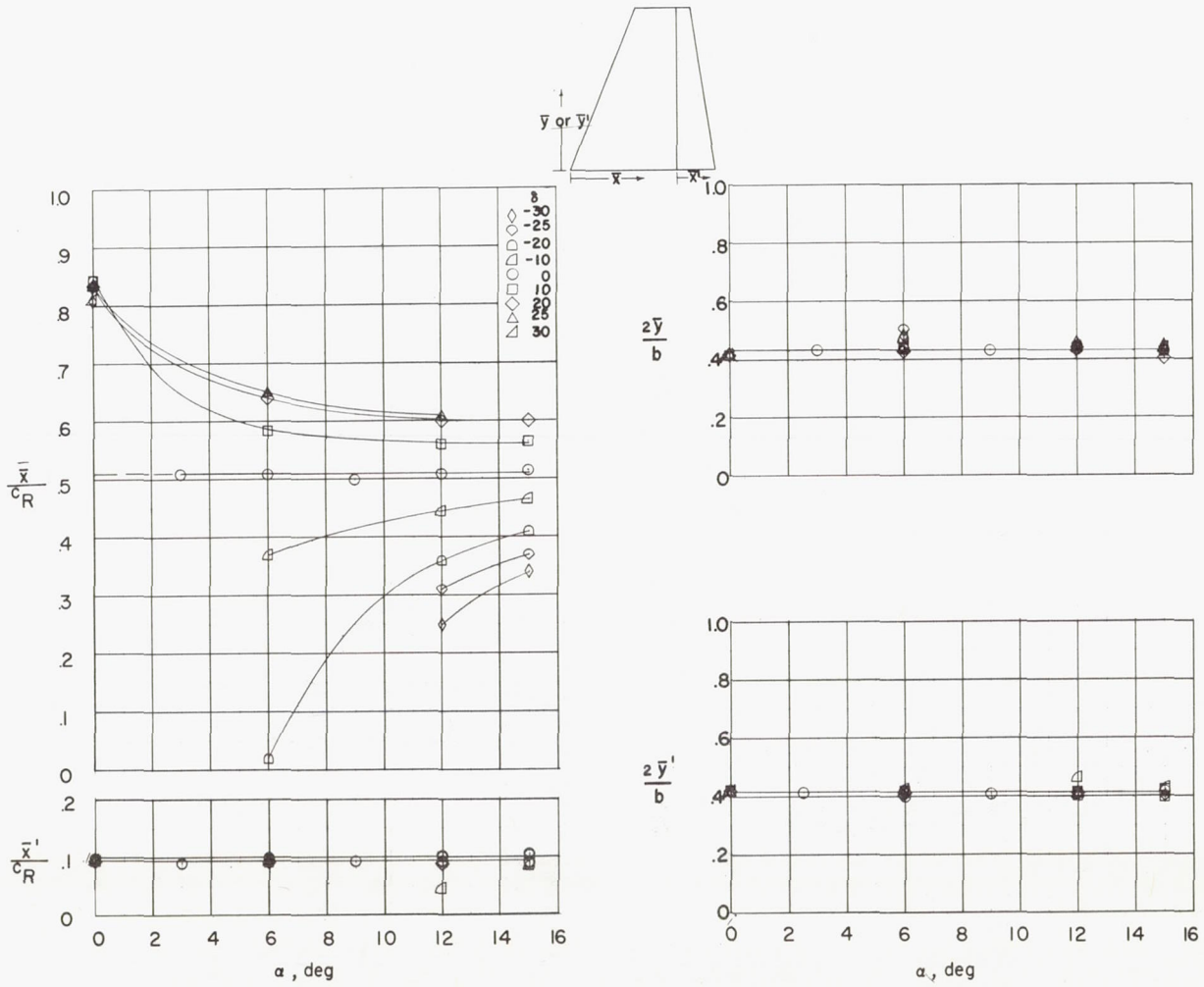

(d) Configuration 4; M = 1.61.

Figure 59.- Continued.

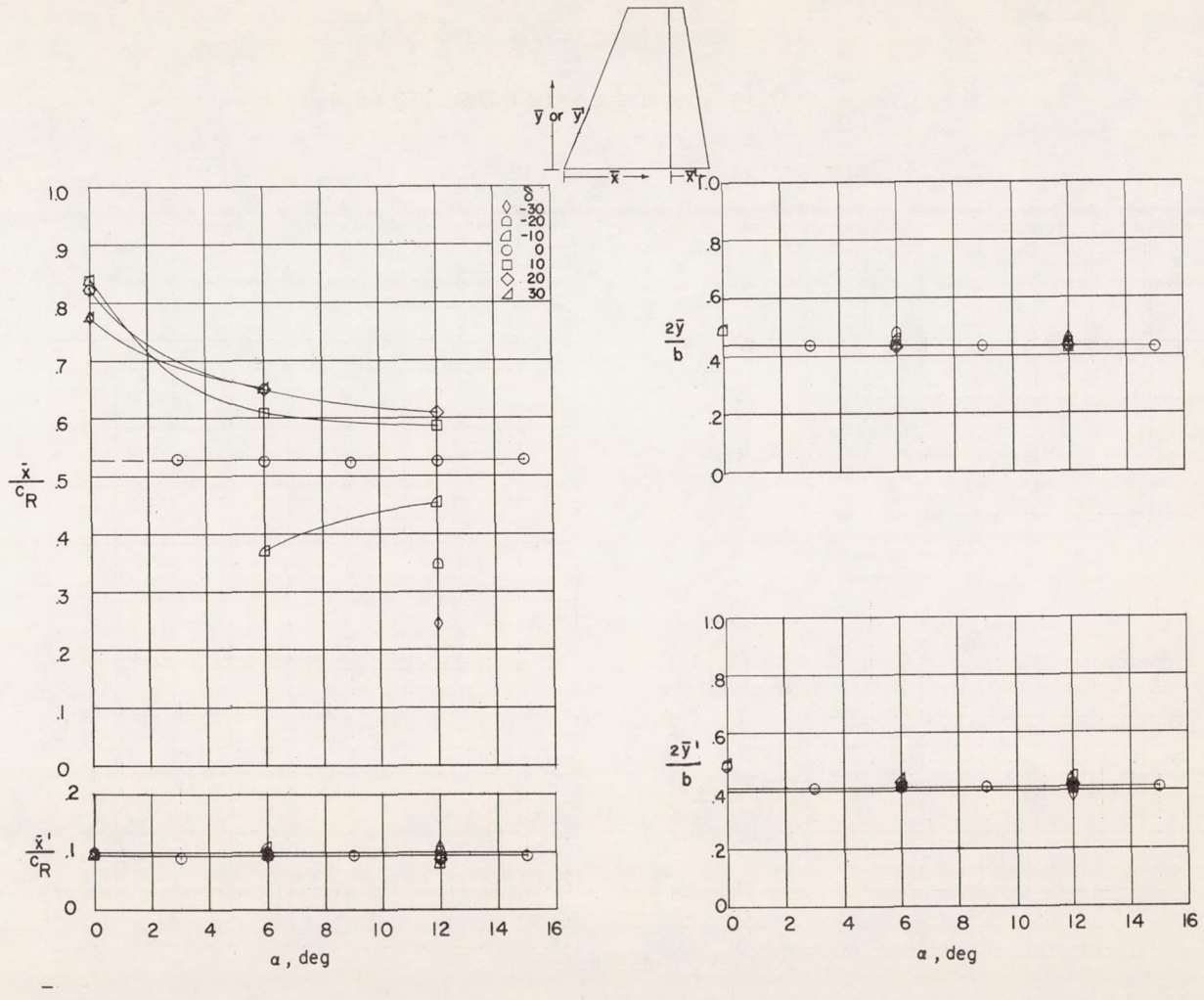

(e) Configuration 5; M = 1.61.

Figure 59.- Continued.

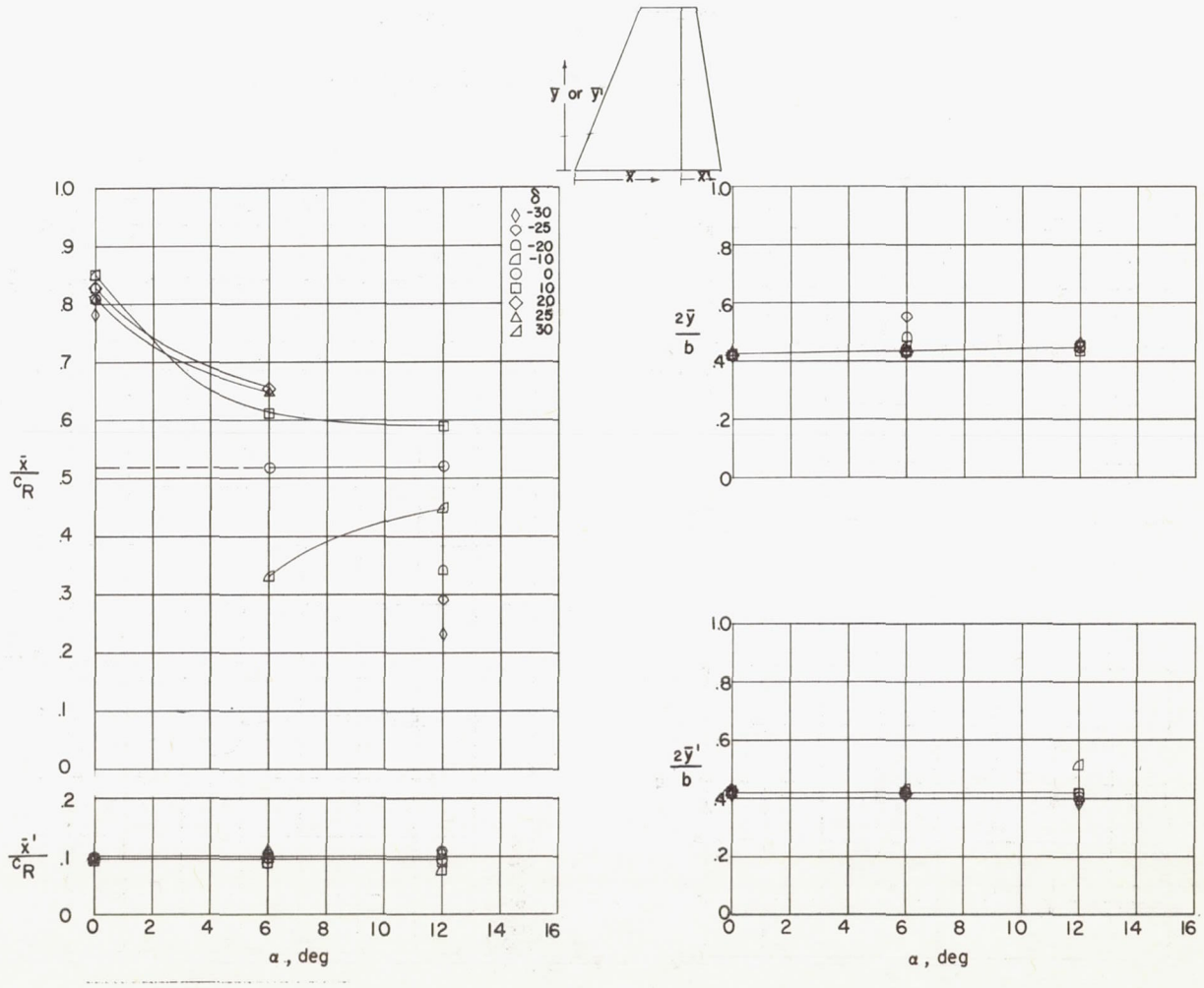

(f) Configuration 6; M = 1.61.

Figure 59.- Continued.

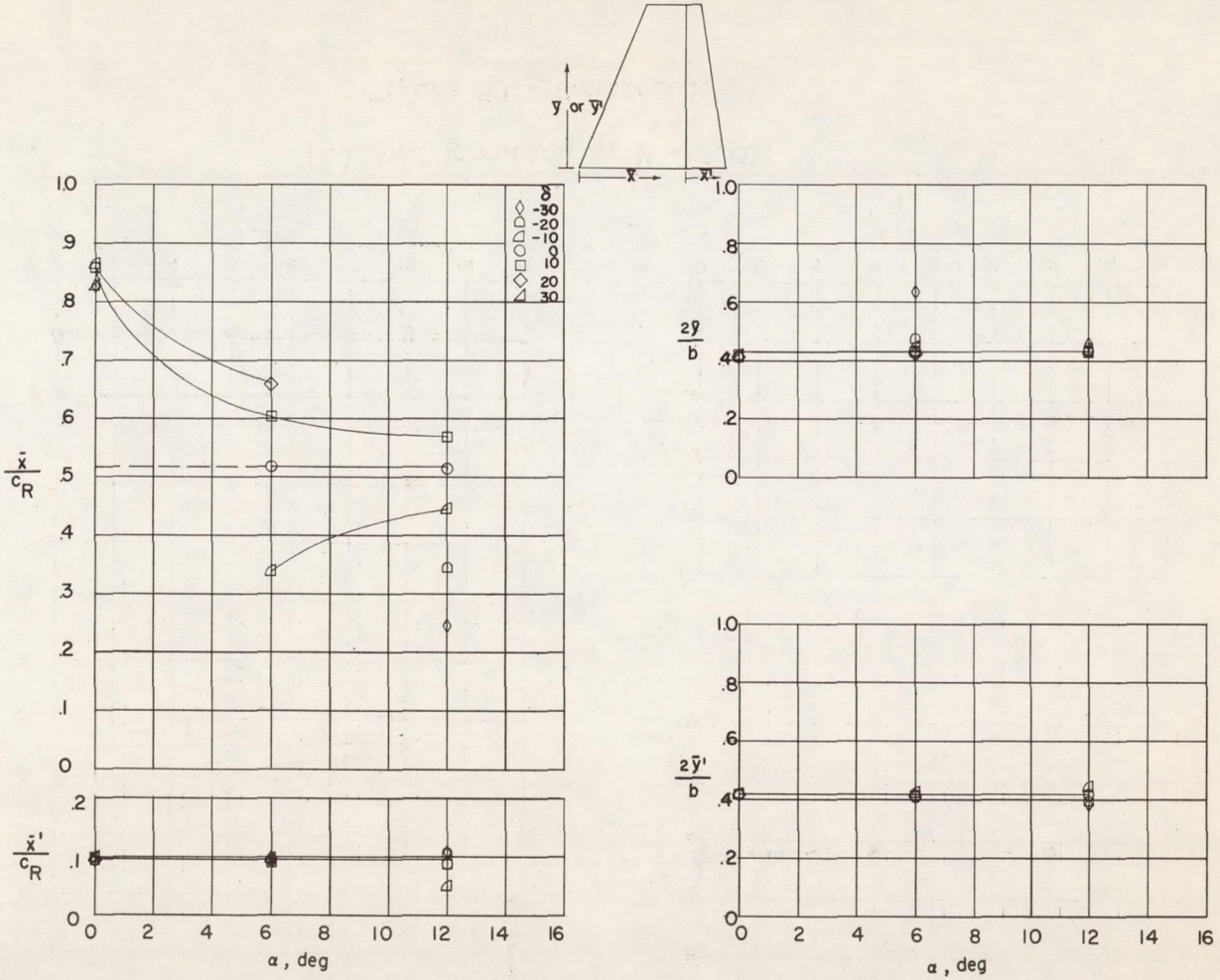

(g) Configuration 4 with 0.20-inch hinge-line gap; M = 1.61.

Figure 59.- Continued.

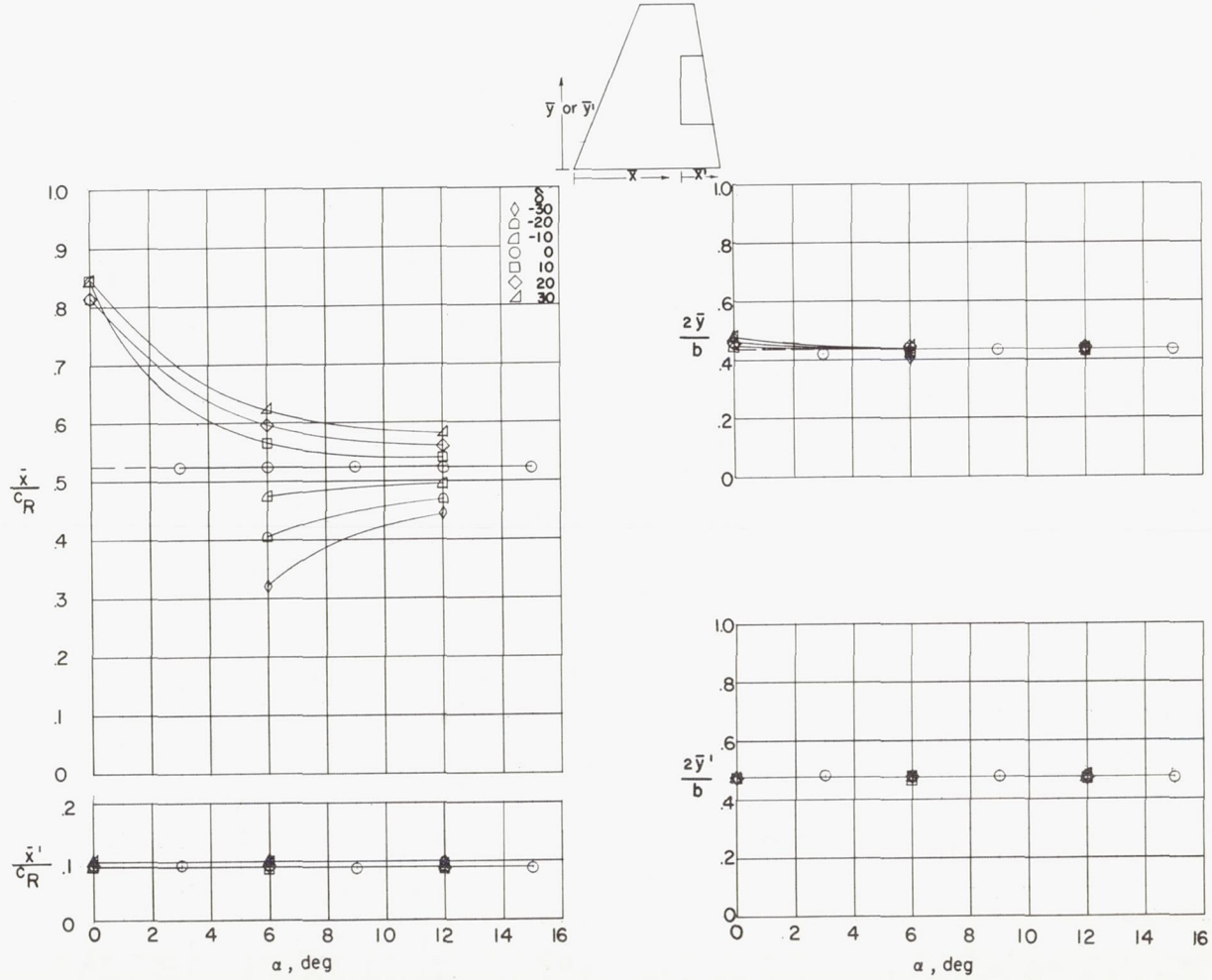

(h) Configuration 2; M = 2.01.

Figure 59.- Continued.

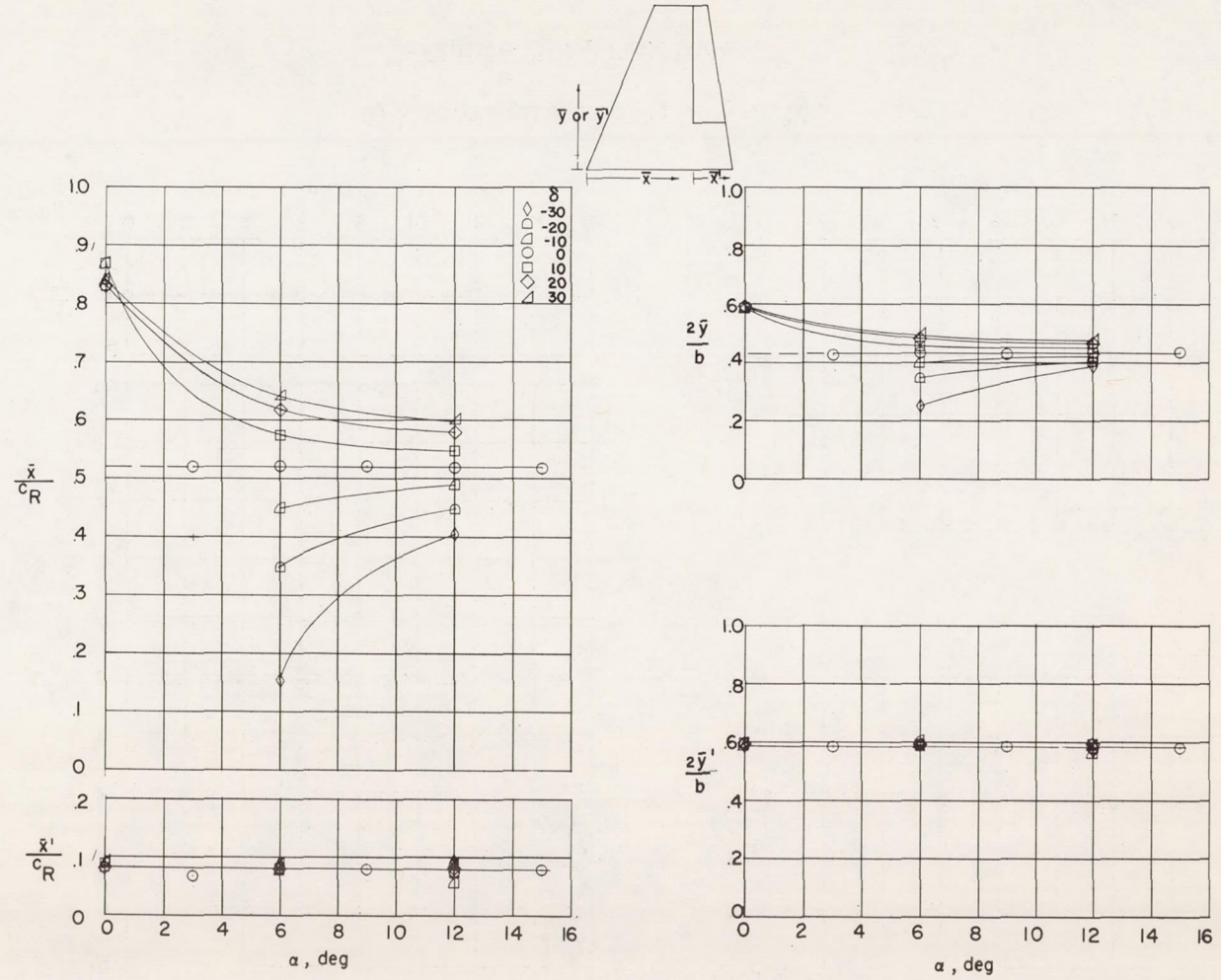

(i) Configuration 3; M = 2.01.

Figure 59.- Continued.

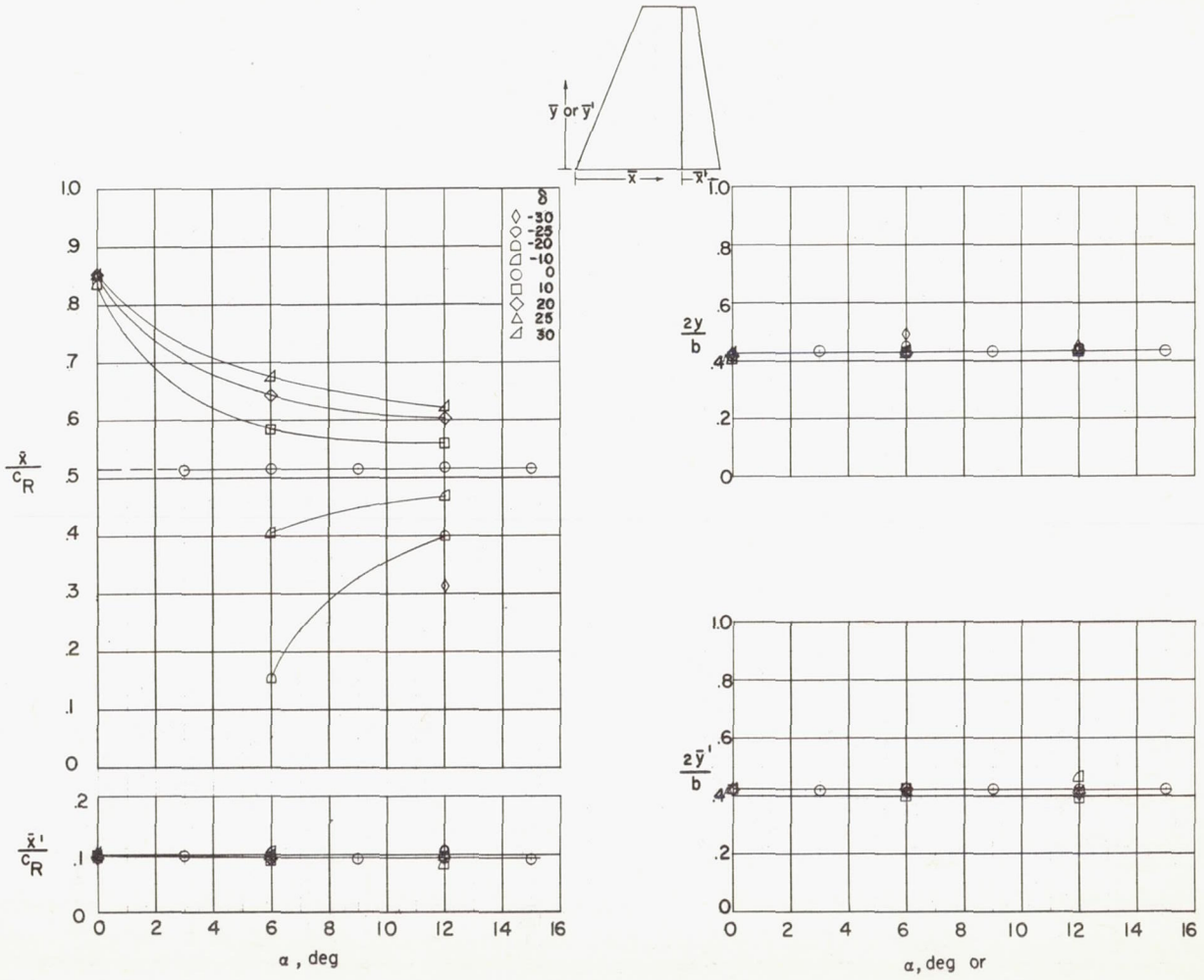

(j) Configuration 4; M = 2.01.

Figure 59.- Concluded.